Potentials of Synchrotron Radiation Induced X-ray Standing Waves and X-ray Reflectivity Measurements in Material Analysis

Markus Krämer

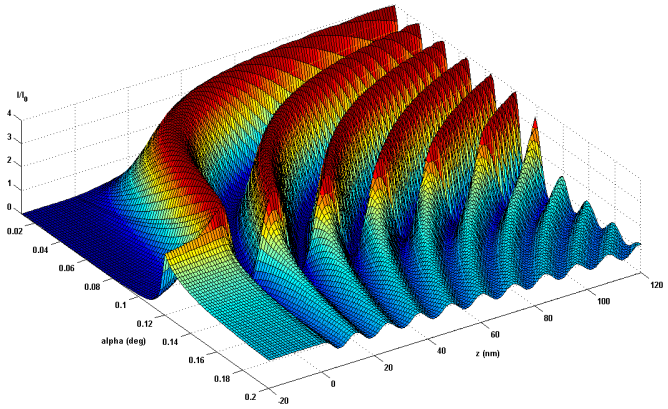

A thesis submitted in fulfillment of the requirements for
the degree of Doctor of Natural Sciences
in the subject of Physics

Department of Physics
at the
University of Dortmund

February 2007

Contents

List of Figures

List of Tables

1. Introduction

The universe into which we were born, and in which our species evolved, runs by rules - and science is our way of trying to work out what the rules are. But the universe that we are now constructing for ourselves is one that, to anyone other than a member of the design team and very possibly even to them, works by magic.

Terry Pratchett, *The Science of Discworld*

Even though science constantly reveals new aspects of this magic, there are still unlimited open questions[1] especially if the very big objects of the universe are regarded, as it is done by astronomers, or if the focus goes to the smallest components such as cells, molecules and atoms. Present day technology is capable of manufacturing devices based on components too small to observe even by a microscope. However, those devices can be found in every home such as many electronic devices. And nature is even more inventive in molecular "machines". Thus, scientists are obliged to have a look at ever smaller dimension.

Thin films, atomic or molecular mono- and multilayers are examples of those increasingly important structures in science and technology. Semiconductor and computer industry [15, 164, 168], laser and X-ray optics [103, 104, 105, 138, 140] as well as molecular biology are fields of major interest in present research [23, 43, 161, 162, 163, 174]. Thus, measurement methods for characterization and quality control of thin films in the nanometer range are increasingly required. Depending on the type of sample, a wide variety of different measurement techniques is available [69]. However, already existing powerful methods such as e.g. X-ray photoelectron spectroscopy (XPS), Auger electron spectroscopy (AES), secondary ion mass spectroscopy (SIMS), sputtered neutron mass spectrometry (SNMS) and glow discharge optical emission spectroscopy/mass spectrometry (GD-OES/MS) still have problems or inherent limitations. Either they are dependent on calibration procedures relying on standards that often do not exist (GD-OES/MS, XPS, AES, SIMS), or they are only vacuum compatible (e.g. SIMS, XPS, AES), or are difficult to use on non-conducting samples.

Thus, new or advanced techniques are still demanded. If nanometer and sub-nanometer in-depth resolution is required, the achievable sensitivity and resolution of existing methods is often not adequate. A comparison between several methods for depth profiling (XPS, SNMS, grazing incidence X-ray fluorescence (GI-XRF), Rutherford backscattering (RBS) and total-reflection

[1] *Sometimes, the best answer is a more interesting question.* (Terry Pratchett)

XRF (TXRF)) showed that discrepancies of up to one order of magnitude in the parameters measured with different methods can occur, mainly due to calibration problems [73].

X-ray related methods such as X-ray reflectivity (XRR) [81, 129, 143, 149, 164], X-ray absorption, or X-ray standing waves (XSW) [83, 82, 171] are techniques that are suitable for a wide range of thin film and multilayer samples, and that have the potential to overcome some of the existing limitations. They are non-consumptive, require little or no sample preparation and no external standards, and have short measuring times if they are used in combination with a synchrotron radiation (SR) source. In addition to a photon flux orders of magnitude more than an X-ray tube synchrotron radiation offers the advantage of precisely tunable photon energy up to several tens of keV. Even if SR-based techniques cannot be used routinely they can serve as a reference method to validate existing methods or as a start and proof of principle to develop new methods that might later be advanced to be applicable in a laboratory.

XRR is a powerful method for measuring dimensions (thickness, roughness) of thin layers in the nanometer range as well as determining optical constants (dispersion, absorption) of layered materials. However, a distinct contrast in these constants at interfaces between layers is essential for XRR analysis. X-ray fluorescence (XRF) methods [117] on the other hand are element sensitive and thus capable of separating optically similar materials. The XSW technique expands XRF fluorescence methods by the feature of lateral sensitivity and thus opens interesting new perspectives in this field of analysis, especially in combination with other methods.

XSW in general is based in the fact that incident longitudinally coherent electromagnetic waves interfere with out-going waves reflected at surfaces or interfaces. Together they form a static intensity pattern that can be regarded as a ruler with subnanometer resolution. Although the XSW technique was developed about 40 years ago, it has only become really exploitable recently with the availability of high photon fluxes provided by second and third generation synchrotrons, such as ESRF [36, 37, 131, 132], NSLS [27, 65, 88, 127, 148], APS [27, 95], SRS [35, 67], DELTA [83, 82] or others [90, 102, 151, 162, 163].

XSW measurements are commonly performed around the Bragg angle of reflection [27, 36, 37, 90, 95, 102, 127, 148] or at normal incidence (NI-XSW) [35, 65, 67, 132]. Multilayers [51, 90, 95] or crystal lattices [65, 88] are subject to most of these investigations, which are well suited to characterize periodic structures. However, a periodicity in the sample (crystal lattice or periodic multilayer) is mandatory for these kinds of XSW measurements and limits its applicability. In contrary, X-ray standing waves at grazing incidence (GI-XSW) [23, 83, 82, 82, 151, 152, 162, 163] - also called long-period XSW - presented in this work require only one or several flat, reflecting interfaces and so-called marker atoms emitting detectable fluorescence radiation. Distances in a GI-XSW intensity pattern are in the range of nanometers and permit characterization of structures of this order of magnitude.

In this work the potential of X-ray standing waves measurements at grazing incidence and of a combination of XRR and XSW based on synchrotron induced X-ray radiation was investigated with a wide variety of layered sample systems in the nanometer range. As the two methods require a very similar experimental set-up combination is easy to realize. XRR and XSW measurement procedures are described in detail and discussion of various experimental results enlightens this novel analysis approach.

Available existing XSW analysis software tools [89, 92, 167] are mainly written to be used with solid multilayers. However, future application envisioned demand a more flexible approach. Solid-liquid interfaces relevant for technological surfaces or biological membranes require evaluation programs capable of calculating XSW intensity distributions customizable for arbitrary sample systems. Therefore, a new software tool was developed and partially tested with a wide selection of solid and liquid, semiconductor, bio-organic, and technological layered systems, and related samples to inspect the potentials and limits of XRR and XSW measurements.

This thesis is structured as follows. First, the *theoretical background* of X-ray scattering and X-ray reflectivity is outlined for a single surface and multilayer systems in chapter 2. Then, the principles of X-ray fluorescence measurements and total-reflection X-ray fluorescence analysis is presented. After that, properties and calculations of X-ray standing waves as the focus of this work are discussed extensively. A presentation of several methods to describe interface roughness quantitatively rounds off the theory chapter.

Chapter 3 introduces the wide selection of *samples* investigated in this work. The first section treats semiconductor samples, namely germanium layers on silicon and ion implantations in silicon substrates. Bio-organic samples are presented in the extensive second section of the sample chapter. Here, biological molecules such as cytochrome proteins or phospholipids are discussed as well as technologically important organic materials such as polymers, dendrimers and nitrobenzene. Some samples have inherent marker atoms (such as Fe in cytochrome, P in phospholipid or N in nitrobenzene), onto some metal atoms as markers were evaporated, or markers were components of mandatory buffer solutions on the sample. Finally, in the third section two other types of samples are presented: A periodic multilayer structure in a laser mirror and different models of ion distributions at solid-liquid interfaces.

Chapter 4 covers the *experimental* procedures utilized in this work. First, the various measurement stations and equipment used for measurements are presented. Then, the specific set-up and measurement procedures for the three methods applied in this work (XRR, TXRF and XSW) are explained.

The following chapter 5 presents the *simulation program for X-ray standing waves* developed during this work. First, the multiple parameters and models and their integration into the computer program are presented. Then, an evolutionary fitting algorithm applied in the program is outlined. Finally, several calculated XSW fields are presented to enlighten the functionality of the program.

Evaluation of measurements of all samples is performed in chapter 6. *Results* are discussed and compared to expected or published values.

The *summary* in chapter 7 gives an overview over the results obtained. Applicability of the methods presented here is valuated.

Finally, the extensive *appendix* lists acronyms and tabulated values used in this work, describes some sample preparation or longer calculations, and computer programs and publications utilized for and evolved from this work are shown.

2. Theoretical background

X-rays as well as electromagnetic waves in general can interact with matter in various ways. *Scattering* (cf. section 2.1) is a very general term for the change in energy and direction of propagation of an X-ray photon hitting an atom. Specular scattering (cf. 2.1.1) - that means the incident beam is reflected at an angle equal to the angle of incidence - and diffuse scattering (cf. 2.1.2) with radiation scattered in any direction can be distinguished here. *Diffraction* can occur if an X-ray beam hits a special ordered structure like a crystal lattice or grating. Depending on the angle of incidence, beams reflected at neighboring lattice planes can interfere constructively and in consequence strong intensity peaks arise. *Refraction* (cf. 2.1.1) as a special case of scattering occurs at interfaces between media with different refractive indices and causes the beam to change its direction of propagation or angle of incidence, respectively. *Fluorescence*, in contrary, differs from the other mentioned interaction types. Here a photon loses energy (and changes direction) kicking out an inner electron of an atom. The "hole" in the electron shell is then refilled by an outer electron. Simultaneously, a detectable fluorescence photon is emitted. Fluorescence is described in section 2.2.

To understand and calculate X-ray standing waves all of these phenomena are important. Scattering describes the interaction between X-rays and the sample, diffraction and refraction explain how the beam is reflected and transmitted in lattice-type or layered samples, respectively. And finally, X-ray fluorescence provides a detectable signal from the atoms in the sample that displays the structure of the XSW field.

2.1. X-ray scattering and X-ray reflectivity (XRR)

Scattering experiments can be performed to analyze the structure of many different materials. Electrons, neutrons and other particles can be utilized for such experiments, as well as electromagnetic waves (in particular X-rays) that are subject to this work. The latter - having a wide spectrum of wavelengths - play an important role in scattering methods because it is possible to choose exactly the wavelength suitable for a certain task. For example, hard X-rays of energies in the range of 10 keV have a wavelength around 1Å that is in principle small enough to resolve atomic structures, which is not possible with visible light of wavelengths around 500 nm. However, also structures in the micrometer range are accessible by X-rays. This chapter gives an overview on properties and requirements of X-ray scattering.

Specular X-ray scattering is discussed in chapter 2.1.1. Here, the beam between incident beam and reflecting surface equals the angle reflected beamand the surface ($\alpha_\mathrm{i} = \alpha_\mathrm{f}$). It has to be noted that "angle of incidence" in this work always denotes the angle between incident beam and reflecting surface. Thus an angle of incidence of 0° means that the beam is parallel

to the surface while 90° stands for normal incidence. If the incident angle is below a material dependent critical angle α_c the entire radiation is reflected at a surface if it is ideally flat. For finite roughnesses or larger angles part of the radiation enters into the material, part is reflected, and the rest is lost by diffuse scattering.

Specular X-ray scattering can deliver averaged information about properties of the sample perpendicular to the surface. For this reason, diffuse X-ray scattering is often a useful method to characterize the lateral structure of a surface. It is described shortly in chapter 2.1.2, a detailed discussion can be found in [42, 139, 149]. Often, samples consist of more than one layer. These multilayer systems with several reflecting interfaces are presented in section 2.1.3. There, the question of how to extract information about the different layers from the whole reflectivity signal is discussed further. Finally, roughness of interfaces is an effect that often cannot be neglected in practical samples. Several models to simulate interface roughness are presented in chapter 2.4, e.g. the effective density model or kind of a Debye-Waller factor.

2.1.1. Specular X-ray scattering

Wave vector transfers in scattering experiments with small incident and exit angles are generally smaller than the reciprocal lattice vectors of a crystal structure. Thus, the influence of this crystal structure (if the sample is a crystal) is negligible, and the intensity distribution of the scattered radiation gives information on the electric potential (and by that on the electron density distribution) of the sample.

In the following, basic equations of X-ray scattering are presented which also introduce the nomenclature for formulae used in this work. An electromagnetic wave can be described by the equation [144]

$$\vec{E}(\vec{r}) \quad = \quad \vec{E}_0 \exp(\mathrm{i}\vec{k}\vec{r}), \tag{2.1}$$

with $\vec{E}(\vec{r})$ representing the electric field at position $\vec{r}$, $\vec{E}_0$ the maximum field amplitude and $\vec{k}$ the wave vector of the electromagnetic wave. In an X-ray reflectivity measurement an electromagnetic wave is incident from vacuum (or air) onto a material with refractive index $n \neq 1$, being partly reflected and partly transmitted (and at the same time refracted). Within a medium the Helmholtz equation [149]

$$\Delta\vec{E}(\vec{r}) + k^2 n^2(\vec{r})\vec{E}(\vec{r}) = 0 \tag{2.2}$$

holds for the propagating wave with k as the absolute value of the wave vector $|\vec{k}|$, related to the wavelength λ by

$$k = \frac{2\pi}{\lambda}. \tag{2.3}$$

A medium containing N atoms per unit cell, that can be considered as harmonic oscillators with

resonance frequencies ω_j, has the refractive index [149]

$$n = 1 + N\frac{e_0^2}{\varepsilon_0 m_\mathrm{e}} \sum_{j=1}^{N} \frac{f_j}{\omega_j^2 - \omega^2 - 2\mathrm{i}\omega\eta_j}. \tag{2.4}$$

Here ω is the frequency of the incident electromagnetic wave, e_0 the unit charge, ε_0 the electrical field constant (permittivity of free space), m_e the rest mass of an electron, η_j the damping constant of the electrons of the respective atom and f_j the corresponding (forced) oscillator strength, the so-called atomic form factor. The latter can be calculated by

$$f_j(\lambda) \;=\; f_j^0 + f_j'(\lambda) + \mathrm{i}f_j''(\lambda), \tag{2.5}$$

where $f_j'(\lambda)$ and $f_j''(\lambda)$ are wavelength dependent dispersion and absorption corrections that are tabulated for virtually all elements and a wide range of photon energies [31, 59]. Equation 2.5 is also written as

$$f_j(\lambda) \;=\; f_j^1(\lambda) + \mathrm{i}f_j^2(\lambda) \tag{2.6}$$

with atomic scattering factors

$$f_j^1(\lambda) \;=\; f_j^0 + f_j'(\lambda) \tag{2.7}$$

$$f_j^2(\lambda) \;=\; f_j''(\lambda). \tag{2.8}$$

For hard X-ray radiation (in the energy range of some keV), $\omega \gg \omega_j$ applies and equation 2.4 can be simplified to [134, 135, 149][1]

$$n \;=\; 1 - \delta + \mathrm{i}\beta. \tag{2.9}$$

Equation 2.9 comprises the dispersion and absorption coefficients

$$\delta \;=\; \frac{\lambda^2}{2\pi} r_\mathrm{e}\rho_\mathrm{e} \sum_{j=1}^{N} \frac{f_j^0 + f_j'(E)}{Z} \tag{2.10}$$

$$\beta \;=\; \frac{\lambda^2}{2\pi} r_\mathrm{e}\rho_\mathrm{e} \sum_{j=1}^{N} \frac{f_j''(E)}{Z} = \frac{\lambda}{4\pi}\mu. \tag{2.11}$$

Here,

$$r_\mathrm{e} = \frac{e^2}{4\pi\varepsilon_0 m_\mathrm{e} c^2} \tag{2.12}$$

is the classical electron radius, c the velocity of light in vacuum, $Z = \sum_j Z_j$ the total number

[1] In some sources [12, 72] equation 2.9 is written as $n = 1 - \delta - \mathrm{i}\beta$. This is valid [146] if the wave equation 2.1 is written with a negative sign as $\vec{E}(\vec{r}) = \vec{E}_0 \exp(-\mathrm{i}\vec{k}\vec{r})$.

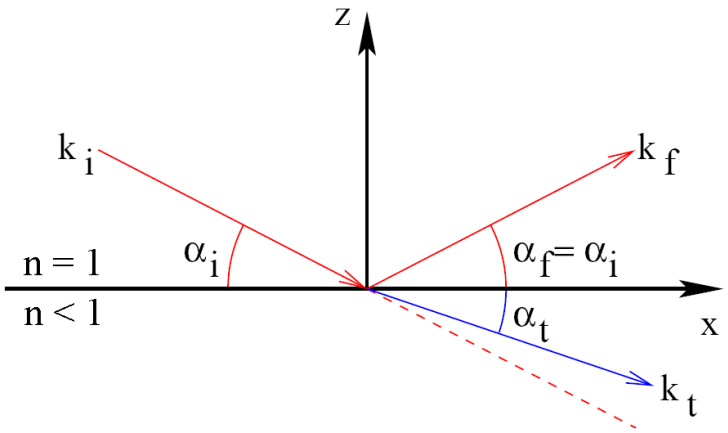

Figure 2.1.: Schematic illustration of reflection and transmission of an electromagnetic wave at grazing incidence on surface. The wave hits the surface at an angle α_i with wave vector $\vec{k}_\mathrm{i}$, is partly reflected at angle $\alpha_\mathrm{f} = \alpha_\mathrm{i}$ (with wave vector k_f) and partly penetrates the layer at angle $\alpha_\mathrm{t} < \alpha_\mathrm{i}$ (with wave vector k_t).

of electrons of each component of the material, μ the linear absorption coefficient and ρ_e the electron density

$$\rho_\mathrm{e} = \frac{Z\rho \cdot N_\mathrm{A}}{M_\mathrm{A}} \tag{2.13}$$

with the mass density ρ (in g/cm^3), Avogadro's number N_A and the atomic mass M_A (in g/mol). f_j^0 is dependent on the wave vector transfer $\vec{q} = \vec{k}_\mathrm{f} - \vec{k}_\mathrm{i}$ between incident ($\vec{k}_\mathrm{i}$) and reflected wave ($\vec{k}_\mathrm{f}$). In the case of small angles the approximation $f_j^0 \approx Z_j$ holds.

If the medium is homogeneous and the photon energy far enough from absorption edges the parameters in equation 2.9 can be simplified to (cf. [12, 72, 149])

$$\delta = \frac{\lambda^2}{2\pi} r_\mathrm{e} \rho_\mathrm{e} \tag{2.14}$$

$$\beta = \frac{\lambda}{4\pi} \mu. \tag{2.15}$$

Dispersion δ for X-rays is positive and usually in the range of 10^{-6}, thus the real part of the index of refraction is slightly smaller than 1. Table B.2 lists some dispersion and absorption coefficients δ and β for materials and energies used in this work.

Figure 2.1 illustrates reflection and transmission of an X-ray beam hitting a flat layer surface at angle α_i. Depending on the index of refraction n of the material, part of the beam is reflected at angle $\alpha_\mathrm{f} = \alpha_\mathrm{i}$ (with wave vector $\vec{k}_\mathrm{f}$) and part of it penetrates the layer at angle $\alpha_\mathrm{t} < \alpha_\mathrm{i}$ (with wave vector $|\vec{k}_\mathrm{t}| < |\vec{k}_\mathrm{f}|$, but $k_{\mathrm{t},x} = k_{\mathrm{f},x}$). The transmission angle α_t can be calculated directly

from Snell's law

$$n_1 \cos\alpha_1 \quad = \quad n_2 \cos\alpha_2 \tag{2.16}$$

with complex refractive indices and angles for upper layer 1 and lower layer 2. In most cases radiation coming from vacuum (n_1 = 1) or air ($n_1 \approx 1$) hits a liquid or solid sample. Then $\alpha_1 = \alpha_i$ is the angle of incidence (that is not complex but real) and $\alpha_2 = \alpha_\mathrm{t}$ the usually complex transmission angle. For a medium with refractive index n it follows

$$\cos\alpha_\mathrm{i} \quad = \quad n \cos\alpha_\mathrm{t}. \tag{2.17}$$

This is still valid in layers inside a multilayer system even if the respective layer does not have an interface to the vacuum, because the angle inside a layer is just dependent on the angle of incidence (from vacuum/air)[2] - apart from the case of total reflection at an interface before the respective layer of course.

As the index of refraction for X-rays is smaller than 1 for all materials except vacuum (or approximatively air or a gas, too) the beam is always refracted away from the perpendicular towards the surface when it enters matter from vacuum. Thus, $\alpha_\mathrm{t} < \alpha_\mathrm{i}$ holds for all angles below 90°. If the angle of incidence is small enough, α_t can get as small as 0° (with $\cos\alpha_\mathrm{t} = 1$) and virtually no radiation penetrates the material. The respective angle of incidence in this case is called critical angle of total reflection α_c and can be calculated (cf. appendix D.4) from equation 2.17 to be

$$\alpha_c \quad \approx \quad \sqrt{2\delta} = \lambda\sqrt{r_\mathrm{e}\rho_\mathrm{e}/\pi}. \tag{2.18}$$

With the help of so-called Fresnel coefficients [18, 72, 149] the reflectivity of a "perfect" (i.e. absolutely smooth) surface can be calculated. Here the amplitudes of the incident $|\vec{E}_{0,\mathrm{i}}|$, reflected $|\vec{E}_{0,\mathrm{r}}|$ and transmitted wave $|\vec{E}_{0,\mathrm{t}}|$ are

$$|\vec{E}_{0,\mathrm{r}}| \quad = \quad r \cdot |\vec{E}_{0,\mathrm{i}}| \tag{2.19}$$

$$\text{and} \qquad |\vec{E}_{0,\mathrm{t}}| \quad = \quad t \cdot |\vec{E}_{0,\mathrm{i}}| \tag{2.20}$$

introducing the Fresnel coefficients

$$\begin{aligned} r \quad &= \quad \frac{k_{\mathrm{i},z} - k_{\mathrm{t},z}}{k_{\mathrm{i},z} + k_{\mathrm{t},z}} \\ \text{and} \qquad t \quad &= \quad \frac{2k_{\mathrm{i},z}}{k_{\mathrm{i},z} + k_{\mathrm{t},z}} \end{aligned} \tag{2.21}$$

for reflection and transmission with z-components of the wave vectors of incident and transmitted

[2] If preceding layers change the angle of incidence more the interface to the respective layer influences it less and vice versa.

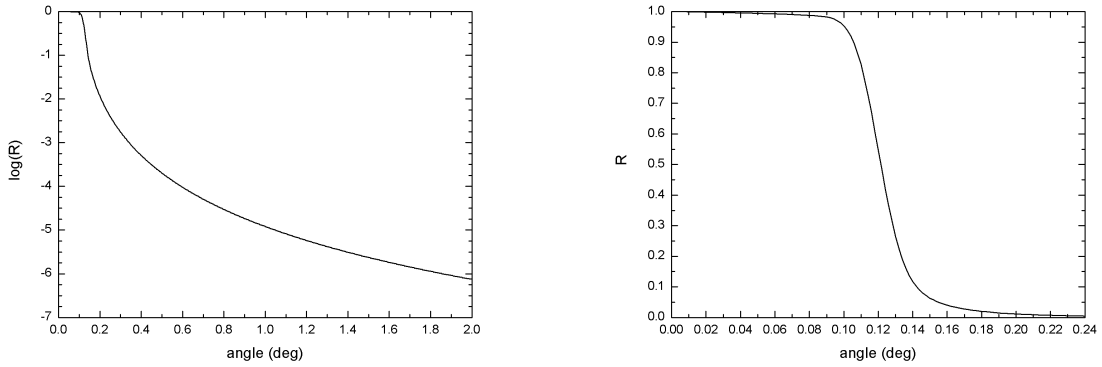

Figure 2.2.: Calculated Fresnel reflectivity of a silicon/air interface at E = 15.2 keV ($\lambda = 0.816$Å) after equation 2.23: Left in logarithmic scale, right additionally in linear scale for small angles.

radiation

$$\begin{aligned} k_{\mathrm{i},z} &= k \sin \alpha_{\mathrm{i}} \\ k_{\mathrm{t},z} &= nk \sin \alpha_{\mathrm{t}} = k\sqrt{(n^2 - \cos^2 \alpha_{\mathrm{i}})}. \end{aligned} \tag{2.22}$$

The Fresnel coefficients are dependent on polarization, but as the index of refraction n for X-rays is virtually 1, this dependence does not play any role in this work and can be neglected [149]. For small angles the relative intensity of reflected radiation (the so-called "Fresnel reflectivity") is given as

$$R_{\mathrm{F}} = |r|^2 = \frac{(\alpha_{\mathrm{i}} - \alpha_{\mathrm{t,r}})^2 + \alpha_{\mathrm{t,i}}^2}{(\alpha_{\mathrm{i}} + \alpha_{\mathrm{t,r}})^2 + \alpha_{\mathrm{t,i}}^2}. \tag{2.23}$$

Figure 2.2 shows the calculated Fresnel reflectivity of a smooth silicon-air-interface. Equation 2.23 comprises the real and imaginary part of the transmission angle $\alpha_{\mathrm{t}} = \alpha_{\mathrm{t,r}} + \mathrm{i}\alpha_{\mathrm{t,i}}$ ([72, 149])

$$\alpha_{\mathrm{t,r}}^2 = \frac{1}{2}\left[\sqrt{|(\alpha_{\mathrm{i}}^2 - 2\delta)^2 + 4\beta^2|} + (\alpha_{\mathrm{i}}^2 - 2\delta)\right] \tag{2.24}$$

$$\alpha_{\mathrm{t,i}}^2 = \frac{1}{2}\left[\sqrt{|(\alpha_{\mathrm{i}}^2 - 2\delta)^2 + 4\beta^2|} - (\alpha_{\mathrm{i}}^2 - 2\delta)\right]. \tag{2.25}$$

It can be easily seen by multiplication that

$$\alpha_{\mathrm{t,r}} \cdot \alpha_{\mathrm{t,i}} = \beta \tag{2.26}$$

holds for all α_{i} and at the critical angle $\alpha_{\mathrm{i}} = \alpha_{\mathrm{c}} = \sqrt{2\delta}$ (cf. equation 2.18)

$$\alpha_{\mathrm{t,r}} = \alpha_{\mathrm{t,i}} = \sqrt{\beta} \tag{2.27}$$

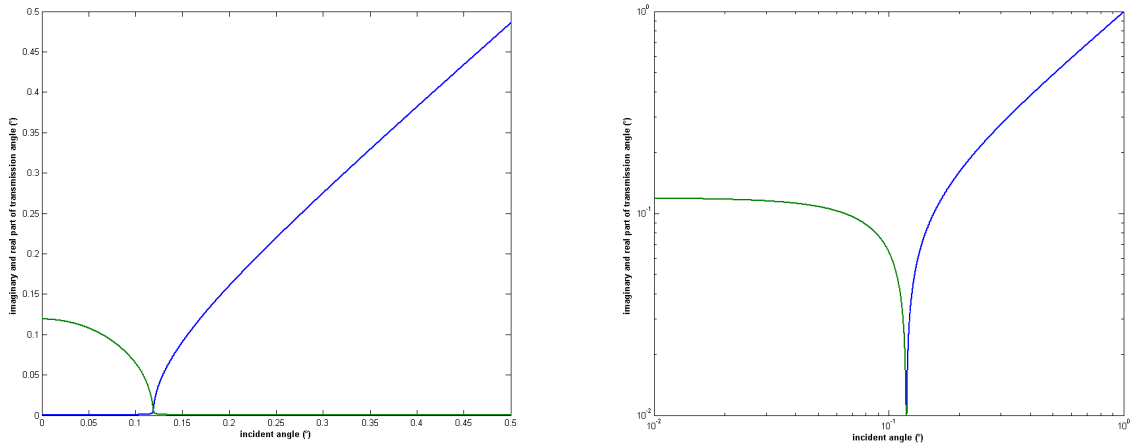

Figure 2.3.: Values of real and imaginary part of the transmission angle for different angles of incidence (linear and logarithmic scale): $\alpha_{\mathrm{t,r}}$ (blue) nearly disappears below the critical angle α_{c} and asymptotically approaches the incident angle α_{i} for large angles. On the other hand $\alpha_{\mathrm{t,i}}$ (green) virtually vanishes above the critical angle and approximates α_{c} for low incident angles.

holds. Figure 2.3 illustrates the values of real and imaginary part of the transmission angle for different angles of incidence. $\alpha_{\mathrm{t,r}}$ decreases to very low values below the critical angle α_{c} and approaches the incident angle α_{i} for large angles. Thus, the beam only penetrates a very thin region below the total reflection angle, and refraction effects decrease with increasing incidence angle, totally disappearing at normal incidence. On the other hand, $\alpha_{\mathrm{t,i}}$ nearly vanishes above the critical angle and approaches α_{c} for low incident angles.

The attenuation length (also called penetration depth) Λ is defined as the depth until that the incident radiation intensity is reduced to $1/e$ of its initial value and amounts to $1/\mu$ for normal incidence. At grazing incidence

$$\Lambda = \frac{\sin \alpha_{\mathrm{t,r}}}{\mu} \approx \frac{\lambda}{4\pi\alpha_{\mathrm{t,i}}} \tag{2.28}$$

holds [72]. Approximations in different angle ranges are [31, 72]

$$\alpha_{\mathrm{i}} \ll \alpha_{\mathrm{c}}: \quad \Lambda \approx \frac{\lambda}{4\pi\sqrt{2\delta}} \approx \frac{\lambda}{4\pi\alpha_{\mathrm{c}}} \tag{2.29}$$

$$\alpha_{\mathrm{i}} \approx \alpha_{\mathrm{c}}: \quad \Lambda \approx \frac{\lambda}{4\pi\sqrt{\beta}} \tag{2.30}$$

$$\alpha_{\mathrm{c}} \ll \alpha_{\mathrm{i}} \ll 90°: \quad \Lambda \approx \frac{\lambda \cdot \alpha_{\mathrm{i}}}{4\pi\beta} \tag{2.31}$$

$$\alpha_{\mathrm{i}} \approx 90°: \quad \Lambda \approx \frac{\lambda \cdot \sin \alpha_{\mathrm{i}}}{4\pi\beta}. \tag{2.32}$$

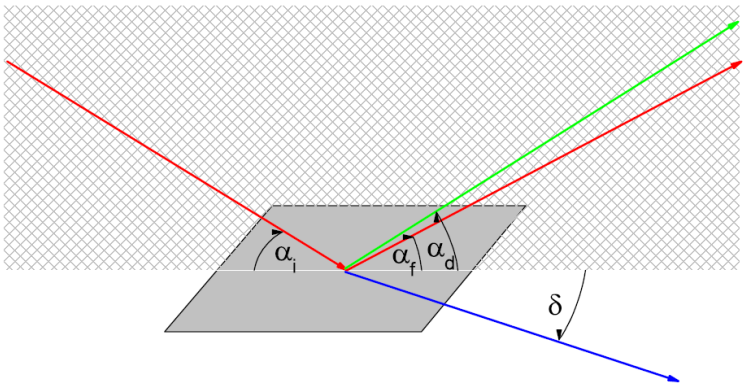

Figure 2.4.: Angles at specular and diffuse scattering, in-plane and out-of-plane:
α_i: angle of incidence; $\alpha_\mathrm{f} = \alpha_\mathrm{i}$: specular exit angle (in-plane)
α_d: diffuse exit angle in plane of incidence (off-specular, in-plane)
δ: diffuse exit angle outside plane of incidence (out-of-plane).

In case of total reflection ($\alpha_\mathrm{i} < \alpha_\mathrm{c}$) radiation penetrates the sample just a few nanometers. Thus, surface sensitive measurements are easily possible with experiments at grazing incidence and properties of thin layers can be characterized. For larger angles part of the radiation penetrates the sample, and the complex transmission angle

$$\alpha_\mathrm{t} = \alpha_\mathrm{t,r} + \mathrm{i}\alpha_\mathrm{t,i} \tag{2.33}$$

inside the sample can be calculated from equation 2.17 to be

$$\alpha_\mathrm{t} \approx \sqrt{\alpha_\mathrm{i}^2 - 2\delta + 2\mathrm{i}\beta}. \tag{2.34}$$

as shown in appendix D.5.

2.1.2. Diffuse (non-specular) X-ray scattering

In specular reflectivity measurements there is only a wave vector transfer perpendicular to the surface, thus these measurements can only deliver information about electron density distributions perpendicular to the sample surface. The lateral structure of the surface can only be analyzed by diffuse scattering ($\alpha_i \neq \alpha_f$). Additionally, reflectivity within the plane of incidence (off-specular) and out of the plane of incidence of the X-ray beam (out-of-plane) have to be distinguished. Figure 2.4 illustrates the three cases.

Calculation of the wave vector transfer values from the angle of incidence α_i and reflection α_f leads to [149]

$$\begin{aligned} q_x &= k(\cos\alpha_\mathrm{f}\cos\delta - \cos\alpha_\mathrm{i}) \\ q_y &= k\cos\alpha_\mathrm{i}\sin\delta \\ q_z &= k(\sin\alpha_\mathrm{i} + \sin\alpha_\mathrm{f}) \end{aligned} \tag{2.35}$$

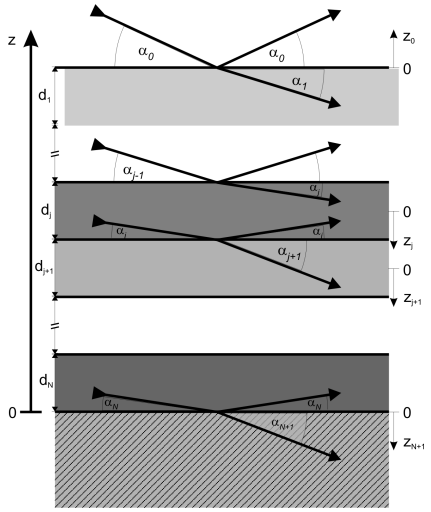

Figure 2.5.: Schematic illustration of a multilayer system with layers of different indices of refraction.

with the out-of-plane angle δ and $k = 2\pi/\lambda$ as the absolute value of the wave vector or so-called wave-number.

Due to the relatively weak interaction between X-ray radiation and matter, often a kinematic description of diffuse scattering following the Born approximation can be utilized. A complex extension of this approximation is the "Distorted Wave Born Approximation" (DWBA). Both theories are described in detail elsewhere [139, 149].

Additionally, even in measurements only perpendicular to the surface diffuse scattering should be considered, because if is not removed from the reflectivity signal, roughness will be underestimated [151]. Further, background noise is reduced and scans can be extended to larger angles and thus better accuracy by diffuse scattering correction. Thus, it is common in reflectivity measurement to measure not only the specularly reflected intensity at $\alpha_\mathrm{f} = \alpha_\mathrm{i}$, but also the reflected intensity off-specular (in-plane) at $\alpha_\mathrm{f} = \alpha_\mathrm{i} + \Delta\alpha$ usually with a fixed offset $\Delta\alpha$. This so-called longitudinal-diffuse scattering intensity is then removed from the intensity at specular position.

2.1.3. Multilayer systems

In the present work samples are investigated that do not only have one reflecting interface but that consist of several layers with different indices of refraction - and thus several reflecting interfaces, too. First, a system of several "flat" layers (like in figure 2.5) shall be considered. The individual layers can be treated separately, and their reflectivity can be calculated as described in section 2.1.1. Vacuum or air are considered as an infinitely thick layer above the sample with refractive index n = 1. The substrate - generally much thicker than the penetration depth of X-ray radiation - is also considered as infinitely thick, and the fraction of radiation T_{N+1} that is transmitted through the lowermost interface z_N is not reflected at any other interface. Addition of all reflected intensities, while regarding the correct phase, leads to the total reflectivity of the system.

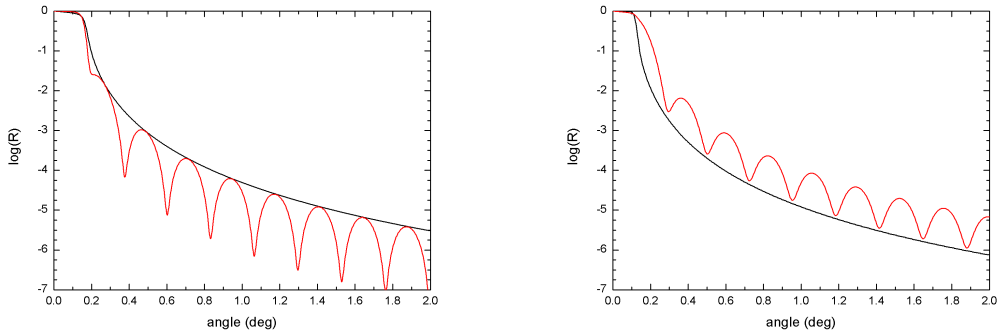

Figure 2.6.: Calculated reflectivity for a 10 nm Si layer on a Ge substrate (left) and a 10 nm Ge layer on a Si substrate at $E = 15.2$ keV ($\lambda = 0.816$ Å). For each curve the Fresnel reflectivity for the pure substrate is shown in addition. It can be seen that the oscillating curve is below the Fresnel reflectivity curve of the substrate if an optically denser material like Si ($\delta = 2.103 \cdot 10^{-6}$) is on an optically less dense material like Ge ($\delta = 4.204 \cdot 10^{-6}$) and vice versa.

Figure 2.6 shows the calculated reflectivity of a sample consisting of a 10 nm thick film of silicon on a germanium substrate (and of 10 nm germanium on silicon) and the Fresnel reflectivity of the corresponding substrate without layer. Oscillations in the reflectivity (so-called "Kiessig-Fringes" [71]) are caused by interference effects between beams reflected at both interfaces (layer-substrate and air-layer), their period $\Delta\alpha$ is reciprocally proportional to the distance between the interfaces and thus to the thickness d of the layer that can be calculated using the Bragg condition

$$m\lambda = 2d \sin\alpha \quad \text{with} \quad m \in \mathbb{N}. \tag{2.36}$$

For small angles of incidence, this leads to [149]

$$d = \frac{2\pi}{\Delta q_z} \approx \frac{\lambda}{2 \cdot \Delta\alpha}. \tag{2.37}$$

This thickness information can be extracted from a reflectivity curve with an accuracy much better than one Å. In multilayer systems, the reflectivity shows a superposition of oscillations from the individual layers, but in principle it is still possible to calculate individual layer thicknesses in a multilayer system from the total reflectivity.

Abelès [1] was the first to address this problem with transfer matrices for each individual layer. A recursive method to solve the problem that is used in most applications today is the Parrat algorithm [113] that can easily be implemented in computational algorithms. So it is possible to calculate reflectivities of multilayer systems with modern computers in rather short times. In this work, the program *LsFit* [135, 134] - that is based on the Parrat algorithm - was used to analyze reflectivity scan curves. Further, calculation of the XSW field discussed in detail in chapter 2.3 is based on a matrix formalism very similar to the one used for calculation of X-ray reflectivity.

2.2. X-ray fluorescence (XRF)

X-ray fluorescence is a phenomenon that is exploited in chemical analysis frequently [117] and also an important aspect in X-ray standing waves measurements discussed later. In this chapter, first X-ray fluorescence in general is described. In a second subsection, a specialization of X-ray fluorescence, Total Reflection X-ray Fluorescence (TXRF), that was utilized for analysis of some samples in this work, is outlined. TXRF is related to XSW analysis but focussed on element detection while averaging over the whole thickness of a nm range sample and thus abandoning the lateral resolution of XSW. The latter is explained extensively in chapter 2.3.

2.2.1. X-ray fluorescence analysis

Fluorescence radiation is generated when an electron of an inner shell of an atom is ejected (e.g. by illumination with hard X-rays or high energy electrons) and this hole is filled by an electron of an outer shell. The difference in potential energy is balanced by emission of a fluorescence photon. The energies/wavelengths of possible fluorescence photons are element specific, thus fluorescence radiation is useful for identifying elements.

Wavelength λ of the emitted fluorescence radiation for an atom of shell number n_2 filling a hole in shell n_1 can be calculated after Moseley's law [72, 157]

$$\frac{1}{\lambda} = R_\infty \cdot (Z - \kappa)^2 \cdot \left(\frac{1}{n_1^2} - \frac{1}{n_2^2} \right) \tag{2.38}$$

with R_∞ being the Rydberg constant ($1.097373156 \cdot 10^7$ 1/m), Z being the atomic number and κ a constant describing the shielding of the nucleus by inner electrons. For transitions between the second (L) and the first (K) shell it is $\kappa \approx 1$, between the third (M) and the second shell $\kappa \approx 7.4$ holds.

The classical and still most common notation (introduced by K. M. G. Siegbahn) of fluorescence emission energies (usually called emission lines) is composed of the name of the inner electron shell, a Greek letter and a number denominating the outer electron shell. A transition from shell L_3 to K_1 is called Kα_1, a transition from L_2 to K_1 is called Kα_2. From the M to K shells the nomination is Kβ_1, Kβ_2, ..., from M to L called L$\alpha_{...}$ and so on. As this nomenclature is not entirely systematic the International Union of Pure and Applied Chemistry (IUPAC) has proposed a notation based on the shell nomenclature, for example K-L_3 (for Kα_1) or L_3-M_5 (for Lα_1). Due to the fine-structure of energy levels an increasing number of transition is possible when regarding outer shells. On the other hand, energies of the K lines are much higher than of the L, M, and other lines and thus usually more important. Energies of emission lines of elements used in this work are listed in table B.4. Table 2.1 shows notations [5, 84, 146] for some of the most important emission lines.

Lower shell	Upper shell	Emission line	Lower shell	Upper shell	Emission line	Lower shell	Upper shell	Emission line
K_1	L_3	$K\alpha_1$	L_3	M_5	$L\alpha_1$	M_5	N_7	$M\alpha_1$
K_1	L_2	$K\alpha_2$	L_3	M_4	$L\alpha_2$	M_5	N_6	$M\alpha_2$
K_1	M_3	$K\beta_1$	L_2	M_4	$L\beta_1$	M_4	N_6	$M\beta$
K_1	N_2,N_3	$K\beta_2$	L_3	N_5	$L\beta_2$	M_3	N_5	$M\gamma$
K_1	M_2	$K\beta_3$	L_2	N_4	$L\gamma_1$			

Table 2.1.: Names of some important emission lines in Siegbahn notation deduced form the electron shell that is refilled (lower shell) and the shell from which the respective electron "falls down" [5, 72, 84, 146].

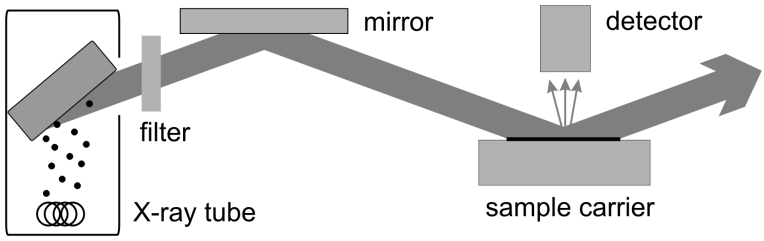

Figure 2.7.: Schematic set-up for TXRF measurements with a conventional X-ray tube. Radiation emitted from the tube passes a filter and a mirror that work as a bandpass to eliminate radiation of undesired wavelengths. Then the beam hits a flat sample carrier at fixed low angle (in the mrad range) and is totally reflected. The sample is deposited as an ultrathin layer (e.g. by drying a droplet of solution containing the material) on the carrier and transmitted by incident and reflected beam. Fluorescence radiation excited in the sample layer is detected by an energy dispersive detector located above the sample.

2.2.2. Total-reflection X-ray fluorescence analysis (TXRF)

The method of total-reflection X-ray fluorescence analysis (TXRF) was discovered in 1971 by Yoneda and Horiuchi [170]. They developed a set-up to reduce spectral background significantly in conventional X-ray fluorescence (XRF) measurements (cf. figure 2.7). By measuring at a very small angle of incidence the X-ray beam is totally reflected at a flat substrate (often glass or quartz) carrying the sample material. Thus, radiation excites mainly the sample but hardly the substrate to fluorescence because the beam penetrates only few nm into the substrate bulk. Further, the reflected beam again passes the sample material and thus increases signal intensity. The excited X-ray fluorescence radiation is then detected by an energy dispersive detector. Liquid nitrogen cooled Si(Li) detectors were very common but are nowadays often replaced be easier to handle and smaller solid stated detectors. In contrary to the common 45° geometry in XRF experiments the detector in TXRF measurements is perpendicular to the sample carrier and thus exposed to far less scattered intensity and influences from the primary beam. These effects improve the signal-to-noise ratio so well that limits of detections can be reduced to nanograms and even picograms [2].

Conventional XRF analysis suffers from so-called matrix effect. These are deviations from the linear concentration-signal relation appearing in "thick" (i.e. some tens of nm for metallic

samples to some tens of micrometers for organic material, hence called matrix effects) samples caused by secondary fluorescence (a fluorescence photon excites another atom) or absorption of a fluorescence photon. This leads to a higher or lower detected element concentration. In TXRF measurements are performed at an "infinitely thin" sample thickness (again depending on the material between few nanometers and few micrometers) [76] that means thin enough to prevent those matrix effects.

The linear concentration-signal relation permits a simple calibration by introducing an internal standard, i.e. a reference element of known concentration that is not yet present in the sample. Knowing the concentration of the internal standard and specific sensitivities of the set-up and detector for each element, the absolute concentrations in the sample can be obtained directly. Calculation procedures for intensities of a given standard and an unknown sample were described in detail by Klockenkämper [72]. Element detection and concentration calculation can nowadays be performed automatically by commercial instruments and software if the sample structure is not too complicated.

In practice, several aspects ought to be considered during measurements. Using hard X-rays (of several keV) the energy flow and absorption in materials for p- and s-polarization is (virtually) equal. This is not the case for soft x-rays [32]. Further, the sample film should be rough enough not to reflect the entire beam. Only the radiation which is absorbed in the sample (and not reflected from the top layer) can cause fluorescence radiation [72]. And TXRF signal intensity is oscillating very much for $\alpha_\mathrm{i} < \alpha_c$ if film thickness is lower than $\approx$ 100 nm, thus films in TXRF measurement should be of several 100 nm thickness if possible [72]. This oscillating effect is related to X-ray standing waves that are discussed in detail in section 2.3.

The energy spectrum of fluorescence radiation from a sample in a TXRF but also an XSW measurement delivers a very detailed structure of energy distributions not only showing fluorescence energies of elements on the sample but also several additional features. Fig. 2.8 shows a spectrum obtained in a TXRF measurement of a quartz substrate covered with a thin layer containing S, Cl and a small amount of Fe. Other elements present in the layer (C, O, N, H) cannot be seen because energy of their fluorescence radiation is so low that it is absorbed by air on the way to the detector. The Kα fluorescence peaks of S (2.308 keV) and Cl (2.622 keV) are very obvious. The difference between Kα_1 and Kα_2 is so small that it cannot be resolved. The Kβ peak of Cl (2.816 keV) is visible as a shoulder on the right sight of the Cl Kα peak, the Kβ signal of S (2.464 keV) is not visible because it is located between the Kα peaks of S and Cl. Further, much lower Kα (6.404 keV) and Kβ (7.058 keV) peaks of Fe are visible whose concentration in the sample is much lower. Si denotes the Kα peak of silicon (1.749 keV) that is present in the quartz substrate (SiO_2). "Esc" denotes the escape peak caused by a Cl fluorescence photon that hits a Si atom leading to a remaining energy of

$$E_\mathrm{Esc} = E_\mathrm{Cl} - E_\mathrm{Si} = 0.873\,\mathrm{keV}. \tag{2.39}$$

The peak at "2Cl" is generated when two Cl fluorescence photons enter the detector in a time too short to separate them imitating a photon of double energy 5.244 keV. The elastic peak ("Elast") results from electrons that are elastically scattered at electrons in the sample keeping their energy but changing direction towards the detector. There, they deposit the energy of the

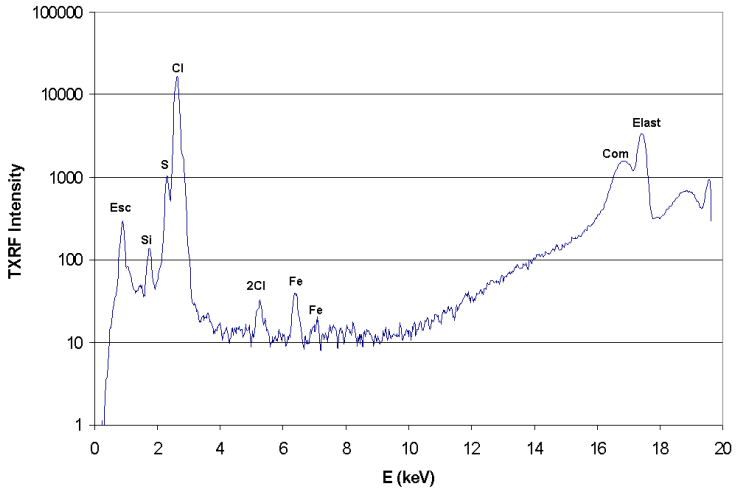

Figure 2.8.: A typical TXRF spectrum. Explanation in the text.

incident radiation that is equal to the fluorescence energy of Mo (17.479 keV) in this case using a Mo X-ray tube. Finally, the second peak at high energies, the Compton peak ("Com"), is caused by Compton scattering. In this case the photon hits an electron and changes direction and energy (respectively wavelength). Compton scattering gives a continuous energy spectrum (depending on the angle of scattering φ) from 0° to a maximum Compton energy at 180° scattering. The photon wavelength change of the scattered photon is [86]

$$\Delta\lambda = \lambda_{\mathrm{C}}(1 - \cos\varphi) \tag{2.40}$$

with the so called Compton wavelength

$$\lambda_{\mathrm{C}} = \frac{h}{m_{\mathrm{e}} c_0} = 2.4263106 \cdot 10^{-12}\,\mathrm{m}. \tag{2.41}$$

Here $h = 6.6260755 \cdot 10^{34}$ is Planck's constant, $m_{\mathrm{e}} = 9.1093897 \cdot 10^{-31}$ kg the electron mass and $c_0 = 299792458$ m/s the velocity of light in vacuum. At grazing incidence, most photons reach the detector at an angle change of φ = 90° leading to a wavelength change of the incident photon with wavelength λ_0 of $\Delta\lambda = \lambda_{\mathrm{C}}$. Using the energy-wavelength relation $E = \frac{hc}{\lambda}$ the energy of the Compton peak can be calculated by

$$E_{\mathrm{C}} = \frac{hc}{\lambda_0 + \lambda_{\mathrm{C}}} = \frac{hc}{\frac{hc}{E_0} + \lambda_{\mathrm{C}}} = \frac{E_0}{1 + \frac{E_0}{hc} \cdot \lambda_{\mathrm{C}}} = \frac{E_0}{1 + \frac{\lambda_{\mathrm{C}}}{\lambda_0}}. \tag{2.42}$$

Typical values of the Compton peak energy for photon energies used in this work are listed in table 2.2.

Incident energy (keV)	Compton peak energy
8.048 (Cu Kα)	7.923
8.398 (W Lα)	8.262
10.050	9.856
13.000	12.677
15.000	14.572
15.200	14.761
17.479 (Mo Kα)	16.901

Table 2.2.: A selection of Compton peak energies.

2.3. X-ray standing waves (XSW)

X-ray standing waves are a phenomenon that occurs when an X-ray beam is reflected on one or several interfaces between materials of different refractive indices. As dimensions of X-ray standing waves are in the nanometer range they are not visible in many types of measurements because the scanned region is much larger. For example, a TXRF measurement is basically a scan of X-ray standing waves that averages over the whole XSW field region and thus does not show any wave characteristics. To detect an XSW field so-called markers are necessary. A layer material itself can serve as a marker as it is the case e.g. for the Ge layers on Si introduced in section 3.1.1, or the layer may comprise certain marker atoms that do not affect the XSW field [160, 174] but fulfill their marker function by emitting fluorescence radiation as e.g. in the phospholipid-buffer layer system described in section 3.2.2. Another important requirement to create X-ray standing waves is (longitudinally) coherent radiation as explained in section 2.3.1 to permit interference effects. Monochromaticity is also important in measurements. In principle radiation of two or more different wavelengths can form superposed XSW fields but creation and evaluation of scans taken from such complex intensity fields can get rather complicated. Thus, calculations performed in this work consider monochromatic radiation. Finally, roughness (as discussed in chapter 2.4) is an aspect to consider in the calculation of XSW fields, too.

An overview article on XSW was published by Zegenhagen [171]. Mathematics of XSW fields was discussed in detail by de Boer [32] and Klockenkämper [72]. These publications are the starting point of calculations and simulations in this work. Other authors [23, 160, 162, 163, 174] also give a short introduction into the calculation process of grazing incidence (variable period) XSW.

2.3.1. Coherence

Coherence of two electromagnetic waves is mandatory for interference and thus for the creation of X-ray standing waves. Coherence of radiation in an X-ray experiment can be quantified by two values called transverse coherence length and longitudinal coherence length. The transverse coherence length ξ_t is defined as the distance in the observation plane at which two wavefronts A and B, which are emitted from both ends of a radiation source of size d_s and observed at a distance R_s, are phase-delayed by exactly the wavelength λ. As can be understood from figure

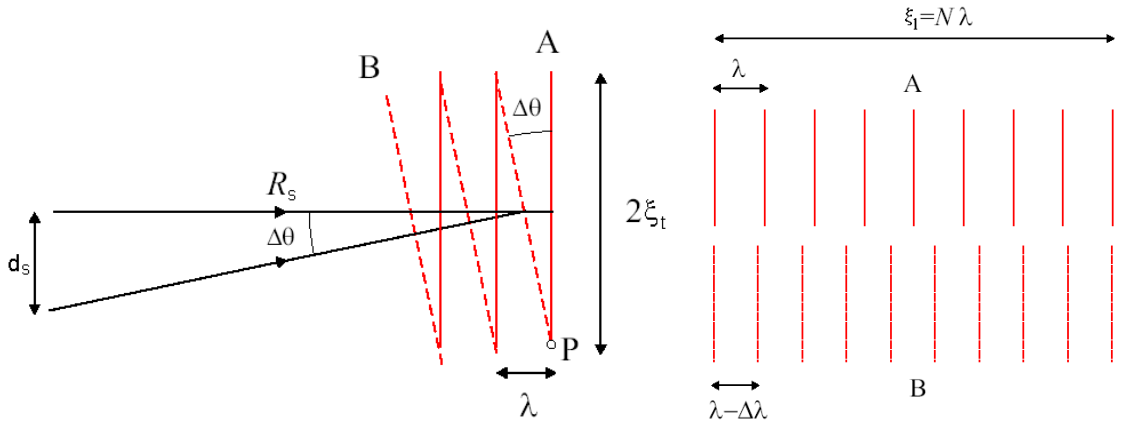

Figure 2.9.: Left: Definition of the transverse coherence length ξ_t. Two wavefronts A and B are emitted from both ends of a radiation source of size d_s and observed at a distance R_s. At one end of a detector of width $2\xi_l$ the waves are in phase and at the other end they are phase-delayed by exactly λ defining the transverse coherence length ξ_t.
Right: Definition of the longitudinal coherence length. A wave A of wavelength λ and a wave B of a shorter wavelength $\lambda - \Delta\lambda$ have the same amplitude at a distance $\xi_l = N\lambda$. This distance defines the longitudinal coherence length ξ_l.

2.9 it follows, with $\Delta\theta$ being the angle at which the radiation source is seen from the observation plane,

$$\tan(\Delta\theta) = \frac{\lambda}{2\xi_t} = \frac{d_s}{R_s}. \tag{2.43}$$

This leads [46, 147] to the transverse coherence length

$$\xi_t = \frac{\lambda R_s}{2d_S}. \tag{2.44}$$

With R_s usually limited it is possible to improve ξ_t by introducing a pinhole of some tens or a hundred micrometers diameter to minimize the source size [81]. This is mainly limited by beam intensity going down with smaller diameter. Taking a pinhole or cross slit of diameter $d_s = 0.1$ mm as a source 1 m from the detector the transverse coherence length at 15 keV is $\xi_t = 413$ nm. At lower energies these values increase, e.g. $\xi_t = 775$ nm for $E = 8$ keV.

The longitudinal coherence length ξ_l is, as illustrated in figure 2.9, the shortest distance between two positions at which a wave A of wavelength λ and a second wave B of a shorter wavelength $\lambda - \Delta\lambda$ have equal amplitudes. With a wavelength difference of $\Delta\lambda$ this happens after $N + 1 = \frac{\lambda}{\Delta\lambda}$ wavetrains. As N generally is a huge number $N + 1 \approx N$ holds, and the longitudinal coherence length is [122, 137, 146]

$$\xi_l = N \cdot \Delta\lambda = \frac{\lambda^2}{\Delta\lambda}. \tag{2.45}$$

Thus, reducing the energy bandwidth of incident radiation increases the longitudinal coherence length. With a monochromator resolution of $\Delta E/E = 10^{-4}$ the longitudinal coherence length is ξ_l = 827 nm at E = 15 keV and ξ_l = 1550 nm at E = 8 keV.

ξ_t is less important in XSW measurements, thus efforts are focussed on improving the longitudinal coherence. Generation of a well-defined XSW intensity field requires coherent superposition of incident and reflected wave amplitudes. This criterion is met if the maximum path length difference ΔL between incident and reflected beam is significantly smaller than the (longitudinal) coherence length ξ_l of the incident beam [151, 152]. In other words, the coherence length must be larger than the structures to be analyzed, e.g. layer thicknesses d. Considering the Bragg condition

$$m\lambda = 2d\sin\alpha \text{ with } m \in \mathbb{N} \tag{2.46}$$

with incident angle α, X-ray standing waves can only be expected in layers of thickness [151, 152]

$$d < \frac{\xi_\mathrm{l}}{2\sin\alpha}. \tag{2.47}$$

d is in the range of some tens of micrometers for hard X-ray radiation and angles up to 1°, thus this condition is fulfilled for all samples investigated in this work.

2.3.2. XSW at Bragg reflection and at normal incidence

X-ray standing waves at Bragg reflection and at normal incidence are common XSW methods that are outlined here only shortly because measurements presented in this work were performed by XSW at grazing incidence. The latter are covered extensively in the next chapters.

In contrary to grazing incidence XSW, X-ray standing waves at a Bragg reflection angle of a lattice structure can naturally only be performed on crystal samples. The principle is outlined here following Scherb [127] and Zegenhagen [171, 172]. XSW measurements at the Bragg reflection are usually performed to localize foreign atoms (like implants or dotations) in a crystal structure. Fluorescence radiation of these foreign atoms, called adatoms here, depends on their position inside the sample structure. This position is described by two factors both in a range between 0 and 1. The coherent distance (also called coherent position) D_c describing the distance z_D of the adatom relative to the lattice planes (in units of the distance D_B between Bragg planes)

$$D_\mathrm{c} = \frac{z_\mathrm{D}}{D_\mathrm{B}}. \tag{2.48}$$

If the adatoms occupy several positions D_c represents the weighted average value of those positions. The coherent fraction f_c represents the lateral distribution of adatoms around the coherent position. f_c takes its maximal value 1 for a sharp lateral distribution, i.e. all positions are equivalent, $f_\mathrm{c} = 0$ means that the adatoms are distributed homogeneously. Coherent position and coherent fraction also represent amplitude and phase of Fourier components of the corresponding atoms' distribution functions. Fluorescence intensity from the adatoms can be calculated

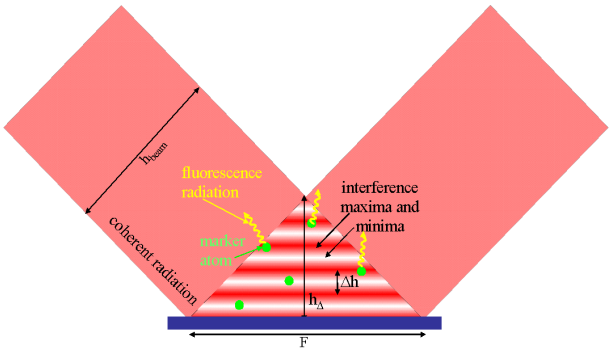

Figure 2.10.: Schematic illustration of the XSW triangle above a substrate. Typical values (calculation see below) are: $\lambda = 8.27 \cdot 10^{-11}$ m (E = 15 keV); $\alpha \approx 0.1°$; $h_{\mathrm{beam}} \approx 0.1$ mm; $h_\Delta \approx 0.05$ mm; $\Delta h \approx 24$ nm; $n = h_\Delta/\Delta h \approx 2080$.

by

$$I_{\mathrm{F}} = I_0 \cdot e(\alpha) \cdot \left(1 + R(\alpha) + s\sqrt{R(\alpha)} f_{\mathrm{c}} \cos(\phi - 2\pi D_{\mathrm{c}})\right) \tag{2.49}$$

with a phase factor ϕ, the incident angle α, the angle dependent reflectivity $R(\alpha)$, and $e(\alpha)$ being a factor representing the absolute depth of the foreign atoms in the sample. $e(\alpha)$ is ≈ 1 if the adatoms are above or slightly (some tens of nm) below the surface and angle dependent for deeper implantations with rising from 0 to 1 when the reflectivity decreases from maximum to 0.

A similar technique is normal incidence XSW analysis (NI-XSW). Like in the Bragg reflection version a crystal lattice is required and localization and distribution of foreign atoms in the lattice plane structure are determined using the values of coherent position and coherent fraction. Calculations are similar and explained together with experiments by Schreiber [131, 132].

2.3.3. Lateral dimensions in XSW at grazing incidence

If a rectangular shaped beam is reflected at a flat surface or interface there is in a cross-sectional view a triangular area (figure 2.10) above the surface in that incoming and reflected beams intersect and - if the radiation is monochromatic and longitudinally coherent - interfere. Depending on the wavelength of the radiation and the angle of incidence a typical pattern of interference maxima and minima (so-called antinodes and nodes) forms above the surface. If matter is present within this pattern atoms located in an antinode will be excited to strong fluorescence while atoms in a node will emit little or no fluorescence radiation.

The area covered by the beam, its footprint, amounts to

$$F = \frac{h_{\mathrm{beam}}}{\sin \alpha} \tag{2.50}$$

and with the vertical dimension of the beam h_{beam} the height h_Δ of this triangle (figure 2.10) can

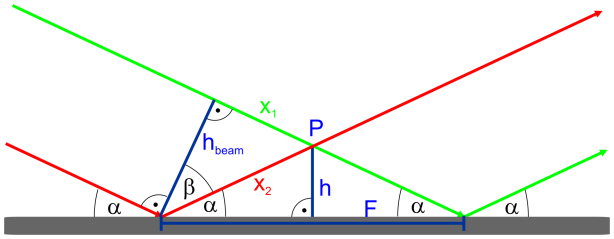

Figure 2.11.: Path length difference between incident and reflected beam at intersection point P (calculation see text).

be calculated by

$$h_\Delta = \frac{F}{2} \cdot \tan\alpha = \frac{h_{\text{beam}}}{2 \cdot \cos(\alpha)}, \tag{2.51}$$

with the angle α between incident beam and the surface (cf. figure 2.11). For small angles this equation can be simplified to

$$h_\Delta \approx \frac{1}{2} h_{\text{beam}}. \tag{2.52}$$

At an arbitrary position P at height h above the mirror surface (figure 2.11) inside this triangle exactly two beams interfere, and depending on the path length difference of both beams ($\Delta x = x_2 - x_1$) constructive or destructive interference may occur. Geometrical considerations lead to path lengths

$$x_2 = \frac{h}{\sin\alpha} \tag{2.53}$$

$$x_1 = x_2 \cdot \cos(2\alpha) = \frac{h \cdot \cos(2\alpha)}{\sin\alpha}. \tag{2.54}$$

Constructive interference occurs if the path length difference is a multiple of the radiation's wavelength

$$x_2 - x_1 = \frac{h - h \cdot \cos(2\alpha)}{\sin\alpha} \stackrel{!}{=} n \cdot \lambda \tag{2.55}$$

$$h = n \cdot \frac{\lambda \cdot \sin\alpha}{1 - \cos(2\alpha)}. \tag{2.56}$$

Obviously, positions of the nodes/antinodes only depend on the angle of incidence and wavelength. The distance between two adjacent nodes or antinodes is the same throughout the whole triangle and amounts to [11, 12, 21]

$$\Delta h = \frac{\lambda \cdot \sin(\alpha)}{1 - \cos(2\alpha)} = \frac{\lambda \cdot \sin(\alpha)}{1 - \cos^2(\alpha) + \sin^2(\alpha)} = \frac{\lambda}{2\sin(\alpha)}. \tag{2.57}$$

α (°)	5 keV	10 keV	15 keV
0.01	710.4	355.2	236.8
0.05	142.1	71.0	47.4
0.10	71.0	35.5	23.7
0.20	35.5	17.8	11.8
0.50	14.2	7.1	4.7
1.00	7.1	3.6	2.4
2.00	3.6	1.8	1.2
5.00	1.4	0.7	0.5

Table 2.3.: XSW intensity antinodes distances (in nm) for different photon energies and angles of incidence α.

For small angles this approximates

$$\Delta h \approx \frac{\lambda}{2\alpha}. \tag{2.58}$$

Some calculated antinodes distances for various angles of incidence α and photon energies E are listed in table 2.3.

In addition to the antinode spacing, the distance from the reflecting surface is of interest. Only considering the geometry of the problem an antinode would be expected directly at the surface. However, X-ray radiation that is totally reflected undergoes an angle dependent phase shift of [11, 72]

$$\phi = \arccos\left[2\left(\frac{\alpha}{\alpha_\mathrm{c}}\right)^2 - 1\right]. \tag{2.59}$$

Thus the phase difference between incident and reflected beam at the point of reflection on the surface decreases from π at an incident angle of $\alpha = 0°$ (parallel to the surface) to 0 for the critical angle α_c and above [11, 12, 72, 176]. This means that there is a node of XSW intensity at the surface for α = 0°. The first antinode approaches the surface from infinity (at $\alpha = 0°$) and reaches it at the critical angle. The period of nodes and antinodes at the critical angle α_c is called critical period [12] and amounts to

$$h_\mathrm{c} = \frac{\lambda}{2\alpha_\mathrm{c}} = \frac{\lambda}{2\sqrt{2\delta}} = \frac{\sqrt{\pi}}{2\sqrt{\rho_\mathrm{e} r_\mathrm{e}}}. \tag{2.60}$$

with electron density ρ_e and electron radius r_e introduced in equation 2.14. If a given atom is located at $h = j \cdot h_\mathrm{c}$ above the substrate then $j+$ 0.5 antinodes will pass the position of the atom when scanning α from 0 to α_c [12]. For $\alpha \geq \alpha_\mathrm{c}$ the first antinode remains at the surface [11, 12] and the others are "compressed" towards it like an accordion.

Figure 2.12 illustrates the position of nodes and antinodes for a 10 keV beam reflected at a Si surface at different angles whereas figure 2.13 displays the intensity at different heights when

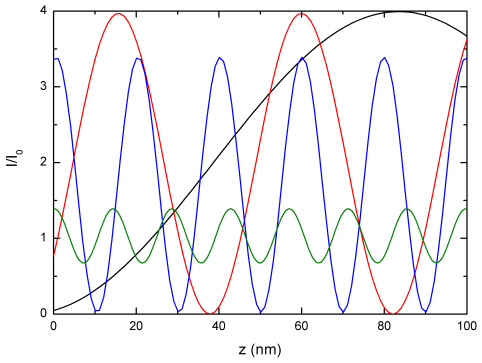

Figure 2.12.: XSW intensity versus height above a Si substrate for different angles of incidence for a photon energy of 10 keV. Angles of incidence: $\alpha = 0.02°$ (black), $\alpha = 0.08°$ nm (red), $\alpha = \alpha_c = 0.179°$ nm (blue), $\alpha = 0.25°$ (green). Intensity oscillates between 0 and $4I_0$ below the critical angle of total reflection and with smaller amplitude above α_c.

the angle of incidence is scanned. Calculation and properties of the curves are described in the subsequent chapter.

As already mentioned, position of nodes and antinodes is only dependent on angle of incident and wavelength but not on the substrate material. This can be advantageous because in general any (sufficiently flat and smooth) material can be used as a substrate. On the other hand, there are little possibilities to tune the strong maxima position especially when very short distances are needed at limited angles as intensity as well as nodes distance decrease with increasing angle (above total reflection).

One chance to achieve different maxima positions is using so-called waveguide structures as a substrate [175, 176]. Instead of a homogeneous substrate a layer system of several elements (e.g. Ni/C/Rh on glass) is used to carry the sample to be observed. The incident beam is then reflected on all interfaces of the substrate leading to a strong XSW intensity inside the carrier at certain angles (waveguide mode) and a shifted position of maxima above the substrate making different maxima positions possible. Further, the XSW signal (intensity versus angle of incidence as explained in more detail later) is intensity modulated thus leading to a more complex curve that lets less degrees of freedom in fitting and might increase resolution of the measurement. A similar possibility would be positioning of a spacer layer with optical properties very similar to the sample layer on the substrate. Then the substrate would still act as a mirror, but the whole sample system would be shifted laterally by a distance equal to the spacer layer thickness. Thus, the smaller period XSW maxima would reach the sample layer at lower angles providing a yardstick different from the one of a mirror without spacer.

2.3.4. Calculation procedure for XSW

In the following, a matrix formalism to calculate the XSW field in samples is introduced that is necessary for analyzing XSW scans and utilized in the program *MXSW* (cf. chapter 5). First,

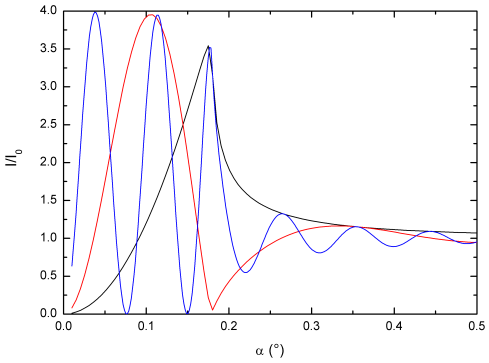

Figure 2.13.: XSW intensity versus angle for different heights above a Si substrate for a photon energy of 10 keV. From left to right: $h = 40$ nm (blue), $h = 20$ nm (red), $h = 0$ nm (black). The most significant peak is at the critical angle of Si ($\alpha_c = 0.179°$).

the simple case of an XSW field above a thick and flat substrate is discussed. In a second step, calculations are expanded to a thin layer on this substrate. Finally, the general case of a multiple layer sample is calculated.

Thick and flat substrate

A beam hitting a surface at angle α_i is partly reflected at angle $\alpha_r = \alpha_i$ and partly transmitted into the layer below at the transmission angle

$$\alpha_t = \sqrt{\alpha_0^2 - 2\delta + 2i\beta} \tag{2.61}$$

defined in equations 2.34 and 2.24[3] with α_0 being the incident angle in vacuum (and not the actual incident angle in the layer above the interface) if δ and β are (as commonly done) defined as values relative to vacuum. This is the case even if the respective interface is inside a multilayer and not in contact with vacuum. α_t on the other hand is the angle inside the layer below the interface as explained in chapter 2.1.1. The well-known Fresnel formulae for the electrical field amplitudes of incident (E_i, α_i), reflected (E_r, α_r) and transmitted (E_t, α_t) beam are (cf. equations 2.21 and literature [72])

$$r = \frac{E_r}{E_i} = \frac{\alpha_i - \alpha_t}{\alpha_i + \alpha_t} \tag{2.62}$$

$$t = \frac{E_t}{E_i} = \frac{2\alpha_i}{\alpha_i + \alpha_t}. \tag{2.63}$$

[3] In some XSW and TXRF literature [32, 72] the form $\alpha_t = \sqrt{\alpha_i^2 - 2\delta - 2i\beta}$ appears based on a different definition as already mentioned with equation 2.9. This leads to complex conjugate values in some equations in this chapter as discussed and calculated in appendix D.6.

Conversion of these formulae to E_i and equalization leads to

$$E_\mathrm{r} \cdot \frac{\alpha_\mathrm{i} + \alpha_\mathrm{t}}{\alpha_\mathrm{i} - \alpha_\mathrm{t}} = E_\mathrm{t} \cdot \frac{\alpha_\mathrm{i} + \alpha_\mathrm{t}}{2\alpha_\mathrm{i}} \tag{2.64}$$

$$\frac{E_\mathrm{r}}{\alpha_\mathrm{i} - \alpha_\mathrm{t}} = \frac{E_\mathrm{t}}{2\alpha_\mathrm{i}} \tag{2.65}$$

and it follows ([72])

$$E_\mathrm{i} = \frac{\alpha_\mathrm{i} + \alpha_\mathrm{t}}{2\alpha_\mathrm{i}} \cdot E_\mathrm{t} \tag{2.66}$$

$$E_\mathrm{r} = \frac{\alpha_\mathrm{i} - \alpha_\mathrm{t}}{2\alpha_\mathrm{i}} \cdot E_\mathrm{t}. \tag{2.67}$$

For a single interface between vacuum (or air) and an infinitely thick substrate, it can be assumed that there is no reflected beam inside the substrate. Further, normalizing the incident beam to $E_\mathrm{i} = 1$ the amplitudes of the electrical field can be written in a matrix form

$$\begin{bmatrix} 1 \\ E_\mathrm{r} \end{bmatrix} = \begin{bmatrix} m_1 & m_2 \\ m_3 & m_4 \end{bmatrix} \cdot \begin{bmatrix} E_\mathrm{t} \\ 0 \end{bmatrix} \tag{2.68}$$

with

$$m_1 = m_4 = \frac{\alpha_\mathrm{i} + \alpha_\mathrm{t}}{2\alpha_\mathrm{i}} \tag{2.69}$$

$$m_2 = m_3 = \frac{\alpha_\mathrm{i} - \alpha_\mathrm{t}}{2\alpha_\mathrm{i}}. \tag{2.70}$$

The intensity at height z above the surface ($z = 0$ on the surface, $z > 0$ above) can be calculated by adding the electrical field vectors of incident and reflected beam (which interfere) and squaring this sum

$$I_\mathrm{vac}(\alpha_0, z) = I_0 \cdot |E_\mathrm{i} \exp(-\mathrm{i}k_0\alpha_0 z) + E_\mathrm{r} \exp(\mathrm{i}k_0\alpha_0 z - \mathrm{i}\phi)|^2 \tag{2.71}$$

with wave vector $k_0 = 2\pi/\lambda$ and the phase shift ϕ of the beam at total reflection (above the critical angle there is no phase shift) calculated by (eq. 2.59, [72])

$$\phi(\alpha) = \arccos[2(\alpha_0/\alpha_\mathrm{c})^2 - 1]. \tag{2.72}$$

It follows [12, 72, 174] with $E_\mathrm{i} = 1$

$$I_\mathrm{vac}(\alpha_0, z) = I_0 \cdot [1 + |E_\mathrm{r}|^2 + 2|E_\mathrm{r}| \cos(2k_0\alpha_0 z - \phi)]. \tag{2.73}$$

Here, the relation between XSW field intensity I and (measurable) reflectivity $R = |E_\mathrm{r}|^2$ is obvious. Further, it can be seen that $I_\mathrm{vac}(\alpha_0, z)$ oscillates between the values 0 and $4I_0$ in the region of total reflection ($|E_\mathrm{r}| = 1$), with smaller amplitude right above and only little amplitude

around I_0 when $|E_\mathrm{r}|$ and even more $|E_\mathrm{r}|^2$ become very small at high angles of incidence. This is illustrated in figure 2.12. Within the substrate, there is just one wave (z is now counted from the surface downwards, with positive values inside the substrate) of intensity

$$I_\mathrm{sub}(\alpha_0, z) = I_0 \cdot |E_\mathrm{t} \exp(\mathrm{i}k_0\alpha_\mathrm{t} z)|^2. \tag{2.74}$$

Using equations 2.69, 2.24 and equation 2.28 for the attenuation length

$$z_n \approx \frac{\lambda}{4\pi \cdot \alpha_{\mathrm{t,i}}} \tag{2.75}$$

some conversions deliver

$$I_\mathrm{sub}(\alpha_0, z) = I_0 \cdot \left|\frac{2\alpha_0}{\alpha_0 + \alpha_\mathrm{t}}\right|^2 \cdot \exp\left(-\frac{z}{z_n}\right). \tag{2.76}$$

This means there is no oscillation anymore and the wave intensity decreases exponentially.

Thin homogeneous layer on a substrate

A beam hitting a (thin) layer at angle α_0 is reflected at angle $\alpha_{r,0} = \alpha_0$ and transmitted at angle

$$\alpha_1 = \sqrt{\alpha_0^2 - 2\delta_1 + 2\mathrm{i}\beta_1}. \tag{2.77}$$

After crossing the layer it is again reflected (at angle $\alpha_{\mathrm{r},1} = \alpha_1$) and transmitted into the substrate at angle

$$\alpha_\mathrm{s} = \sqrt{\alpha_0^2 - 2\delta_\mathrm{s} + 2\mathrm{i}\beta_\mathrm{s}}. \tag{2.78}$$

As in the previous chapter, the electrical field amplitude of the incoming beam shall be $E_0^\mathrm{i} = 1$ and there shall be no reflection inside the substrate, meaning $E_\mathrm{s}^\mathrm{r} = 0$. Then we can form an equation for each interface similar to equation 2.68:

$$\begin{bmatrix} 1 \\ E_0^\mathrm{r} \end{bmatrix} = M_{0,1} \cdot \begin{bmatrix} E_1^\mathrm{i} \\ E_1^\mathrm{r} \end{bmatrix} \tag{2.79}$$

$$\begin{bmatrix} E_1^\mathrm{i} \\ E_1^\mathrm{r} \end{bmatrix} = M_{1,\mathrm{s}} \cdot \begin{bmatrix} E_\mathrm{s}^\mathrm{i} \\ 0 \end{bmatrix} \tag{2.80}$$

with

$$M_{0,1} = \begin{bmatrix} m_{1,1} & m_{2,1} \\ m_{3,1} & m_{4,1} \end{bmatrix} \tag{2.81}$$

$$M_{1,\mathrm{s}} = \begin{bmatrix} m_{1,\mathrm{s}} & m_{2,\mathrm{s}} \\ m_{3,\mathrm{s}} & m_{4,\mathrm{s}} \end{bmatrix} \tag{2.82}$$

wherein the matrix elements are

$$m_{1,1} = \frac{\alpha_0 + \alpha_1}{2\alpha_0} \exp\left(-\mathrm{i}\frac{k_0}{2}\alpha_1 d_1\right) \qquad m_{1,\mathrm{s}} = \frac{\alpha_1 + \alpha_\mathrm{s}}{2\alpha_1} \exp\left(-\mathrm{i}\frac{k_0}{2}\alpha_1 d_1\right) \tag{2.83}$$

$$m_{2,1} = \frac{\alpha_0 - \alpha_1}{2\alpha_0} \exp\left(+\mathrm{i}\frac{k_0}{2}\alpha_1 d_1\right) \qquad m_{2,\mathrm{s}} = \frac{\alpha_1 - \alpha_\mathrm{s}}{2\alpha_1} \exp\left(-\mathrm{i}\frac{k_0}{2}\alpha_1 d_1\right) \tag{2.84}$$

$$m_{3,1} = \frac{\alpha_0 - \alpha_1}{2\alpha_0} \exp\left(-\mathrm{i}\frac{k_0}{2}\alpha_1 d_1\right) \qquad m_{3,\mathrm{s}} = \frac{\alpha_1 - \alpha_\mathrm{s}}{2\alpha_1} \exp\left(+\mathrm{i}\frac{k_0}{2}\alpha_1 d_1\right) \tag{2.85}$$

$$m_{4,1} = \frac{\alpha_0 + \alpha_1}{2\alpha_0} \exp\left(+\mathrm{i}\frac{k_0}{2}\alpha_1 d_1\right) \qquad m_{4,\mathrm{s}} = \frac{\alpha_1 + \alpha_\mathrm{s}}{2\alpha_1} \exp\left(+\mathrm{i}\frac{k_0}{2}\alpha_1 d_1\right). \tag{2.86}$$

The matrix elements corresponding to equations 2.69 and 2.70 are expanded here by a phase shift factor dependent on the wave vector $k_0 = 2\pi/\lambda$ (respectively wavelength), thickness d_1 of the layer and angle α_1 inside the layer. Based on these parameters the transfer matrices for both interfaces, $M_{0,1}$ (vacuum - layer) and $M_{1,\mathrm{s}}$ (layer - substrate) can be calculated. To obtain the electric field amplitudes $E^{\mathrm{r,i}}_{0,1,\mathrm{s}}$ in vacuum, layer and substrate the equation

$$\begin{bmatrix} 1 \\ E_0^\mathrm{r} \end{bmatrix} = M_\mathrm{t} \cdot \begin{bmatrix} E_\mathrm{s}^\mathrm{i} \\ 0 \end{bmatrix} \tag{2.87}$$

with the total transfer matrix

$$M_\mathrm{t} = M_{0,1} \cdot M_{1,\mathrm{s}} = \begin{bmatrix} m_{1,\mathrm{t}} & m_{2,\mathrm{t}} \\ m_{3,\mathrm{t}} & m_{4,\mathrm{t}} \end{bmatrix} \tag{2.88}$$

has to be solved. With the boundary conditions for the incident beam in vacuum, $E_0^\mathrm{i} = 1$, and reflected beam in the substrate, $E_\mathrm{s}^\mathrm{r} = 0$, it follows

$$1 = E_\mathrm{s}^\mathrm{i} \cdot m_{1,\mathrm{t}} \tag{2.89}$$

$$E_0^\mathrm{r} = E_\mathrm{s}^\mathrm{i} \cdot m_{3,\mathrm{t}} \tag{2.90}$$

and

$$E_\mathrm{s}^\mathrm{i} = \frac{1}{m_{1,\mathrm{t}}} \tag{2.91}$$

$$E_0^\mathrm{r} = \frac{m_{3,\mathrm{t}}}{m_{1,\mathrm{t}}}. \tag{2.92}$$

Then

$$\begin{bmatrix} E_1^\mathrm{i} \\ E_1^\mathrm{r} \end{bmatrix} = M_{1,\mathrm{s}} \cdot \begin{bmatrix} E_\mathrm{s}^\mathrm{i} \\ 0 \end{bmatrix} = \begin{bmatrix} m_{1,\mathrm{s}}/m_{1,\mathrm{t}} \\ m_{3,\mathrm{s}}/m_{1,\mathrm{t}} \end{bmatrix} \tag{2.93}$$

gives the field amplitudes inside the layer. XSW field intensities in vacuum and substrate are analogue to the previous section

$$I_{\mathrm{vac}}(\alpha_0, z) = I_0 \cdot |\exp(-\mathrm{i}k_0\alpha_0 z) + E_0^{\mathrm{r}} \exp(\mathrm{i}k_0\alpha_0 z - \mathrm{i}\phi_0)|^2 \quad (2.94)$$

$$I_{\mathrm{sub}}(\alpha_0, z) = I_0 \cdot |E_{\mathrm{s}}^{\mathrm{i}} \exp(\mathrm{i}k_0\alpha_{\mathrm{s}} z)|^2, \quad (2.95)$$

while inside the layer

$$I_1(\alpha_0, z) = I_0 \cdot |E_1^{\mathrm{i}} \exp(\mathrm{i}k_0\alpha_1 z) + E_1^{\mathrm{r}} \exp(-\mathrm{i}k_0\alpha_1 z + \mathrm{i}\phi_1)|^2 \quad (2.96)$$

holds with z being the position inside the layer ranging from $-d_1/2$ to $d_1/2$ with positive values towards the substrate. Both, in vacuum and layer a phase shift in the reflected beams

$$\phi_0 = \arccos[2(\alpha_0/\alpha_{\mathrm{c},1})^2 - 1] \quad (2.97)$$

$$\phi_1 = \arccos[2(\alpha_0/\alpha_{\mathrm{c,s}})^2 - 1] \quad (2.98)$$

occurs (only) in the case of total reflection, i.e. $\alpha_0 \leq \alpha_{\mathrm{c},1}$ or $\alpha_0 \leq \alpha_{\mathrm{c,s}}$. This happens for small angles of incidence at the vacuum-layer interface and can occur at the layer-substrate interface if $\delta_1 < \delta_{\mathrm{s}}$.

Several layers on a substrate

The preceding considerations can finally be expanded to a system of an arbitrary number of layers. Figure 2.14 illustrates a multilayer system of N layers already outlined in chapter 2.1.3. The beam enters from vacuum at angle α_0, penetrates each layer j (if it is not totally reflected at an interface) at an angle α_j depending on the corresponding refractive index and is partly reflected at each interface. Electrical field amplitudes E_n^{i} and E_n^{r} in every layer have to be calculated and added similar to the procedure discussed in the preceding sections:

$$\begin{bmatrix} E_n^{\mathrm{i}} \\ E_n^{\mathrm{r}} \end{bmatrix} = M_{n,n+1} \begin{bmatrix} E_{n+1}^{\mathrm{i}} \\ E_{n+1}^{\mathrm{r}} \end{bmatrix}. \quad (2.99)$$

First the transfer matrices $M_{n,n+1}$ for all interfaces between a total of N layers have to be calculated. $n = 0$ here represents the vacuum and $n = N+1$ the substrate, both considered to be infinite. The transfer matrices are then

$$M_{n,n+1} = \begin{bmatrix} m_{1,n+1} & m_{2,n+1} \\ m_{3,n+1} & m_{4,n+1} \end{bmatrix} \quad (2.100)$$

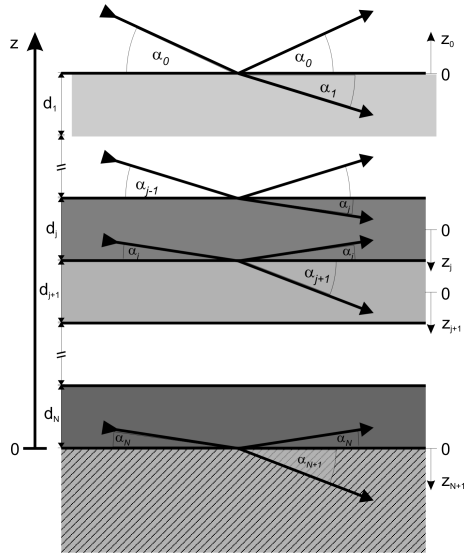

Figure 2.14.: Schematic illustration of a multilayer system with layers of different indices of refraction.

with matrix elements

$$m_{1,n+1} = \frac{\alpha_n + \alpha_{n+1}}{2\alpha_n} \exp\left[-i\frac{k_0}{2}(\alpha_n d_n + \alpha_{n+1} d_{n+1})\right] \tag{2.101}$$

$$m_{2,n+1} = \frac{\alpha_n - \alpha_{n+1}}{2\alpha_n} \exp\left[-i\frac{k_0}{2}(\alpha_n d_n - \alpha_{n+1} d_{n+1})\right] \tag{2.102}$$

$$m_{3,n+1} = \frac{\alpha_n - \alpha_{n+1}}{2\alpha_n} \exp\left[+i\frac{k_0}{2}(\alpha_n d_n - \alpha_{n+1} d_{n+1})\right] \tag{2.103}$$

$$m_{4,n+1} = \frac{\alpha_n + \alpha_{n+1}}{2\alpha_n} \exp\left[+i\frac{k_0}{2}(\alpha_n d_n + \alpha_{n+1} d_{n+1})\right]. \tag{2.104}$$

These can be understood as a combination of matrix elements in equation 2.83 representing upper and lower interface of each layer. Calculation of the electrical field amplitudes is performed in an analogue way as in the previous section with the total transfer matrix

$$M_\mathrm{t} = \prod_{n=0}^{N} M_{n,n+1} = \begin{bmatrix} m_{1,\mathrm{t}} & m_{2,\mathrm{t}} \\ m_{3,\mathrm{t}} & m_{4,\mathrm{t}} \end{bmatrix}. \tag{2.105}$$

Again,

$$\begin{bmatrix} 1 \\ E_0^r \end{bmatrix} = M_\mathrm{t} \cdot \begin{bmatrix} E_{N+1}^\mathrm{i} \\ 0 \end{bmatrix} \tag{2.106}$$

with

$$E_{\mathrm{s}}^{\mathrm{i}} = \frac{1}{m_{1,\mathrm{t}}} \text{ and } E_0^{\mathrm{r}} = \frac{m_{3,\mathrm{t}}}{m_{1,\mathrm{t}}} \tag{2.107}$$

holds, and electric field amplitudes in all layers can be calculated by subsequently multiplying transfer matrices and electrical field vectors from the substrate

$$\begin{bmatrix} E_N^{\mathrm{i}} \\ E_N^{\mathrm{r}} \end{bmatrix} = M_{\mathrm{N,N+1}} \cdot \begin{bmatrix} E_{\mathrm{s}}^{\mathrm{i}} \\ E_{\mathrm{s}}^{\mathrm{r}} \end{bmatrix} \tag{2.108}$$

to vacuum

$$\begin{bmatrix} E_0^{\mathrm{i}} \\ E_0^{\mathrm{r}} \end{bmatrix} = M_{0,1} \cdot \begin{bmatrix} E_1^{\mathrm{i}} \\ E_1^{\mathrm{r}} \end{bmatrix} \tag{2.109}$$

where E_0^{i} is supposed to be 1. Finally, XSW intensity depending on incident angle α_0 and position z inside layer j can be calculated by

$$I_j(\alpha_0, z_j) \quad = \quad I_0 \cdot |E_j^{\mathrm{i}} \exp(\mathrm{i}k_0\alpha_j z_j) + E_j^{\mathrm{r}} \exp(-\mathrm{i}k_0\alpha_j z + \mathrm{i}\phi_j)|^2. \tag{2.110}$$

Here, z_j is the position inside the layer ranging from $-d_1/2$ to $d_1/2$ with positive values towards the substrate. z values in vacuum and substrate are positive inside the respective layer with their origin at the border. Again, a phase shift

$$\phi_j \quad = \quad \arccos\left[2(\alpha_0/\alpha_{\mathrm{c},j})^2 - 1\right] \tag{2.111}$$

can occur at total reflection in vacuum and all layers.

2.4. Roughness

The preceding calculations for specular and diffuse scattering as well as XSW apply to perfectly smooth interfaces at which the refractive index jumps from one layer to the next. However, in reality interfaces have a finite roughness so that the refractive index n not only depends on the coordinate z perpendicular to the surface but also on its coordinates x and y within the plane leading to a relation $n(x, y, z)$. Usually, roughness of single-layer films increases with film thickness. Roughness of multilayer films depends on the types of materials, e.g. a W-on-C interface is rougher than a C-on-W interface, because the surface free energy of W is higher: $\sigma_{\mathrm{W}} < \sigma_{\mathrm{C}}$ [51]. Finally, it is noticeable that large roughness limits the applicability of XSW. If large thickness variations occur the phase relation between X-ray is lost and the typical XSW intensity distribution vanishes. The cosine term in equation 2.73 becomes 0 in average resulting in a beam intensity of $I \approx I_0 + R$ (with reflectivity R). Thus, the maximum XSW intensity is reduced from $4I_0$ to $2I_0$ [32, 176]. Further, marker atom distribution can be modified by rough interfaces [174]. If the roughness structure of a reflecting interface is reproduced on the marker layer - a so-called conform roughness - the detected marker layer thickness (marker distribution

range) is thicker than in an ideal flat sample. Generally, XRR measurements (especially at higher angles) are favorable to XSW scans in regard of roughness determination [51]. On the other hand, XSW with its element sensitivity can determine the transition between two element layers accurately even for large roughness values that would complicate XRR scans, which just rely on differences in electron density, a lot. Several works have been published related to roughness, some are discussed below.

The program *LsFit* [134, 135] utilized to analyze X-ray reflectivity scans provides the possibility of calculations using both modified Fresnel coefficients and effective density model. XSW calculations with the program *MXSW* (introduced in detail in chapter 5 and appendix E) permit implementation of roughness after the effective density model, too, and using Debye-Waller factors. Those roughness models are described in the following.

2.4.1. Debye-Waller factor

An approach to model roughness effects uses the fact that (little) interfacial roughness does not disturb the beampath very much but mainly damps reflectivity and thus interference and XSW intensity [32, 151]. Thus, if roughness is small then this damping can be included in the reflection coefficients r_j as a Debye-Waller type factor

$$DF = \exp\left[-(2k_0 \sin(\alpha)\sigma)^2\right] = \exp\left[-(q\sigma)^2\right] \tag{2.112}$$

with k_0 and q defined as in equation 2.3 and 2.35 and an rms (root mean square) roughness σ leading to

$$r'_j = r_j \exp\left[-(q\sigma)^2\right]. \tag{2.113}$$

Here, roughness effects are strongly dependent on the angle of incidence α. Implementing this factor into the matrix calculation of the XSW field described in section 2.3 is performed as described in appendix D.7 and leads to

$$E_\mathrm{i} = \frac{\alpha_\mathrm{i} + \alpha_\mathrm{t}}{(1+DF)\alpha_\mathrm{i} + (1-DF)\alpha_\mathrm{t}} \cdot E_\mathrm{t} = m_{1,4} \cdot E_\mathrm{t} \tag{2.114}$$

$$E_\mathrm{r} = \frac{DF\alpha_\mathrm{i} - DF\alpha_\mathrm{t}}{(1+DF)\alpha_\mathrm{i} + (1-DF)\alpha_\mathrm{t}} \cdot E_\mathrm{t} = m_{2,3} \cdot E_\mathrm{t} \tag{2.115}$$

replacing the matrix elements m_1 to m_4 in equations 2.101ff. In the limit $\sigma \to 0$ it follows $DF \to 1$ and E_i and E_r converge to the values given in section 2.3.

2.4.2. Modified Fresnel coefficients

As the wave vector transfer $\vec{q}$ in (specular) reflectivity scans is perpendicular to the sample surface the detected signal does not deliver any direct information about the lateral structure of the surface. The same applies for XSW scans as the XSW field intensity only varies with height. In the detector all contributions of the x-y-plane (for one specific z) are summed up leading to an

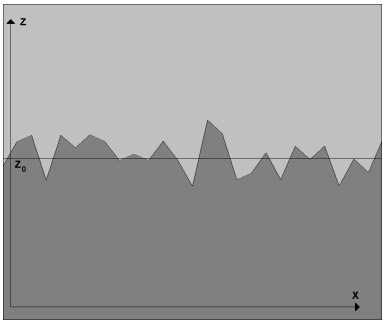

Figure 2.15.: Illustration of roughness of an interface between two layers 1 (light gray) and 2 (dark gray) of different refractive indices n_1 and n_2. The straight horizontal line represents the "nominal" interface at $z = z_0$ between n_1 and n_2 but at a rough interface n_2 can also be found at some positions above z_0 and vice versa. The average deviation of the interface from z_0 is zero but the rms roughness (cf. equation 2.118) is > 0. If measurements of n are only sensitive in vertical direction (like in XRR and XSW) a value $n(z)$ averaged in horizontal dimension is detected. $n(z)$ is equal to n_1 and n_2, respectively, far from z_0 and varies continuously from n_2 to n_1 in a transition region. Roughness can be quantified by the thickness of this region, for example by the above mentioned rms roughness.

averaged index of refraction or electron density $n(z)$ and $\rho_{\mathrm{e}}(z)$, respectively, that itself is only dependent on z as illustrated in figure 2.15. $n(z)$ is continuous and can be written as

$$n(z) \;=\; \lim_{X,Y\to\infty} \frac{1}{XY} \int_0^X \int_0^Y n(x,y,z)\,\mathrm{d}x\,\mathrm{d}y. \tag{2.116}$$

Thus, at each height z_0 the refractive index $n(z_0)$ is the integrated refractive index in the x-y-plane at z_0. $n(z)$ approaches a Heaviside step function for infinitely low roughness and leads to the case of perfectly smooth layers with n jumping at interfaces as discussed in section 2.1.3. A rough system can be regarded as if the interface between the two layers is not only at position z_0 as for a smooth interface but distributed around z_0 at positions $z = z_0 + z'$.

In the general case of multiple layers the transition from one layer j to the next one $j+1$ can be modeled by a number of smooth layers around z_j. Their absolute z-values are then calculated from z_j and the relative layer coordinates z' to be $z = z_j + z'$. Defining $P_j(z')\,\mathrm{d}z'$ as the probability to find interface j in the region between $z_j + z'$ and $z_j + z' + \mathrm{d}z'$ and with

$$\int z' P_j(z')\,\mathrm{d}z' \;=\; 0 \tag{2.117}$$

vanishing because z_j is the average position of the interface

$$\int z'^2 P_j(z')\,\mathrm{d}z' = \sigma_j^2 \tag{2.118}$$

defines the so-called "root-mean-square" (rms roughness) that is 0 only for a perfectly flat inter-

face. It gives a quantitative measure of the distortion of the interface from the perfectly smooth shape. With the mean value

$$\mu_j = \int z P_j(z)\,\mathrm{d}z \tag{2.119}$$

and the function

$$f_j(k) = \exp(\mathrm{i}k\mu_j) \cdot \int \exp(-\mathrm{i}kz) P_j(z)\,\mathrm{d}z \tag{2.120}$$

the Fresnel coefficients $r_{j+1,j}$ and $t_{j+1,j}$ introduced in equation 2.21 can be changed (cf. [42, 149]) to the so-called modified Fresnel coefficients

$$\tilde{r}_{j+1,j} = \frac{f_j(k_{z,j+1} + k_{z,j})}{f_j(k_{z,j+1} - k_{z,j})} r_{j+1,j} \tag{2.121}$$

$$\tilde{t}_{j+1,j} = \frac{1}{f_j(k_{z,j+1} - k_{z,j})} t_{j+1,j} \tag{2.122}$$

that can be applied in calculation of a layer system like the "ordinary" Fresnel coefficients. If the refractive index between two neighboring layers is continuous (in kind of a hyperbolic tangent or error function shape as discussed in appendix D.8) $P_j(z)$ shows a Gaussian profile

$$P_j(z) = \frac{1}{\sqrt{2\pi}\sigma_j} \exp\left(-\frac{z^2}{2\sigma_j^2}\right), \tag{2.123}$$

and the modified Fresnel coefficients can be written as [149]

$$\tilde{r}_{j+1,j} = \exp(-2k_{z,j}k_{z,j+1}\sigma_j^2) \cdot r_{j+1,j} \tag{2.124}$$

$$\tilde{t}_{j+1,j} = \exp\left[\frac{(k_{z,j} - k_{z,j+1})^2 \sigma_j^2}{2}\right] \cdot t_{j+1,j}. \tag{2.125}$$

2.4.3. Effective density model

The modified Fresnel coefficients deduced in the preceding chapter only make sense for small roughnesses $\sigma_j \ll d_j$, because otherwise the resulting refractive index profile can get discontinuous and lead to unrealistic results. Silicon substrates (as they are also used in this work) for example are usually covered with an oxide layer of which thickness and roughness often both are in the range of few nm. To be able to use the Parrat algorithm the previously introduced method has to be modified to the so-called "effective density model" [133, 134, 139, 143, 149].

Here, the continuous refractive index profile $n(z)$ is split into sufficiently thin slices (usually in the sub-nm range) and an individual average n_j can be calculated for each slice. Then, the sample is again treated like a multilayer system with smooth interfaces but more layers. For smaller roughnesses the effective density model merges into the case for individual layers. In the following, the calculation of the index of refraction $n(z)$ using the effective density model is

outlined. Detailed calculations can be found in [149].

Regarding a rough interface between layers j and $j-1$ the dispersion $\delta(z)$[4] can be described by calculating the fraction of material j at position z by

$$W_j(z) = \begin{cases} \frac{1}{2}\left[1 + Y_j(z - z_j)\right] & \text{for } z \leq \zeta_j \\ \frac{1}{2}\left[1 - Y_j(z - z_{j-1})\right] & \text{for } z > \zeta_j \end{cases} \tag{2.126}$$

with the shape of the $\delta(z)$ profile defined by the error function (cf. appendix D.8)

$$Y_j(z) = \operatorname{erf}\left(\frac{z}{\sqrt{2}\sigma_j}\right) \tag{2.127}$$

like in the previous section. At the position

$$\zeta_j = \frac{\sigma_j z_{j-1} + \sigma_{j-1} z_j}{\sigma_j + \sigma_{j-1}} \tag{2.128}$$

the neighboring layers' profiles are connected continuously. The dispersion profile of the entire layer sample composed of N layer with individual dispersion δ_j can then be described by

$$\delta(z) = \frac{\sum_{j=1}^{N+1} \delta_j W_j(z)}{\sum_{j=1}^{N+1} W_j(z)} \tag{2.129}$$

with the boundary conditions of infinitely thick vacuum (layer 0) and substrate (layer $N+1$) and roughness 0 at their outer boundaries. For small roughnesses $\sigma_j \ll d_j$ this profile corresponds to the one calculated with modified Fresnel coefficients. Thus, it is a generalization of reflectivity calculation for rough interfaces (see 2.4).

Nevertheless, it has to be considered that the parameters have a slightly different meaning here. The "layer thicknesses" $d_j = z_{j-1} - z_j$ define the parameter z_j of the $W_j(z)$ functions. The "roughness" σ_j symbolizes the width of the intermediate layer between layers j and $j+1$ that can become thicker than the layer itself for large roughnesses. In this case the real (physical) dispersion can be much smaller than δ_j (in the interval $[z_{j-1}, z_j]$), and 2.129 denotes an "effective dispersion or density in depth z". That is why this way of parameterization is called "effective density model".

Summarizing, considering roughness of an interface between two neighboring layers means that both layers contribute to the optical behavior in the transition region, the influence of one layer gradually decreasing with the other one increasing. Roughness is then defined as the overall thickness of these transition layers, at the same time decreasing the thickness of the neighboring layers to maintain the overall sample thickness. Using this method the sample system can still be treated like a layered sample with sharp (but numerous) interfaces and the Parrat algorithm [113] is still applicable.

[4] With $n = 1 - \delta + \mathrm{i}\beta$ and both δ and β proportional to the electron density ρ_e, δ can be regarded here instead of n following calculations by [149].

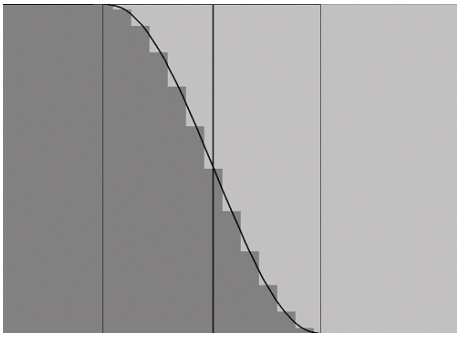

Figure 2.16.: Simulation of interface roughness by a cosine shaped stepwise transition.

2.4.4. Implementation of roughness in the XSW calculation program

Two different roughness models are implemented in the XSW calculation program *MXSW* developed during this work, a kind of effective density model and a Debye-Waller type damping factor.

The effective density roughness model is similar to the one used in [134, 135] and described in the previous section. A "roughness" σ between two layers A and B here means that the physical properties of the material in a range $\pm 0.5\sigma$ around the interface position are different from those of the pure materials A and B. Roughnesses can generally be of any size but the program prevents roughnesses that are thicker than the neighboring layers because these would cause unreasonable results. Further, overlapping of roughness regions from neighboring interfaces are prevented for the same reason.

A rough interface effects that at any position inside this roughness area at height h above the substrate material A or B can be encountered with the probability for A higher near the A bulk region and lower near the B bulk region. As XSW technique is only sensitive in a direction perpendicular to the surface, measurements show an average of physical properties of both materials for an infinitesimal thin layer at height h above the substrate, contribution of each material weighted with the position. Thus, a continuous transition between the values of material A and B occurs in the roughness region that is modeled in a sine/cosine shape (other transition shapes such as $\tanh$, erf, $\exp$, linear can also be selected) to prevent non-differentiable points ("edges") as illustrated in figure 2.16.

As XSW calculations in the program are based on layer models this continuous transition has to be divided into a number of discrete layers each with homogeneous optical properties as proposed by the effective density model (cf. chapter 2.4.3). If the number of these intermediate layers is large enough the simulation of a continuous transition is rather accurate.

Alternatively, the Debye-Waller roughness model can be implemented, but this is only recommended for small roughnesses. In contrary to the effective density model, it uses the given layer structure as it is but simulates roughness by modifying the Fresnel reflection and transmission coefficients. Calculation is described in detail in section 2.4.1.

Being always approximative the different roughness models can deliver different results. Thus,

it has to be kept in mind that the roughness values of these two models have a different meaning and cannot be compared directly.

3. Samples

In this work, a wide variety of sample types was analyzed by XRR and XSW measurements. With the main focus on GI-XSW, samples were selected that could test the capabilities of this method. A certain marker element was mandatory for each sample. This marker preferably needed to be a heavy element (heavier than Si) for most measurements. Only scans with soft X-rays at the plane-grating monochromator (PGM) beamline for undulator radiation [136, 130] at the Physikalisch-Technische Bundesanstalt (PTB) [119] laboratory at BESSY II [14], Berlin, permitted analysis of light elements. Further, one or several specific properties of the sample were interesting for analysis. Layer thicknesses or concentration/material amount were of interest in some samples while others were analyzed to determine the lateral orientation or distribution of certain components. Table 3.1 lists the sample systems analyzed during this work together with the corresponding marker and purpose of measurements.

Sample type	Marker	Specific property, purpose of measurement
Ge layers on Si	Ge	thickness determination of a single layer
Ion implantations in Si	As, Co, Zn	position of buried layers, marker distribution, concentration
Phospholipid bilayers	P	layer thickness, orientation of laterally ordered bio-molecules
Clusters on polymer	Au, Ag	layer thickness, concentration/coverage, total material amount
Dendrimer - gold layer	Au	layer thickness, density, coverage
Nitrobenzene films	N, C, Au	layer thickness, orientation, density
Multilayer laser mirror	Ti	element composition, layer thicknesses, periodicity
Buffer solution	K, Cl	ion distribution in a solution

Table 3.1.: List of sample systems analyzed in this work together with the selected marker atoms and sample properties to be investigated.

3.1. Semiconductors

Semiconductors are of increasing importance in modern technology especially in computers and other electronic devices. As produced structure dimensions are constantly getting smaller, analysis tools to characterize thicknesses of thin semiconductor layers or forms are required. Further, properties of semiconductors applied in modern technology can be enhanced by implanting foreign atoms into the material. Thus, characterization of such doped structures is of high interest.

Sample	No.	Substrate	Implant.	E (keV)	Nominal implantation dose (cm^{-2})
XSW010*	20	Si	As	100	$1.0 \cdot 10^{17}$
XSW011	10	Si	As	100	$1.0 \cdot 10^{17}$
XSW012	13	Si	Co	25	$1.0 \cdot 10^{16}$
XSW015	9	Si	Co	100	$1.0 \cdot 10^{17}$
XSW016	8	Si	Co, Zn	100	Co: $1.0 \cdot 10^{17}$, Zn: $0.49 \cdot 10^{17}$
XSW017	12	Si	Co, Zn	100	Co: $1.0 \cdot 10^{16}$, Zn: $1.0 \cdot 10^{16}$

Table 3.2.: List of implantation samples that were analyzed with XRR and XSW. Implantation was performed at 100 keV or 25 keV at normal incidence (* Sample XSW010 was implanted at 60°).

3.1.1. Semiconductor layers

As examples for semiconductor layers a set of commercially available Ge layers on Si wafers *(JENOPTIK, Jena, Germany)* with different layer thickness (29 nm, 76 nm, 309 nm) [158] was analyzed. XRR and XSW measurements were performed to obtain information about layer thicknesses and roughnesses of the sample systems.

3.1.2. Implantations

Different kinds of implantation samples were analyzed with XRR and XSW techniques in this work. Table 3.2 lists the samples under investigation. Implantation was performed at Johannes Kepler University of Linz [73, 74, 75, 77] by bombarding a silicon substrate with different ions (As, Co, Zn) at 100 keV (sample XSW012: 25 keV). The nominal implantation dose was between $1.0 \cdot 10^{16}$ cm^{-2} and $1.0 \cdot 10^{17}$ cm^{-2}. Implantation was executed at normal incidence (one sample was implanted at 60°) at room temperature without subsequent annealing. Several samples of this type (cobalt [73, 74, 77] and arsenic [74, 75] ion implantations in silicon) have been characterized in the past utilizing destructive methods like repeated etching in combination with Rutherford Backscattering (RBS) and Total Reflection X-ray Fluorescence (TXRF) analysis [73, 74, 75, 77]. Contrarily, in this work the layered structures were determined by XSW technique which is non-destructive. Furthermore, no sample preparation was needed and measurement time was short.

3.2. Bio-organic samples

Links between physics, chemistry and biology are rapidly growing in modern technology and science, terms such as bio-engineering and life science are indicating these connections. Thus, biological and organic materials are often subject to physical analysis. X-ray related methods with their nanometer scale resolution are capable of analyzing basic components of life-forms such as proteins and lipids and other organic materials such as polymers, dendrimers or nitrobenzene that have important functions in industry and technology. In this work, the potentials of XRR and XSW with this family of samples are analyzed.

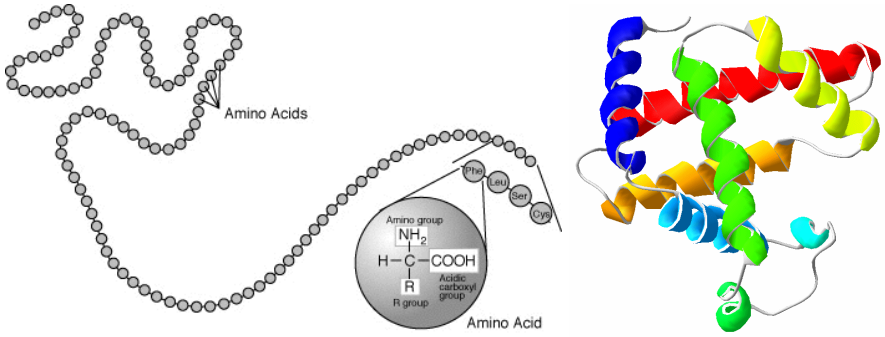

Figure 3.1.: Left: Schematic illustration of the primary structure of a protein composed of a large number of amino acids.
Right: Three-dimensional (tertiary) structure of myoglobin with colored alpha helices (secondary structure elements), the first protein structure to be characterized using X-ray crystallography by Kendrew et al. [70, 165].

3.2.1. Proteins

Background

Proteins are essential components of every living cell and thus subject to wide examinations. The word protein is derived from the Greek word "protos" (primary, first) and was introduced in 1839 by Gerardus Johannes Mulder [100] after a suggestion from Jöns Jakob Berzelius. The functions of proteins in organisms are widespread, from enzymatic catalysis of biochemical reactions, signaling functions, cell adhesion to formation of the cytoskeleton of a cell. Being composed of amino acids linked by peptide bonds, proteins form a complex chain consisting of a huge number of atoms as illustrated in figure 3.1. Proteins often join complexes to perform certain biological functions.

The structure of a protein can be described as follows [156]. First, the primary structure of a protein is the sequence of amino acids linked to compose the protein. As a linear chain is not the energetically most favorable structure it folds to a so-called secondary structure. Some known types of these secondary structures are α, π or 3_{10} helices, β sheets, β turns and random coils. Generally, a mixture of different secondary structures occurs in a single protein. Thus, helices, sheets and other components form a three-dimensional bundle called tertiary structure as shown in figure 3.1. The quaternary structure is an arrangement of several equal proteins to a larger complex.

Apart from its elemental composition, the three-dimensional structure and orientation of a protein are important for its functionality [156]. Commonly, structure determination of proteins with atomic resolution is performed by X-ray crystallography or NMR spectroscopy. The worldwide Protein Data Bank [13, 169] lists thousands of solved proteins structures as Cartesian coordinates of all atoms inside the structure. Figure 3.1 shows the three-dimensional structure of myoglobin, the first protein structure determined by X-ray crystallography by Sir John Cowdery Kendrew et al. in 1958 [70] rewarded with the Nobel Prize in Chemistry. As X-ray crystallogra-

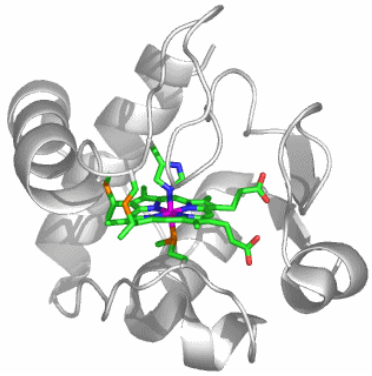

Figure 3.2.: Three-dimensional representation of cytochrome c secondary and tertiary protein structure. The roughly spherical shape shows helices (gray) in the outer region and the iron (magenta) containing hem molecule (colored) in the center. Image from [126].

phy is the main structure determination technique, proteins that can be crystallized (for example globular proteins) form the majority of so-far known structures [38, 106] while other proteins such as membrane proteins are generally less well known. As 20-40% of all proteins cannot be crystallized [97] other methods have to be used [96, 125].

Like all biological molecules, proteins are radiation sensitive and get damaged or even destroyed if X-ray intensity is too high. The conventional damage barrier for protein molecules is about 200 X-ray photons per $Å^2$ for X-rays of 12 keV energy (1 Å wavelength). It may be extended to very high dose rates at very short exposure times [107]. Within about 10 femtoseconds biomolecules can withstand an X-ray intensity of $\approx 3.8 \cdot 10^6$ photons/$Å^2$ with minimal structural changes [97]. Thus the Free Electron Laser (FEL) is a promising tool for future protein analyses.

Cytochrome

Cytochromes are proteins acting as redox catalysts in biochemical processes like photosynthesis or cellular respiration. Approximately 50 types of cytochromes are subdivided into groups called cytochrome a, b, c, and d, depending on their light absorption properties ("cytochrome" is Greek meaning "cell coloring"). Each cytochrome comprises one or more heme molecules containing an iron atom. Cytochrome c, which was analyzed during this work, is one of the best known cytochromes. Its three-dimensional molecular structure (illustrated in figure 3.2) containing around 100 amino acids is well characterized by protein crystallography. Contrarily to most other cytochromes, cytochrome c is soluble in water and acts as an electron mediator in oxidation and reduction but cannot bind oxygen. It is a quite small cytochrome (molecular weight about 12 kg/mol, diameter approximately 3.4 nm [126]) and present in plants, animals and many unicellular organisms. As a rather old protein (regarding evolution of life-forms) it is useful in biological taxonomy of animals because closely related animals show little differences in the structure of their cytochrome c.

In this work cytochrome c was utilized as a representative protein model system with a nat-

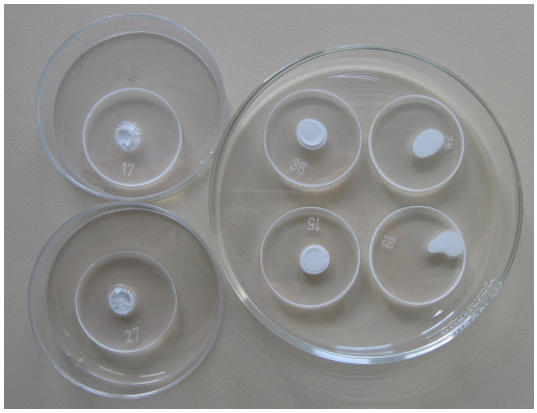

Figure 3.3.: Picture of quartz carriers covered with silane solution.

urally embedded marker atom (Fe) necessary for X-ray fluorescence studies. To permit XSW measurements, cytochrome c molecules had to be immobilized on a reflecting substrate. Quartz glass carriers were chosen as substrates for these films.

First, the carriers were cleaned in a special cleaning procedure that has proven to be useful during years of application at ISAS. This procedure is explained in detail in appendix C.1. Then 15 μL of a silane solution (3-(Triethoxysilyl)-propylamine ($C_9H_{23}NO_3Si$); *Merck Schuchardt, Hohenbrunn, Germany*) were dropped onto the carrier (cf. figure 3.3) and dried to prepare a hydrophobic surface.

A cytochrome c solution was prepared and immobilized on the sample carrier in cooperation with Dunja Zimmermann [177] at ISAS Dortmund. The multi-step procedure is described in detail in appendix C.2. These samples were then investigated using TXRF and XSW technique as described in sections 4 and 6.2.1. It had to be checked if those methods were capable of detecting the little Fe concentration in this sample and, with the help of Fe as a marker, could measure sample parameters like distances inside the molecule or relative to the substrate.

3.2.2. Lipids

Background

Like proteins, lipids are essential components of living cells, important both for structure and function. The term lipid is deduced from the Greek word "lipos" (fat), but fat (biological term: "triglyceride") is just a subgroup of the lipids [156]. Many lipids show a polar (hydrophilic) head group combined with a non-polar (hydrophobic) tail of one, two or three hydrocarbon chains. Phospholipids are amphiphilic (at the same time hydrophobic and hydrophilic) lipids composed of a hydrophilic, phosphorus-containing head and two hydrophobic hydrocarbon tails (cf. figure 3.4). Being so-called membrane lipids phospholipids are a major component of lipid bilayers in biological membranes and cell walls. Biomembranes can selectively block or let pass ions to maintain a certain concentration inside the cell [43, 176]. Due to their amphiphilic behavior

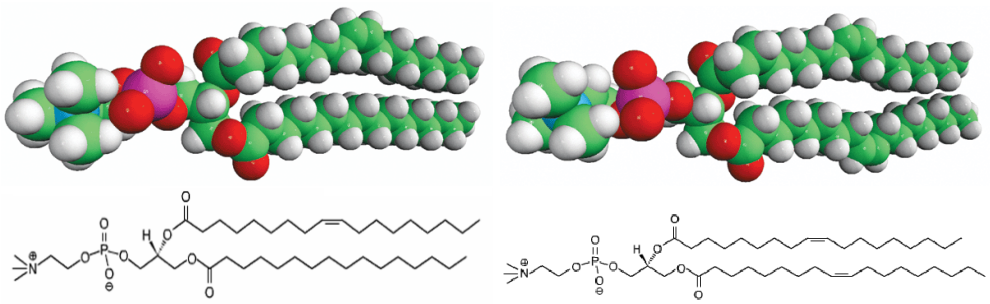

Figure 3.4.: Calotte models and structural formulae of two phospholipids: POPC (left) and DOPC (right). The head containing phosphorus and nitrogen is hydrophilic, the two hydrocarbon tails are hydrophobic. Images from [3].

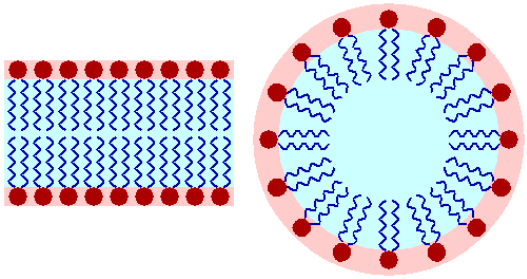

Figure 3.5.: Schematic of a phospholipid bilayer and micelle. In contact with water or other polar liquids, phospholipids form structures to minimize contact of their hydrophobic tails to the solution such as the bilayer or spherical micelle shown here. The nonpolar tail region (blue) tends to evade water, the polar head (red) is oriented towards the water molecules outside the sphere or above the bilayer [64, 165].

phospholipids form bilayers, spherical micelles or other shapes at contact with water or polar liquids to minimize contact of their hydrophobic tails to the solution (cf. figure 3.5).

Furthermore, phospholipids can be well analyzed with XSW measurements because they incorporate atoms of typical elements such as phosphorus that virtually do not affect the XSW field [160, 174] formed by substrate and phospholipid layer but can serve as marker atoms. Additionally, absorption effects inside a lipid are much smaller than refraction effects, i.e. $\beta/\delta < 0.001$ [161, 174], thus β may be negligible in some calculations.

Phospholipids in experiment

In cooperation with Prof. Niemeyer (Biological-Chemical Microstructure Technology Group [64, 108], Department of Chemistry at the University of Dortmund), phospholipid bilayers on mica were analyzed. Ideally, the lipids are compressed to a maximum density and form a "solid" layer of molecules aligned exactly perpendicular to the substrate surface as illustrated in figure 3.6. If the lipids are not packed in the closest way the molecules are still able to move in certain limits similar to a liquid (cf. figure 3.7) leading to a lower bilayer thickness [64]. Two different

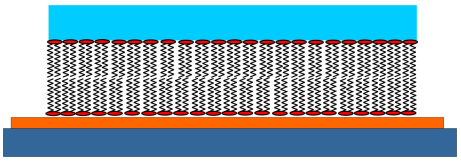

Figure 3.6.: Schematic structure of a phospholipid bilayer sample: Phospholipids adhere to a thin mica substrate glued to a glass carrier. A second layer of phospholipids is located on the first layer with reversed orientation and in contact with a stabilizing KCl buffer solution.

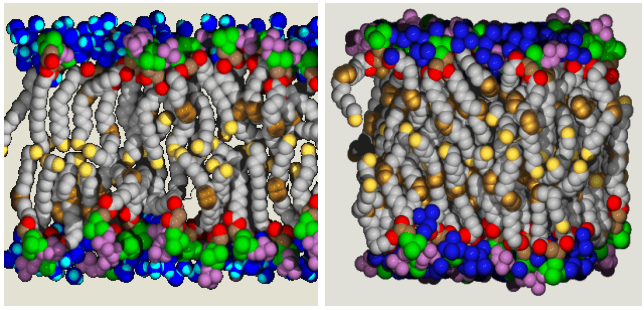

Figure 3.7.: 3D calotte model representation of POPC (left) and DOPC (right) bilayers [41]. As can be seen the phospholipids are not packed in the closest way here, thus the bilayer is kind of flexible or "liquid". Due to this flexibility phospholipid chains are not exactly perpendicular to the substrate surface and the bilayer thickness is lower than in a "solid" bilayer. Tails of the phospholipids are colored in gray, the phosphorus containing part green and the nitrogen containing head violet. A thin water film is shown as blue molecules.

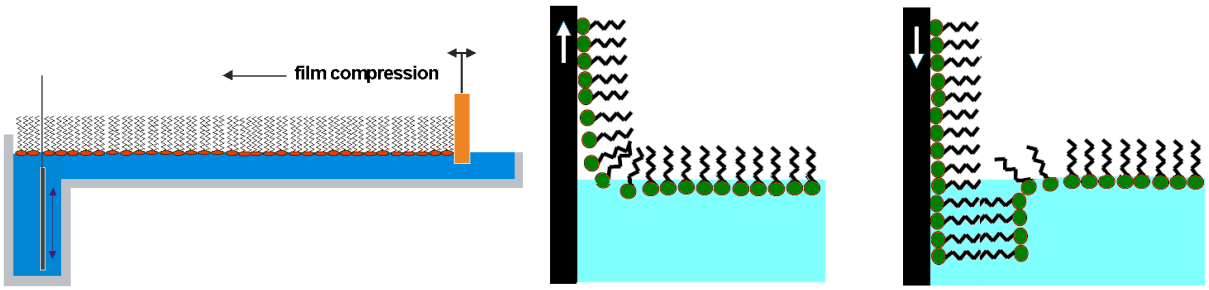

Figure 3.8.: Illustration of the Langmuir-Blodgett technique to create ordered mono- or multilayers. A solution containing the amphiphilic molecules dissolved in chloroform is spread onto a water-filled Langmuir trough leaving the amphiphiles on the water surface. The molecules are compressed isothermally by a Teflon barrier to form an ordered lipid monolayer. Then a sample carrier (on the left side of each image) is pulled out of the solution slowly taking along a monolayer of the amphiphilic molecules. When the carrier is introduced again an additional layer adheres to the sample. Illustrations based on data from [54, 64].

types of phospholipids were analyzed, POPC and DOPC, that only vary slightly in the structure of their tails as shown in figure 3.4.

Samples were prepared by Jessica Irrgang [64] applying the Langmuir-Blodgett method [16, 110, 129] as described in the following. A solution containing the amphiphilic phospholipid molecules dissolved in chloroform was spread onto a water-filled Langmuir trough leaving the amphiphiles on the water surface. The molecules were compressed isothermally by a movable Teflon barrier to form a "solid" phospholipid monolayer (cf. figure 3.8). Then a mica substrate glued to a glass carrier (for easier handling) was pulled out of the trough taking along the phospholipid monolayer that adhered to the substrate by the polar heads of the phospholipids. With the pressure and thus the monolayer on the solution remaining, the substrate was again put into the trough then taking along a second layer that was applied via the tails of the lipids to the first monolayer to create a bilayer, a so-called solid supported phospholipid bilayer (SPB). After deposition of the second lipid monolayer, the remaining lipids on the water surface were removed. The coated substrate was then taken out of the water and immediately stored in an aqueous KCl buffer solution. By repeating this procedure, in principle a third, forth and further phospholipid layers can be attached to the substrate with orientation of heads and tails switching each turn.

The polar heads of the first layer adhered to the mica substrate and the heads of the second layer were in contact with an aqueous cover film, so this bilayer remained relatively stable. A schematic structure of such a bilayer is shown in figure 3.6. However, if the water/buffer evaporates into air stabilization of the second layer is expected to break down (especially in a "liquid" Langmuir-Blodgett film) letting the sample decompose to a monolayer.

After preparation of the film an AFM (atomic force microscope) scan was performed on the sample as shown in figure 3.9 to check if the production process was successful. Finally, the sample was analyzed by XRR and XSW measurements as described in the experimental chapter 4.

Bond	Bond length (Å)	Bond angle (°)	Length in chain (Å)	Source/Remarks
C-C	1.48-1.54	109.5	1.26	[28, 123, 154]
C-C	1.40	120	1.21	benzene ring [28]
C=C	1.33	180	1.33	[28, 123]
C-H	1.08-1.10	109.5	0.89	[123]
C-O	1.43	(110)	1.17	[80, 154]
C=O	1.22	(110)	1.17	[80]
C-O	1.31	120	1.17	in CO_3^{2-} [80]
C-N	1.47-1.54	(110)	1.26	[22, 154]
N-O	1.47	(120)	1.27	[57]
N=O	1.15	(120)	1.00	[57]
O-H	0.96	104.5	0.76	angle for HOH [123]
P-O	1.50	104	1.18	[40]

Table 3.3.: Bond lengths in biomolecules used in this work. The bond length is the distance between centers of two bond atoms, length in chain is the length contribution of this bond to a long molecule because in most cases atoms are not in a stretched chain but form a zigzag structure with different bond angles as can be seen in figure 3.4. The bond angles in brackets are estimated. It has to be kept in mind that the bond length can be shorter or longer in certain compounds.

To facilitate evaluation the chain lengths of the phospholipids can be estimated by taking into account the known structure of the molecule (cf. 3.4) and typical bond lengths (distance between centers of two bond atoms) and bond angles (the angle between the straight lines connecting an atom in a molecule chain with its direct neighbors) in biomolecules. Table 3.3 shows tabulated bond lengths and bond angles of compounds used in this work as well as the resulting length in a molecule chain. In most cases atoms are not in a stretched chain but form a zigzag structure with different bond angles, thus the overall length of the chain is shorter than the sum of the individual bond lengths. The total length of POPC molecules analyzed in this work amounts to approximately 35.3 Å, composed of a head length of 10.6 Å and chain lengths of 24.7 Å and

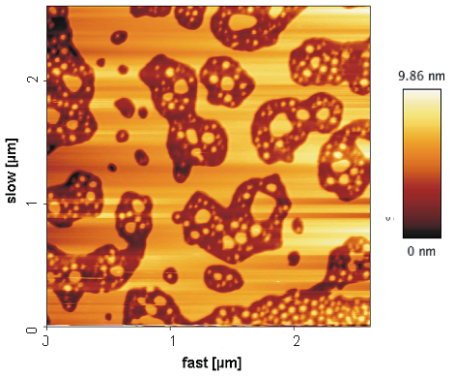

Figure 3.9.: AFM image of DOPC phospholipids on a mica substrate [64].

23.4 Å, respectively. The DOPC molecule is slightly longer (36.6 Å) with the same head size as POPC and both tails with equal length 25.9 Å.

3.2.3. Polymers

Background

Polymers are important materials in state of the art technology [66, 81, 116, 164, 168]. They can be produced and processed easily and inexpensively. Depending on their chemical composition they feature a wide range of physical and chemical properties (e.g. elasticity can vary from very soft to extremely hard) and thus can be applied in many fields. Polymers occur in everyday life for example as polycarbonate in CDs and DVDs, in the form of acrylic bone cement in prostheses, as adhesives (as a welding alternative) [20] or embedding polymer electrolytes for metal catalyzers in fuel cells [87] in automobile production. Polyacrylates are also applied as binding materials in paints and varnishes (acrylic paints), as material in dental medicine and many other fields. Further, polymers are utilized as substrates for metallic conductors in integrated circuits [29, 168], organic displays [63] and other applications in the field of micro-electronics. Especially in technological applications, a combination of metals and polymers is important, for example as metallic conductors on polymer substrates or aluminum coatings of CDs and DVDs. Metal atoms in the form of clusters rather than continuous layers on polymers have been analyzed using different X-ray techniques [15], like X-ray reflectivity (XRR) or X-ray photon correlation spectroscopy (XPCS) [68, 81, 164], but to our knowledge not yet using XSW. However, the combination of a nanometer range layered structure with metals as good fluorescence markers can be analyzed very comfortably by X-ray standing waves technique.

Polymer layers with and without metal clusters

Several samples of silicon substrates covered with a native oxide layer of approximately 1 nm were coated with polystyrene. Figure 3.10 shows a styrene monomer [C_8H_8] which is the basis of polymer chains that can be composed of up to several ten thousands of these monomers. Thus molecular weight of those polymers is typically in the range of tens or hundreds of kg/mol. PS mass density at 25°C is 1.05 g/cm^3 [116] and its monomer's molecular weight amounts to 104.1 g/mol. A second type of polymer utilized in this work is poly(butyl-methacrylate), shortly PBMA. Like polystyrene it is a polymer that forms long chains composed of thousands of butyl-methacrylate monomers [$C_8H_{14}O_2$] displayed in figure 3.10. The molecular weight of each monomer is 142.20 g/mol and its mass density at 25°C is 1.053 g/cm^3 [116]. Depending on the orientation of side groups, polymers can be subdivided into isotactic (all side groups are located on the same side of the main chain), syndiotactic (alternating regular orientation) or atactic (irregular orientation) polymers. Polymers investigated in this work belong to the latter group that cannot be crystallized because of their irregular structure but show a glass transition from the liquid to the "solid" state when cooled. Strictly speaking a glass is still a liquid but moving very slowly because of its high viscosity. The glass transition temperature is defined as the temperature at which the viscosity reaches the value $\eta = 10^{12}$ Ns/m^2 [47, 164].

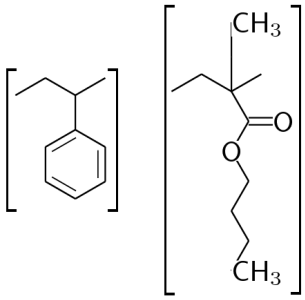

Figure 3.10.: Structural formulae of a polystyrene [C_8H_8] (left) and PBMA [$C_8H_{14}O_2$] (right) monomer. Further monomers are connected to the C-C string forming the linear polymer chain of hundreds or thousands of monomers.

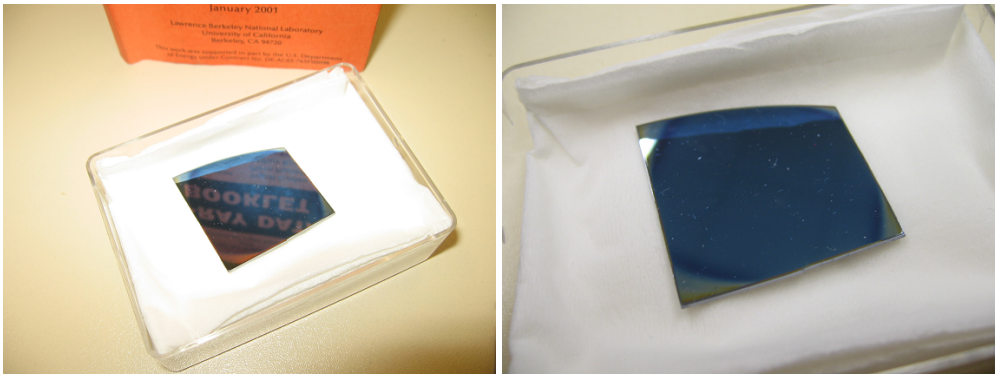

Figure 3.11.: Photos of the silicon substrate carrying a 134 nm PBMA film with silver clusters.

Polymer films in this work were produced using the spin-coating technique. This was done by dropping a small amount of the respective polymer solution onto the center of a clean, untreated silicon wafer rotating at a defined speed. Due to rotation the solution was spread homogeneously on the substrate, excess solution flowed from the wafer. After vaporization of the solvent a thin polymer film remained on the silicon. The thickness of this film could be adjusted by changing rotational speed and concentration of the polymer solution. To remove remaining solvent and to turn the polymer film into equilibrium the samples were annealed for several hours above the glass transition temperature and cooled down slowly afterwards to prevent dewetting (contracting of the polymer layer due to surface tension). Later, gold or silver were evaporated onto the polymer samples in a high vacuum evaporation chamber. If evaporation was performed sufficiently slowly the metal atoms did not form a continuous layer but agglomerated to nanometer sized clusters. A detailed description of the preparation process and devices can be found in [81, 164].

Pure polymer layers and polymer layers covered with Au or Ag clusters (the latter sample is shown in figure 3.11) were measured. These samples were prepared at Lehrstuhl E1a, Department of Physics, University of Dortmund [81, 142, 145]. Table 3.4 lists parameters of the

Sample Number	Polymer	M_w (kg/mol)	d_P (nm)	Metal	$d_{M,n}$ (nm)
scan21	PS	N/A	6.9	–	–
scan20	PS	N/A	16.5	–	–
scan18	PS	N/A	45.3	–	–
scan19	PS	N/A	71.3	–	–
XSW003	PS	34.4	80	Au	1
XSW004	PBMA	337	134	Ag	1.5

Table 3.4.: Polymer and polymer/metal samples analyzed in this work: Two types of polymers have been used: Polystyrene (PS) and PBMA. M_w is the molecular weight of the polymer chains, d_P the thickness of the polymer layer and $d_{M,n}$ the nominal thickness of the metal layer evaporated onto the polymer. This is the thickness of a continuous layer. However, as the metals occur as clusters the actual thickness of the "layer" is larger.

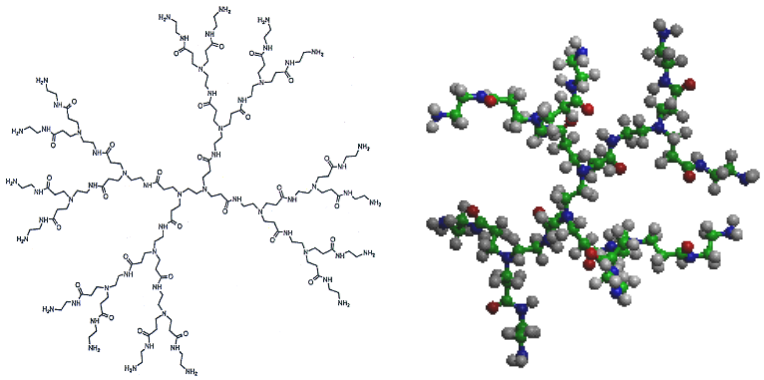

Figure 3.12.: PAMAM dendrimer of the second generation shown as structural formula and as ball-and-stick model [34]. The tree branch growing structure is obvious.

samples under investigation.

3.2.4. Dendrimers

Background

Dendrimers (Greek "dendros" means "tree") are (artificial) macromolecular chemical structures that grow in a dendritic (reticulated) way, similar to the branches of a tree. This means that, starting from an initiator core, with each new "generation" repetitively similar molecules are attached to the existing structure forming a huge macromolecule that finally - due to steric reasons - approximates a spherical shape. Figure 3.12 shows the 2D and 3D structure of an ethylenediamine-core poly(amidoamine) (PAMAM) dendrimer. Figure 3.13 illustrates the fast rising of molecular weight and number of functional groups at the dendrimer surface with each new generation. Dendrimers are especially useful because of the multiple functionality of their surface and the large number of functional groups leading for example to strong adhesion even if adhesion forces

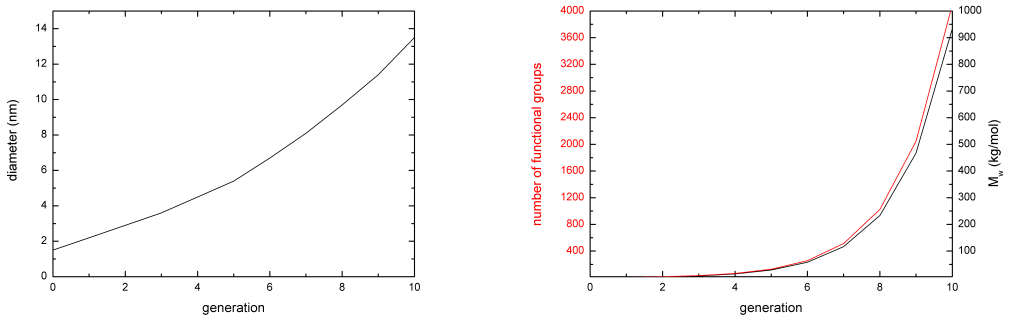

Figure 3.13.: Diameter (left), number of functional groups and molecular weight (right) of PAMAM dendrimers from 0th to 10th generation [34]. Molecular weight and group number are growing exponentially while the molecule diameter increases approximately in a linear way.

of a single functional group are weak [4].

Dendrimers with gold

In this work PAMAM dendrimers (*Dendritech Inc., Midland, MI, USA* [34]) of the forth generation with a molecular weight of $M_w \approx 14$ kg/mol, 64 amino surface groups and a diameter of roughly 4.5 nm were used to immobilize DNA molecules bound to gold atoms or clusters on a glass substrate. These samples were prepared at Microstructure Technology Group, Department of Chemistry, University of Dortmund [64] by successively attaching NH_2, glutaric acid anhydride (GA), NHS, PAMAM (from a 10% amino-PAMAM solution) and NH_2 activated DNA hybridized to complementary functionalized gold particles.

3.2.5. Nitrobenzene

Background

Nitrobenzene is an important intermediate product in chemical industry. It is colorless, liquid at room temperature, and has a large index of refraction. As the magneto-electrical Kerr-effect of nitrobenzene is rather strong, it is utilized in Kerr cells to rotate the polarization planes of incident light. Some physical properties of nitrobenzene are listed in table 3.5.

Ultrathin nitrobenzene films

Ultrathin nitrobenzene ($C_6H_5NO_2$; figure 3.14) layers on Si have been analyzed in cooperation with the Interface Spectroscopy Group [124] of ISAS - Institute for Analytical Sciences, Department Berlin. The nitrobenzene layers were produced by Jörg Rappich at Hahn-Meitner Institute (HMI) Berlin [55] by electrochemically depositing nitrobenzene onto etched H-passivated silicon substrates [50, 56, 121]. However, oxidation of the surface could have taken place on samples

Property	Value
Molecular weight	123.06 g/mol
Density	1.19867 g/cm^3
Melting point	5.85°C
Boiling point	210.85°C
Flash point	88°C
Autoignition temperature	525°C
Index of refraction (for visible light)	1.55

Table 3.5.: Physical properties of nitrobenzene for norm conditions (index of refraction for 20°C). Sources: [153, 155]

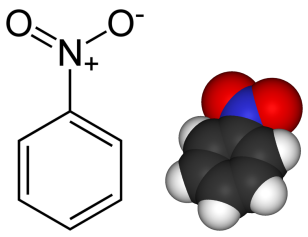

Figure 3.14.: Structural formula and calotte model of a nitrobenzene molecule ($C_6H_5NO_2$). The overall length of the molecule is approximately 0.6 nm, the distance between N and the center of the benzene ring is about 0.3 nm. (Values estimated from bond lengths listed in table 3.3).

Figure 3.15.: Different possible orientations of nitrobenzene (NB) molecules and gold atoms on the substrate: The nitrobenzene molecules can form a monolayer, bilayer or multilayer. They can be ordered or disordered (with different density), and gold can stay on top of the NB layer or diffuse down to the substrate.

that were stored in air before deposition. Depending on air humidity a significant oxide layer forms on Silicon within 1-2 hours. Thickness of this layer then increases for 1-2 days [62]. Information about (native) oxide layers can also be found in the literature [17, 111]. Further, gold was sputtered onto some of the nitrobenzene layers in vacuum [124].

The prepared samples were then characterized by Katy Roodenko [124] at ISAS Berlin using spectroscopic ellipsometry technique [7, 50, 61]. However, further studies were necessary to determine the sample structure. It had to be clarified if the nitrobenzene layers were ordered or disordered, if the gold atoms stayed on the top surface or diffused to the substrate and if a monolayer or multilayers were formed. The different possibilities are illustrated in figure 3.15.

3.3. Other sample types

Apart from the sample types presented in the previous sections countless other system might be analyzed by XRR and XSW. Exemplarily, two very different types of sample systems will be presented. First, a periodic multilayer mirror was be subject to analysis. With numerous smooth reflecting interfaces and several elements to be detected this mirror appears to be an ideal system for XSW analysis. On the other hand, ion distributions presented thereafter usually do not have a smooth reflecting interface if at all an interface is present. Nevertheless, these distributions still provide a lateral distribution of marker atoms that might be gaged by the moving XSW maxima.

3.3.1. Periodic multilayers

A commercial multilayer laser mirror *(Spectra-Physics, Mountain View, USA)* of unknown composition was investigated. Periodic multilayers with known element content have been analyzed using XSW at the Bragg reflection by Ghose at al. [51]. However, as not only layer thicknesses but also element composition were not known another approach had to be made. Typically a multilayer mirror consists of multiple (here 24) double layers of appropriate materials with the condition that each layer thickness corresponds to 1/4 of the central laser wavelength divided by the index of refraction of the respective layer. This results in a phase shift of 2π if the beam is

Material	Refractive index
TiO_2	2.700
MgO	1.740
SiO_2	1.548
Quartz glass	1.462
LiF	1.394

Table 3.6.: Indices of refraction of possible component materials at λ = 570 nm of the investigated multilayer laser mirror. Data from [91].

passing and being reflected at a bottom of each double layer leading to constructive interference at normal incidence.

The central laser wavelength utilized with this mirror was about 570 nm and possible materials for the mirror were TiO_2, MgO, SiO_2, quartz glass or LiF. Indices of refraction of these materials at 570 nm are listed in table 3.6. Measurement and corresponding evaluation procedures to characterize this mirror are described in detail in the respective chapters.

3.3.2. Ion distribution

At liquid-solid interfaces but also in some solids, atoms of the included elements are not arranged in layers but distributed with a concentration dependent on the position e.g. height z above the substrate

$$c = c(z). \tag{3.1}$$

A prominent example for such ion distribution is the lateral dependence of ion concentration near a charged surface or interface (like biologically important interfaces such as membranes). Several models have been developed to describe this ion distribution [12, 151].

The most simple approach is a so-called Helmholtz layer [58]. The electrical field of a negatively charged surface is compensated by a thin layer of positive ions, so-called counter-ions, packed closely at the surface. The thickness of this layer is equal to the ion diameter d_{ion} and electrostatic potential decreases linearly from ϕ_0 at the surface to 0 at the outer side of the ion layer:

$$\phi(z) = \phi_0 \cdot \left(1 - \frac{z}{d_{\mathrm{ion}}}\right). \tag{3.2}$$

The thermal motion of counter-ions is ignored in the simple Helmholtz model. If it is taken into account, the Gouy-Chapman model [26, 52] emerges. This model comprises a diffuse ion layer above the charged interface with ion concentration decreasing with distance. The resulting potential (for a small surface charge) amounts to [12]

$$\phi(z) = \phi_0 \cdot \exp\left(-\frac{z}{L_{\mathrm{D}}}\right) \tag{3.3}$$

with ϕ_0 being the potential at the surface

$$\phi_0 = \frac{\sigma L_{\mathrm{D}}}{\epsilon}. \tag{3.4}$$

Here σ represents the surface charge density and L_{D} the so-called Debye length

$$L_{\mathrm{D}} = \sqrt{\frac{\epsilon kT}{Se_0^2}} \tag{3.5}$$

as a measure for the thickness of the diffuse layer with ϵ being the permittivity

$$\epsilon = \epsilon_{\mathrm{r}} \cdot \epsilon_0 \tag{3.6}$$

calculated from the relative permittivity ϵ_{r} and the permittivity of free space ϵ_0. Further, k is the Boltzmann constant, T the absolute temperature, e_0 the elementary charge and S the ionic strength

$$S = \sum_i z_{\mathrm{i}}^2 c_{\mathrm{i}}. \tag{3.7}$$

with the charge valence z_{i} and bulk concentration c_{i} of ion i.

Stern [141] expanded the Gouy-Chapman model by introducing a type of Helmholtz layer of counter-ions bound to the charged interface by ion binding that does not completely compensate the surface charge. This layer, also called Stern layer [173], is followed by a diffuse layer like in the previous model. This combination leads to a potential that first decreases linearly (in the vicinity of the surface i.e. within a distance corresponding to the ion diameter) and then exponentially from the summed potentials of charged surface and Stern layer. All three models are illustrated in figure 3.16 with their ion distribution and their position dependent electrostatic potential ϕ. Using these models [12] for a system with only one kind of counter-ions leads to an ion concentration distribution

$$c(z) = c_{\mathrm{S}} \exp(-z/L') + c_0 \tag{3.8}$$

in the diffuse region with the bulk concentration c_0, the concentration at the surface (relative to the bulk) c_{S} and the ion Debye length L'. The potential Debye length L_{D} is only equivalent to L' if the surface potential is weak and the electrolyte is dilute, otherwise L' is somewhat smaller.

Successful results of a few XSW measurements of ion distributions were published in the past. Trainor et al. [151] scanned the ion distribution near a substrate-solution interface, Bedzyk et al. [12] investigated the distribution of ions in an electrolyte solution in contact with a phospholipid membrane. In this work, ion distributions were incorporated in several samples that were investigated for other parameters, too. Thus, ion concentration inside the KCl buffer solution above the phospholipid bilayer (cf. section 3.2.2) and the non homogeneous distribution of implantation ions in silicon (cf. section 3.1.2) were investigated.

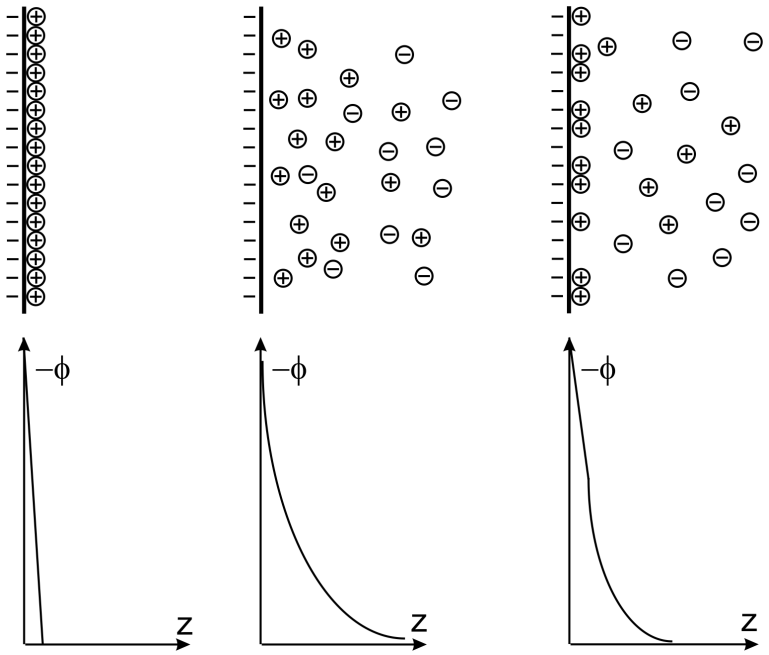

Figure 3.16.: Schematic illustration of ion distribution near a negatively charged surface. From left to right: Helmholtz model, Gouy-Chapman model, Stern model. Positions of the ions are depicted above, the electrostatic potential ϕ is shown below. Detailed explanations can be found in the text.

4. Experiment

4.1. Measurement stations

Measurements performed in this work were accomplished at different measurement stations. Some element contents were determined at a TXRF spectrometer at ISAS, Dortmund. XSW and XRR scans were performed at beamline BL9 of DELTA synchrotron, Dortmund. Finally, a sample cell developed for measurements of volatile liquids or under vacuum conditions is described.

4.1.1. TXRF spectrometer EXTRA II

TXRF measurements in this work were performed at ISAS by a commercial "*X-ray spectrometer EXTRA II*" (*Seifert, Ahrensburg, Germany; now Atomika Instruments GmbH / CAMECA GmbH, Oberschleißheim, Germany*) that is depicted in figure 4.1. Radiation can be selected between a tungsten (W) or molybdenum (Mo) anode. Tube voltage and current can be chosen up to values of 50 kV and 38 mA. Evaluation of measurement data is supposed to be performed using the attached control computer. Due to the age of the instrument (built in 1991) there are no suitable options to export measurements at formats readable by other programs. Thus, the binary EXTRA II save file had to be analyzed and a conversion program had to be developed to extract measurement data into multi-platform compatible ASCII data files. This conversion program is outlined in appendix E.2.

4.1.2. DELTA synchrotron radiation source

The utilization of synchrotron radiation in X-ray analysis provides several significant advantages. Generally, X-ray radiation from a synchrotron is much more intense than from a laboratory tube, it is polarized and shows low divergence. Photon energy can be chosen by a monochromator from a continuous energy spectrum giving the possibility to apply a wavelength optimal for the respective measurement.

Most measurements presented in this work were performed at DELTA (Dortmunder Elektronen Speicherring Anlage) synchrotron facility [128, 150] at the University of Dortmund. DELTA is a third generation synchrotron radiation source that supplies - with the help of special magnetic structures (insertion devices) - soft and hard X-ray radiation (synchrotron radiation) for non-destructive analysis of various kinds of samples. The synchrotron facility consists of three main components: A linear accelerator (Linac) to pre-accelerate electrons to energies of 75 MeV, a booster synchrotron (BoDo) for further acceleration up to 1.5 GeV and a storage ring (Delta)

Figure 4.1.: Photos of the X-ray spectrometer EXTRA II (*Seifert, Ahrensburg, Germany; now Atomika Instruments GmbH / CAMECA GmbH, Oberschleißheim, Germany*) utilized for TXRF measurements in this work. The left picture shows the entire instrument with tube and generator section (left), measurement section with radiation protection door (center) and control computer (right). The right picture displays a more detailed view of the measurement section. The selectable Mo and W X-ray tubes are located in the boxes on the left and behind, respectively. Samples can be introduced using a sample changer box (in front). Fluorescence radiation is measured by a nitrogen cooled Si(Li) detector (above).

to store the electrons with energies between 300 MeV and 1.5 GeV [33]. Electron current in the storage ring amounts to $\approx$ 120 mA after injection and decreases exponentially until the next injection. During experiments it is usually roughly between 60 and 120 mA. Re-injection is performed if the electron current and thus the intensity of the generated synchrotron radiation gets too low. This is usually necessary every 8-12 hours. DELTA comprises 13 beamlines (cf. figure 4.2) located at different insertion devices and optimized for different types of measurements [85, 159]. The superconducting asymmetric wiggler beamline BL9 (section 4.1.3), where most experiments described in this work were performed, is described in more detail below.

4.1.3. Beamline BL9 (SAW2) at DELTA

The BL9 beamline (SAW2) [85] is located behind a superconducting asymmetric wiggler (SAW) with critical energy 7.9 keV. The magnetic flux density at the SAW is 5.3 T (in asymmetric mode) and 2.79 T (in symmetric mode), respectively. Horizontal beam divergence (opening angle) ranges from $\pm$13 mrad (symmetric mode) to $\pm$25 mrad (asymmetric mode) [33]. The horizontal beam fan generated by the wiggler is distributed to three neighboring beamlines (BL8, BL9, BL10) providing approximately 5 mrad to each beamline (in asymmetric mode). Vertical beam divergence is calculated by $1/\gamma$ and amounts to $\approx$ 0.7 mrad [142].

The distance from the source (wiggler) to the sample at this beamline is approximately 34-

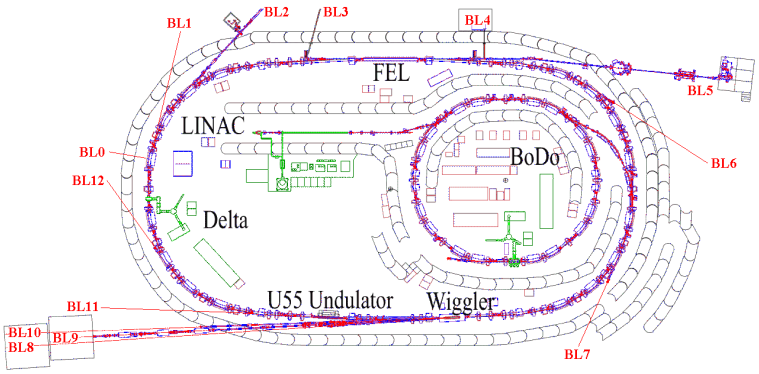

Figure 4.2.: Layout of DELTA synchrotron facility and position of beamlines.

Parameter	Value	E (keV)	ξ_l (nm)
Selectable energy range	4-30 keV	10.05	1234
Max. photon flux		13.00	954
- total, with mirror	$2 \cdot 10^{10}$ mm^{-2}s^{-1}	15.00	827
- monochromatic, without mirror	$5 \cdot 10^{7}$ mm^{-2}s^{-1}mA^{-1}	15.20	816
Energy resolution $\Delta E/E$	$\approx 10^{-4}$ (0.01%)		

Table 4.1.: Important parameters of BL9 beamline (SAW2): Photon flux, energy parameters and longitudinal coherence length ξ_l for different energies calculated using equation 2.45.

36 m [114, 142]. A computer controlled silicon (311) double crystal monochromator permits selection of radiation energies between 4 keV and 30 keV. The second crystal can be utilized for sagittal focusing. Further features of this beamline are a focusing silicon mirror, an absorber and fast-shutter system (*XIA LLC, Hayward, CA, USA*), variable slit systems (*JJ X-Ray, Roskilde, Denmark*) and computer control of all devices by a SPECTRA software [33]. Distances and devices at BL9 from the source to the detector are illustrated in figure 4.3.

Achievable photon flux is around $2 \cdot 10^{10}$ mm^{-2}s^{-1} or $5 \cdot 10^{7}$ m^{-2}s^{-1}mA^{-1} for monochromatic radiation [142]. Energy resolution of the monochromator is $\Delta E/E \approx 10^{-4}$ (0.01%). This leads to a longitudinal coherence length ξ_l between 816 nm (at 15.2 keV) and 1234 nm (at 10.05 keV) for energies used in this work.

A 6-axis diffractometer (*Huber Diffraktionstechnik, Rimsting, Germany*) and a spectrometer in Rowland geometry permit small angle, wide angle and inelastic X-ray scattering experiments. Various detector systems are available: A NaI point detector e.g. for reflectivity scans, an energy dispersive detector (*Amptek Inc, Bedford, MA, USA*) e.g. for fluorescence analyses and a Mar345 area detector (*Marresearch GmbH, Norderstedt, Germany*) e.g. for (surface) diffraction measurements. A schematic set-up (for XRR measurements) of the experimental hutch of beamline BL9 is shown in figure 4.4. The specific set-ups for measurements performed in this work are described in detail in sections 4.2.1 and 4.2.3. According to sample requirements different photon energies were selected during the different beamtimes at BL9. The energy of the exciting

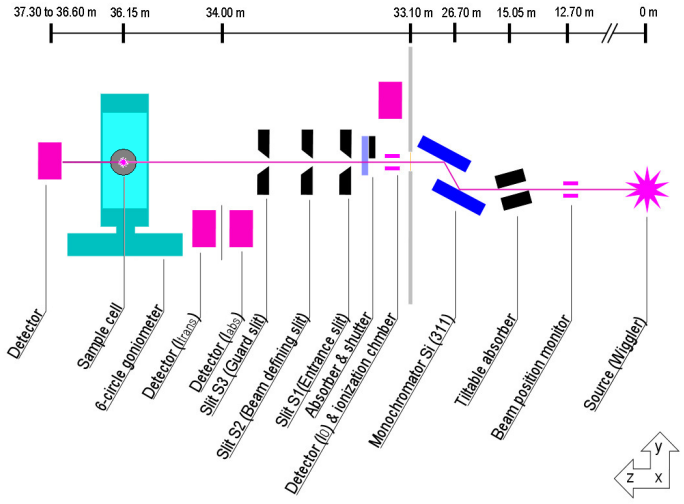

Figure 4.3.: Schematic representation of the set-up of the set-up at BL9 from the source (wiggler) to the detector.

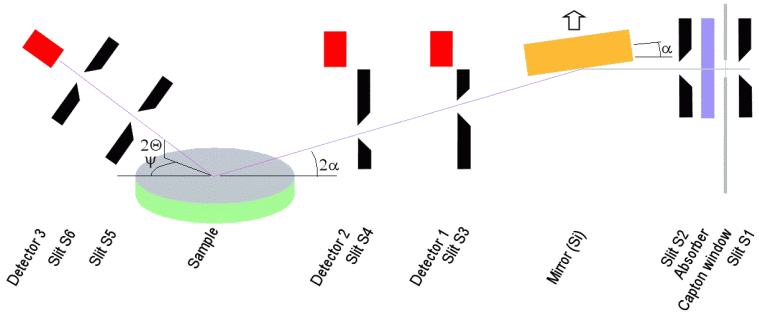

Figure 4.4.: Schematic representation of the experimental hutch of BL9: Path of the beam from the entrance slit to the sample and detector for XRR measurements.

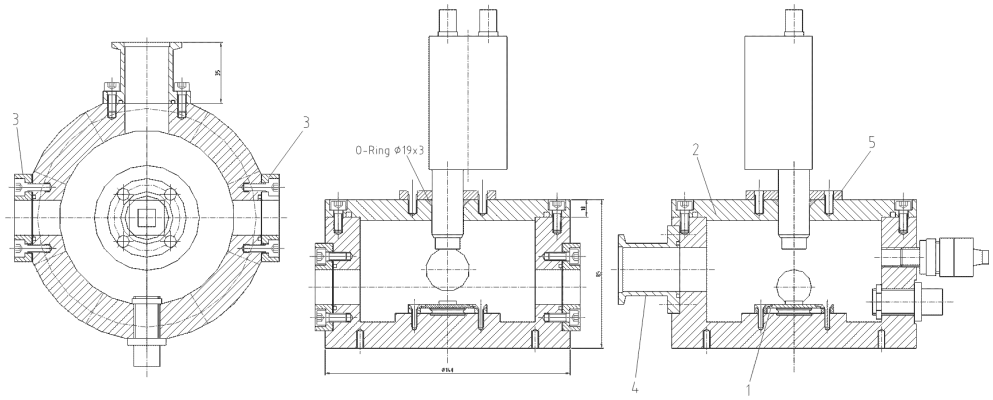

Figure 4.5.: Design drawing of the sample cell. From left to right: Top view, side view, front view. A removable Kapton window (3) can be seen on each side of the top and side view drawing. The beam enters from one side, hits the sample on the carrier in the middle and leaves the cell on the other side. Fluorescence radiation can be detected by the EDX detector that can be fixed by a brass ring (5) and sealed with an O-ring in the removable top cover (2) of the sample cell. The front view of the cell shows a connection flange (4) for a vacuum pump including gas pressure sensor on the left side and a vacuum plug (lower right) for electrical temperature control devices. Further, an optional flange (upper right) permits easy venting of the cell or flooding of the cell with gases like helium or nitrogen. Finally, the copper block (1) carrying the sample holder can be cooled or heated.

photons had to be higher than the energy of the fluorescence radiation to be observed [5, 84, 146] (cf. table B.4), to be more exact, higher than the binding energy [6, 24, 49, 146] of the electron to be ejected. Also the current set-up of the beamline at the date of measurement was regarded. If the actually adjusted energy at the beamline was appropriate, time-consuming modification and re-alignment of the set-up could be prevented.

4.1.4. Sample cell for liquid, vacuum and gas measurements

While many XSW scans can be performed at atmospheric pressure without much preparation in the experimental hutch, some samples require special measurement environments. Samples comprising thin liquid films have to be stored in a closed cell during long-time measurements to prevent vaporization of the liquid over time. This was e.g. necessary for the cytochrome and phospholipid samples that were covered with a thin film of buffer solution. By positioning these samples in a small cell (eventually together with a little container filled with additional liquid) vaporization can be reduced significantly because the small gas volume inside the cell is saturated with vapor.

Another application of a closed sample cell is measurement in a shielding gas or vacuum. Particularly X-ray fluorescence of light elements like C or Si is difficult to detect because the emitted low-energy photons (cf. table B.4) are strongly absorbed by air. Replacing air in the cell by helium or even better vacuum reduces absorption of fluorescence photons between sample and detector significantly and reduces detection limits. Measurements of the laser multilayer mirror and polymer layers on silicon were performed at vacuum conditions.

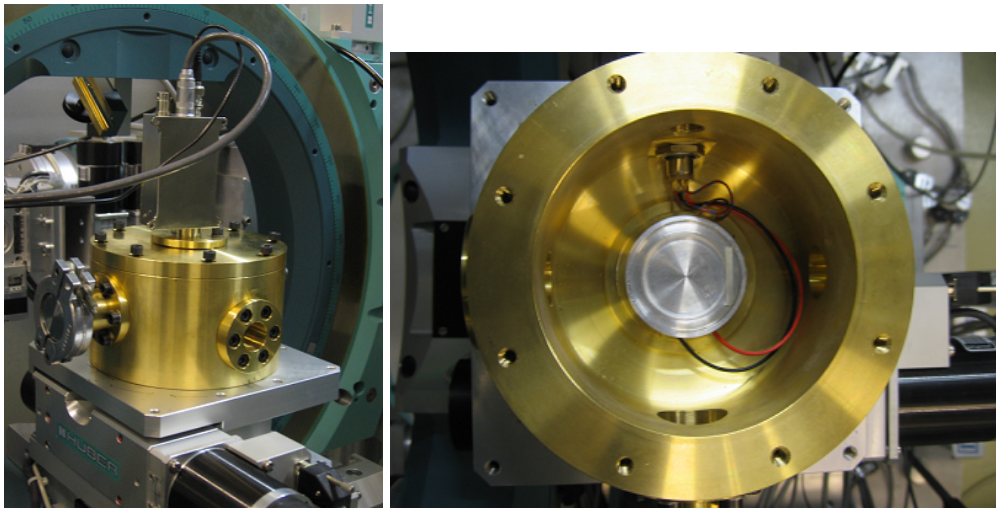

Figure 4.6.: Photos of the sample cell. Left: Set-up during experiment. The beam enters through the window on the right side, the vacuum flange on the left side is closed during experiments with constant liquid vapor pressure. The energy-dispersive detector is mounted on top of the cell. Right: Top view of the open cell. The beam passes from right to left, electronics connections can be seen in the upper, vacuum pump flange in the lower part of the picture.

A sample cell for measurements of liquids and samples in gases or vacuum was developed during this work (cf. figures 4.5 and 4.6). The cell is made of brass and sealed with O-ring sealings. It comprises two windows made of Kapton (polyimide) foil (*DuPont, Wilmington, USA*) to permit the X-ray beam to enter and exit, and a trough to hold buffer solution or water. Connection flanges for a vacuum pump, gas pressure sensor, and for easily venting or flooding the cell with nitrogen or helium are provided. Further, a multi wire vacuum plug permits easy and flexible connection to different electrical devices e.g. for temperature control. Vapor pressure and thickness of liquid films in the cell can be regulated by changing the temperature. For this purpose, a Cu block carrying an aluminum sample holder comprises an electrical resistor for heating and a peltier element (*Telemeter Electronic GmbH, Donauwörth, Germany*) for cooling. Temperature can be measured and controlled by a Pt100 sensor (*Telemeter Electronic GmbH, Donauwörth, Germany*) also located inside the Cu block. Due to the big heat capacity of the Cu block temperature can be controlled very precisely.

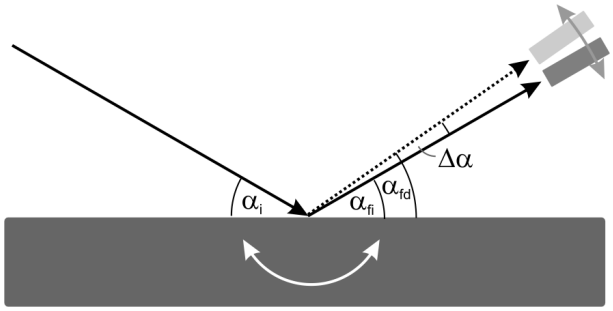

Figure 4.7.: Schematic illustration of the set-up in XRR measurements. The angle of incidence α_i is defined by tilting the sample. Specular scans are performed with the detector at $\alpha_{\mathrm{fi}} = \alpha_{\mathrm{i}}$, (in-plane) longitudinal diffuse scans at a shifted exit angle $\alpha_{\mathrm{fd}} = \alpha_{\mathrm{i}} + \Delta\alpha$ with an angle offset $\Delta\alpha$.

4.2. Experimental set-ups and procedures

Different types of X-ray measurements were performed in this work. The corresponding set-ups, measurement and evaluation procedures for XRR, TXRF and XSW methods are described in the following.

4.2.1. XRR

A schematic illustration of the set-up in X-ray reflectivity (XRR) measurements is shown in figure 4.7. As the synchrotron cannot be moved the angle of incidence α_{i} is defined by tilting the sample. In (specular) reflectivity scans the exit angle is then defined by moving the (NaI point) detector to $\alpha_{\mathrm{f}} = \alpha_{\mathrm{i}}$ relative to the sample surface, i.e. $2\alpha_{\mathrm{i}}$ relative to the incident beam. At BL9 beamline, the incident angle is denominated θ and the detector angle (relative to the incident beam) 2θ. This is why this set-up is called θ-2θ geometry. However, for conformity reasons the denomination α is used in this work. To measure (and subtract) the intensity contribution caused by diffuse scattering from the total measured intensity another reflectivity scan is recorded with the detector shifted by $\Delta\alpha$ = 0.1° from the specular position $\alpha_{\mathrm{fi}} = \alpha_{\mathrm{i}}$. This so called longitudinal-diffuse (LD) scan shows intensities orders of magnitudes lower than the specular scan in the low angle area around total reflection but becomes comparable to the specular scan at higher angles. Thus, the accessible angle range (and by this the resolution) down to background noise can be improved by considering the LD scan.

As angles are measured very accurately in XRR scans, a precise alignment of the sample is mandatory for reliable results. The center of rotation for the angles must be located exactly on the surface in the middle of the sample. This is achieved by the alignment procedure described in the following. First, the detector angle ("2θ") range is scanned without a sample, the position of maximum intensity is defined as 2θ = 0. Then, the sample is positioned in the center of the sample stage by visual judgment. The angle of incidence (sample angle) is set to θ = 0 and intensity at $2\theta = 0$ is recorded while the sample position z is moved upwards into the beam. The sample position where the intensity reaches half of the full intensity (the "half-shading")

is selected because at that position the center of the beam hits the center of the sample for all angles of incidence. Then a "rocking scan" is performed by tilting the sample from $\theta = -0.5^\circ$ to $\theta = 0.5^\circ$ with $2\theta = 0$. The scan should have the shape of a symmetric triangle with its vertex at 0°. If this is not the case the angle of incidence θ is moved to the maximum and the z-scan for the "half-shading" is repeated. Once alignment is finished, it has to be checked at higher angles of incidence. θ is moved to 0.2° and 2θ to 0.4° and another rocking scan of θ around 0.2° is run. The maximum of intensity should be at specular position ($\theta = 0.2^\circ$). If not, θ is moved to the maximum and declared to be 0.2° at that position. After completing this control, a third test is performed at $\theta = 0.5^\circ$ and $2\theta = 1.0^\circ$ equivalently, and finally at $\theta = 0^\circ$ and $2\theta = 0^\circ$ again. After that, sample and set-up are aligned. Further information about aligning and XRR scans can be found in [42, 81].

Typically, a reflectivity scan is run from 0° to 2°-6° with a step size of 0.002° or larger depending on the structure of the reflectivity curve. Short period oscillation from layered samples demand a small step size while e.g. the simply exponentially decreasing reflectivity of a pure silicon surface can be scanned with larger steps. Measurement time for each point depends on the angle of incidence. While intensity is very high at low angles around total reflection and even an absorber has to be introduced into the beam to prevent damage to the detector, it decreases rapidly at high angles requiring acquisition times of 40-60 seconds per point. Total scanning time for one reflectivity curve (depending on the angle range covered) typically amounts to 1 to 4 hours. Due to the lower intensity, LD scans take roughly twice the time as specular scans. For most samples presented in this work both XSW and XRR scans were accomplished. The two measurements can be performed with the same combined set-up and they can deliver complementary information [51] allowing kind of an iterative evaluation process.

For evaluation of reflectivity scans, intensities at longitudinal diffuse scattering (LD) position $\alpha_{\mathrm{fd}} = \alpha_{\mathrm{i}} + \Delta\alpha$ have to be subtracted from intensities at specular position $\alpha_{\mathrm{fi}} = \alpha_{\mathrm{i}}$. The LD-scattering corrected curve usually provides better accuracy than the specular reflectivity scan, especially for large angles with lower signal-to-noise ratio. As angles in specular and LD scan are not directly comparable ($\alpha_{\mathrm{fd}} \neq \alpha_{\mathrm{i}}$) they have to be transformed to wave vector transfers q_{z} according to formula 2.35

$$q_z = \frac{2\pi}{\lambda}(\sin\alpha_{\mathrm{i}} + \sin\alpha_{\mathrm{f}}) \tag{4.1}$$

with radiation wavelength λ and α_{f} being α_{fi} or α_{fd}, respectively. Then intensities for corresponding q_z can be subtracted and the difference be re-transformed to the angle space by

$$\alpha = \arcsin\left(\frac{\lambda \cdot q_z}{2\pi}\right). \tag{4.2}$$

This procedure can be done automatically using the program *D8opt* outlined in appendix E.3.

The measured reflectivity curve must then be compared to a calculated one to obtain the sample structure responsible for the measured scan. For this purpose, a layered structure is assumed and reflection, transmission and absorption of X-ray radiation in this model is calculated. This task was handled using the *LsFit* software [134, 135]. Thickness and roughness (as discussed

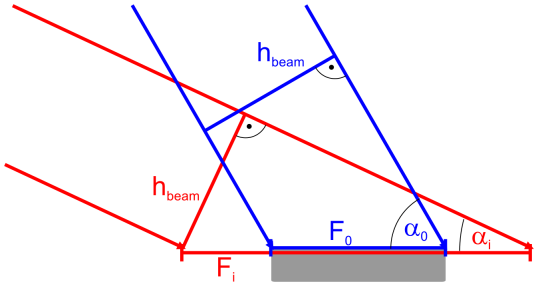

Figure 4.8.: Illustration of the reduced reflectivity due to a footprint effect: If a beam of height h_{beam} hits a sample of length F_0 at angle α_0 the beam covers the whole sample and is completely reflected (considering respective reflection coefficients). If the incident angle is larger than α_0 it only covers part of the sample and again the whole beam is reflected. However, if the incident angle is $\alpha_{\mathrm{i}} < \alpha_0$ the beam footprint F_{i} is larger than the sample and radiation beyond the borders of the sample is lost.

in chapter 2.4) need to be input for each layer as well as the optical constants δ and β of the respective materials. These values are tabulated [31, 59] for all elements and a number of important compounds. Further, experimental parameters such as photon energy, detector resolution, sample size or intensity offset must be considered, too. Then, parameters are varied to achieve the best possible fit. Here, δ and β are usually fixed (if the layer is homogeneous), parameters like detector resolution have to be determined only once for a whole set of measurements, and thicknesses are often limited to certain ranges. Thus, the number of free parameters reduces and the fit can be optimized "by eye" rather well. For fine-tuning, *LsFit* provides the possibility to utilize a fitting procedure based on minimizing the chi-square deviations that can improve results but might also lead to non-physical values. Thus, an evaluation of the calculated parameters is mandatory. If the sample structure cannot be described by a discrete layers system quality of fits is limited. This might be the case if roughnesses are too large, materials are mixed inhomogeneously at interfaces or if the sample is not plane but bended. Some examples of fitting and interpretations are given in the evaluation chapter.

Furthermore, it has to be considered that, in contrary to the calculated Fresnel reflectivity curves presented in figure 2.2, measurements do not show constant maximum intensity for angles below the critical angle of total reflection but decrease for angles below α_{c}. This happens due to a geometric effect: At very low angles, the footprint of the beam (i.e. the area of the sample that is covered by the beam) is larger than the sample itself as illustrated in figure 4.8.

At a footprint angle α_0 the beam covers the whole sample and is completely reflected (considering respective reflection coefficients), the same holds if $\alpha_{\mathrm{i}} > \alpha_0$. Then the beam only covers part of and its footprint is entirely on the sample and thus reflected. But if the incident angle is smaller than the footprint angle, $\alpha_{\mathrm{i}} < \alpha_0$, the beam footprint F_{i} exceeds the sample area[1] F_0 and radiation beyond the borders of the sample is lost. This effect can be corrected by calculating the

[1] Actually, the expressions "sample area" and "footprint area" denote a length namely the length of the region covered by the beam footprint. The width (in the surface plane, perpendicular to the length) of the illuminated area is not affected by effects discussed here. Thus, every "footprint length" is related to a "footprint area" and both expressions are utilized here.

ratio of radiation beyond the sample boundaries. With the footprint angle

$$\alpha_0 = \arcsin\left(\frac{h_{\mathrm{beam}}}{F_0}\right) \tag{4.3}$$

and the footprint at incident angle α_i

$$F_\mathrm{i} = \frac{h_{\mathrm{beam}}}{\sin\alpha_\mathrm{i}} \tag{4.4}$$

the ratio of theoretical and detected reflectivity intensity is

$$f_{\mathrm{foot}} = \frac{F_\mathrm{i}}{F_0} = \frac{\sin\alpha_0}{\sin\alpha_\mathrm{i}}. \tag{4.5}$$

Thus, the measured intensity has to be multiplied by (or the theoretical intensity divided by) the factor f_{foot} for angles $\alpha_\mathrm{i} < \alpha_0$. This geometrical correction not only applies to XRR measurements but also to XSW scans [51] as discussed in the simulation chapter 5.

4.2.2. TXRF

The principle of TXRF is explained in theory section 2.2.2, a schematic set-up is displayed in figure 2.7. As a commercial instrument was used for this measurement performing scans did not require a special set-up or alignment. Samples were fixed to a quartz sample carrier or dropped onto the carrier as a solution and dried in air, an oven or by an infrared heating lamp. Then, the carrier was introduced into the spectrometer and illuminated by X-ray radiation at a small fixed angle (0.1°) below the critical angle of reflection of the carrier material. Fluorescence radiation was detected by a Si(Li) energy dispersive detector and transmitted to an analysis computer. As no export function of measurement data to another computer was available a program was developed to handle this task. The conversion process is described in appendix E.2.

TXRF scans consist of a large number of data channels (typically 2048 or 4096) related to a certain photon energy and containing the number of photons of this energy counted. Analysis of such a spectrum first requires alignment of the energy scale (if it is not yet aligned in a commercial instrument) usually by localizing known typical fluorescence lines of elements in the sample or a reference sample. The structure of a TXRF spectrum is discussed in the theory section 2.2.2, alignment calculations are explicated in appendix D.9. Having the energy scale aligned, the other peaks present in the spectrum have to be characterized concerning two aspects. First, the energy position of each peak has to be compared to tabulated values [5, 84, 146] to determine the respective element. And second, the height of each element's peaks is a measure of its concentration in the sample [72] which can be calculated with the concentration of a known internal standard element. These analyses can in to a large extent be performed by commercial software or programs developed during this work (cf. appendix E.2).

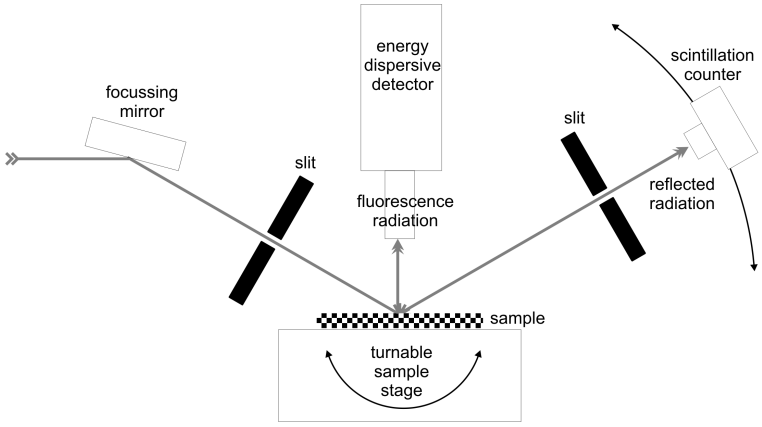

Figure 4.9.: Experimental Set-Up for XSW, explanations can be found in the text.

4.2.3. XSW

A schematic set-up for XSW measurements is shown in figure 4.9. Synchrotron radiation for XSW experiments presented in this work was generated inside a superconducting asymmetric wiggler (SAW) at beamline BL9 (cf. section 4.1.3) of DELTA synchrotron (cf. section 4.1.2), and photons of the desired energy were selected by a Si (311) double crystal monochromator. Energies used for measurements in this work ranged from 10.05 keV to 15.20 keV.

Subsequently, radiation was focused and bended down by a curved silicon mirror. Then it passed two slit systems to reduce the beam profile to 100-150 micrometers in height and 1 mm in width. Finally, the beam illuminated the sample placed on a goniometer at small angle, partly being reflected and partly exciting fluorescence radiation. An energy dispersive X-ray detector *(XR-100CR, Amptek, Bedford, Ma, USA)* was adjusted as outlined in appendix D.9 and positioned approximately 1 cm perpendicular above the sample (cf. photo in figure 4.6 and schematic in figure 4.9). The energy spectrum of the fluorescence radiation was recorded and one or up to three regions of interest (ROIs) comprising peaks of the marker elements to be observed were defined as shown in figure 4.10. For example, the channels containing the Kα and Kβ peaks of germanium fluorescence were selected for a Ge XSW scan. Due to overlapping these peaks appeared to form one broad peak with a shoulder at the position of the Kβ peak.

Attention has to be paid when measuring certain (especially light) elements that might appear in the set-up, too, and lead to misinterpretation of the sample composition. N, O and Ar are present in air, Si or Ge can occur in the substrate, mirrors and the solid state detector crystal [37], and several metallic elements could be part of the stage, goniometer or other components. Problems may also occur if peaks of different elements overlap or if the peak of a certain element of interest is very weak. Then, the total number of photons counted in a selected ROI may contain high unwanted contributions from other elements or background noise that can lead to errors. This effect might be prevented or at least reduced significantly by fitting a calculated peak shape into the peak of interest and only counting the area below this calculated peak. This fitting procedure can be performed during measurement by automatically calculating the peak shape for

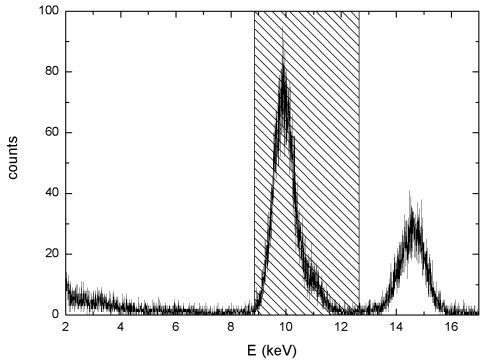

Figure 4.10.: Fluorescence radiation energy spectrum for a 29 nm Ge layer on Si. The peak around 15 keV incorporates the elastic scattering peak (15.200 keV) and the Compton peak (14.761 keV). Ge Kα_1 (9.886 keV) and Kα_2 (9.855 keV) fluorescence form the high peak in spectrum. Ge Kβ_1 (10.982 keV) is visible as a shoulder in this peak. The shaded area represents the selected MCA channels (region of interest, ROI) recorded for an XSW scan. For energies below 2 keV a background noise peak arises.

each energy spectrum before saving the integrated intensity of this peak. Alternatively, the entire energy spectrum recorded for each angle during an angle scan can be saved and fitting of the peaks is performed during evaluation afterwards. The latter method requires more data storage space while the former method needs more computing power and might lead to longer scanning times. However, neither method was available at SAW2 beamline at the time of measurements but it would be advantageous to implement this feature in future.

Angle scans were performed by tilting the goniometer sample stage. In that way, the angle of incidence of the synchrotron radiation onto the sample was changed in small steps of 0.002° from 0.01° to 0.3°-0.8° (depending on the sample) while the detector recorded fluorescence radiation for the defined ROIs at each angle position. Subsequently, but with the same set-up, a reflectivity scan (cf. section 4.2.1) utilizing a scintillation counter positioned behind the sample was performed under specular conditions $\alpha_{\mathrm{in}} = \alpha_{\mathrm{out}}$. This reflectivity scan served as cross-check (minima in reflectivity should coincide with maxima in XSW signal) and as additional information for determining the layer structure of the sample.

With typical values for the beam height (defined by the entrance slit) of $h_{\mathrm{beam}} = 0.150$ mm and incidence angle $\alpha_{\mathrm{i}} = 0.6°$, the footprint, i.e. the sample area covered by the incident beam (as calculated in the theory chapter) amounts to $F > 14$ mm and thus usually covers all or at least most of the sample. Consequently, lateral resolution mainly depends on position and opening of the detector. With a distance between detector and sample of roughly 1 cm, a detector area of 7 mm^2 and an opening angle of approximately 110° the observed area is 3.5 cm in diameter. Thus, only averaged values of the whole layers are measured. By reducing the detector entrance slit a scan area diameter of a few mm and thus lateral mapping of a sample is feasible, however at expense of signal intensity and longer measurement times.

XSW scans as described above give an intensity versus angle of incidence curve. As the electron current in the synchrotron and thus intensity of the incident beam decreases with time, first

the measured intensity has to be divided by the incident intensity that is automatically recorded during the scan, too. Then, measured intensity is normalized to a value of 1 at the largest measured angle similar to the procedure in [151] because at large angles intensity approximates a value of 1 like in a wave without interference. This normalization is only valid for small angles of incidence, thus in virtually all scans performed with hard X-rays of several keV. If soft X-rays around or below 1 keV are utilized scan angles increase to several degrees. Them, further geometric effects have to be considered as outlined in the simulation chapter 5.1.6.

This adjusted measured curve is then compared to a calculated one of selected sample parameters using the program *MXSW* that is described extensively in chapter 5. Parameters are varied manually or automatically until a satisfying agreement between experiment and calculation is achieved delivering the best fit parameters (like layer thicknesses or element distribution) of the sample. Often, it is helpful to combine results of XSW and XRR scans [51] to approach the best fit in kind of an iterative process with using approximative preliminary XRR results to improve the XSW fit and vice versa. For complicated sample systems further considerations and calculations such as a Fast Fourier Transform have to be applied which as described in detail in the respective sample evaluation sections. Evaluation of other XSW analysis methods (cf. theory chapter 2.3.2) like measurements at a Bragg peak [36, 37, 51] or at normal incidence [35] are described elsewhere.

5. Simulation

For fitting curves from XSW measurements it is necessary to simulate the whole sample system (with electron densities, diffraction and absorption) and change various parameters until a best fit is reached. Thus, the fitting procedure is somewhat complicated. Several computer programs to calculate X-ray reflectivities and X-ray fluorescence signals for multilayers have been published [89, 92, 134, 135, 167]. However, neither of these programs fulfills all requirements to analyze the samples discussed above neither is expansion of these programs for further problems possible. Thus, a computer program called *MXSW* was developed in this work that is capable of calculating XSW fields in various kinds of multilayer samples and at the same time expandable to cover new areas and include further parameters. Basic calculation procedures are based on [32, 60, 72]. Also, aspects discussed in [10, 93, 94, 167] are included as well as in numerous works cited in the theory chapter 2.

In the following sections the calculation of XSW intensity fields and scans are presented. First, the main steps of the simulation program *MXSW* developed during this work are listed and explained. Then, an evolutionary fitting algorithm also included in *MXSW* is outlined. Finally, some exemplary calculations are shown to illustrate the functionality of the program and some general aspects of XSW intensity fields. Some screenshots of *MXSW* can be found in appendix E.

5.1. Calculation of X-ray standing waves

In this section, the calculation procedure of the simulation program *MXSW* developed during this work is described step by step in the same order in which the tasks are handled by the program, starting with a list of parameters required for calculation.

5.1.1. Required parameters

Before an XSW field can be calculated several parameters of the sample have to be provided to the program. In the following the parameters included in calculation are listed and explained. This list relates to *MXSW* program version 1.1 at the time of writing of this work. Future versions may include further values. Several parameters are also discussed in detail in the following sections.

- Material of each layer (element or compound) to calculate δ and β
- Dispersion δ and absorption constants β for each layer (can be calculated automatically)

- Absorption coefficient μ for each layer (can be calculated automatically)
- Thickness d and roughness σ in nm for all layers (thickness values are also needed for vacuum above and substrate below the layer system to define the region to be displayed)
- Step size (i.e. resolution) for thickness Δd and roughness $\Delta\sigma$ calculation
- Selected roughness model (effective density, Debye-Waller or none)
- Energy E or wavelength λ of exciting and detected radiation (can be calculated automatically for emission lines of all elements)
- Position of the markers/marker layer
- Shape of the marker atom distribution (homogeneous, linear, $\sin/\cos$, $\tanh$, erf, $\exp$)
- Angle range $[\alpha_{\min}, \alpha_{\max}]$ and resolution $\Delta\alpha$
- Detector resolution (in °) and detector length[1] D (in mm)
- Length of the sample L (in mm) and height of the beam h_{beam} (in micrometers)
- Footprint angle α_{F} (i.e. angle at which the sample is entirely covered by the beam, can be calculated from sample length and beam height)
- Scaling factor for XSW measurement data

5.1.2. Optical constants

Apart from layer thicknesses and roughnesses that are subject to fitting and should be at least approximately known, the dispersion and absorption constants δ and β for the material of each layer for the energy of the incident beam and the absorption constant μ for the fluorescence radiation to be observed need to be known. These values can be obtained from literature or electronic sources [31, 59] or calculated. To simplify the procedure automatic calculation of these values was implemented. Equations 2.10 and 2.11 for mono-elemental layers can be written as

$$\delta = \frac{\lambda^2}{2\pi} r_{\mathrm{e}} \rho_{\mathrm{e}} \cdot \frac{f^0 + f'(E)}{Z} \tag{5.1}$$

$$\beta = \frac{\lambda^2}{2\pi} r_{\mathrm{e}} \rho_{\mathrm{e}} \cdot \frac{f''(E)}{Z}. \tag{5.2}$$

Replacing the electron density ρ_{e} by the density of atoms

$$\rho_{\mathrm{A}} = \frac{\rho_{\mathrm{e}}}{Z} \tag{5.3}$$

[1] The term "detector length" is explained in section 5.1.6.

and renaming

$$f_1(E) = f^0 + f'(E) \tag{5.4}$$
$$f_2(E) = f''(E) \tag{5.5}$$

leads to

$$\delta = f_1 \cdot \rho_\mathrm{A} r_\mathrm{e} \cdot \frac{\lambda^2}{2\pi} \tag{5.6}$$
$$\beta = f_2 \cdot \rho_\mathrm{A} r_\mathrm{e} \cdot \frac{\lambda^2}{2\pi}. \tag{5.7}$$

The atom density ρ_A can be calculated from the mass density ρ (g/cm^3), atomic weight M (g/mol) and Avogadro's number N_A by

$$\rho_A = \frac{N_\mathrm{A} \cdot \rho}{M}, \tag{5.8}$$

and the atomic scattering factors f_1 and f_2 are tabulated for all elements up to uranium [31, 59] for an energy range between 30 eV and 30 keV. These f_1, f_2 tables have been integrated into the program to calculate δ and β automatically. There are no scattering factor files available for many compounds. But δ and β can be calculated from [31] for a number of common compound materials. Utilizing a set of 500 δ, β values for each material and inverting formulae 5.6 and 5.7

$$f_1 = \frac{2\pi\delta}{\rho_\mathrm{A} r_\mathrm{e} \lambda^2} \tag{5.9}$$
$$f_2 = \frac{2\pi\beta}{\rho_\mathrm{A} r_\mathrm{e} \lambda^2} \tag{5.10}$$

the required f_1, f_2 tables for the program were computed for compounds occurring in measurements during this work such as air, mica, polystyrene, quartz and water. Others can be added to the program easily. Further parameters necessary for the simulation can be calculated from the given radiation energy E or wavelength λ, respectively, δ and β by formulae 2.11 and 2.18

$$\mu = \frac{4\pi\beta}{\lambda} \tag{5.11}$$
$$\alpha_\mathrm{c} \approx \sqrt{2\delta}. \tag{5.12}$$

5.1.3. Calculation of the 3D XSW field

If monochromatic and longitudinally coherent radiation hits a flat surface or interface always an XSW field is generated. Usually, it is necessary to calculate the XSW intensity for each angle of incidence α and each position z above or even below the substrate that might be of interest. This

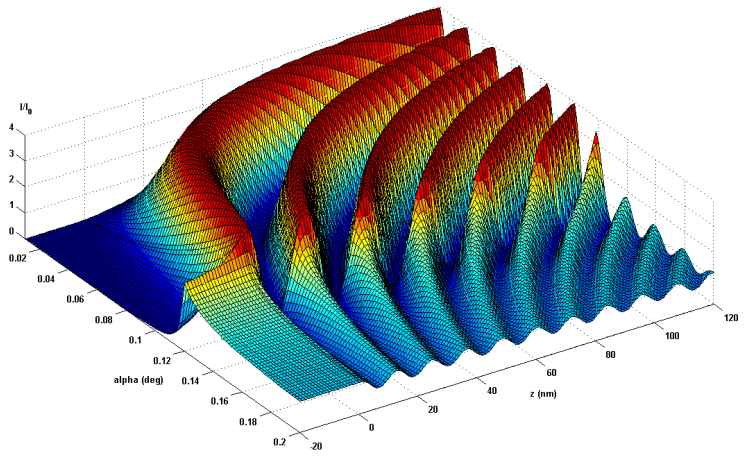

Figure 5.1.: XSW field above a pure Si wafer for E = 15 keV

leads to an intensity distribution

$$I_{\mathrm{XSW}} = I_{\mathrm{XSW}}(z, \alpha). \tag{5.13}$$

Thus, the XSW field can be displayed in a 3-dimensional form with one I value for each combination of α and z. Calculation of I with a matrix formalism is described in detail in the theory section 2.3. Also, roughness of interfaces can be considered during calculation. The user may selected a kind of effective density model and a Debye-Waller type damping factor. Implementation is explained in section 2.4.4.

A typical calculated X-ray standing waves field above a Si substrate at photon energy E = 15 keV is shown in figure 5.1. This 3-dimensional graph can be read in two different ways. First, if the angle of incidence is fixed (e.g. to 0.7°) and the excitation position of a "marker" atom changes (for example during diffusion processes in liquids) while crossing minima and maxima of the XSW field, an intensity curve as shown in figure 5.2 appears. This graph can be calculated for any angle in the program *MXSW* where it is called "angle cut". The second reading is related to the more common praxis of XSW measurements: The position of observation ("marker position") is fixed (e.g. inside one layer in a multilayer system) and the angle of incidence changes (by moving the X-ray tube or turning the sample) and intensity minima and maxima of the exciting field are moving through the marker layer and generating detectable fluorescence emission patterns. A typical scan at fixed position is shown in figure 5.2, too.

The oscillation field shown in fig. 5.1 cannot be measured directly, because a detector inside the XSW region would disturb and alter the standing waves field dramatically. Nevertheless, if a tiny probe (a so-called marker atom) is positioned inside the field it hardly disturbs the standing waves field in its neighborhood, but on the other hand the XSW excite the atom to emit fluorescence radiation with intensity proportional to the XSW field intensity at its position. This fluorescence radiation can be detected far away (several mm or cm) from the region of XSW. Thus, marker atoms at a certain position above the reflecting surface make the XSW intensity at

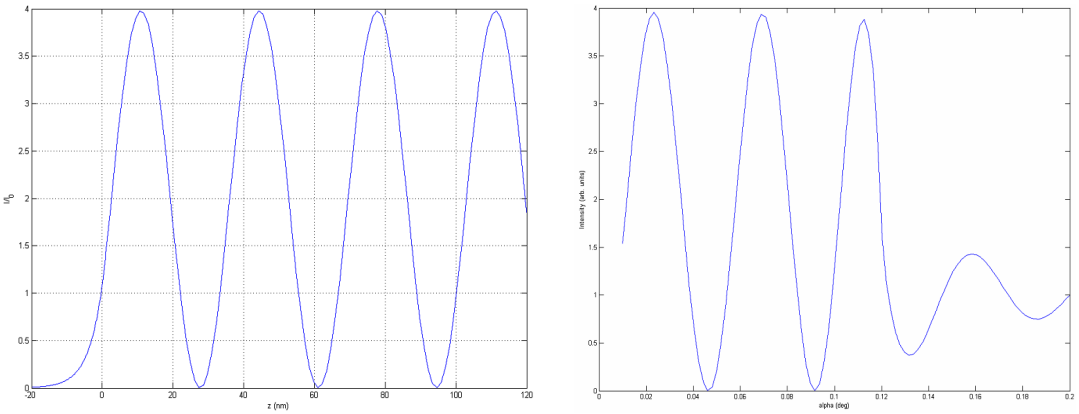

Figure 5.2.: Left: XSW field intensity for various positions from 20 nm below to 120 nm above the substrate surface at fixed angle 0.0708° ("angle cut").
Right: XSW field intensity for incident angles from 0° to 0.2° at fixed height 45 nm above the substrate ("angle scan").

their position visible as is demonstrated in Fig. 5.3.

5.1.4. Extraction of a 2D scan

Generally, observation of the XSW field intensity is performed with the help of markers, atoms of a certain element that are already located inside the layered sample or positioned artificially as a probe without disturbing the rest of the structure to be analyzed. These marker atoms are usually not only located at one defined z position but distributed over a wider z range like a layer. Sometimes, an already existing layer of the sample can be employed as fluorescence marker (e.g. Ge in section 3.1.1). Alternatively a layer may include certain marker atoms whose effect on the XSW field is negligible [160, 174] but that nevertheless work as markers by emitting fluorescence radiation with intensity proportional to the XSW field at their position as for example in the phospholipid-buffer layer system described in section 3.2.2.

The procedure to extract the 2-dimensional XSW scan from the 3-dimensional XSW field is illustrated in figure 5.3. Here marker atoms are supposed to be distributed in the region between 40 nm and 45 nm above the substrate. Consequently, if only fluorescence radiation of these markers is detected contributions from the rest of the sample disappear and the full XSW field in figure 5.3a reduces to the detectable part shown in figure 5.3b. Scanning the angle of incidence, the integrated fluorescence intensity of all marker atoms between 40 nm and 45 nm is detected as a function of the angle. Figure 5.3c displays the corresponding intensity vs. angle measurement. With a given marker layer position the computer program returns the integrated XSW intensity for all positions inside this region for each angle leading to a fluorescence intensity versus angle relation that can be compared to an experiment.

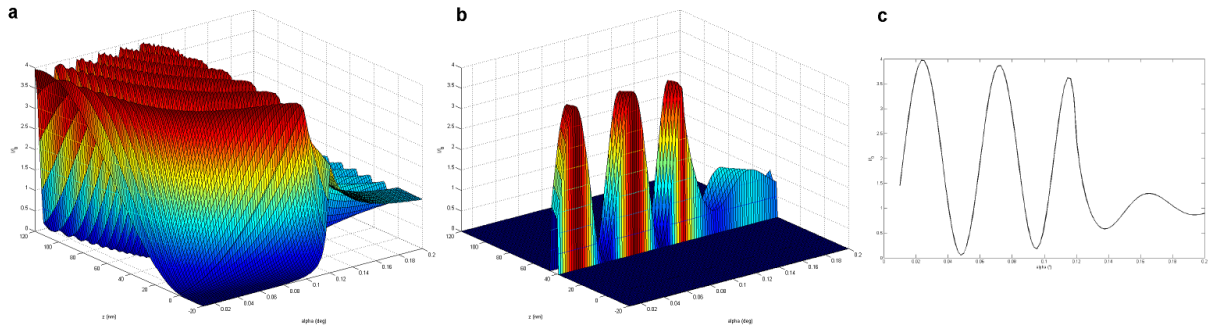

Figure 5.3.: Extraction of the measured XSW scan from the 3D XSW field:
(a:) 3D simulation of XSW in vacuum for a photon energy of 15 keV above a Si substrate for positions from 20 nm below to 120 nm above the surface (left axis) and angles of incidence from 0.01° to 0.2° (right axis).
(b:) Only the part of the XSW field between 40 nm and 45 nm above the surface where marker atoms are located is visible.
(c:) Resulting fluorescence signal versus angle of incidence from marker atoms distributed between 40 nm and 45 nm above the surface.

5.1.5. Marker atom distributions

Often, marker atoms are not distributed homogeneously inside a certain z region but their concentration varies with position. An example for this are ions in a liquid near an interface as described in section 3.3.2 or marker atoms in biological films. To cover problems like this a variable marker distribution is implemented in the *MXSW* program with several possible options. Apart from a homogeneous (layer) marker distribution a linear decrease or increase of marker concentration from one boundary of the marker region to the other can be implemented. This might be the case in industrial samples in which a linear transition between two materials occurs e.g. in coatings. To simulate a "soft", more "natural" transition without edges application of a sine/cosine, a hyperbolic tangent or error function shape are possible. Finally, an exponential decrease (or increase) can be chosen as expected for ions as already mentioned. The different kinds of marker distributions are illustrated in figure 5.4. The effect of such marker distribution is that the XSW signal from the marker region contributes to the measured signal in a weighted way depending on the position of interest inside the region. For example, the XSW field in the left part of the region contributes with almost full intensity and in the right part with hardly any. Further, the resulting XSW signal must be renormalized to be comparable to a homogeneous marker layer.

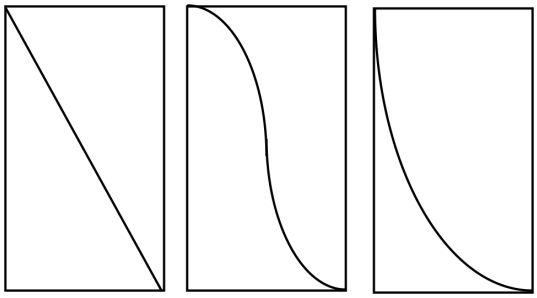

Figure 5.4.: Different models of marker distribution (from left to right): Linear decrease, "soft" cosine decrease, exponential decrease.

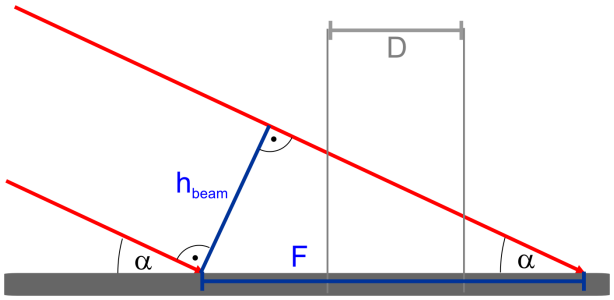

Figure 5.5.: Influence of beam footprint and detector length: At small angles the footprint F of the beam on the sample is larger than the detector length D. Then, only part of the incoming intensity can generate detectable fluorescence radiation.

5.1.6. Geometrical effects

Detector length

If the incoming beam hits the sample at very low angles (as it often happens in experiments described in this work) the footprint (area covered by the beam) gets large and can exceed the "detector length" as shown in figure 5.5. Here, "detector length" denotes the part of the sample (in direction of the beam) that can be "seen" by the detector. This length increases with distance of the detector from the sample and with a larger detector solid angle. The latter depends on the sensor size inside the detector housing, the size of the detector window and distance between these two components. As especially the detector solid angle is often unknown, the value of the detector length is utilized in the program *MXSW*. For one fixed set-up the detector length has to be determined just once.

If the beam footprint is larger than the detector length only part of the fluorescence radiation generated by the incident beam will be detected and the signal will be lower. With a given detector length D, a beam height h_{beam} and an angle of incidence α respectively a footprint of $F = h_{\mathrm{beam}} / \sin\alpha$ the detected intensity I_{D} is lower than the total intensity from the whole

illuminated area I_{F}:

$$I_{\mathrm{D}} = I_{\mathrm{F}} \cdot \frac{D}{F} = I_{\mathrm{F}} \cdot \frac{D \cdot \sin\alpha}{h_{\mathrm{beam}}}. \tag{5.14}$$

Thus a small beam height or larger detector window lead to higher intensities at low incidence angles. If the angle of incidence exceeds a critical footprint angle

$$\alpha = \arcsin\left(\frac{h_{\mathrm{beam}}}{D}\right) \tag{5.15}$$

the beam footprint is completely inside the detectable area D and

$$I_{\mathrm{D}} = I_{\mathrm{F}}. \tag{5.16}$$

Footprint larger than sample

A very similar effect can occur at small angles when the beam footprint

$$F_{\mathrm{i}} = \frac{h_{\mathrm{beam}}}{\sin\alpha_{\mathrm{i}}} \tag{5.17}$$

is larger than the sample length F_0 as already discussed for XRR measurements in section 4.2.1. The same calculations lead to a footprint angle

$$\alpha_{\mathrm{F}} = \arcsin\left(\frac{h_{\mathrm{beam}}}{F_0}\right) \tag{5.18}$$

at which the entire sample is covered by the beam and a "footprint corrected" detected intensity

$$I_{\mathrm{D}} = I_{\mathrm{F}} \cdot f_{\mathrm{foot}}^{-1} \tag{5.19}$$

with the correction factor

$$f_{\mathrm{foot}} = \frac{F_{\mathrm{i}}}{F_0} = \frac{\sin\alpha_{\mathrm{F}}}{\sin\alpha_{\mathrm{i}}} \quad \text{for} \quad \alpha_{\mathrm{i}} < \alpha_{\mathrm{F}} \tag{5.20}$$

f_{foot}^{-1} is 0 at incident angle $\alpha_{\mathrm{i}} = 0°$ and increases to 1 for values $\geq \alpha_{\mathrm{F}}$.

Both effects have the same origin that only part of the beam hits the sample in a detectable location and detected intensity decreases. Thus, only the more limiting effect i.e. the smaller dimension (sample length F_0 or detector length D) needs to be taken into account in calculations of *MXSW*.

Path length

Finally, a third geometric effect has to be included in calculations. With incident angles usually very small in GI-XSW measurements the difference between layer thickness d_j of a layer j and

Emission line	Energy (keV)	Sample composition	Absorption (%)
Mg Kα_1	1.254	Mg below a 100 nm Zn, 50 nm Mg bilayer	41.9
Si Kα_1	1.740	Si below 100 nm of Ge	18.8
Si Kα_1	1.740	Si below 80 nm PS and 1 nm Au	0.7
P Kα_1	2.014	P below 20 nm of water	0.6
Ge Kα_1	9.886	Ge below 100 nm of Si	0.1

Table 5.1.: Absorption of fluorescence radiation inside different layered samples.

the path length of the beam inside this layer

$$L_j = \frac{d_j}{\sin \alpha_j} \tag{5.21}$$

is huge and also changes rapidly with α_j. With the X-ray beam exciting fluorescence photons on its entire length in the sample, the detected fluorescence yield I_D is proportional to the path length

$$I_\mathrm{D} \sim L_j \tag{5.22}$$

and the above calculated fluorescence intensity I_F has to be corrected by

$$I_\mathrm{D} = \frac{I_F}{\sin \alpha_j}. \tag{5.23}$$

For measurements with hard X-rays and consequently small angles the above mentioned footprint and path length effects roughly cancel each other out and the resulting angle scan approximates the XSW field intensity deduced in section 5.1.4. However, for soft X-rays around or below 1 keV these geometric effects cannot be neglected.

5.1.7. Absorption

Absorption of the radiation penetrating the sample is already considered in the calculation of the XSW field described above. But it is still important after fluorescence radiation is generated inside the marker atoms. This fluorescence radiation has a wavelength that is element specific and different from that of the incident beam. Thus, absorption of photons of this wavelength has to be considered on the way from the point of origin of the fluorescence radiation (POF) to the sample surface within all layers. The beampath to be considered is the shortest way from the POF to the uppermost surface (i.e. perpendicular to the surface) and independent of the angle of incidence because the detector is positioned directly perpendicular above the sample. Distance between the uppermost sample surface and detector can be neglected because it is the same for all photons generated inside the sample and not important after normalization of the measured curve. For the same reason it is irrelevant for calculation if the sample is in vacuum, air or another gas. Table 5.1 lists absorption of fluorescence radiation in some exemplary layered samples.

5.1.8. Scaling of the measured curves

While XSW calculations directly deliver absolute normalized values for XSW intensities at any angle of incidence (for the case of hard X-rays when geometrical effects cancel each other out as explained in section 5.1.6) normalization of the measured data is a bit more complicated. By default the program normalizes intensity to 1 at the highest measured angle because in the high angle range XSW oscillations approximate the intensity of 1 like in a wave without interference [151]. Due to limited measurement time, scans are often only performed up to a small angle below 1° where the high angle condition is not yet fulfilled. Then the XSW measurement data must be multiplied by a constant factor in the program manually. This scaling is also necessary if geometrical effects have to be considered and the calculated intensity curve shows values far above 1.

5.1.9. Fit quality

To obtain information about the sample under investigation it is necessary to modify the parameters (cf. section 5.1.1) of the system until the calculated curve fits to the measured one as good as possible. This can be done by visual judgment or automatically. For the latter case it is necessary to quantify the quality of the fit by a single number that can be minimized/maximized. In the *MXSW* program, a version of the least-squares method is utilized that is well established in non-linear fitting procedures [44, 45]. For this case the accordance between experimental I_{E} and fit intensity I_{F} for each angle α is quantified by the deviation factor

$$f(\alpha) = \frac{(I_{\mathrm{E}} - I_{\mathrm{F}})^2}{I_{\mathrm{E}}}. \tag{5.24}$$

Then the average deviation factor for all measurement points is calculated by

$$f_{\mathrm{avg}} = \frac{\sum f(\alpha)}{\sum I_{\mathrm{E}}(\alpha)} \tag{5.25}$$

and normalized to 100% for a perfect fit

$$f\% = 100 \cdot (1 - f_{\mathrm{avg}}). \tag{5.26}$$

This quality factor $f\%$ can then be utilized to optimize manual or automatic fitting procedures like the evolutionary fitting algorithm introduced in chapter 5.2.

5.2. Evolutionary fitting algorithms

With more complex layered samples the parameters to fit in the simulation can get too numerous to comfortably achieve a good fit manually. Thus, so-called evolutionary algorithms have been implemented into the simulation program to achieve automatic results easily. The method of

evolutionary algorithms is described below, followed by a description of the implementation of this algorithm in the *MXSW* simulation program.

5.2.1. General description of evolutionary algorithms

Hildebrand [60] has described evolutionary fitting strategies in detail. Here, a short description of the method is given. Generally, the object of fitting is a set of values p_j (here experimental parameters listed in section 5.1.1 such as layer thicknesses, marker positions, detector resolution, ...) that can be written as a vector V, for example

$$V = [p_1; p_2; p_3; \ldots]. \tag{5.27}$$

A fitting interval $I_\mathrm{j} = [p_{1,\min}, p_{1,\max}]$ of possible values for each parameter has to be defined to limit the variable space to be analyzed. Further a stepwidth σ_j for the fit procedure (i.e. an average or maximum value by which this parameter is changed in each evolution step) is assigned to all parameters p_j. As a simplification just one (relative) stepwidth σ can be assigned to all parameters of the vector and the absolute stepwidth for each element is calculated by

$$\sigma_\mathrm{j} = \sigma \cdot \frac{p_{1,\max} - p_{1,\min}}{2}. \tag{5.28}$$

Finally, a "fitness parameter" Ψ is assigned to each vector which defines how well the vector fulfills the given task, e.g. the root-mean-square deviation. Thus V can be written as

$$V = [\Psi; \sigma; p_1; p_2; p_3; \ldots]. \tag{5.29}$$

Step 1

To start the fitting algorithm a first set of vectors V_i (usually 3 or 8) is generated by creating (linearly distributed) random parameter values $p_{i,j}$ and stepwidths σ_i for each vector in the set:

$$\begin{aligned} V_1 &= [\Psi_1; \sigma_1; p_{1,1}; p_{1,2}; p_{1,3}; \ldots] \\ V_2 &= [\Psi_2; \sigma_2; p_{2,1}; p_{2,2}; p_{2,3}; \ldots] \\ V_3 &= [\Psi_3; \sigma_3; p_{3,1}; p_{3,2}; p_{3,3}; \ldots]. \end{aligned} \tag{5.30}$$

The values of Ψ_i are not yet defined in this step.

Step 2

The three (eight) vectors are then recombined randomly to create 24 (alternatively 100) new vectors. Different recombination methods are possible. The easiest one is just mixing the parameters

of the three parent vectors to create 24 child vectors, for example

$$\begin{aligned} V_1 &= [\Psi_1; \sigma_3; p_{2,1}; p_{1,2}; p_{3,3}; \ldots] \\ V_2 &= [\Psi_2; \sigma_1; p_{3,1}; p_{3,2}; p_{3,3}; \ldots] \\ V_3 &= [\Psi_3; \sigma_1; p_{1,1}; p_{2,2}; p_{2,3}; \ldots] \\ V_4 &= \ldots \end{aligned} \tag{5.31}$$

$$\ldots \tag{5.32}$$

The Ψ values do not need to be changed in this step. A better method of recombination is to utilize average values as new parameters, e.g.

$$\begin{aligned} V_1 &= \left[\Psi_1; \frac{\sigma_1+\sigma_3}{2}; \frac{p_{2,1}+p_{1,1}}{2}; \frac{p_{2,2}+p_{2,2}}{2}; \frac{p_{3,3}+p_{1,3}}{2} \ldots\right] \\ V_2 &= \left[\Psi_2; \frac{\sigma_2+\sigma_3}{2}; \frac{p_{1,1}+p_{1,1}}{2}; \frac{p_{3,2}+p_{1,2}}{2}; \frac{p_{1,3}+p_{2,3}}{2} \ldots\right] \\ V_3 &= \left[\Psi_3; \frac{\sigma_2+\sigma_3}{2}; \frac{p_{3,1}+p_{2,1}}{2}; \frac{p_{3,2}+p_{3,2}}{2}; \frac{p_{1,3}+p_{2,3}}{2} \ldots\right] \\ &\ldots \end{aligned} \tag{5.33}$$

Of course, other combinations are possible here, too.

Step 3

As recombination only leads to more or less discrete values the parameters p_j are mutated by adding a normal distributed random value N_j.

$$p_j \rightarrow p_j + N_j \tag{5.34}$$

with the center of mass of N_j being 0 and the full-width half-maximum equal to $\sigma_j/2$ or σ_j (depending on the model utilized). Then possible results are distributed continuously around the start value p_j.

Step 4

Now, the fitness parameter Ψ_i for each of the 24 (100) generated vectors V_i is calculated, e.g. by determining the root-mean-square deviation of calculations using the parameters given by V_i from a measurement curve. The three (eight) vectors with best fitness parameters are kept, the others dropped. In this step, two different strategies can be distinguished: If both the μ (here $\mu = 3$) elder vectors from the start and the λ child vectors (here $\lambda = 24$) can be candidates to be one of the three fittest vectors, the method is called ($\mu + \lambda$) strategy or shortly "+" strategy. If the elder vectors are always skipped and only child vectors are allowed for the next generation, it is called (μ, λ) or shortly "," strategy. The "," strategy can be advantageous because all vectors are new in each generation, thus it is easier possible to move out of a local (but not global)

minimum and not getting stuck by a relatively fit vector pointing to that minimum that survives all generations. After determination of the three fittest vectors calculation starts again at step 2 with these vectors as starting vectors.

Stop criterion

The evolutionary algorithm is continued until a stop criterion is fulfilled. This can be a fixed number of calculation turns, a desired fitness value to be reached or the effect that the fitness value did not improve any further within a certain number of calculations.

5.2.2. Implementation of evolutionary algorithms in MXSW

To allow both manual and automatic fitting and analysis, *MXSW* is built up in a modular way. All parameters of the sample can be entered manually or as an input parameter file in a special format. Then, *MXSW* calculates XSW field and a theoretical curve that can be compared to the measurement. Quality of the fit is quantified by the quality factor $f\%$ introduced in section 5.1.9 that can be assigned as fitness parameter to the evolutionary fitting algorithm. Then, the sample parameter file is modified (in given limits) following the algorithm to achieve a better quality factor until a maximum is achieved. Of course, finally it has to be checked manually if this result is physically reasonable. In the following, it is described how the calculation procedure outlined in section 5.2.1 is realized in *MXSW*. The fitting vector V is set up from experimental and sample parameters:

$$V = \begin{bmatrix} \text{fit quality} \\ \text{evolution stepsize} \\ \text{beam size } (\mu\text{m}) \\ \text{detector resolution } (^\circ) \\ \text{sample length (mm)} \\ \text{detector length (mm)} \\ \text{XSW measurement scaling} \\ \text{lower marker limit (nm)} \\ \text{upper marker limit (nm)} \\ \dots \\ \text{thickness of layer 1 (nm)} \\ \text{thickness of layer 2 (nm)} \\ \text{thickness of layer 3 (nm)} \\ \dots \end{bmatrix} . \tag{5.35}$$

Combination is performed randomly using the average value method described in step 2. The normal distributed mutation factor N_j in step 3 is calculated using the Box-Muller method [19, 78, 98, 166] to be

$$N_j = \sqrt{-2 \cdot \ln(1 - v_1)} \cdot \cos(2\pi \cdot v_2) \cdot \sigma_j \tag{5.36}$$

with v_1 and v_2 being some (linearly distributed) random numbers between 0 and 1. The generated parameter vectors are then introduced into the *MXSW* simulation program which returns a fit quality value that is used as fitness parameter to be optimized towards 100%. To prevent misinterpretation of local minima the "," strategy for selecting the fittest (surviving) vectors was chosen for the program described here. The stop criterion in the fitting procedure is a manually set number of calculation steps. If agreement between measurement and calculation is not satisfying after these number of calculations another run can be started.

5.3. Discussion of exemplary calculated intensity fields

To illustrate the functionality of *MXSW* but also to give an overview over different types of XSW intensity fields that can occur in different samples, some exemplary calculated XSW fields are presented in this section. First, the simple case of a flat silicon surface is presented. Then, single layers of germanium on silicon are discussed, followed by a more complex sample structure of gold clusters on a polymer film. Finally, the effect of interface roughness on the XSW field is discussed.

5.3.1. Pure silicon wafer

A calculation of a typical XSW field at 10 keV above a simple flat silicon wafer as reflecting surface is presented in figure 5.6 showing XSW intensities both dependent on angle of incidence and distance from the reflecting surface. The silicon-vacuum interface is located at z = 0 with z positive in direction towards vacuum. It can be seen that virtually no radiation penetrates the substrate at an angle of incidence smaller than the critical angle of total reflection for silicon (α_c = 0.102°) and that XSW intensity decreases exponentially with depth inside the substrate for higher angles. Above the substrate, oscillations occur that are caused by interference between incident and reflected beam. Amplitudes of these oscillations are higher in the region of total reflection because more (virtually all) radiation is reflected. Intensity reaches values of four times the intensity of the incident beam. This effect can be explained by the fact that in an antinode electrical field amplitudes of the incident and reflected wave sum up to a double value, squaring this amplitude to calculate the intensity leads to the factor of four. On the other hand, intensity in the nodes goes down to zero when two opposing amplitudes extinguish each other. In contrary, in the region above the critical angle part of the radiation enters the substrate and thus the reflected wave amplitude is smaller than the incident one's leading to smaller oscillations around the intensity value of the incoming beam, neither reaching a value of 0 nor 4.

Furthermore, figure 5.6 displays the XSW field intensity inside the Si wafer itself. As discussed before, no oscillations occur inside the substrate but nevertheless the intensity is dependent on incident angle and depth. The narrow peak near the surface ($z \approx 0$) and critical angle of Si is caused by the XSW field above the substrate that only penetrates few nm.

Of course, the Si itself can be utilized as marker, too. Then the entire material of the substrate (in practice just the first micrometers as the attenuation length of SiKα fluorescence radiation inside Si is about 12 μm) acts as marker. By averaging over a large marker region the typical

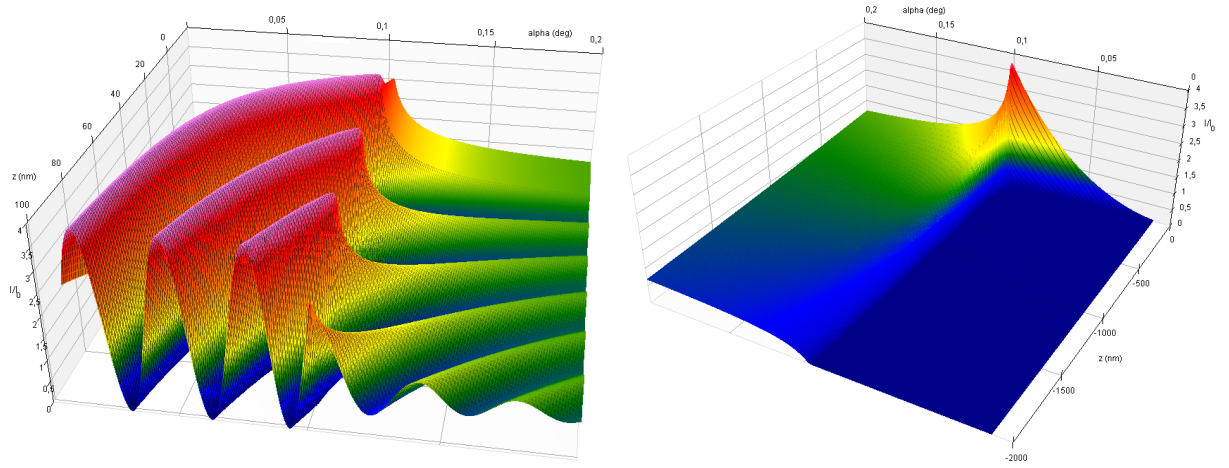

Figure 5.6.: XSW field above (left) and inside (right) a thick pure Si wafer for E=10 keV for angles of incidence (backside axis) between 0° and 0.2° and z region (side axes) up to 100 nm above and 2000 nm below the surface, respectively.

significant structure of XSW angle scan curves presented before then turns into the ones shown in figure 5.7. As expected, signal intensity is almost 0 for incident angles below α_c = 0.102°. Above, radiation penetrates the wafer resulting in a rapid increase of signal intensity. Still in the low angle region, intensity then increases roughly linearly with incident angle as known from literature [72]. Finally, with higher angles of several degrees intensity approximates a constant value.

This can be understood considering the path of the beam in the sample. First, almost all radiation is reflected and thus cannot excite the Si to fluorescence. Beyond the angle of total reflection, more and more radiation penetrates the sample with decreasing reflectivity and thus fluorescence constantly increases. Finally, when radiation penetrates the sample several micrometers, absorption of the generated fluorescence radiation deep inside the material plays a more important role and fluorescence intensity growth slows down.

5.3.2. Germanium layers on silicon

One or several layers of matter on the substrate lead to different and more complicated field patterns, especially inside the layers. Figure 5.8 shows XSW calculations for germanium layers of various thicknesses on silicon substrates like the ones analyzed in this work.

The XSW field above the Ge layer is quite similar for both samples but the structure inside the layer differs notably. Inside the 29 nm thick layer there are oscillations visible at angles above the critical angle of Ge (α_c = 0.168°). These oscillations are not as high as the ones above the Si substrate shown before (cf. figure 5.7) or in the gold-polystyrene-silicon sample that is described in the next section because the critical angle of Ge is higher than that of Si. Thus, the photons entering Ge also penetrate Si and only part of them is reflected.

Contrarily to that, the sample with a 309 nm thick layer does not show any oscillations inside

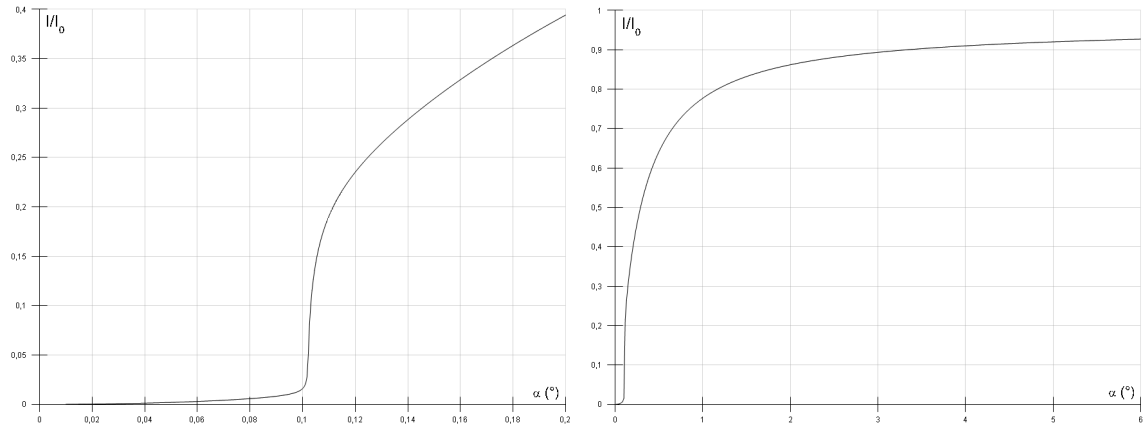

Figure 5.7.: Calculated XSW intensity (ordinate) versus angle of incidence (abscissa) a pure Si wafer at 10 keV. Angles range from 0° to 0.2° (left) or 6° (right). The Si wafer is mirror to create and marker to detect the XSW field at the same time. Intensity is almost 0 below the critical angle (α_c = 0.102°) then first rises rapidly and later roughly linearly with incident angle. Finally, for high angles of several degrees intensity approximates a constant value of 1.

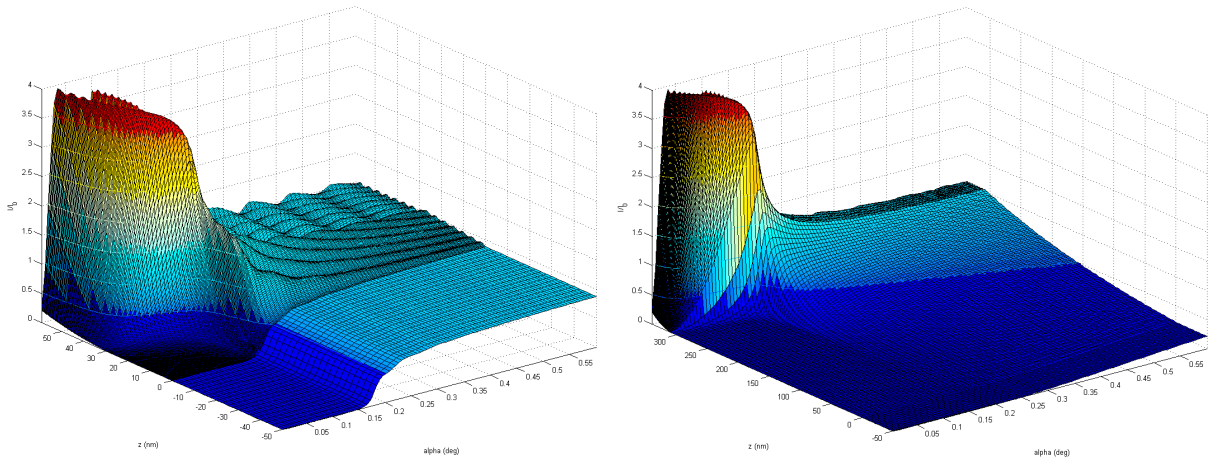

Figure 5.8.: XSW 3D simulation for Si covered with a 29 nm layer (left) and with a 309 nm layer (right) of Ge for a photon energy of 15 keV. The vertical position (in nm) inside the sample is shown on the left axis, the angle of incidence (in degree) on the right axis. It is obvious that the oscillations visible inside the 29 nm thick Ge disappear with rising thickness leading to an exponential decrease in the 309 nm thick Ge layer.

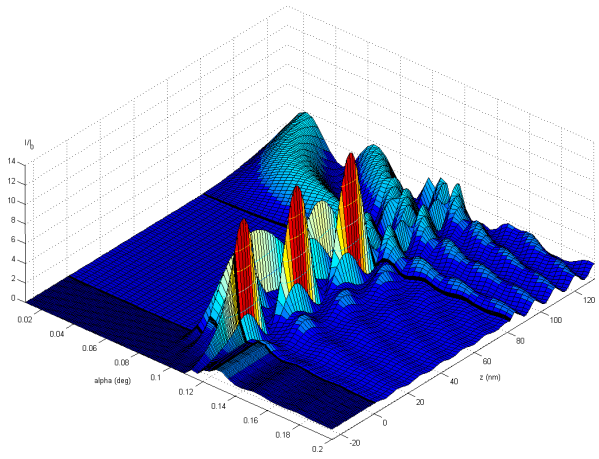

Figure 5.9.: XSW 3D simulation for a layered structure of gold clusters on an 80 nm polystyrene film on a Si substrate for a photon energy of 15 keV. Angle of incidence is shown on the left axis, height above or depth below the substrate surface on the right axis.

the germanium but only an exponential decrease of intensity. This can be explained by high absorption of radiation on its rather long way through the layer leading to much lower amplitude of the reflected wave. This reflected wave virtually does not affect the incoming wave by interference, thus constructive or destructive interference do not appear.

5.3.3. Gold clusters on a polymer layer

Fig. 5.9 shows the calculated XSW field for a sample consisting of a silicon substrate, an 80 nm thick layer of polystyrene on this substrate and a loose layer of gold of 1 nm nominal thickness for a photon energy of 15 keV as it was analyzed in this work. Gold does not form a continuous layer here but discrete clusters [81, 164] as already discussed in the experimental section. This loose layer can be modeled by a homogeneous gold layer with lower dispersion and absorption, incorporating the averaging effect of XSW in a plane parallel to the surface. It can be seen that there is no XSW field inside the 80 nm polystyrene layer below the critical angle of polystyrene ($\alpha_c = 0.085°$), because hardly any radiation enters the layer. Furthermore, only a very weak field occurs inside the polystyrene for angles above the critical angle of silicon ($\alpha_c = 0.119°$) because most of the radiation also penetrates the substrate, too, and is not reflected. Between these two angles the XSW field rises to huge values (much higher than the maximum possible value $4I_0$ in vacuum), especially at angles where layer thickness is a multiple of the oscillation wavelength. Such a signal can easily be measured and comfortably be compared to theoretical values as shown in the results chapter 6.2.4.

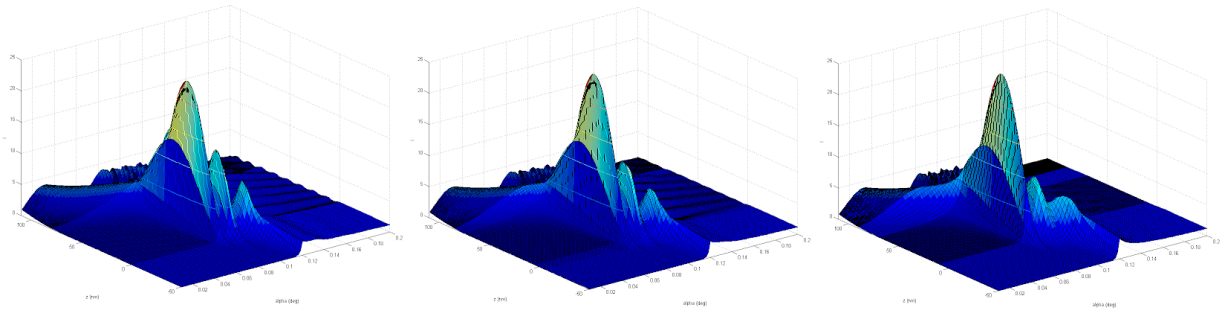

Figure 5.10.: XSW field at 15 keV above a Si wafer covered with 80 nm polystyrene of different roughnesses: 0 nm, 10 nm and 20 nm (from left to right). Each roughness region is simulated by 5 homogeneous intermediate layers. The left axis represents the z position while the angle of incidence is given on the right axis. Further explanations can be found in the text.

5.3.4. Roughness

Figure 5.10 shows calculations of an XSW field at 15 keV above a Si wafer covered with a 80 nm polystyrene film of different roughnesses: 0 nm, 10 nm and 20 nm. Each roughness region is simulated by 5 homogeneous intermediate layers using the effective density model (cf. section 2.4.3). It is clearly visible that amplitudes of oscillations above the critical angle of Si (0.119°) decrease with increasing roughness. This is a result of lower contrast between the layers (caused by the slower and not sharp transition between refractive indices of the two materials) leading to less coherent incident and reflected beams. Apart from the decrease in oscillation amplitudes described above it can be seen that less radiation penetrates the sample especially above the critical angle of Si if the roughness is lower (and thus reflectivity is higher). It is somewhat surprising that the amplitude of the highest interference peak is hardly affected by roughness, contrarily to the other oscillations. It might happen because its oscillation period is much longer than the region of roughness, in contrary to the short period oscillations at higher angles.

6. Evaluation and results

In this chapter measurement results of the samples analyzed in this work are presented and evaluated. Samples are presented in the same order as introduced in chapter 3 and applied methods for each sample system are discussed and compared.

6.1. Semiconductors

6.1.1. Semiconductor layers

Three different Ge layers on Si were analyzed using XRR and XSW technique at a photon energy of 15.2 keV. First, XRR measurements were evaluated following the procedure described in section 4.2.1. Results are listed in table 6.1 and compared to nominal values and XSW measurements. Agreement between nominal parameters and thicknesses obtained from XRR scans is rather good. However, some XSW results deviate significantly as discussed in the following.

XSW measurements and calculated fits are displayed in figure 6.1. For each scan two calculated curves are shown: One curve was calculated for the nominal thickness provided by the manufacturer *(JENOPTIK, Jena, Germany)* that in some cases does not agree very well with measurement. And another calculation was aimed to achieve the best agreement between measurement and computing even if the thickness of the calculated curve deviated strongly from the nominal one. Calculations were performed with the simulation program *MXSW* (cf. chapter 5) for various thicknesses with tabulated optical properties [31, 59] of Ge and Si at 15.2 keV listed in table B.2. Results for the best fits with variable thickness are listed in table 6.1. The measured thickness for the thinnest Ge layer meets the one provided by the manufacturer with an error below 1.5 nm, showing that XSW method can provide accurate results for thin samples. The signal of the sample of 76 nm nominal thickness leads to experimental values between 57 nm and 60 nm. The deviation for the 309 nm Ge sample is even more dramatic. The best fit is reached for a thickness of 106 nm. The calculated theoretical XSW curves for the nominal thicknesses (76 nm

Thickness (nm)		
nominal	XRR	XSW
29	29.5 ± 0.2	29.0 ± 1.5
76	69.8 ± 0.2	58.5 ± 1.5
309	306.1 ± 0.5	106.0 ± 4.0

Table 6.1.: Thicknesses of Ge layers obtained from XSW and XRR measurements. Explanations can be found in the text.

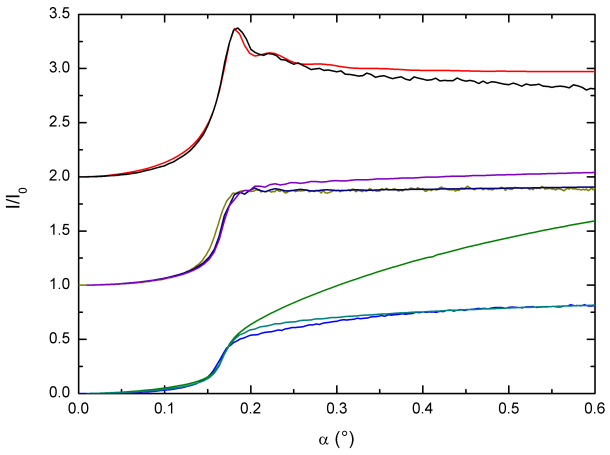

Figure 6.1.: Fluorescence intensity versus angle of incidence of the X-ray beam. Measurements and best fits based on a computer simulation by *MXSW* are shown for germanium layers of different thickness (from top to bottom: 29 nm, 76 nm and 309 nm) on silicon substrates. The energy of the incident beam is 15.2 eV. For the 76 nm and 309 nm samples two fits are shown: A calculated curve for the nominal Ge thickness and a best fit calculation leading to thicknesses of 59 nm and 106 nm, respectively. It can be seen that deviations between the 309 nm simulation and measurement are huge while the best fit for the 29 nm leads to the nominal thickness exactly. Curves are shifted vertically for clarity.

and 309 nm) displayed for comparison in figure 6.1, too, show that deviation from measurement is huge for the thickest sample.

Figure 6.2 illustrates problems of characterization of thick layers by XSW. The 3D graph shows the calculated XSW field for 15.2 keV radiation impinging onto a 100 nm Ge layer on Si. Oscillations inside the Ge layer are clearly visible for angles of incidence above the critical angle of Ge ($\alpha_c = 0.166°$). However, these oscillations have disappeared in the XSW angle scan shown in the figure, too. This is due to the fact that fluorescence radiation from the entire Ge layer contributes to the measured signal. Thus, integration is performed over tens of nodes and antinodes leading to a virtually not oscillating average signal. Obviously, XSW offers best resolution and results if the size of the structure to be analyzed is of the same order of magnitude as the XSW antinodes distance. Hence, a thickness of approximately 100 nm can be regarded as an upper limit for characterizable Ge layer samples under this experimental conditions.

This accessible distance can be increased by reducing the angle of incidence (with a lower limit at the critical angle of Ge below that no radiation can penetrate the layer) or by increasing the wavelength of the incident radiation, i.e. reducing its energy as can be understood from equation 2.58: $\Delta h \approx \lambda/(2\alpha)$. However, the energy of the incident beam has to be higher than the binding energy of the inner electrons of Ge (11.1 keV) to be able to excite fluorescence radiation. Consequently, even with lower energies the maximum thickness is limited to roughly 140 nm. Nevertheless, layers of larger thickness can in principle be analyzed if not the thick

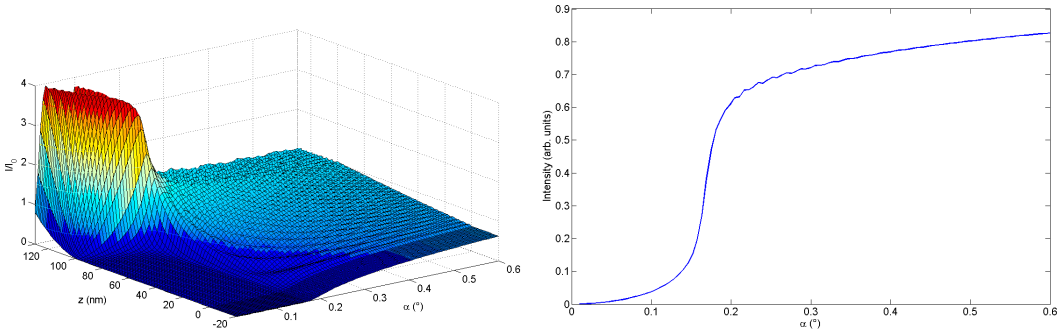

Figure 6.2.: XSW calculation for a 100 nm Ge layer on Si at E = 15.2 keV.
Left: In the 3D visualization of the XSW field (XSW intensity versus height above the substrate and angle of incidence) oscillations are clearly visible.
Right: Angle scan calculated by integrating the intensity of the entire Ge layer for each angle shows hardly any oscillations.

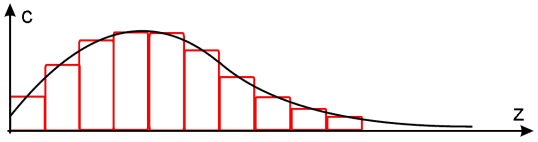

Figure 6.3.: Schematic illustration of implanted ion concentration distribution c depending on depth z in a silicon substrate based on measurements with RBS and TXRF [73, 74, 75, 77] (black) and approximation of this distribution by a number of layers of homogeneous concentration (red).

layer itself but a thin film above the layer serves as a marker as shown with other sample systems in section 6.2.4, 6.2.4 or 6.3.1.

Although XRR gives good results for this kind of sample here, the thickest sample represents an upper limit for thickness determinations using XRR, too, because a layer thickness of 300 nm results in an oscillation of reflectivity (cf. equation 2.37) of period 0.008°. With a goniometer resolution of 0.002° this corresponds to only 4 measurement points which is a minimum of points to display a sine shaped curve.

6.1.2. Implantations

Another type of samples analyzed with XRR and XSW at a photon energy of 15.2 keV are Si wafers containing implanted ions. Interpretation of XSW scans of ion implantations is more difficult than characterizing a layered system. Due to the implantation process ions do not form a distinct layer but are distributed inside the substrate in a more complicated way [73, 74, 75, 77] as illustrated in figure 6.3. To simulate the XSW signal of such a sample both the layer structure and marker distribution have to be different from a simple layer structure. Thus, the situation is similar to an ion distribution discussed in chapter 3.3.2 and analyzed in 6.2.3 or a roughness modeled by a continuous transition explained in chapter 2.4.2. In the following, an exemplary

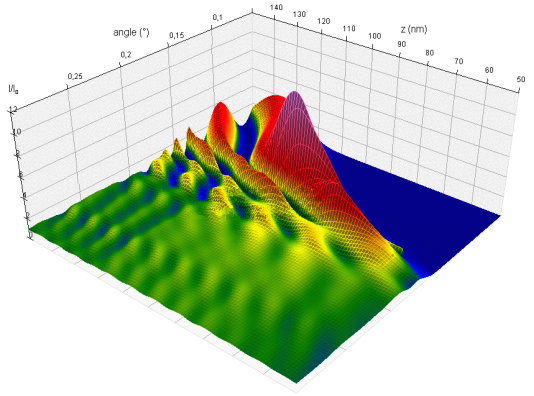

Figure 6.4.: Calculated 3D XSW field for As implantations in Si. As is distributed in a 120 nm thick region below the Si surface (from z = 120 nm to z = 0 nm). Energy of the incident radiation is 15.2 keV.

XSW field is calculated and discussed for a layer structure consisting of a Si substrate and several thin layers (like in the effective density model presented in chapter 2.4.3) approximating the curve in figure 6.3. After that, measurements of samples with different implantation concentrations, different implantation angles and samples with implantations of two different elements are presented and discussed.

XRR and XSW analysis of a Si substrate implanted with As ions

As an example, XRR and XSW analysis are presented for an implantation sample (XSW011) of As in Si. Implantation was performed at 100 keV at normal incidence with a nominal implant concentration of $1.0 \cdot 10^{17}$ cm^{-2}. Based on RBS and TXRF measurements performed on an equivalent sample [75] the XSW field for a sample model of a Si substrate with a distribution approximated by 7 layers was simulated. Thickness of each layer was approximately 20 nm and the optical parameters δ and β were varied between those of Si and As depending on their position. By that, a concentration distribution like the one suggested in figure 6.3 and in [75] was approximated. Figure 6.4 shows the calculated 3D XSW field for that sample. The corresponding calculated XSW scan was extracted by considering marker atoms in the entire layer region above the substrate (here defined as the lower boundary of the Si-As mixture region) with marker concentration increasing in a sine shape (cf. section 5.1.5). Layer thicknesses and δ, β were varied to optimize the correspondence between measurement and calculated XSW scan. Figure 6.5 shows measurement and fit for this sample. Correspondence is visible for small angles (up to 0.3°-0.5°) in XSW and XRR scans. Position of the fluorescence peak is the same in calculation and measurement at $\approx 0.13°$ which is between the critical angle of silicon ($\alpha_c = 0.119°$) and arsenic ($\alpha_c = 0.174°$) but closer to the Si value. This suggests that concentration of As is significantly lower than Si concentration throughout the sample. The oscillations in the calculated XSW curve around 0.15° are caused by strong interference maxima in the implantation region between vacuum and bulk Si as can be seen in figure 6.4. Apparently, these oscillation

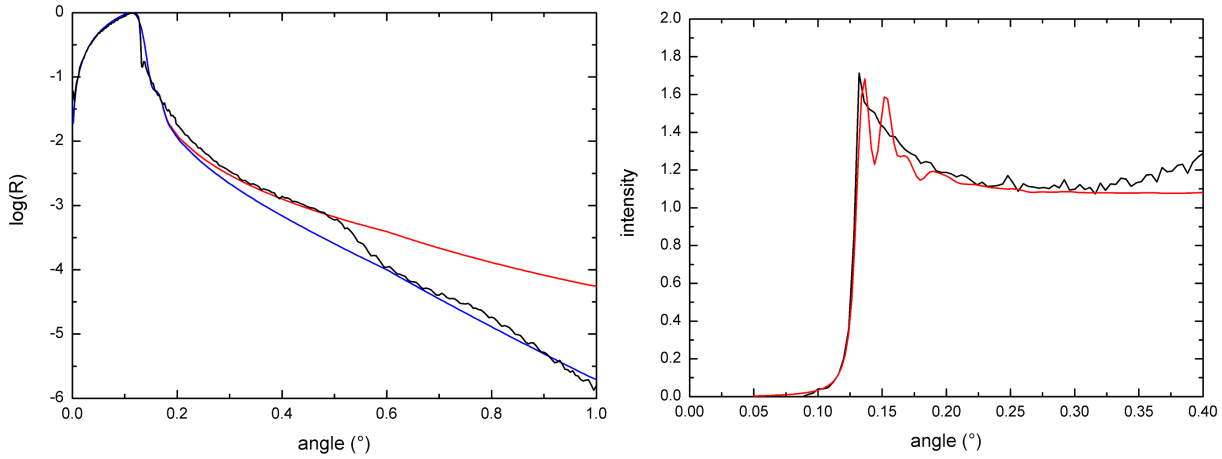

Figure 6.5.: Calculated and measured XRR (left) and XSW (right) scans for As implantations in Si. Energy of incident radiation was 15.2 keV. In both simulations As is distributed in a 120 nm thick region below the Si surface modeled by dividing this region into several homogeneous layers with different indices of refraction. Two fit curves are shown for the XRR scan: The red curve models the measurement well until $\approx 0.5°$ but is based on a rather unlikely low roughness of the lowest layer. The blue curve gives a better fit for large angles and a more realist roughness value. Further explanations can be found in the text.

were not measured. Probably, this is due to a stronger deviation of the real sample from the idealized layer system. Further, the increase of the detected fluorescence for higher angles in the XSW scan might be caused by implantation ions deeper inside the wafer. The simulated intensity could only be calculated for the upper part of the implantation region where As concentration is rising.

The same might hold for the reflectivity scan that was difficult to fit. Two calculated reflectivity curves are shown in figure 6.5 that are based on a stack of three 40 nm layers on a silicon substrate. The index of refraction for those layers was varied similar to the system in the XSW fit. Roughness of the layers is large (10 nm) because the real sample was no discrete layer system but a rather continuous distribution of As ions in Si. The two fit curves differ in roughness of the substrate below the layers. The best fit for angles below $0.5°$ is achieved for an unlikely low substrate roughness of approximately 0.5 Å. Calculations for a more realistic substrate roughness of 0.8 nm lead to the second curve that fits mainly for larger angles. Further, the slight modulation in reflectivity at higher angles is reproduced by neither fit. The oscillation period corresponds to a layer of approximately 8 nm thickness, maybe a sub-structure formed by implantation ions. However, achieving a satisfying fit probably requires a far more complicated sample structure model that could not be achieved here due to too little information.

Different implant concentrations

Figure 6.6 shows reflectivity and XSW scans of Co implantation in Si samples with different Co concentration $1.0 \cdot 10^{16}$ cm^{-2} (sample XSW012) vs. $1.0 \cdot 10^{17}$ cm^{-2} (sample XSW015) and

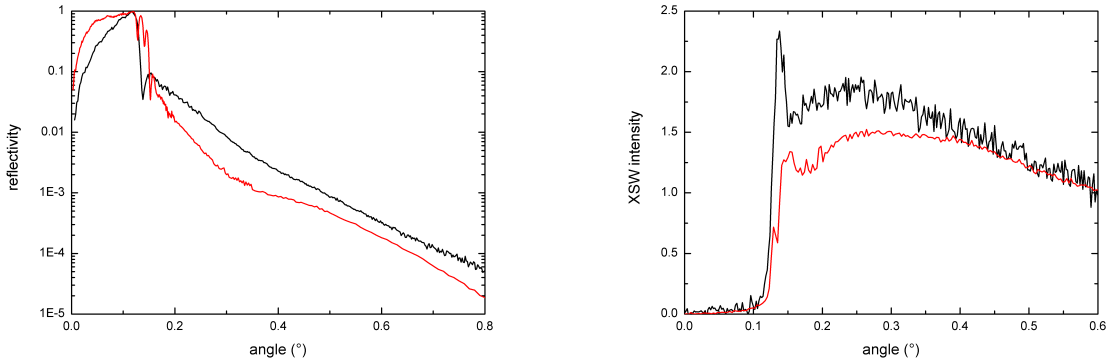

Figure 6.6.: Reflectivity (left) and XSW scan (right) for Co implantations in Si scanned at 15.2 keV. The black curves are for a Co concentration of $1.0 \cdot 10^{16}$ cm^{-2} (sample XSW012), the red ones for $1.0 \cdot 10^{17}$ cm^{-2} (sample XSW015). Explanations are given in the text.

different implantation energies (25 keV vs. 100 keV). Energy of incident photons was 15.2 keV. Regarding the reflectivity scans, strong deviations are visible. First, an intensity modulation as already discussed with sample XSW011 in the previous section can be seen in the reflectivity curve of the high concentration sample XSW015 but not the low concentration system XSW012. Further, the detected critical angle[1] for sample XSW012 is at $\alpha_{c,t}^2 \approx 0.124°$ while it is at $\alpha_{c,t}^2 \approx 0.145°$ for XSW015. Both values are between the critical angles of pure Si ($\alpha_{c,Si} = 0.117°$) and Co ($\alpha_{c,Co} = 0.221°$) with the higher angle for the higher concentration sample as expected. Assuming a homogeneous distribution, the content of cobalt in the whole sample (cf. appendix D.10)

$$n_{Co} = \frac{\alpha_{c,t}^2 - \alpha_{c,Si}^2}{\alpha_{c,Co}^2 - \alpha_{c,Si}^2} \tag{6.1}$$

can be calculated from the detected total critical angle $\alpha_{c,t}^2$ and tabulated values $\alpha_{c,Co}$ and $\alpha_{c,Si}$. The ratio implant/substrate is

$$\frac{n_{Co}}{n_{Si}} = \frac{\alpha_{c,t}^2 - \alpha_{c,Si}^2}{\alpha_{c,t}^2 - \alpha_{c,Co}^2}. \tag{6.2}$$

Table 6.2 lists this ratio extracted from reflectivities of both samples compared to published values obtained by TXRF and RBS measurements of equivalent samples [73, 77]. Agreement of results is rather good proving that XRR is capable of implant concentration estimations in that kind of samples. Furthermore, a second critical angle can be seen in the reflectivity curve of

[1] At the critical angle α_c radiation penetrates the sample and reflectivity decreases drastically. α_c for a reflectivity scan is determined by the angle position of the intersection point of the almost horizontal tangent to the part of the graph below α_c and the nearly vertical tangent to the curve above α_c.

	10^{16} cm^{-2}			10^{17} cm^{-2}			10^{17} cm^{-2} secondary$^{(2)}$		
Parameter	XRR	XSW	Lit	XRR	XSW	Lit	XRR	XSW	Lit
$\alpha_c(^\circ)$	0.124	0.127	—	0.145	0.138	—	0.123	0.125	—
n(Co)/n(Si)$^{(1)}$	0.048	0.075	0.04	0.209	0.152	0.245	0.043	0.058	0.06

Table 6.2.: Element concentration ratios of Co implantations in a Si substrate for two different nominal implant concentrations analyzed by XRR and XSW in this work, and published TXRF and RBS results [73, 77].
$^{(1)}$: Ratio of Co and Si concentrations. Calculated from α_c for XRR and XSW scans and taken from [77] as value at the peak plateau.
$^{(2)}$: Two critical angles can be observed for this sample.

sample XSW015 at a first short intensity drop. The corresponding Co/Si ratio of 0.043 might correspond to the implant concentration directly on the substrate. As illustrated in figure 6.3 implant concentration is highest in a certain depth inside the substrate but still significant on the surface. RBS and TXRF measurement of an equivalent sample [73, 77] had shown a value of 0.2-0.6 which is roughly the same as detected here.

Regarding XSW scans, a full analysis with perfect fit could not be achieved using the layered system model described in chapter 5. Nevertheless, the critical angle[2] can also be extracted from XSW scans as the angle where XSW intensity jumps up. Results from these measurements are given in table 6.2, too, showing that XSW accuracy for this task is not as good as by XRR but still delivers results in the correct order of magnitude.

Different implantation angles

Commonly, implantation of ions is performed at normal incidence. In this work, also a sample was analyzed that was prepared by implantation at a different angle. Figure 6.7 shows XRR and XSW scans of two Si samples implanted with As atoms at 100 keV and a nominal implant concentration of $1.0 \cdot 10^{17}$ cm^{-2}. Ions in sample XSW011 were implanted at normal incidence while the incidence angle for sample XSW010 was 60°. Shape of these curves is significantly different. Determining the critical angles of total reflection in those scans and calculation of implant concentrations like in the previous section deliver values that are listed in table 6.3. Critical angles for the pure Si or As layers here are $\alpha_{c,Si} = 0.117^\circ$ and $\alpha_{c,As} = 0.172^\circ$. It can be seen that results from literature [75] can be well reproduced for the normal incidence sample XSW011. In contrary to that, the detected critical angles for sample XSW010 is equal to or even below α_c of the Si substrate. This cannot be caused by a mixture of As and Si (that would increase α_c). Perhaps an askew incidence of sputtered As atoms leads to a roughening of the surface resulting in a lower density and thus lower critical angle that can be detected both by

[2]The critical angle in an XSW graph is the angle position of the inflection point of the curve in the region where intensity rises drastically from 0 to the first peak. α_c can also be determined as angle at half intensity of this rising flank. Due to the high slope the deviation from the inflection point is minimal and usually below detector resolution. In some XSW scans several critical angles can be defined for rising intervals interrupted by short intensity drops or plateaus.

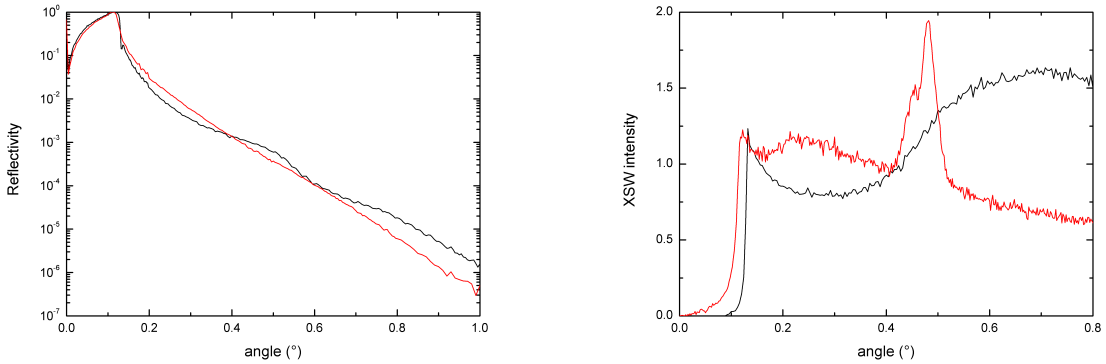

Figure 6.7.: Reflectivity (left) and XSW scan (right) for As implantations in Si scanned at 15.2 keV. Both samples were prepared at 100 keV with a nominal As concentration of $1.0 \cdot 10^{17}$ cm^{-2}. Sample XSW011 (black curves) was prepared by implantation in a common way at normal incidence, sample XSW010 (red curves) at an incidence angle of 60°. Analysis and explanations are given in the text.

	XSW010			XSW011		
Parameter	XRR	XSW	Lit	XRR	XSW	Lit
$\alpha_c(^\circ)$	0.117	0.11	—	0.127	0.128	—
n(As)/n(Si)$^{(1)}$	0	–	0.2$^{(2)}$	0.181	0.204	0.2

Table 6.3.: Element concentration ratios of As implantations in a Si substrate for two different nominal implant concentrations analyzed by XRR and XSW, and TXRF and RBS literature values [75].
$^{(1)}$: Ratio of As and Si concentrations. Calculated from α_c for XRR and XSW scans and taken from [77] as value at the peak plateau.
$^{(2)}$: Value for normal incidence, no data was available for 60° incidence.

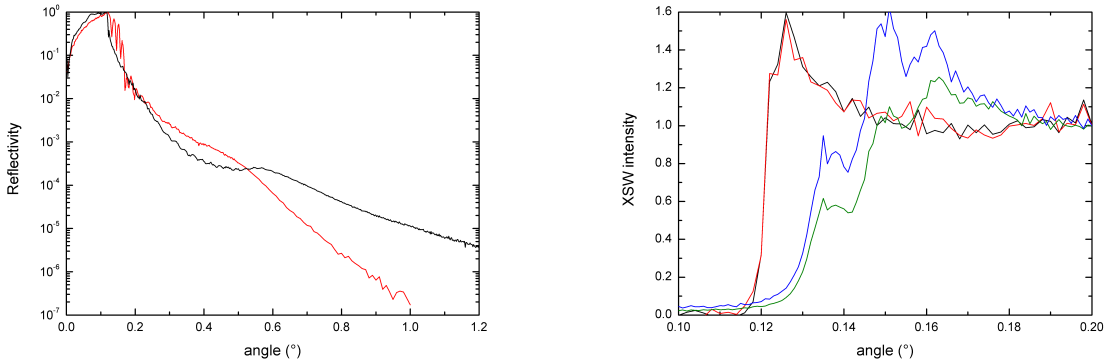

Figure 6.8.: Left: Reflectivity curves for Co and Zn implantations in Si scanned at 15.2 keV. Both samples were prepared at 100 keV. Nominal concentration for Co and Zn was $1.0 \cdot 10^{16}$ cm^{-2} for sample XSW017 (black curve). Concentrations for sample XSW016 (red curve) were $1.0 \cdot 10^{17}$ cm^{-2} (Co) and $0.49 \cdot 10^{17}$ cm^{-2} (Zn).
Right: XSW measurements of the same samples. XSW intensity is normalized to 1 for an angle of 0.2°. The two curves on the left side show XSW scans for Co (black) and Zn (red) of sample XSW017. The other curves are Co (green) and Zn (blue) for sample XSW016. Absolute detected intensities were equal for Co and Zn for sample XSW017. In sample XSW016, Co showed an absolute intensity roughly 2 to 3 times higher than Zn. Analysis and explanations are given in the text.

XRR and XSW. Further, it might be possible that a channeling effect occurs when sputtering at an angle of 60° which is equal to the angle formed by atoms in a close packed structure of Si atoms. A channeling effect would let implant atoms penetrate deeply into the substrate with low concentration near the surface and thus a surface behavior similar to pure silicon. Consequently, the reflectivity curve for XSW010 in figure 6.7 resembles the one of a pure Si wafer. On the other hand, the signal in the element specific XSW scan proves presence of As in the sample.

Implantation of two different elements

Finally, sample systems of a Si substrate with implantations of two different implantation elements (Co and Zn) were analyzed. Sample XSW016 was implanted with $1.0 \cdot 10^{17}$ cm^{-2} of Co and $0.49 \cdot 10^{17}$ cm^{-2} of Zn, implantations in sample XSW017 were $1.0 \cdot 10^{16}$ cm^{-2} for both Co and Zn. Reflectivity and XSW scans for the two samples are displayed in figure 6.8.

Regarding the reflectivity measurement of sample XSW017 one critical angle of total reflection can be determined at approximately 0.118° which is only slightly above the critical angle for pure Si ($\alpha_{c,Si} = 0.117°$). Nevertheless, the shape of the reflectivity curve deviates strongly from a curve for pure Si (cf. figure 2.2) at higher angles. Thus, the implantations have a significant influence when radiation penetrates the sample into deeper regions. Contrarily, the reflectivity signal for sample XSW016 ($1.0 \cdot 10^{16}$ cm^{-2} and $0.49 \cdot 10^{16}$ cm^{-2}, respectively) shows two critical angles, 0.127° and 0.165°, that are between the values of pure Si and pure implant materials ($\alpha_{c,Zn}$ = 0.197°, $\alpha_{c,Co} = 0.221°$). Here, the surface of the substrate might have been modified

	XSW017		XSW016				
Parameter	XRR	XSW	XRR_1	XRR_2	XSW_1	XSW_2	XSW_3
$\alpha_{c,ref}(^\circ)$	0.118		0.127	0.165			
$\alpha_{c,Co}(^\circ)$		0.121			0.131	0.145	0.158
$\alpha_{c,Zn}(^\circ)$		0.121			0.131	0.145	0.158
n_{Co}	0.004	0.016	0.051	0.285	0.073	0.155	0.238
n_{Zn}	0.004	0.016	0.025	0.140	0.036	0.076	0.116

Table 6.4.: Critical angles (as defined in section 6.1.2) of total reflection and implant concentrations (ratio $n_{implant}/n_{total}$) in double implanted samples. Nominal concentration for Co and Zn was $1.0 \cdot 10^{16}$ cm^{-2} for sample XSW017 and $1.0 \cdot 10^{17}$ cm^{-2} (Co) and $0.49 \cdot 10^{17}$ cm^{-2} (Zn) for sample XSW016. Several critical angles (2 for XRR and 3 for XSW) can be defined for sample XSW016. No published data was available for this sample.

by implants and total reflection on pure Si could not occur. Further, signal intensity decreases much faster at higher angles than for the other sample, which is another indication for higher roughness.

XSW scans for each implantation element were recorded for summed Kα and Kβ fluorescence intensity. Measured curves are shown in figure 6.8. It can be seen that Co and Zn give virtually the same signal for sample XSW017 as could be expected concerning the equal implantation concentration. On the other hand, fluorescence intensity of Co was about 2-3 times higher as Zn in sample XSW016 (not visible in figure 6.8 due to normalization) which corresponds to the nominal element ratio of $\approx$ 2:1. Critical angles obtained from theses curves are listed and compared to XRR results in table 6.4. The value of $\alpha_c = 0.121^\circ$ for sample XSW017 agrees well with the XRR measurement. However, very different XSW curves were recorded for sample XSW016 for Co and Zn with three critical angles, all of them lower than α_c detected by XRR. Apparently, in this sample different regions contribute to intensity jumps in XRR and XSW scans. Nevertheless, positions of these jumps are equal for Co and Zn. Regarding the structure and dynamics of the XSW field with increasing incident angle outlined in the theory and simulation chapters 2.3 and 5, this means that the two implant elements are distributed equally in depth with only their concentration being different. Published measurements of a similar double implanted sample (As and Co in Si) [74] and single implanted samples (As or Co in Si) [75, 77] showed that lateral distribution of implantations in the substrate is strongly dependent on the kinetic energy of implantation ions during implantation. On the other hand, the type of element has little influence on its final implantation position, at least if ions of similar size such as As, Co and Zn are regarded. This effect could be confirmed using XSW measurements presented here, too.

It has been shown that XRR and XSW are capable of delivering qualitative and even some estimated quantitative information about ions implanted in a semiconductor substrate. The implants appear to change the substrate strong enough to create interfaces of dispersion contrast that permit reflectivity observations and forming of X-ray standing waves fields. Further, XSW has proven to be element sensitive to ions even inside a sample.

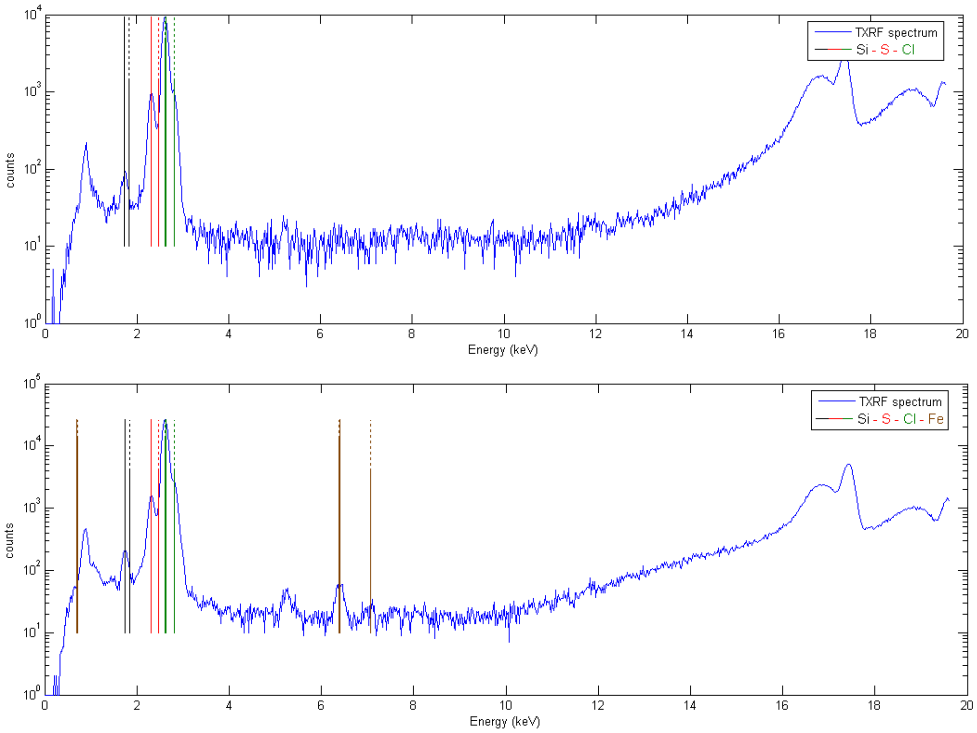

Figure 6.9.: TXRF scan of silane/cytochrome sample 01 (above) and 02 (below). Si (from the sample carrier), S and Cl (from the buffer solution) are clearly visible in both scans. Fe (the intended marker element included in cytochrome) is only visible in the scan of sample 02.

6.2. Bio-organic samples

6.2.1. Proteins: Cytochrome

Thin cytochrome films on glass carriers were prepared as described in section 3.2.1 and first analyzed by TXRF scans using a molybdenum X-ray tube ($E = 17.48$ keV). Figure 6.9 shows scans of two cytochrome-silane samples analyzed using the program (cf. section E.2). In both scans, strong fluorescence peaks of S and Cl are visible, elements that are present in the buffer solution covering the cytochrome sample. Further, Si from the substrate material and silane layer is visible. Only sample 02 shows an obvious iron fluorescence peak. With Fe being the intended marker element for XSW scans of this sample this shows that sample preparation is already a crucial part of the experiment. Furthermore, even analysis of sample 02 can be expected to be difficult because peaks from the buffer elements are much more intense than from the marker element. As cytochrome layers decompose with time on a scale of hours to days, new cytochrome films were prepared for XRR and XSW measurements at DELTA shortly before the measurements. Due to this, samples in these scans and TXRF analysis discussed above cannot be expected to be absolutely equivalent.

Figure 6.10 shows an energy spectrum of fluorescence from a cytochrome sample recorded

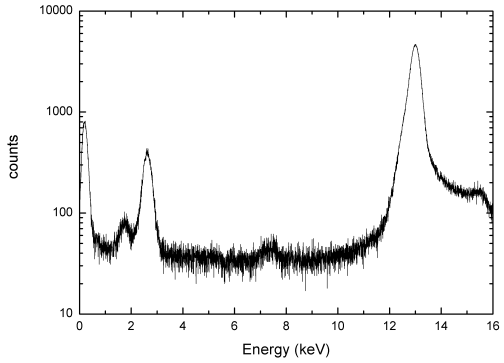

Figure 6.10.: Energy spectrum of fluorescence from a cytochrome sample at an excitation photon energy of 13 keV. Intensity peaks from electronic noise (around 0.1 keV), Si from the sample carrier and maybe from the detector (1.74 keV), Cl from the buffer solution (2.62 keV) and elastic scattering (13.00 keV) are clearly visible. The signal from Fe (6.40 keV) is very weak, even much lower than the Ni signal (7.48 keV) that probably comes from some components of the set-up.

at DELTA at an excitation photon energy of 13 keV. It can be seen that fluorescence intensity from Fe is too low to perform reasonable XSW scans with this element. Apparently, only a small amount of Fe could be attached onto the sample carrier. A further problem is that each cytochrome c molecule contains just one single Fe atom strictly limiting Fe concentrations in a cytochrome film to low values. Using a peak fitting software for the Fe fluorescence peak instead of defining a fixed ROI might permit a fluorescence scan even with low concentrations. However, this features was not installed at SAW2 beamline. Thus, Cl (present in the buffer solution above the cytochrome film) was chosen as a marker element to obtain information about the layer indirectly.

Figure 6.11 shows XSW and XRR scans of the sample, both performed at 13.0 keV photon energy. No satisfying fit could be achieved for the XSW scan. The best result, shown in figure 6.11, is for a SiO_2 sample carrier with a 1 nm Si layer and a 6 nm cytochrome film covered with 1 nm of water. Cl is the marker element distributed homogeneously inside the water layer. The significant difference between calculation and measurement for higher angles might be caused by partly overlapping of the Cl and Si fluorescence peak or another unintended signal or noise.

Regarding the XRR scan, no oscillations (Kiessig fringes) are visible. This means that the layer(s) on the carrier must be very thin (i.e. less than 5 nm which corresponds to an oscillation period of 5.5°) and/or very rough to suppress strong oscillations. However, a pure glass or silicon surface does not deliver a theoretical reflectivity curve fitting to the measurement.

With a cytochrome c diameter of ≈ 3.4 nm these results are consistent with a mono or double layer. However, results are not very significant. Assuming a more complex sample structure of several layers with various parameters could lead to better fits. However, this was not possible here due to too little information about the sample composition and materials. Obviously, utilizing Cl as an "indirect" marker element due to the insufficient Au signal was not very successful

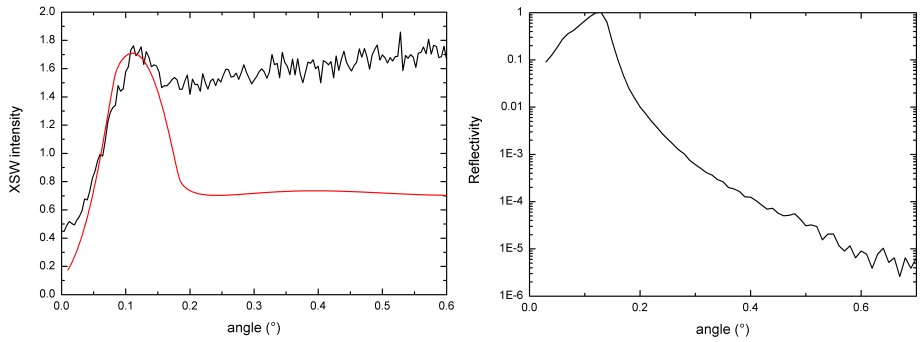

Figure 6.11.: XSW and XRR scans of a cytochrome film performed at 13 keV.
Left: XSW measurement and calculated angle scan for a 6 nm cytochrome film on SiO_2 substrate (with 1 nm Si) covered by a 1 nm water (buffer) film. The marker atom in this scan is Cl, a component of the buffer solution.
Right: XRR measurement of the same sample. No oscillations (Kiessig fringes) are visible. Thus, the layer(s) on the carrier must be very thin (less than 5 nm) and/or rough enough to suppress significant oscillations.

with this sample. Hence, future experiments with this type of sample should focus on improving preparation of the cytochrome layer to obtain a detectable concentration of incorporated iron marker atoms.

6.2.2. Lipids: Phospholipid

A phospholipid (POPC) bilayer was prepared by Langmuir-Blodgett technique [16] on a mica substrate glued to a glass carrier as described in section 3.2.2. This POPC sample was then analyzed by XSW measurement. Figure 6.12 shows results of an XSW measurement performed at 13 keV scanning three elements (P, K and Cl) simultaneously. P is part of the "head" of the POPC chain (cf. figure 3.4), K^+ and Cl^- are components of the buffer solution which covers the POPC film. This scan was performed on a "dried" phospholipid sample, that means KCl buffer solution was drained from the sample carrier as a rather thick buffer layer disturbed XSW measurements too much, leaving only a very thin film on the sample.

Position of XSW intensity maxima

A first interpretation of this scan can be made considering the angles of total reflection for mica ($\alpha_c = 0.151°$) that is simulated with an empirical formula of $KAl_3Si_3O_{12}H_2$, and the buffer solution ($\alpha_c = 0.095°$) approximated as water. It can be seen that K and Cl show strong fluorescence peaks at angles below the critical angle of water. In this region, radiation penetrates only few nm of the sample i.e. just the upper part of the buffer solution but not the phospholipid bilayer below. Consequently, hardly any signal is detected from phosphorus. Above this critical angle, radiation penetrates the buffer solution with potassium and chlorine fluorescence decreasing and increasing intensity from phosphorus. Fluorescence intensity from P increases continuously until

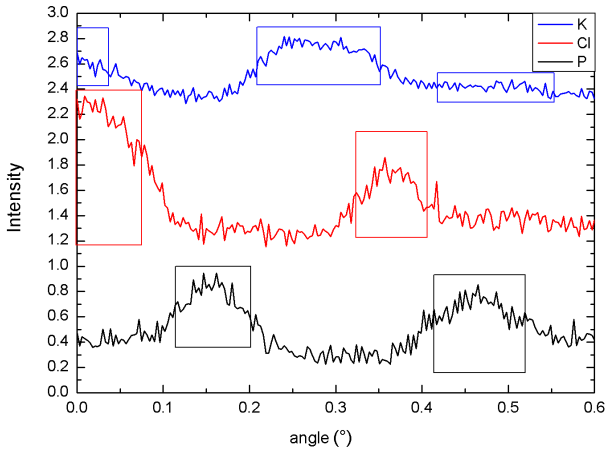

Figure 6.12.: Evaluation of phospholipid XSW scans of K (blue), Cl (red) and P (black). Explanations can be found in the text.

an angle of approximately 1.5° which is exactly the critical angle of mica. This means that more radiation penetrates the sample and excites P atoms with rising angle. Radiation is then totally reflected at the mica surface below the phospholipid leading to additional excitation of P by the reflected beam. Above the critical angle of mica, an increasing amount of radiation enters into the substrate leaving less for excitation in the phospholipid layer.

To extract quantitative results from the scan, a theoretical layer sample model had to be developed as explained in the following. As intensity maxima are rather wide, an angle range was set as maximum position by locating the angle interval where XSW intensity is more than half the peak intensity. These ranges are marked as boxes in figure 6.12. Then a layered sample was simulated consisting of a 20 nm water layer on a mica substrate. This can be taken as an approximation to a biofilm covered with buffer solution because ions of low concentration are expected not to alter the beampath and XSW field in the water very much. Then, the lateral positions (height above the substrate) of XSW intensity maxima for several angles of incidence were calculated. A first maximum enters the layer below $\approx 0.1°$, a second one around 0.15° and a third maximum around 0.25° as can be seen in figure 6.13. Each maximum wanders downwards through all layers exciting typical fluorescence radiation for each element at certain angle intervals. If the measured angle intervals from figure 6.12 are marked in figure 6.13 with a rectangle defined by the first and last point of the curve corresponding to the angle range, a height range corresponding to the element's position in the sample can be obtained. Considering the significant maximum in the XSW scan of K (0.2°-0.35°), it can be seen in figure 6.13 that it may only occur if K is located in the region from 8 to 15 nm or from 17 to 30 nm. If K was between 8 and 15 nm another maximum in the angle range from 0.4° to 0.55° could be expected. In fact, the signal is (at least a little) higher than the rest of the curve in this region. The first maximum in the K scan is at a low angle range. As explained in the simulation chapter the first maximum is very broad and cannot be well localized thus agreement in this range is not very good.

The second material, Cl, shows intensity maxima in the low angle range and between 0.31°

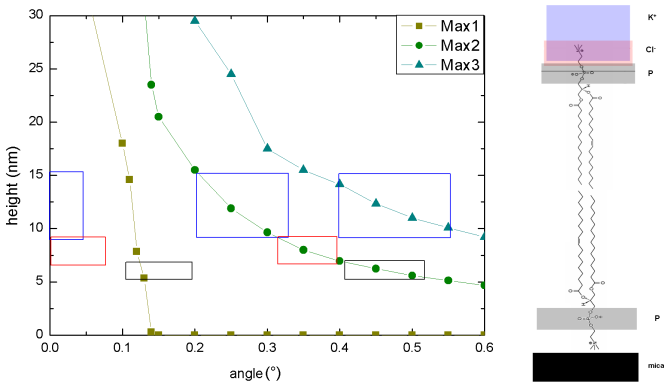

Figure 6.13.: Left: Analysis of the layer structure of the phospholipid bilayer. Elements K (blue), Cl (red) and P (black) are colored like in figure 6.12. Evaluation of phospholipid scans is explained in the text. Right: Schematic layer structure of the phospholipid bilayer with buffer as obtained from the measurements with a K^+ enriched water/buffer region (blue), a Cl^- enriched buffer region (red) and two zones in the phospholipid bilayer that contain P (gray).

and 0.4°. This could be caused by a Cl layer between 15 and 17 nm. Then another maximum would be expected at angles 0.15° to 0.18° caused by the second maximum. However, that maximum is not visible in the scan. A Cl layer between 7 and 9 nm would show a maximum in the observed region (caused by the second penetrating XSW maximum) and another one in the low angle region. The measured maximum of fluorescence intensity from P between 0.41° and 0.52° can be well explained with a P layer between 5 and 7 nm. This layer would also cause a maximum around 0.14° which is very obvious in the scan.

Finally, combining this possible layer positions and thicknesses with basic knowledge about the sample, a combination (cf. figure 6.13) that makes sense can be assumed: First a thin P layer between 5 and 7 nm above the substrate that would correspond to a phospholipid bilayer with the P containing heads directly on the substrate surface and around 6.5-7 nm (i.e. 2 POPC chains lengths) above the surface. A thin Cl^- layer (or a layer containing more Cl^- than K^+ ions) is located above the P layer, which could be expected for Cl^- ions tending to be closer to the positive N atom in the head of the POPC (cf. figure 3.4). Finally, the K^+ enriched layer follows to achieve charge equilibrium.

Of course, other layer combinations might fulfill the conditions given by the measured curves. However, the one given here is the most simple combination that explains the measurements and makes sense considering the known sample structure.

Analyzing the P fluorescence signal

Another approach to characterize the scan of the P fluorescence signal is to consider signals from two P layers separately. The sample system is simulated as a mica substrate covered with some nanometers of phospholipid (optical constants of polystyrene were taken as a model for phospholipid) covered with a thin water layer. Best results were achieved for thickness, dispersion

Layer	d (nm)	$10^6\delta$	$10^6\beta$
Water	4	1.366	0.0017
POPC	6	1.468	0.0008
Mica	–	3.478	0.0224

Table 6.5.: Sample model for the phospholipid (POPC) sample providing the best fits for XSW measurements. The 6 nm thickness of the POPC layer suggests the presence of a bilayer that is covered by a very thin water (buffer solution) film.

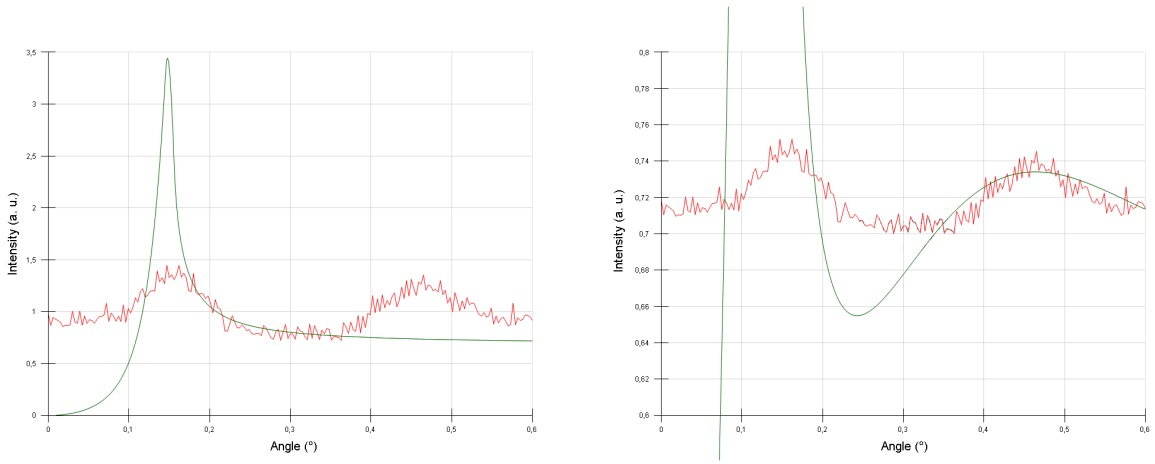

Figure 6.14.: Left: XSW signal from P located closely above the substrate (between 0.4 and 0.5 nm). It can be seen that the first peak position in the measurement can be explained by a P atom close to the substrate.
Right: XSW signal from P located in a layer between 5.4 nm and 5.5 nm above the substrate. A first peak here again appears at $\approx 0.15°$ that overlaps with the one shown in the other graph. And a second peak arises at $\approx 0.45°$. Thus, P located between 5.4 nm and 5.5 nm above the substrate can explain both peak positions.

and absorption values given in table 6.5. The 6 nm thickness of the POPC layer and a POPC chain length of 3-4 nm suggest the presence of a bilayer as intended.

Assuming a P layer closely above the mica surface - as would be expected considering the bilayer structure shown in figure 3.5 with POPC heads in contact with the substrate - calculations lead to an intensity peak at $\approx 0.15°$ nm. This angle position agrees very well with measurements as can be seen in figure 6.14. However, accordance in peak shape of calculation and measurement is low, clearly showing the limits of this simple model for a complex sample system. Nevertheless, the calculated marker layer is between 0.4 and 0.5 nm above the substrate, which is in good accordance with the position of the lower P atom in the layer structure shown in figure 6.13. The second peak in the scan should then arise from the second P layer in the sample formed by the POPC heads of the upper phospholipid monolayer. Simulations of this case lead to agreement with measurements for a P position between 5.4 nm and 5.5 nm above the surface. This marker position would generate a small peak around 0.45° and a strong one at $\approx 0.15°$ (like the P atoms

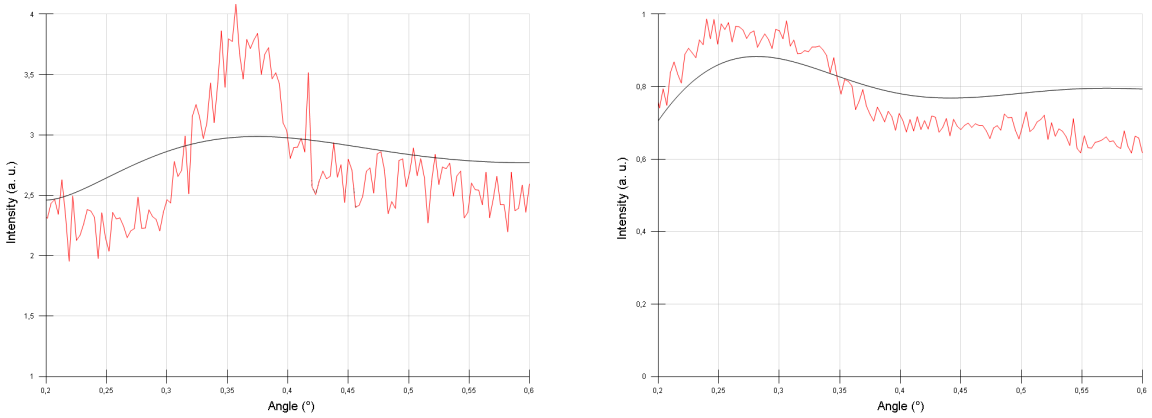

Figure 6.15.: XSW scan and fit (fluorescence intensity vs. angle of incidence) of Cl (left) and K (right) in buffer solution above the phospholipid sample described in sections 3.2.2 and 6.2.2. Further explanations can be found in the text.

directly on the substrate). At least angle positions of maxima in measurement and simulation agree well. Thus, it can be stated that P located at 0.4-0.5 nm and 5.4-5.5 nm would generate the measured signal. These distances agree well with expectations and previous considerations regarding a phospholipid chain length of 3-4 nm. Thus, they give an additional evidence of the correctness of the sample model.

6.2.3. Ion distribution: Buffer solution

In addition to the phospholipid bilayer analyzed in the previous section, that sample provides another interesting type of structure. The buffer solution film above the bilayer contains K^+ and Cl^- ions that are not be expected to be located homogeneously in a layer but in a concentration distribution depending on the distance from the positive P comprising heads of the lipids as already mentioned in section 6.2.2.

Considerations made in chapter 3.3.2 suggest a somewhat exponential decrease of Cl^- and increase of K^+ with distance from the upper boundary of the phospholipid bilayer. This distribution was included in *MXSW* calculations (cf. section 5.1.5), and best fits to measurements performed at photon energy 13.00 keV were sought. Figure 6.15 shows XSW scans and best fits for K^+ and Cl^- in the buffer solution. Even though fits are far from being perfect, some semi-quantitative results can be extracted that are listed in table 6.6 and illustrated in figure 6.16. Varying simulation parameters to achieve the best fit leads to best results for an exponential marker distribution of K and Cl rather than a homogeneous layer like for P. This is in agreement with expectations that Cl^- ions are more concentrated near the phospholipid bilayer while consequently K^+ shows higher concentration farther away near the upper boundary of the 4 nm water film.

marker	$z_{\min}$	$z_{\max}$	concentration with increasing z
K	6	10	increasing exponentially
Cl	6	8	decreasing exponentially
P	5.4	5.5	homogeneous
P	0.4	0.5	homogeneous

Table 6.6.: Marker distribution in the phospholipid sample with buffer solution depending on the distance from the mica substrate surface at z = 0.

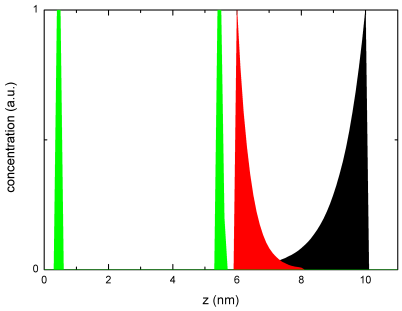

Figure 6.16.: Marker distribution in phospholipid buffer sample. The phospholipid bilayer of 6 nm thickness contains P (green) atoms in the lipid heads close to its lower and upper boundary. Further, Cl^- (red) ions are more concentrated near the phospholipid while K^+ (black) shows higher concentration far away near the upper border of the 4 nm water layer.

6.2.4. Polymers: Gold and silver clusters on polymer films

Polymer layers on silicon

Samples of polystyrene layers on silicon substrates were analyzed at a photon energy of 13 keV. Due to the elemental composition of polystyrene $[C_8H_8]_n$ no fluorescence signal from the film was recorded. Hydrogen is not able to emit fluorescence radiation and carbon fluorescence is of very low energy (277 eV) that it cannot be detected with the set-up utilized in our experiments at DELTA. Nevertheless, Si as the substrate material emitted fluorescence radiation which was recorded. Figure 6.17 shows XSW scans performed at four samples of nominal polystyrene thicknesses 71.3 nm, 45.3 nm, 16.5 nm, and 6.9 nm. The curves show a similar behavior as the theoretical ones discussed in section 5.3.1 but already level off at about 0.4°. Calculating the beam footprint at this angle as shown in figure 5.5 by $F = h_{\text{beam}}/\sin\alpha_0$ gives a value around 2 cm which corresponds to the size of the sample in direction of the beam. This means that the fluorescence signal does not change further once the entire beam hits the sample. The scan of the 45.3 nm thick polystyrene layer strongly deviates from the others. The detected signal does not correspond to a thick substrate but to a thin layer. Maybe this effect is caused by contaminations of Si or neighboring elements such as Al or P. Furthermore, due to the featureless structure of the curves not much information can be extracted from corresponding fits. Summarizing, it can be stated that using the substrate fluorescence to obtain information on the layer above does not promise to give very accurate results.

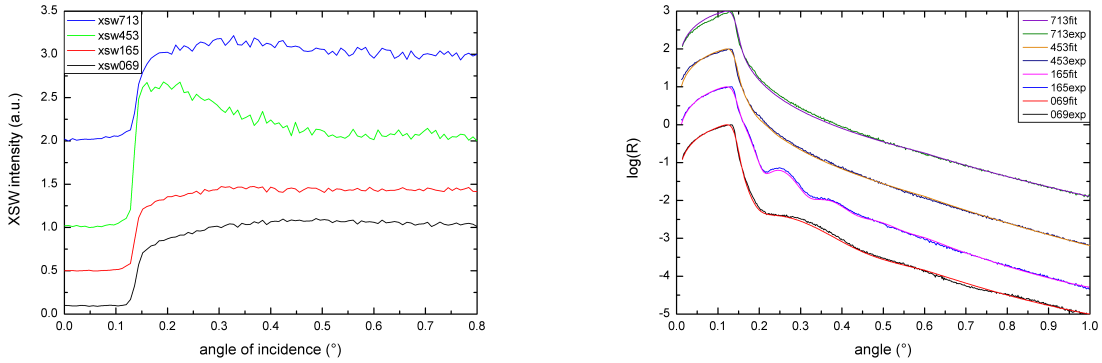

Figure 6.17.: Left: XSW scans of four different polystyrene films (from top to bottom: 71.3 nm, 45.3 nm, 16.5 nm and 6.9 nm thickness) on a silicon substrate. Virtually no signal is detected below the critical angle of Si for 13 keV (0.138°) and the signal reaches a constant value for angles above $\approx 0.4°$. Further explanations can be found in the text.
Right: Reflectivity scans for the same films (from top downwards: 71.3 nm, 45.3 nm, 16.5 nm and 6.9 nm). Weak Kiessig fringes are visible for the thinner layers but not for the thicker ones. This might be an indication for bad sample quality.

In a second step, reflectivity scans were performed on the Si-PS samples, shown in figure 6.17. No Kiessig fringes are visible for the thicker layers and only weak ones for the thinner layers. This could be due to degeneration of the old samples. Fitting theoretical curves with tabulated δ, β values [31, 59] to these scans reveals thicknesses and roughnesses listed in table 6.7. The scans of the two thin samples showing Kiessig fringes can be fitted comfortably using the least-square fit-program *LsFit* [134, 135] revealing PS thicknesses higher than the nominal ones provided with the sample. However, no automatic thickness fitting was possible for the two thick films because they did not show any Kiessig fringes expected for samples of these dimensions. Their reflectivity curves are rather similar to the curve of a pure Si layer without PS film. For this reason the result for the 45.3 nm sample is kind of estimative. Fitting of the 71.3 film scan is even more problematic. Here the nominal thickness had to be kept fixed during evaluation and PS roughness had to be estimated. Thus, values for this fit are rather unreliable.

However, some information can be extracted from evaluation of these scans. Calculated roughness of all polymer films is huge. And the complete vanishing of Kiessig fringes in two of the scans can only be explained by large roughness. This suggests that the spin-coating production process did not work ideally or samples had suffered from damage for example by heat or radiation.

Gold clusters on a polystyrene layer on silicon

A second, expanded sample system proved to give better results. The calculated XSW field for a photon energy of 15.0 keV and a complex three layer sample structure (Au clusters on a

Material	Value	6.9 nm	16.5 nm	45.3 nm	71.3 nm
Si	$10^6\delta$	2.8800	2.8800	2.8800	2.8800
	$10^6\beta$	0.02619	0.02619	0.02619	0.02619
	σ (nm)	0.020	0.1245	0.052	0.049
SiO_2	$10^6\delta$	2.7140	2.7140	2.7140	2.7140
	$10^6\beta$	0.01381	0.01381	0.01381	0.01381
	d (nm)	1.435	1.645	0.095	1.554
	σ (nm)	0.3003	0.4850	0.6506	0.3025
PS	$10^6\delta$	1.4680	1.4680	1.4680	1.4680
	$10^6\beta$	0.00081	0.00081	0.00081	0.00081
	d (nm)	7.958	21.966	41.851	71.300
	σ (nm)	2.8988	3.2568	7.8248	13.300

Table 6.7.: Tabulated δ, β values [31, 59] and measured parameters (thickness d, roughness σ) for four different PS layers on Si. Nominal thicknesses [142, 145] are given in the first row. Explanations can be found in the text.

polystyrene film on a quartz covered Si wafer) is shown in figure 6.18.

Data supplied with the sample [145] were the nominal thickness of the polystyrene and gold layer estimated from the settings of the spin-coater for PS and the evaporator for Au. Here, it has to be considered that the values for gold are nominal values for a continuous layer and not for a clustered structure. Tabulated values for dispersion δ and absorption β were taken from CXRO database [31, 59]. Further, an X-ray reflectivity scan of the sample was performed (cf. figure 6.19) and thicknesses and roughnesses of the layers were determined using the fit-program *LsFit*. Figure 6.19 shows XSW and XRR measurements and fits. Nominal values compared to XRR and XSW results are listed in table 6.8.

Accuracy for the parameters in XRR is rather good (better than 1% for most values), while it varies in XSW measurement. The thickness of the polystyrene layer (80 nm) can be determined with an error less than 1 nm while thickness of the SiO_2 layer cannot be measured with XSW. This is due to the very similar optical constants of Si and SiO_2 and the position of the marker far from the SiO_2 layer. In the fits a thickness of 1 nm was assumed for the silicon oxide layer, but a thickness of 10 nm does not change the fit very much either. Finally, a simplified simulation of the gold layer of the sample as a continuous layer with bulk values (cf. table B.2) leads to the curve shown in figure 6.19. It can be seen that measurement and fit already agree very well. Considering the clustered layer structure, a layer of double thickness and at the same time dispersion and absorption values twofold smaller can be assumed. In this case, the simulation delivers a very similar curve. Accordingly, satisfying fits are achieved up to thicknesses of about $5d_{\mathrm{n,Au}}$ as long as the product of d and δ is kept constant. Thus, the XSW method is very accurate for determining the nominal thickness (i.e. the total amount of gold on the sample). The accuracy for measuring the layer thickness of this not well known structure ranges within the limits of a few nm. Roughness characterizations with XSW at this sample - contrary to XRR scans - appear to be not very accurate as roughness effects from the effective density model used in the simulation are very small.

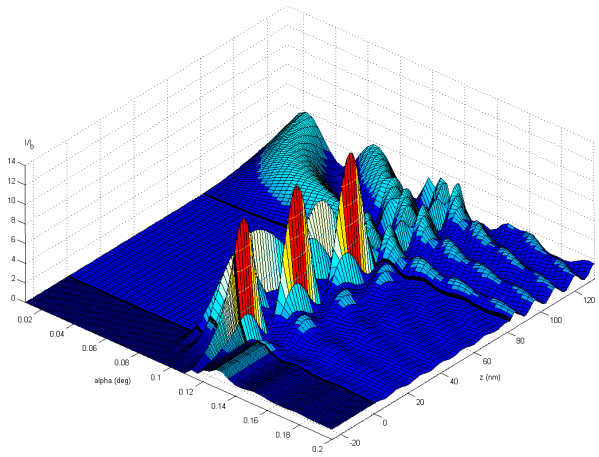

Figure 6.18.: Calculated XSW field of the Au-PS-SiO_2-Si sample for a photon energy of 15.0 keV. The angle of incidence is given on the left axis, height above or depth below the Si substrate surface on the right axis. Explanations can be found in the text.

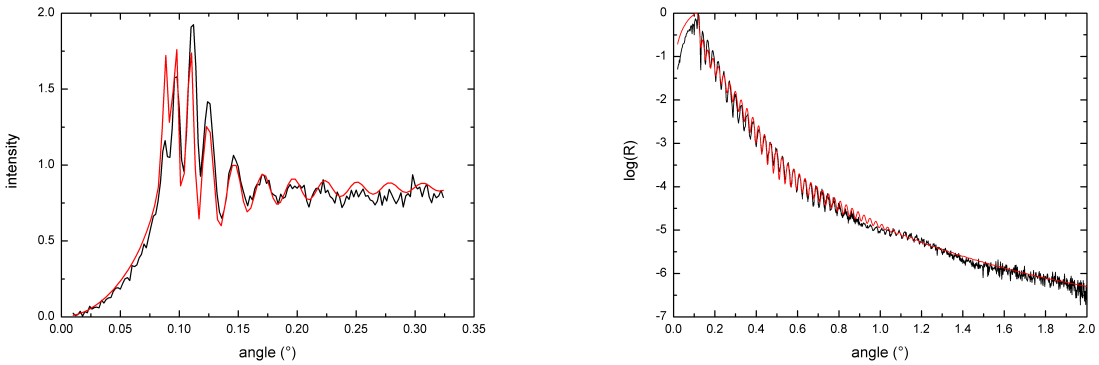

Figure 6.19.: XSW (left) and XRR (right) scans and fits for a polystyrene layer on Si/SiO_2 sample covered with Au clusters. Detected intensity is shown versus angle of incidence. Given values for the sample were 80 nm polystyrene thickness, 1 nm nominal gold thickness and silicon with a native oxide layer of unknown thickness. The fit curves were calculated for 1 nm gold on 80 nm polystyrene on 1 nm SiO_2 on silicon for XSW and slightly different values for XRR.

Material	Value	Tabulated/nominal	XRR result	XSW result
Si	$10^6\delta$	2.159	2.159	2.159
	$10^6\beta$	0.0149	0.0149	0.0149
	σ (nm)	N/A	0.1500	N/A
SiO_2	$10^6\delta$	2.036	2.036	2.036
	$10^6\beta$	0.0078	0.0078	0.0078
	d (nm)	N/A	0.69	N/A
	σ (nm)	N/A	0.126	N/A
PS	$10^6\delta$	1.102	1.102	1.102
	$10^6\beta$	0.00048	0.00048	0.00048
	d (nm)	80	78.644	80
	σ (nm)	N/A	1.7506	<2
Au	$10^6\delta$	13.480	3.0092	13.480
	$10^6\beta$	2.0217	0.00479	2.0217
	d (nm)	1	3.911	1
	σ (nm)	N/A	1.3322	<1

Table 6.8.: Tabulated [31, 59], nominal [145] and measured parameters (dispersion δ, absorption β, thickness d and roughness σ) of the Au-PS-SiO_2-Si sample. Explanations can be found in the text.

Furthermore, the surface coverage of the sample by gold clusters can be considered. Systematic measurements and calculations on gold polymer samples [81, 164] delivered a relation between nominal thickness and surface coverage of the gold. Using that relation leads to a coverage of 38% for the sample observed here which corresponds to a gold layer of roughly threefold thickness (in comparison to the nominal thickness) with δ and β divided by the same factor. This is in good agreement with the range of gold thickness determined by XRR and XSW ranging from one to fivefold the nominal thickness. Overall, the experimental results of the XSW measurement could be well described and showed good agreement with expected values.

An XRR measurement of this sample was already performed earlier [25, 145] with a photon energy of 8.048 keV (Cu X-ray tube). Both XRR scans are compared in figure 6.20. After removing differences in δ, β values and angle scale due to the different photon energies by rescaling, still a significant difference between the two graphs is visible. Fitting procedures using *LsFit* [134, 135] were performed on both scans and the dispersion profile was calculated. Figure 6.21 shows a comparison of both δ profiles. As the 2004 scan was performed at 15 keV, δ values in this graph are rescaled to a photon energy of 8.048 keV (as in the 2002 scan) to permit comparison. It is obvious that the δ peak caused by the Au layer changed significantly: The height of the peak decreased and width increased while the overall peak area remained constant. Apparently, the total amount of gold did not change (as can be expected) but the gold clusters moved and spread over a wider z region. Thus, a long-time degeneration of this kind of samples was detected.

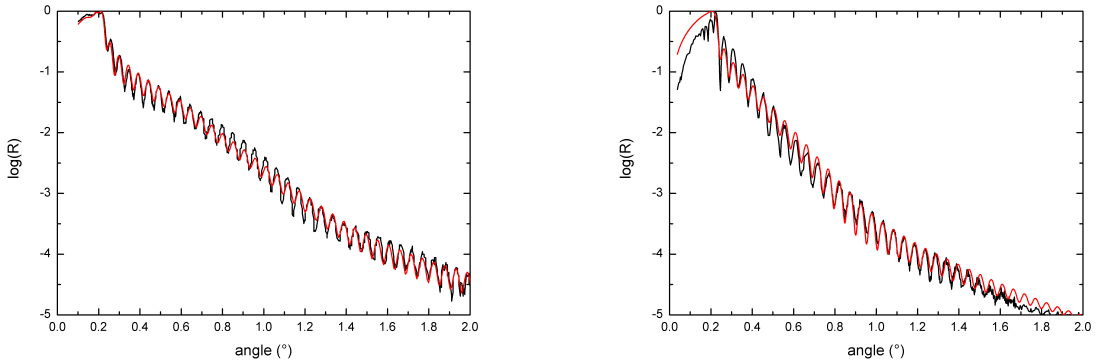

Figure 6.20.: XRR scans (black) and fits (red) for the PS layer on Si/SiO_2 with Au clusters presented in figure 6.19 measured at two different times and energies. The reflectivity scan from November 2002 (left) was performed at 8.048 keV, the XRR measurement in December 2004 (right) at 15 keV. The angle scale of the latter curve is rescaled to 8.048 keV to permit comparison.

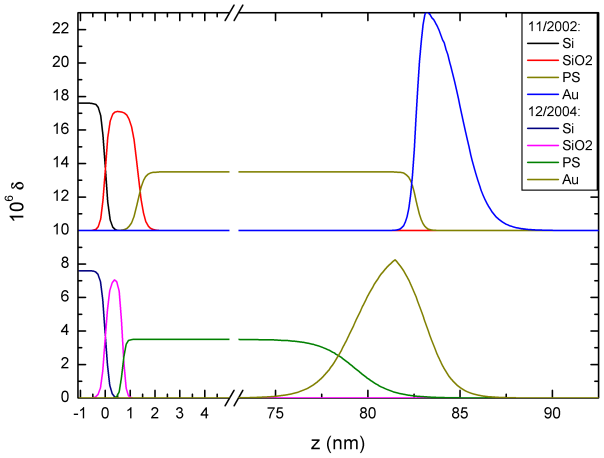

Figure 6.21.: Comparison of dispersion profiles (δ versus height z above the substrate) of the same Si-PS-Au sample calculated from reflectivity curves shown in figure 6.20. The profile of the 2002 scan (8.048 keV) is shifted by 10 for clarity. The 2004 scan was performed at 15 keV but δ values in this graph are rescaled to a photon energy of 8.048 keV to permit comparison. It can be seen that the δ peak caused by the Au layer changed significantly. Height of the peak decreased with increasing width while the overall peak area remained constant. Thus, the total amount of gold did not change but the gold clusters spread over a wider z region.

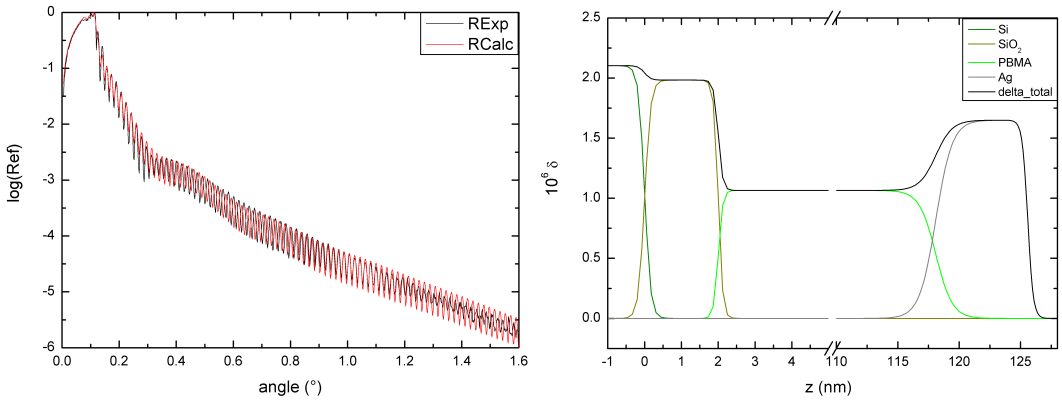

Figure 6.22.: Left: Reflectivity scan and fit for the Ag-PBMA-Si sample. Fitting parameters are given in table 6.9 and discussed in the text.
Right: Calculated δ profile of the sample versus height above the substrate. Materials are (from left to right) Si substrate, native SiO_2 layer, PBMA layer (disrupted for clearness of display), Ag layer. The total (summarized) delta value at each position is shown, too. Details are discussed in the text.

Silver clusters on a PBMA layer on silicon

As a third type of sample, silver clusters on a PBMA (poly(butyl-methacrylate), $[C_8H_{14}O_2]_n$) film on silicon were analyzed, that time with photon energy 15.2 keV. First, a reflectivity scan of the sample was performed. The scan and the corresponding best fit are shown in figure 6.22. Analoguely to the gold-polymer sample, a native oxide layer had to be inserted between the substrate and the PBMA layer during fitting procedure. Further, the silver layer is much thicker than its nominal value but at the same time the δ value of the layer is much lower than noted in literature [31, 59]. The product of dispersion and layer thickness $\delta \cdot d$ (that can be regarded as a measure for the total material amount) is the same in both cases. Apparently, again the metal is distributed on and inside the polymer film rather than forming a continuous layer. This results in a PMBA-Ag mixture layer with physical values between those of the pure materials. The sample structure is well illustrated by the δ profile shown in figure 6.22. Nominal values and experimental results of the measurement are compared in table 6.9.

Material	Value	Nominal/tabulated	XRR result	XSW result
Si	$10^6\delta$	2.103	2.103	2.103
	$10^6\beta$	0.0141	0.0141	0.0139
	σ (nm)	N/A	0.1500	N/A
SiO_2	$10^6\delta$	1.983	1.983	1.983
	$10^6\beta$	0.0074	0.0074	0.0074
	d (nm)	N/A	0.1088	N/A
	σ (nm)	N/A	2.00	3
PBMA	$10^6\delta$	2.1706	1.102	1.14
	$10^6\beta$	0.00120	0.00048	0.00046
	d (nm)	134	116.102	122
	σ (nm)	N/A	1.2175	N/A
Ag	$10^6\delta$	8.114	1.6494	8.115
	$10^6\beta$	0.2456	0.00036	0.2451
	d (nm)	1.5	7.482	2.06
	σ (nm)	N/A	0.4053	N/A

Table 6.9.: Nominal thickness values [145], tabulated δ, β values [31, 59] and measured parameters (dispersion δ, absorption β, thickness d and roughness σ) of the Ag-PBMA-SiO_2-Si sample. Explanations can be found in the text.

Additionally, an XSW scan was performed on the Ag-PBMA sample. The measured curve and best fit are shown in figure 6.23, sample parameters of the best fit are listed and compared to nominal values and XRR results in table 6.9

Comparison of XRR and XSW measurements points out some differences: Like in the Au-PS sample the nominal metal layer is modeled as a polymer-metal mixture region of larger thickness but lower dispersion value as the metal only in interpretation of the XRR scan. This is the result of the cluster-like distribution of Ag on and partly inside of the polymer film. XSW measurements on the other hand propose a homogeneous Ag layer. This is due to the fact that XSW is sensitive mainly to the total amount of marker material and less to its position if regarding the sub-nanometer range. Similar fits could be achieved with a thicker Ag layer with lower δ value as already outlined for the Au-PS sample. On the other hand, the XSW scan is still rather sensitive to the thickness of the PBMA layer because it strongly affects period and position of intensity maxima in the scan.

Furthermore, XRR and XSW scans give the same film thickness when silver and PBMA layer thicknesses are added for the reasons discussed before. Contrary to this, the nominal thickness of the PBMA film is about 10 nm thicker which suggests a mistake made in sample characterization or labeling after production. Finally, it is notable that the tabulated dispersion value for PBMA [31] ($\delta = 2.1706 \cdot 10^{-6}$) differs from the measured ones ($1.102 \cdot 10^{-6}$; $1.14 \cdot 10^{-6}$) almost by a factor of 2. This could be caused by the fact that physical parameters of unknown compounds are only extrapolated from known ones in [31] which can lead to errors if the molecule structure is not known and thus the material composition is approximated in a wrong way. Other sources give for example also deviating values for the mass density of PBMA: 1.053 g/cm^3 [116] vs. 2.2

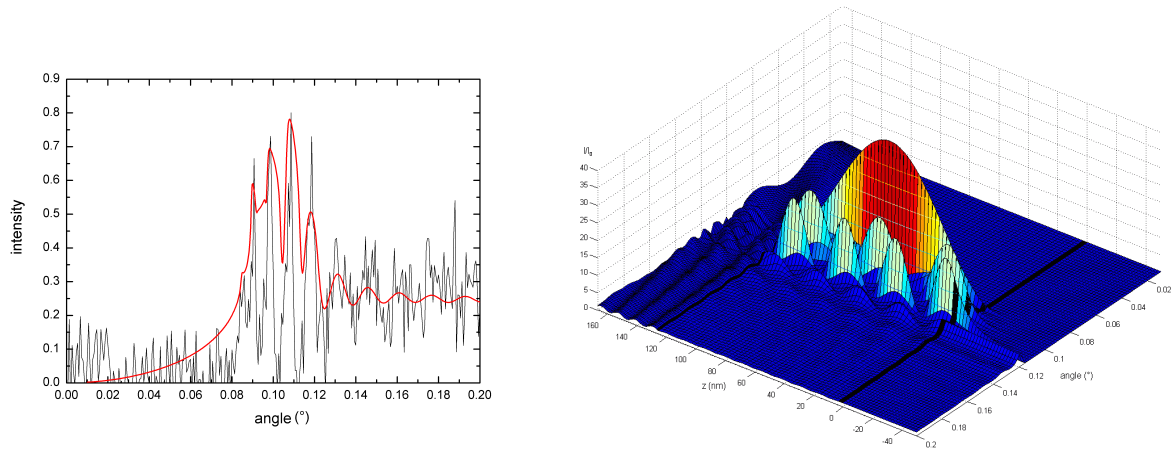

Figure 6.23.: Left: XSW scan and fit for the Ag-PBMA-Si sample. Fitting parameters are given in table 6.9 and discussed in the text.
Right: Calculated 3D XSW field inside and above the sample. Intensity is shown versus height (left axis) and angle of incidence (right axis) above the Si substrate.

g/cm^3 [31]. The doubled mass density used by [31] leads to a doubled dispersion δ following equations 5.8 and 5.6 as was experienced.

In summary, XSW and XRR are techniques suitable to characterize samples of unknown properties and even containing materials of which parameters are not yet tabulated or that occur in an uncommon state. Results of both methods confirm each other. Thus, a combination of XRR and XSW can be utilized to facilitate evaluation. Values in this chapter were achieved by iteratively improving fits in either method and implementing the outcome of one to improve the other. And finally they give a good cross-check for each other, especially when tabulated values might not be sure.

6.2.5. Dendrimers: Gold and DNA on PAMAM

Two equivalent samples (616 and 617) of a thin gold covered PAMAM film (cf. sample section 3.2.4) on a glass carrier were analyzed using XSW and XRR measurements at a photon energy of 15.2 keV. Figure 6.24 shows the detected fluorescence energy spectrum of PAMAM sample 617. It can be seen that gold fluorescence intensity is very low. Further, contributions from other elements present in the sample cell or set-up (Au, Fe, Cu, Zn and Pb) are equal to or higher than gold fluorescence.

Not the gold peak was selected as ROI but the Cu/Zn double peak (ROI1), the Pb peak (ROI2) and the whole energy region from Cu to Zn (including Au) as a summarizing ROI3. Fluorescence intensity in ROI1 (Cu/Zn) slowly decreased with increasing angle of incidence. This can be understood considering that the sample cell in this experiments was made of brass (i.e. Cu and Zn) and the beam reflected from the sample might have hit the cell. Contrarily, intensity in ROI2 (Pb) jumped up at the critical angle of SiO_2 and remained constant for higher angles. Traces of

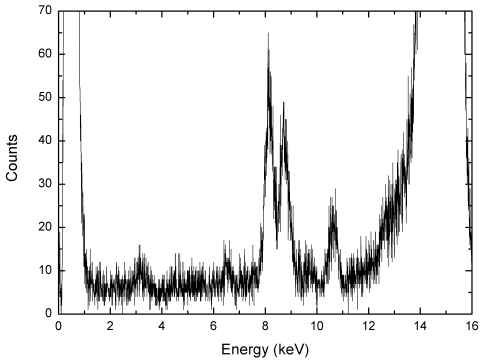

Figure 6.24.: Fluorescence energy spectrum for PAMAM sample 617. Peaks are (from left to right): Electronic noise ($\approx$ 0.52 keV), Ar (3.00 keV), Fe (6.40 keV), Cu (8.05 keV), Zn (8.64 keV), Au (9.71 keV), Pb (10.55 keV), elastic scattering peak (15.20 keV). All metal peaks but the gold peak are caused by components of the set-up making analysis of the sample difficult.

Pb were incorporated in the sample cell material but it was also present as a shielding material in various locations of the set-up.

For characterization of the PAMAM sample only gold fluorescence was of importance. Thus, intensity values from XSW scans of ROI1 and ROI2 were subtracted from XSW intensity of ROI3 to obtain a gold XSW scan. Comparison of this scan of sample 617 to calculations is shown in figure 6.25. Even though intensity is very low, a rough estimation of the sample structure can be made based on the calculated curve. The best fit was achieved for 2 nm Au on 1 nm PAMAM (due to unavailable data for PAMAM, δ and β values of C_8H_8 were applied here) on SiO_2.

Reflectivities recorded for both PAMAM samples are shown in figure 6.26 together with best fits obtained by *LsFit* [134, 135]. A sample structure of glass (SiO_2) as a substrate, a PAMAM film and a top layer modeled as a mixture of PAMAM and Au (i.e. δ and β values between those of PAMAM and Au) was assumed. Table 6.10 lists results of XSW and XRR measurements together with literature values. δ and β values for SiO_2 and PAMAM agree for both measurement techniques and literature values as well. No roughness was included in XSW calculations because signal quality was too bad to extract the rather small roughness effect in this method. On the other hand, it can be seen that *LsFit* gives roughness values for the PAMAM layer that are more than two times the thickness value. Thus, in this model there is no real layer but only a δ and β correction between substrate and top layer. Further, δ for the gold layer ($\approx 2 \cdot 10^6$) is significantly lower than the literature value ($13.198 \cdot 10^6$). This means that no continuous gold layer is present but a mixture of gold and PAMAM. On the other hand, XSW analysis delivers the nominal gold value. As explained in section 6.2.4, XSW scans are more sensitive to the total material amount than to the actual layer thickness. Thus, it is often hardly possible to distinguish between a thin compact gold layer and a thick amorphous layer with lower gold content. Consequently, the detected Au layer thickness by XSW is lower than that by XRR.

To compare those values, it is necessary to consider the geometry and arrangement of the

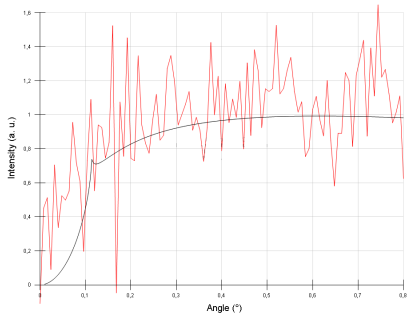

Figure 6.25.: XSW scan and fit for PAMAM sample 617. The signal is strongly noise affected, most probably to the low detected fluorescence intensity and only indirect measuring by subtraction of other scans. The best fit was achieved for 2 nm Au on 1 nm PAMAM on SiO_2.

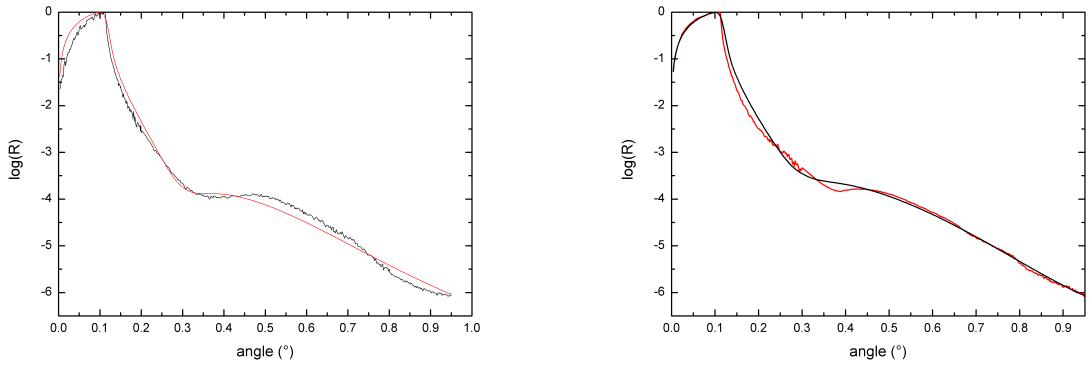

Figure 6.26.: XRR scans and fits by *LsFit* [134, 135] for PAMAM samples 616 and 617. The fits were performed for a SiO_2 substrate with a PAMAM layer covered by a PAMAM/Au mixture layer. Details can be found in the text and in table 6.10.

Layer	Parameter	Literature	XSW_{617}	XRR_{616}	XRR_{617}
SiO_2	$10^6\delta$	1.983	1.983	1.983	1.983
	$10^6\beta$	$7.4 \cdot 10^{-3}$	$7.4 \cdot 10^{-3}$	$7.4 \cdot 10^{-3}$	$7.4 \cdot 10^{-3}$
	σ (nm)	—	—	0.713	0.713
PAMAM	$10^6\delta$	1.073	1.073	1.073	1.073
	$10^6\beta$	$4.626 \cdot 10^{-4}$	$4.626 \cdot 10^{-4}$	$4.6 \cdot 10^{-4}$	$4.6 \cdot 10^{-4}$
	d (nm)	—	1	0.602	0.556
	σ (nm)	—	—	1.696	1.271
Au	$10^6\delta$	13.198	13.197	2.1824	1.8698
	$10^6\beta$	1.931	1.930	0.5067	0.4341
	d (nm)	—	2	2.613	2.657
	σ (nm)	—	—	2.005	1.522

Table 6.10.: Literature values [31, 59], XSW (cf. figure 6.25) and XRR (cf. figure 6.26) results for PAMAM-Au samples 616 and 617. Due to missing data for PAMAM, corresponding δ and β values of C_8H_8 were applied. d and σ denominate thickness and roughness (i.e. transition region between two neighboring layers) of the respective layers. Discussion of results can be found in the text.

rather huge gold clusters (nominal diameter $2r_{\mathrm{Cluster}} \approx 25$ nm) on the sample. Assuming that XSW measurements are sensitive to the total amount of gold, a nominal gold layer thickness $d_{\mathrm{n,Au}}$ of approximately 2 nm has to be estimated. 25 nm thick clusters and holes in between lead to an averaged "thickness" of 2 nm. On the other hand, reflectivity scans are more sensitive to the surface coverage f, i.e. the percentage of surface that is covered by gold. The relation between f, r_{Cluster} and $d_{\mathrm{n,Au}}$ was analyzed in [81] and can be described by

$$f = \frac{3d_{\mathrm{n,Au}}}{4r_{\mathrm{Cluster}}}. \tag{6.3}$$

With experimental results from the XSW scan a coverage of 12 percent can be calculated. With this factor for gold and correspondingly 88 percent for PAMAM a weighted dispersion factor of $\delta = 2.528 \cdot 10^{-6}$ can be calculated compared to an average XRR result of $\delta = 2.0261 \cdot 10^{-6}$.

Summarizing, it can be stated that XRR and XSW scans can give a rough estimation and show mostly agreeing results for the layer structure of the PAMAM gold samples. Due to the low gold content in the sample, Au fluorescence intensity is only slightly higher than background noise and thus the XSW measurement at its lower limit of quantitation. On the other hand, interpretation of the XRR measurement is difficult due to the lack of an appropriate model sample system. Thus, quantitative results have to be regarded with large error bars. However, both methods concordantly show that gold is probably located about 1-3 nm above the substrate on a thin PAMAM film and also surrounded by PAMAM. Gold was intended to be deposited on the PAMAM film but apparently partly diffused inside that film if the thickness of a single PAMAM molecule ($\approx$ 4.5 nm, cf. section 3.2.4) is considered. Further, an estimation of dimensions of the PAMAM film could be made suggesting that PAMAM forms a monolayer. To obtain more accurate results, a more detailed sample structure needs to be applied in calculation which was

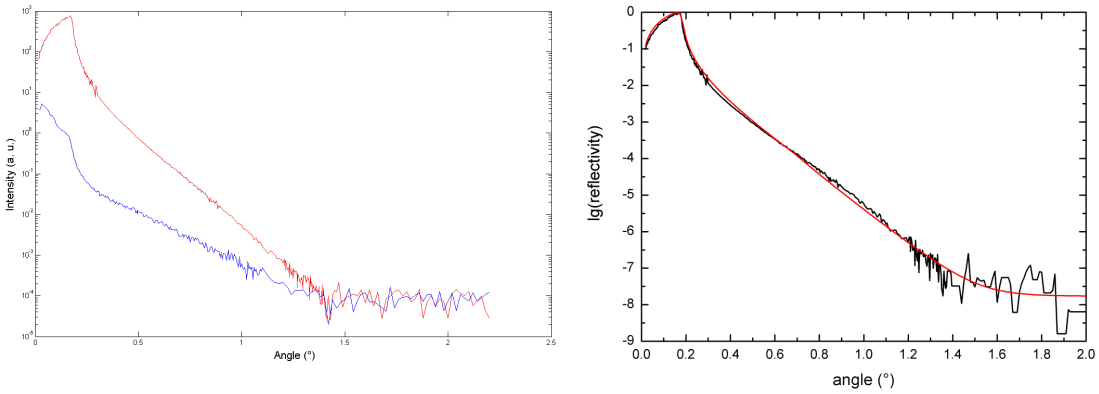

Figure 6.27.: Reflectivity scan of the pure Si substrate.
Left: Reflectivity for specular condition (upper curve) and longitudinal diffuse scattering (lower curve).
Right: Difference between the two curves and best fit.

difficult here due to the limited data available for these samples.

6.2.6. Nitrobenzene: Thin films and nitrobenzene-gold samples

Several nitrobenzene (NB) layer samples were analyzed by XRR and XSW measurements. Pure NB films on Si were characterized at 10.05 keV. NB films on Si onto that gold was sputtered were analyzed using photons of 15.20 keV. A reflectivity scan (angle of incidence α_i = exit angle α_f) followed by a longitudinal-diffuse scan (with the detector shifted by 0.1°: $\alpha_\mathrm{f} = \alpha_\mathrm{i} + 0.1°$ to measure diffuse scattering) were performed on each sample. The intensity of the longitudinal-diffuse (LD) scan was then subtracted from the reflectivity scan according to the scattering vector (wave vector transfer) by converting the angles of both scans into q-values as explained in section 4.2.1. Calculations lead to the curves discussed in the following.

Pure silicon wafer

Figure 6.27 shows a reflectivity and LD scan of a reference sample of pure Si. Comparing them to the theoretical Fresnel reflectivity of a smooth silicon wafer as shown in figure 2.2, several differences attract attention. The decreasing intensity below the critical angle of refraction appears because the beam footprint is larger than the sample as already discussed in chapter 4.2.1. The slight modulation of the measured curve around 0.3° and 0.9° is probably caused by the existence of a thin native oxide layer on the silicon substrate. Finally, intensity levels off for angles above $\approx 1.5°$ when intensity of the reflected beam becomes lower than the background noise of the set-up and detector.

Modeling the sample using the program *LsFit* [134, 135] to create the best agreement between calculation and measurement leads to the curves shown in figure 6.27. This fit was achieved for a silicon substrate with roughness 1.41 nm. Introducing a thin SiO_2 layer above the silicon due to oxidation at ambient air might improve the fit. However, this sample was analyzed as a basis

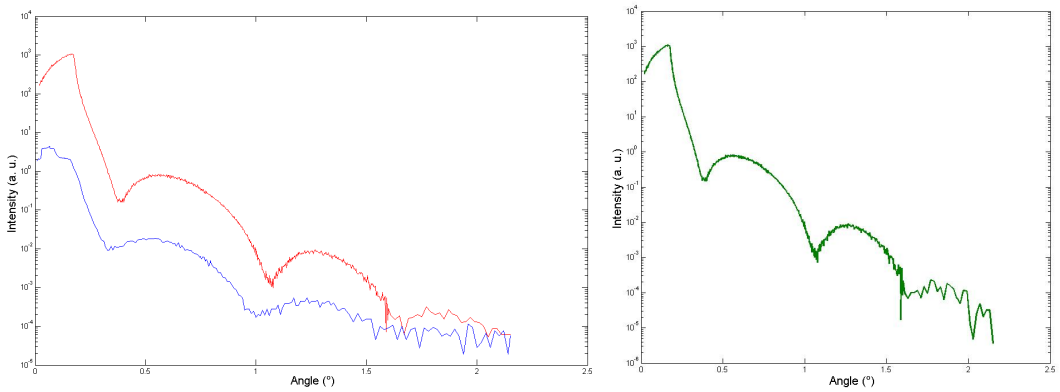

Figure 6.28.: Reflectivity scan of a nitrobenzene film on a Si substrate.
Left: Reflectivity at specular condition (upper curve) and at longitudinal diffuse scattering (lower curve).
Right: Difference between the two curves.

for nitrobenzene films on Si described below. In contrary to the pure Si wafer, the substrates for nitrobenzene we not exposed to air to prevent this oxide layer between Si and nitrobenzene. Thus, only the parameters of the pure Si wafer are of importance.

Nitrobenzene on silicon

The second sample to be analyzed was a thin nitrobenzene film on a Si substrate. As electrochemical deposition of nitrobenzene was performed directly after H-passivating the substrate surface, no oxide layer is expected [124]. The reflectivity scan in figure 6.28 shows typical Kiessig fringes [71] as discussed in chapter 2.1.3. It has to be pointed out that both the reflectivity and the longitudinal-diffuse scattering curve have the same oscillatory form. This happens if a "conform roughness" exists. This means, the roughness or bumps on the wafer surface are reproduced on the NB surface which only occurs for a well defined, ordered layer.

Based on results from the pure Si wafer discussed above analysis was performed using *LsFit* [134, 135]. The fit required thickness and roughness of the nitrobenzene film to be varied in a rather wide range as not much was known about the NB layer. Furthermore, dispersion and absorption constants δ and β of nitrobenzene do not need to be equal to tabulated values because they are highly dependent on the order and packaging of the molecules in the sample. Figure 6.29 shows the best fit obtained for the measurement and the corresponding dispersion profile. The resulting sample parameters are listed in table 6.11. Between Si substrate and nitrobenzene layer *LsFit* inserts a thin "layer" with roughness much bigger than its thickness. This is necessary to achieve a good fit and can be understood as a transition region rather than a real layer. Nominal dispersion δ of this transition layer is between the values of the substrate and the nitrobenzene layer. This comparatively high electron density might be caused by forming of surface dipoles during electrochemical deposition of NB [56, 124]. Further, it has to be pointed out that δ for NB ($2.053 \cdot 10^{-6}$) differs notably from the tabulated value ($4.714 \cdot 10^{-6}$ [31]) and is in the range of δ for water ($2.290 \cdot 10^{-6}$). Thus, it is not clear if a nitrobenzene or water layer is present

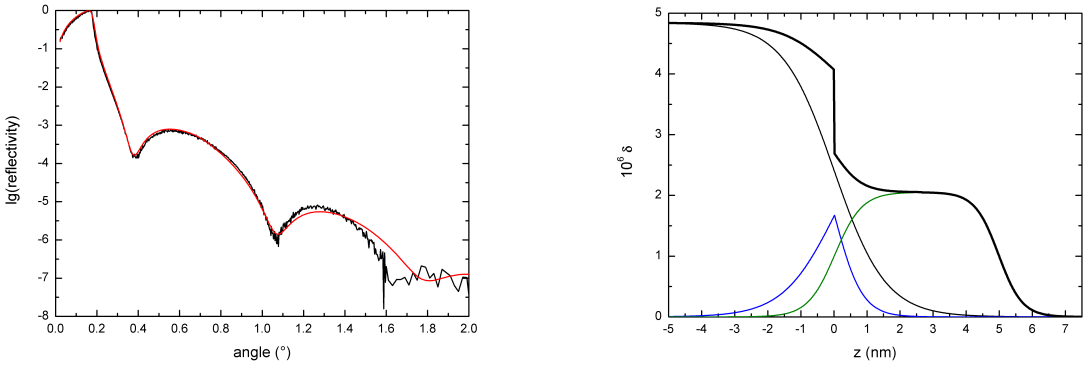

Figure 6.29.: Left: Best fit of the reflectivity scan of the nitrobenzene film on Si.
Right: Dispersion profile obtained from the reflectivity of the NB film on Si. Between Si substrate and nitrobenzene layer *LsFit* inserts a thin transition "layer".

Layer	$10^6\delta$	Thickness (nm)	Roughness (nm)
Silicon wafer	4.840	–	1.41
Transition layer	3.306	0.03	0.74
Nitrobenzene	2.053	4.95	0.65

Table 6.11.: Sample parameters of a thin nitrobenzene film on silicon. Between Si substrate and nitrobenzene layer, a thin "layer" of large roughness (more than "thickness") is inserted to improve the fit. Explanations can be found in the text.

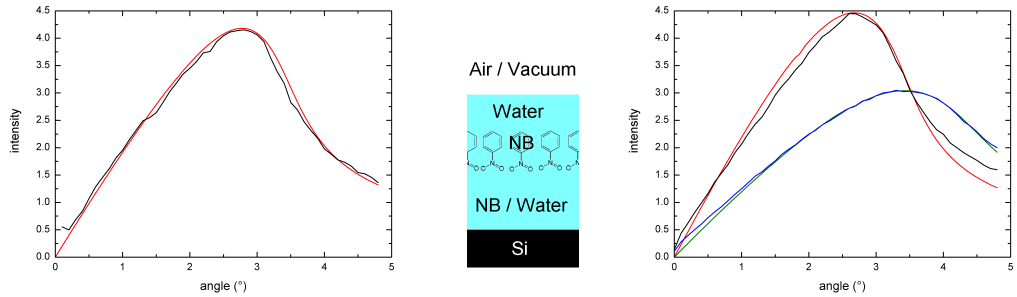

Figure 6.30.: Soft X-ray XSW measurements and best fits of nitrobenzene on silicon.
Left: XSW measurement and fit of N located 3.0 nm above the substrate at 510 eV.
Right: XSW measurements and fits of C located 3.6 nm above the substrate at 510 eV (upper curves) and 396 eV (lower curves).
Center: Corresponding orientation of the nitrobenzene molecules in a 5 nm water film above the silicon substrate.

on the Si substrate. Probably, a mixture of nitrobenzene from deposition and water from air are present. Assuming the presence of nitrobenzene and considering a molecule size for NB of about 0.7 nm, there are probably several layers (not only one monolayer) on the substrate, maybe not very closely packed but rather loosely causing the lower (average) electron density. This is consistent with ellipsometry measurements of the samples performed at ISAS Berlin [124] that showed a significant difference of nitrobenzene dispersion δ between liquid NB and a NB film on a substrate.

To improve characterization of nitrobenzene films on silicon also measurements with soft X-rays were performed at the plane-grating monochromator (PGM) beamline for undulator radiation [136, 130] at the Physikalisch-Technische Bundesanstalt (PTB) [119] laboratory at BESSY II [14], Berlin. The UHV experimental set-up of the PTB [9] has some similarities to the one at DELTA beamline BL9 described in chapter 4.1.3. The sample was investigated under vacuum conditions and different photon energies were selected using a plane-grating monochromator (PGM).

Evaluation of the measured data was based on XRF spectra deconvolution techniques employing experimentally determined detector response functions embedded in a completely reference-free fundamental parameter XRF quantitation [8, 79, 101]. Both, measurements and deconvolution were performed by Beatrix Pollakowski, PTB Berlin [119].

For simulation of the XSW field, a sample system of 5 nm water on a silicon substrate (as acquired by XRR scans discussed above) was assumed for each measurement, and marker positions were varied to achieve the best fit. Figure 6.30 shows XSW scans and fits performed at 510 eV (exciting N and C fluorescence) and 396 eV (only exciting C fluorescence). Best accordance was achieved for N located approximately 3.0 nm and for C about 3.6 nm above the substrate. Scans for both photon energies delivered consistent results concerning the distance of the atom from the reflecting substrate as well as the spacing between C and N. The latter corresponds to the size

Excitation energy (eV)	Element	Peak position (°)
396	C	3.40
510	C	2.65
510	N	2.80
684	C	2.10
684	N	2.20
684	O	2.30

Table 6.12.: Fluorescence peak positions for light elements in nitrobenzene at different excitation energies.

of a nitrobenzene molecule ($\approx$ 0.6 nm) as can be seen in figure 3.14. Thus, these measurements suggest the nitrobenzene to be in a monolayer located inside a thin water (or similar material) film and oriented with its NO_2 group pointing towards the substrate as illustrated in figure 6.30.

Evaluating fluorescence peak positions of the above discussed XSW scans and three additional scans performed at a photon energy of 684 eV for three elements (C, N and O) leads to the values given in table 6.12. It is obvious that the angle position of the peaks for each energy increases in the sequence C - N - O. Considering the angle dependence of antinode positions in an XSW field calculated in chapter 2.3 this means that the O atoms[3] are closest to the substrate and the C atoms the farthest. This corresponds to a molecule orientation shown in figure 6.30, too. Further, the small angle difference suggests small distances between the atoms like in a molecule. Thus, evaluating fluorescence peak positions gives results consistent with XSW scan fits discussed before.

Contrarily to this orientation, nitrobenzene is expected to bond to the silicon substrate by its benzene ring and its NO_2 directed upwards [56, 121]. This applies for the first monolayer, further nitrobenzene layers are not expected to be oriented [124]. The reason for the ordered layer with inverted orientation that was detected by XSW measurements is not yet understood. Explanations could be a thick nitrobenzene or water layer (as also detected by XRR and XSW measurements with hard X-rays) that could give the uppermost layer a defined position. Further, at low angles the XSW maxima might only scan the uppermost nitrobenzene layer. Disordered NB layers below could give a constant fluorescence signal without significant structure. Hence, further investigations of this sample system are necessary.

Gold on nitrobenzene on silicon

The third sample that was analyzed is again more complex. Gold was sputtered onto the NB layer. Two possibilities of layer composition had to be taken into account: The gold atoms either remained on top of the layer or penetrated into the nitrobenzene. Figure 6.31 shows that the reflectivity scan (performed at 15.20 keV) can be best fitted by the theoretical curve for a gold layer on the NB film. The corresponding layer parameters are listed in table 6.13. It can be

[3] As this sample was stored in air before deposition of nitrobenzene an oxide layer of up to 3 nm thickness might have formed on the Si surface [124]. For this reason, fluorescence intensity from O atoms has to be regarded carefully.

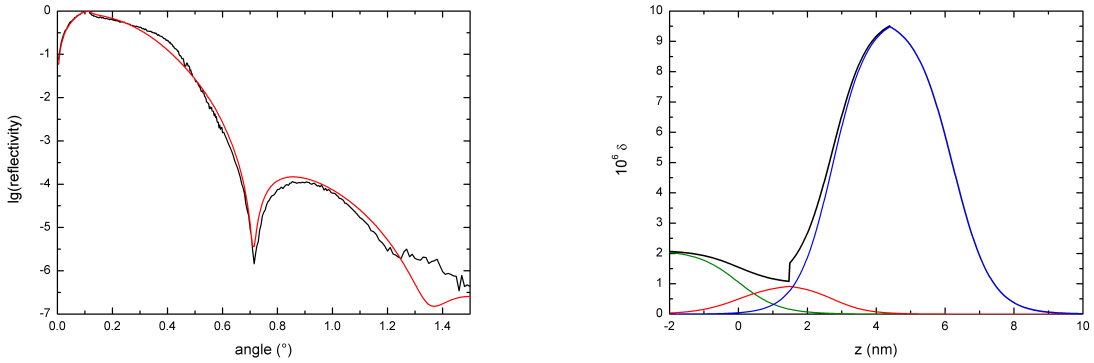

Figure 6.31.: Reflectivity scan and fit for the nitrobenzene film on silicon with gold (left) performed at 15.20 keV and δ-profile obtained from the reflectivity fit (right). Explanations can be found in the text.

Layer	$10^6\delta$	$10^6\beta$	Thickness (nm)	Roughness (nm)
Si wafer	2.103	0.0141	–	1.08
NB	0.990	0.00093	2.73	0.91
Au	9.832	1.438	3.49	1.00

Table 6.13.: Parameters of the fit for the reflectivity scan of NB on Si with Au. Explanations in the text.

seen that δ and β for the gold layer are lower than literature values ($\delta_{\mathrm{Au}} = 13.198 \cdot 10^6$, $\beta_{\mathrm{Au}} = 1.931 \cdot 10^6$). Obviously, gold did not form a continuous layer but rather kind of particles or clusters leading to a lower averaged electron density. Thus, the upper film could be considered as a mixture of Au and NB like in the samples discussed in the previous chapters. Further, the optical constants for NB are almost equal to literature values for water ($\delta_{\mathrm{Water}} = 0.999 \cdot 10^6$, $\beta_{\mathrm{Water}} = 0.0009 \cdot 10^6$) like in the pure nitrobenzene films. Thus, again a thin water layer or a less dense nitrobenzene film with water-like properties could be assumed.

Finally, characterization of the sample using an X-ray standing waves scan was performed. The scan and best fit are shown in figure 6.32. Fit parameters are listed in table 6.14. The best fit is not achieved for a homogeneous gold layer but a gold distribution with Au concentration decreasing exponentially with depth. This illustrates that gold forms a layer on top of the nitrobenzene film with some gold atoms penetrating this film. Even though the fit and measurement curve deviate for higher angles, there is agreement for small angles. Further, optical constants

Layer	$10^6\delta$	$10^6\delta$	Thickness (nm)
Si wafer	2.10	0.0139	–
NB	0.99	0.00094	3.0
Au	13.20	1.930	2.2

Table 6.14.: Sample parameters of gold on a thin NB film on Si scanned with XSW.

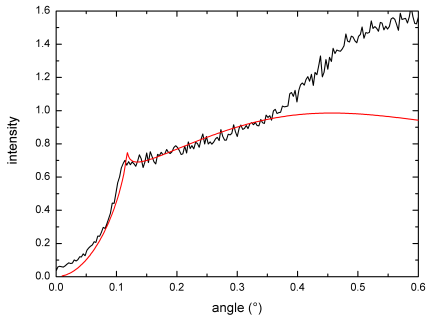

Figure 6.32.: XSW scan and fit of the nitrobenzene film on Si with Au. The sample system was modeled as Au on a water film (representing NB) on a Si substrate. The intensity increase for high angles in the measurement might be caused by some background signal not considered in calculation.

and layer thicknesses obtained by XRR and XSW are consistent considering differences in interpretation of XSW and XRR results already discussed in sections 6.2.4 and 6.2.5 for the gold on polymer and gold on PAMAM samples. XSW measurements deliver the nominal layer thickness and bulk δ, β values (being sensitive to the total amount of gold on the surface). Contrarily, XRR analysis leads to δ, β values averaged for a mixed layer of gold and nitrobenzene. Even though little information about the sample system was available before, characterization of gold on nitrobenzene layers by XRR and XSW could provide - in certain limits - various qualitative and quantitative results.

6.3. Further samples

6.3.1. Periodic multilayers: Laser mirror

A commercially available multilayer (approximately 24 layers) laser mirror *(Spectra-Physics, Mountain View, USA)* was analyzed using TXRF at 17.48 keV (Mo Kα_1 fluorescence) and XSW at 13.00 keV. TXRF showed Ti content in the mirror. However, light elements such as C, Li, Si or Mg which were possibly incorporated in different layers were not accessible by this technique. In XSW measurement (cf. figure 6.33) again only the Ti signal could be detected. However, together with the angle information - that is complementary to the element information obtained with TXRF - other materials can be characterized indirectly as shown in the following.

Fitting of the measurement shown in figure 6.33 with the XSW simulation program turned out to be too complicate because the layout of the sample (i.e. materials and number of layers) was not known. To extract information from the strongly noise-affected measurement, a computer program was developed to calculate periodicities in the signal using Fast Fourier Transform (FFT) algorithms [30, 39, 48, 112, 120]. Transforming the frequencies of interest back to the angle space leads to an oscillation wavelength spectrum shown in figure 6.33. From these angular periods and the wavelength of the synchrotron radiation used, the typical (multi)layer thicknesses

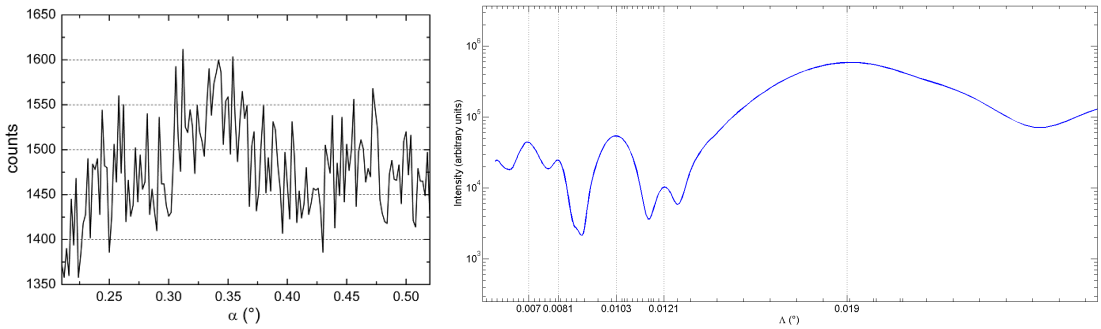

Figure 6.33.: XSW scan of a multilayer laser mirror, scanning the Ti fluorescence signal (left) and Oscillation wavelength spectrum obtained from FFT of that scan (right).

No. TiO_2	No. 2nd mat.	$d_{\mathrm{calc,ges}}$ (nm) MgO	$d_{\mathrm{calc,ges}}$ (nm) SiO_2	$d_{\mathrm{calc,ges}}$ (nm) quartz glass	$d_{\mathrm{calc,ges}}$ (nm) LiF	$d_{\mathrm{exp,ges}}$ (nm) scan
0	1	81.9	92.1	97.5	102.2	N/A
1	1	134.7	144.8	150.2	155.0	143.8
1	2	216.6	236.9	247.7	257.2	225.8
2	2	269.3	289.7	300.5	310.0	265.3
2	3	351.2	381.7	398.0	412.2	337.3
3	3	404.0	434.5	450.7	465.0	390.3
3	4	485.9	526.6	548.2	567.2	477.3

Table 6.15.: Calculated and measured layer thicknesses inside a multilayer laser mirror of alternating layers of TiO_2 and a second material (MgO, SiO_2 or LiF).

$d_{\mathrm{exp,ges}}$ listed in the last column of table 6.15 can be deduced. To obtain qualitative and quantitative information about the mirror, a sample structure had to be assumed. Typically, a laser mirror consists of several double layers of two materials. As TXRF measurements detected Ti in the sample, titanium dioxide (TiO_2) was taken as one component, the second one had to be a light element or compound, for example MgO, SiO_2 or LiF. Furthermore, each layer thickness had to be 1/4 of the central laser wavelength (i.e. 570 nm) the mirror was used for divided by the known index of refraction n of the respective compound.

Table 6.15 lists the added thickness values of a periodic stack of alternating TiO_2 (52.8 nm) plus MgO (81.9 nm), SiO_2 (92.1 nm), quartz glass (97.5) or LiF (102.2 nm). These values are the summarized thicknesses of the sample region that a beam passes through if it is reflected at the first, second to the seventh interface. The very first layer is not visible because its small thickness corresponds to a long oscillation wavelength located inside the very broad maximum beyond the large angle limit in figure 6.33. The ratio of measured and calculated thicknesses for different materials is illustrated in figure 6.34. It can be seen that theoretical and experimental values agree very well (only) if, in addition to TiO_2, MgO is assumed as a second component. Thus, XSW method has proven to be capable of determining composition and thicknesses of an unknown multilayer sample in just a single scan.

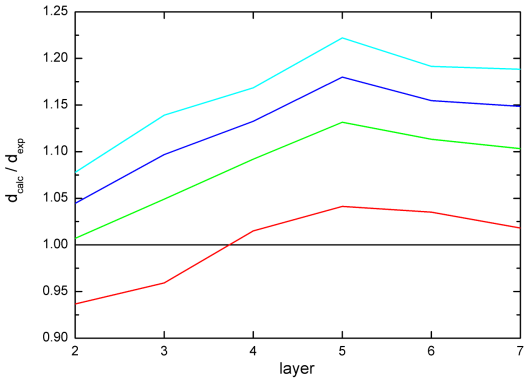

Figure 6.34.: Ratio of calculated and measured total layer thickness in the multilayer laser mirror for different layer materials together with TiO_2. Curves are (from top to bottom) for LiF (cyan), quartz glass (blue), SiO_2 (green), MgO (red) and measured thickness (black). The best accordance is found for MgO.

7. Summary and Outlook

It has been shown for various types of samples that X-ray standing waves at grazing incidence are a versatile and powerful tool to analyze layered structures on a nanometer scale, both concerning distances/layer thicknesses and element determination and distribution. As preconditions for these kinds of analysis (basically a a flat, smooth surface or interface and any kind of marker atoms incorporated in the sample) are often easy to fulfill liquids and solids, non-conducting and conducting, monolayer and periodic multilayer, homogeneous and inhomogeneous could be investigated.

Not being a standard measurement technique little evaluation software was available for grazing incidence X-ray standing waves scans. Hence, a complex computer program was developed during this work that can calculate the XSW intensity distribution for a wide variety of samples, is easy to handle even for non-specialists and provides the possibility for nearly unlimited upgrades for handling special sample systems such as liquid/solid interfaces.

Furthermore, the high potential of a combination of X-ray standing waves and X-ray reflectivity scans has been proven. Experimental implementation is simple as both techniques require a very similar set-up. Evaluation could be performed much more effective by improving XSW and XRR fits in an iterative way. On one hand, XRR scans are more sensitive in thickness and roughness determination. On the other hand, XSW measurements are very accurate in measuring elemental concentrations and material amounts. Further, the element sensitivity of XSW is very useful to analyze samples of low contrast in electron density and to scan several elements simultaneously.

Germanium layer thicknesses on a silicon substrate could be measured in a range below 100 nm. Increasing thickness of the layer corrupted the signal more and more. However, as has been shown, the accessible thickness range can be expanded by moving to longer wavelengths. Further, concentration and a non-homogeneous distribution of implanted ions in silicon wafers could be measured in certain limits.

Only few methods are sensitive to low contrast interfaces especially in biological samples that are of increasing importance in life science. As has been shown, the combination of XSW and XRR can deliver - with limitations depending on the sample type - qualitative and even quantitative information about element composition, concentration and orientation of biological compounds using marker elements already incorporated in the materials under investigation. Analysis of cytochrome and dendrimer-gold layers on a glass substrate turned out to be difficult mainly due to problems in demobilizing sufficient amounts of the material of interest (and thus enough marker atoms to obtain a strong fluorescence signal) and sparse information available for calculating a model system. On the other hand, an ordered bilayer of phospholipid could be characterized both by phosphorus atoms incorporated in the lipid as well as chlorine and potassium ions in the buffer solution above the bilayer. Here, the possibility to scan several

elements simultaneously delivered much information in short measuring time. Additionally, the expected laterally varying concentration of ions in the buffer solution could be analyzed using marker distribution features of the developed computer program.

As a model for technologically relevant metal-organic compounds samples of gold or silver clusters on a polymer film were characterized qualitatively and quantitatively. Incorporating heavy marker atoms, a weakly absorbing matrix and dimensions in the nm range, XSW measurements appear to be ideal for this kind of sample. Further, various ultrathin nitrobenzene films of silicon were investigated using several set-ups and photon energies in XRR and XSW measurements. Results were in contradiction with previous expectations but consistent in the different scans. Thus, new aspects and new questions concerning this kind of sample have emerged demanding further investigations.

Finally, a complicated and previously unknown periodic multilayer structure - in this case a laser mirror - could be analyzed qualitatively and quantitatively. Combined with a Fast Fourier transform algorithm and general information about laser multilayer mirrors, the advantages of XSW (element sensitivity, periodicity and nm resolution) could be exploited to obtain composition and dimensions of this sample.

Limits of XSW methods have become visible during this work, too. Very thick layers or strongly scattering materials (like buffer solutions in biological samples) can cause problems. A marker of sufficient concentration positioned at a characteristic location in the sample is essential for XSW measurements especially if background noise or contributions from other components of the sample or set-up are large. Some restrictions might be reduced by changing experimental parameters like the wavelength, photon flux, measurement time or by sample preparation. Further, generating a theoretical curve fitting to the measurements gets increasingly difficult with the number of unknown parameters. On the other hand, well known system structures can be analyzed quickly, easily and accurately if only one or few parameters have to be adjusted. Due to the need for high photon fluxes and the tunability of the energy, XSW is a typical synchrotron technique. Nonetheless, XSW has been proven to be a versatile technique which can be employed in a wide variety of problems which otherwise are difficult to tackle. Especially in the field of biological samples XSW promises new approaches and results based on basic research performed in this work.

A. List of Acronyms

AES	Auger electron spectroscopy
AFM	Atomic force microscope
APS	Advanced Photon Source, Argonne, USA
ASCII	American Standard Code for Information Interchange
BESSY	Berliner Elektronenspeicherring-Gesellschaft für Synchrotronstrahlung, Berlin, Germany
BL	Beamline
CXRO	Center for X-ray Optics, Lawrence Berkeley National Laboratory, Berkeley, USA
Da	Dalton = atomic mass unit (u)
DELTA	Dortmunder Elektronen Speicherring Anlage, Dortmund, Germany
DNA	Desoxyribose nucleic acid
DOPC	1,2-Dioleoyl-*sn*-glycero-3-phosphocholine
EDX	Energy-dispersive X-ray (analysis)
ESRF	European Synchrotron Radiation Facility, Grenoble, France
eV	Electronvolt (1 eV = $1.602177 \cdot 10^{-19}$ J)
FEL	Free electron laser
FFT	Fast Fourier Transform
FZK	Forschungszentrum Karlsruhe, Karlsruhe, Germany
GA	Glutaric acid anhydride
GD	Glow discharge
GI	Grazing incidence
h, hex	Hexadecimal number system
HMI	Hahn-Meitner Institute
Im	Imaginary part of a complex number
ISAS	Institute for Analytical Sciences, Dortmund and Berlin, Germany
IUPAC	International Union of Pure and Applied Chemistry

Table A.1.: List of acronyms appearing in this work (I)

keV	Kiloelectronvolt (1000 eV)
LD	Longitudinal-diffuse
MCA	Multi channel analyzer
MXSW	Mighty X-ray Standing Waves (simulation program)
NB	Nitrobenzene
NI	Normal incidence
NMR	Nuclear magnetic resonance
NSLS	National Synchrotron Light Source, Brookhaven, USA
OES/MS	Optical emission spectroscopy/mass spectrometry
PAMAM	Ethylenediamine-core poly(amidoamine)
PBMA	Poly(butyl-methacrylate)
PGM	Plane grating monochromator
POPC	1-Palmitoyl-2-oleoyl-*sn*-glycero-3-phosphocholine
PS	Polystyrene
PTB	Physikalisch Technische Bundesanstalt, Berlin and Braunschweig, Germany
PTFE	Polytetrafluoroethylene, Teflon
RBS	Rutherford backscattering
Re	Real part of a complex number
ROI	Region of interest (e.g. selected detector/MCA channels)
rms	Root mean square (roughness)
SAXS	Small angle X-ray scattering
SAW	Superconducting asymmetric wiggler
SIMS	Secondary ion mass spectroscopy
SNMS	Secondary neutral mass spectroscopy
SPB	Solid supported phospholipid bilayer
SRS	Synchrotron Radiation Source, Daresbury, UK
TEM	Transmission electron microscope
TXRF	Total reflection X-ray fluorescence (analysis)
UHV	Ultra high vacuum
XPCS	X-ray photon correlation spectroscopy
XPS	X-ray photoelectron spectroscopy
XRF	X-ray fluorescence (analysis)
XRR	X-ray reflectivity (measurement)
XSW	X-ray standing waves (analysis)

Table A.2.: List of acronyms appearing in this work (I)

B. Physical and Optical Constants

B.1. Physical constants

α	$7.297353 \cdot 10^{-3}$	fine-structure constant
c_0	299 792 458 m/s	speed of light in vacuum
Da	$1.6605 \cdot 10^{-27}$ kg = 931.49 MeV/c^2 = u	Dalton = atomic mass unit u
e_0	$1.602177 \cdot 10^{-19}$ C	elementary charge
ε_0	$8.854188 \cdot 10^{-12}$ F/m	permittivity of vacuum/
	= $1/(\mu_0 c^2)$	electric constant
F	96485.3383 C/mol	Faraday constant
h	$6.626069 \cdot 10^{-34}$ J s = $4.135666 \cdot 10^{-15}$ eV	Planck's constant
$\hbar$	= $h/2\pi$ = $1.05457 \cdot 10^{-34}$ J s = $6.582117 \cdot 10^{-16}$ eV	Planck's constant
k	$1.38066 \cdot 10^{-23}$ J/K	Boltzmann constant
m_e	$9.1093826 \cdot 10^{-31}$ kg = 0.511 MeV/c^2	electron mass
μ_0	$4\pi \cdot 10^{-7}$ N/A^2 = $1.256637 \cdot 10^{-6}$ N/A^2	permeability of vacuum/
	= $1/(\varepsilon_0 c^2)$	magnetic constant
N_A	N_A = $6.0221415 \cdot 10^{23}$ 1/mol	Avogadro's number
R_∞	$1.097373156 \cdot 10^{7}$ 1/m	Rydberg constant
	= $\alpha^2 m_\mathrm{e} c_0 / 2h$	
u	u = $1.6605 \cdot 10^{-27}$ kg = 931.49 MeV/c^2 = $\frac{1}{12} m_\mathrm{C}$	atomic mass unit

Table B.1.: List of physical constants used in this work. Values taken from [99, 109, 118, 144, 157].

B.2. Optical constants of various materials

Material	ρ (g/cm^3)	E (eV)	λ (Å)	$10^6\delta$	$10^6\beta$	δ/β	α_c (°)
Silver (Ag)	1.19	15200	0.816	8.115	0.2456	33.039	0.231
Arsenic (As)	5.73	15200	0.816	4.491	0.3626	12.384	0.172
Gold (Au)	19.32	15000	0.827	13.480	2.0217	6.667	0.297
		15200	0.816	13.198	1.9306	6.836	0.294
Cobalt (Co)	8.9	15200	0.816	7.422	0.3368	22.034	0.221
Copper (Cu)	8.96	15000	0.827	7.612	0.4384	17.364	0.224
Iron (Fe)	7.874	13000	0.954	9.120	0.5012	18.197	0.245
Germanium (Ge)	5.323	15200	0.816	4.204	0.3114	13.498	0.166
Potassium (K)	0.862	13000	0.954	1.045	0.0253	41.376	0.083
Magnesium (Mg)	1.738	13000	0.954	2.123	0.0124	171.919	0.118
Phosphorus (P)	2.2	13000	0.954	2.646	0.0304	86.954	0.132
Selenium (Se)	4.5	15000	0.827	3.499	0.3115	11.233	0.152
Silicon (Si)	2.33	10050	1.234	4.840	0.0724	66.889	0.178
		13000	0.954	2.880	0.0262	109.979	0.138
		15000	0.827	2.159	0.0149	145.304	0.119
		15200	0.816	2.103	0.0141	149.104	0.117
Titanium (Ti)	4.54	13000	0.954	5.215	0.1842	28.305	0.185
Zinc (Zn)	7.133	13000	0.954	8.003	0.6524	12.266	0.229
		15200	0.816	5.919	0.3663	16.159	0.197

Table B.2.: Density ρ, dispersion δ and absorption β of elements used in this work at different photon energies utilized at DELTA [31, 59, 164]. Additionally the ratio δ/β (that is needed in the *LsFit* program [135]) and the critical angle of total reflection $\alpha_c \approx \sqrt{2\delta}$ (eq. 2.18) are listed.

Material	ρ (g/cm^3)	E (eV)	λ (Å)	$10^6\delta$	$10^6\beta$	δ/β	α_c (°)
Air[1]	1.25E-3	10050	1.234	2.575E-3	5.840E-6	441.014	0.004
		13000	0.954	1.537E-3	2.078E-6	739.791	0.003
		15000	0.827	1.154E-3	1.187E-6	972.011	0.003
		15200	0.816	1.124E-3	1.128E-6	996.107	0.003
Cytochrome [7] (C,H,O,Fe)	1.11	13000	0.954	1.468	8.106E-4	1810.64	0.098
Magn.oxide (MgO)	3.58	13000	0.954	4.388	0.0181	242.771	0.170
Mica[2]	2.83	13000	0.954	3.478	0.0225	154.802	0.151
Nitrobenzene[3]	2.2	10050	1.234	4.714	0.0068	696.249	0.176
($C_6H_5NO_2$)		15200	0.816	2.058	0.0013	1542.651	0.116
PAMAM[7] ($C_xH_yO_z$)	1.1	15200	0.816	1.073	4.626E-4	2320.26	0.084
PBMA[4]	2.2	15200	0.816	2.171	0.0012	1808.83	0.119
($C_8H_{14}O_2$)	1.053	15200	0.816	1.1	0.0005	2200	0.086
Phospholipid[5,7]	1.11	13000	0.954	1.468	8.106E-4	1810.64	0.098
Polystyrene[6]	1.05/	13000	0.954	1.468	8.106E-4	1810.64	0.098
(C_8H_8)	1.11	15000	0.827	1.102	4.842E-4	2276.03	0.085
		15200	0.816	1.073	4.626E-4	2320.26	0.084
Pot-Chl. (KCl)	*(0.862)*	13000	0.954	1.038	0.0213	48.616	0.083
Quartz/Glass	2.20	10050	1.234	4.555	0.0384	118.723	0.173
(SiO_2)		13000	0.954	2.714	0.0138	196.513	0.133
		15000	0.827	2.036	0.0078	259.988	0.116
		15200	0.816	1.983	0.0074	266.788	0.114
Rutile (TiO_2)	4.26	13000	0.954	5.035	0.1069	47.105	0.182
Water (H_2O)	1.00	10050	1.234	2.290	0.0049	465.976	0.123
		13000	0.954	1.367	0.0017	785.938	0.095
		15000	0.827	1.026	0.0010	1036.364	0.082
		15200	0.816	0.999	0.0009	1059.987	0.081

Table B.3.: Density ρ, dispersion δ, absorption β and other properties of compounds used in this work at different photon energies [31, 59, 164]. Calculations as mentioned in table B.2 and in the theory chapter 2.

[1] Air = $N_{1.562}O_{0.42}C_{0.0003}Ar_{0.0094}$

[2] Mica = $KAl_3Si_3O_{12}H_2$

[3] CXRO values for nitrobenzene are estimations.

[4] The first line gives values from [31], the second line values from [116] and experimental data discussed in section 6.2.4.

[5] Phospholipid = C_3H_9N-C_2H_4O-PO_4-COH -$C_{18}H_{33}O$ -$C_{17}O_2H_{33}$

[6] Density value of polystyrene differs in various references [31, 164].

[7] Values for cytochrome c, PAMAM and phospholipid were not available. Values for polystyrene were taken as alternative starting values in fitting procedures.

B.3. X-ray emission lines of elements used in this work

No	El	Kα_1	Kα_2	Kβ_1	Lα_1	Lα_2	Lβ_1	Lβ_2	Lγ_1	Mα_1
6	C	277								
7	N	392.4								
8	O	524.9								
12	Mg	1253.60	1253.60	1302.2						
13	Al	1486.70	1486.27	1557.45						
14	Si	1739.98	1739.38	1835.94						
15	P	2013.7	2012.7	2139.1						
17	Cl	2622.39	2620.78	2815.6						
18	Ar	2957.70	2955.63	3190.5						
19	K	3313.8	3311.1	3589.6						
22	Ti	4510.84	4504.86	4931.81	452.2	452.2	458.4			
25	Mn	5898.75	5887.65	6490.45	637.4	637.4	648.8			
26	Fe	6403.84	6390.84	7057.98	705.0	705.0	718.5			
29	Cu	8047.78	8027.83	8905.29	929.7	929.7	949.8			
30	Zn	8638.86	8615.78	9572.0	1011.7	1011.7	1034.7			
32	Ge	9886.42	9855.32	10982.1	1188.00	1188.00	1218.5			
33	As	10543.72	10507.99	11726.2	1282.0	1282.0	1317.0			
34	Se	11222.4	11181.4	12495.9	1379.10	1379.10	1419.23			
42	Mo	17479.34	17374.3	19608.3	2293.16	2289.85	2394.81	2518.3	2623.5	
47	Ag	22162.92	21990.3	24942.4	2984.31	2978.21	3150.94	3347.81	3519.59	
74	W	59318.24	57981.7	67244.3	8397.6	8335.2	9672.35	9961.5	11285.9	1775.4
79	Au	68803.7	66989.5	77984	9713.3	9628.0	11442.3	11584.7	13381.7	2122.9

Table B.4.: Photon energies of K-, L- and M-shell emission lines (in eV) of elements analyzed in this work. Values from [5, 84, 146].

C. Sample preparation procedures

C.1. Cleaning procedure for quartz glass carriers

The following special cleaning procedure for TXRF sample carriers has proven to be useful during years of application at ISAS:

Required material

- quartz glass sample carriers
- PTFE disc holder
- petri dishes, glass beakers, glass covers
- RBS-50 (*RBS-50 Konzentrat, Carl Roth, Karlsruhe, Germany*)
- silicone solution (*Serva, Heidelberg, Germany*)
- concentrated nitric acid HNO_3 (p.a. grade)
- distilled water
- scientific cleaning wipes (*Kimwipes, Kimtech Science, Kimberly-Clark, Irving, Texas, USA*)

Cleaning the quartz glass carriers

- put the sample carriers into the PTFE disk holder and the disk holder into a covered beaker containing a 1+7 solution of RBS-50 and distilled water
- boil disk holder and carriers inside the beaker with RBS-50, cool down afterwards
- take the disk holder and carriers out, rinse them with distilled water, put them into another covered beaker containing distilled water
- boil holder and carriers in distilled water and cool down afterwards
- remove the carriers from the holder, disassemble the holder and clean holder and carriers with Kimwipes
- put the carriers into the disk holder and the holder into a covered beaker containing concentrated nitric acid

- boil holder and carriers in concentrated nitric acid for 1 hour and cool down afterwards
- rinse holder and carriers with distilled water
- heat holder and carriers in another beaker with distilled water at $\approx 50^{\circ}\mathrm{C}$ and cool down to $\approx 35^{\circ}\mathrm{C}$
- take the carriers out of the holder and dry only the borders with Kimwipes carefully
- if necessary hydrophobize one face of each carrier with silicone solution (10 μL for 3 carriers)
- fix the silicone by baking the sample carriers in closed petri dishes (5 carriers per dish) in an oven for 1 hour at $110^{\circ}\mathrm{C}$
- check the cleaned sample carriers by TXRF for any contamination

Cleaning of the glass materials

- put petri dishes, beakers and the other glass parts into a big covered beaker filled with approximately 3 cm concentrated nitric acid and providing a glass grid about 5 cm from its bottom
- boil the concentrated nitric acid for 1 hour to clean the glass materials by HNO_3 vapor
- rinse the glass materials with distilled water after cooling down and dry them with Kimwipes

C.2. Preparation of cytochrome c films

The cytochrome c molecules were immobilized on quartz glass carriers by the following procedure [53, 115, 177]:

- prepare a MES-NaCl buffer solution with 0.1 M MES hydrate powder (2-(N-Morpholino)-ethanesulfonic acid hydrate a.k.a. 4-Morpholineethanesulfonic acid - $C_6H_{13}NO_4S \cdot xH_2O$; *M5287, Sigma-Aldrich, St. Louis, Missouri, USA*) and 0.5 M NaCl in deionized water
- mix 4 mg EDC hydrochloride (N-(3-Dimethylaminopropyl)-N'-ethylcarbodiimide hydrochloride a.k.a. N-Ethyl-N'-(3-dimethylaminopropyl)carbodiimide hydrochloride - $C_8H_{17}N_3 \cdot HCl$; *E1769, Sigma-Aldrich, St. Louis, Missouri, USA*) with 1 ml of the MES-NaCl buffer
- mix 6 mg NHS (N-hydroxysuccinimide - $C_4H_4O_2NOH$) with 1 ml of the MES-NaCl buffer
- mix 400 μL of this EDC solution and 400 μL of this NHS solution to create the coupling reagent
- dissolve 50 μg of cytochrome c powder from bovine heart (*C2037, Sigma-Aldrich, St. Louis, Missouri, USA*) in 5 ml deionized water
- mix 400 μL of this cytochrome solution with 3.6 ml MES-NaCl buffer solution
- add 800 μL of EDC-NHS coupling reagent
- leave this mixture for 10 min with casual pivoting to enhance mixing
- put cleaned sample carriers (cf. section C.1) that are hydrophobized with 15 μL of a silane solution (3-(Triethoxysilyl)-propylamine ($C_9H_{23}NO_3Si$); *Merck Schuchardt, Hohenbrunn, Germany*) into a petri dish and cover these carriers with 2 ml of the cytochrome coupling agent solution for 20 min
- remove the solution and cover the carriers with 4 ml of deactivation reagent (1 M ethanolamine (C_2H_7NO) and 1 M NaCl in deionized water) for 10 min
- remove this reagent, too, and rinse the carriers twice with 2 ml MES-NaCl buffer
- store the carriers in 5 ml MES-NaCl buffer solution at 4°C

D. Calculations and approximations

D.1. sin, cos, tan for small angles

As mainly very small angles are used in experiments of this work, very often some mathematical approximations can be made when using $\sin$, $\cos$ and $\tan$. Taylor series [21] up to second order lead to the following simplifications:

$$\sin(0+x) = \sin(0) + \cos(0)\cdot x - \frac{1}{2}\sin(0)\cdot x^2 - \ldots \approx x \tag{D.1}$$

$$\cos(0+x) = \cos(0) - \sin(0)\cdot x - \frac{1}{2}\cos(0)\cdot x^2 + \ldots \approx 1 - \frac{1}{2}x^2 \tag{D.2}$$

$$\tan(0+x) = \tan(0) + \frac{1}{\cos^2(0)}\cdot x + \frac{\sin(0)}{\cos^3(0)}\cdot x^2 + \cdots \approx x \tag{D.3}$$

D.2. Complex square root

Complex numbers are utilized throughout this work, thus some short remarks shall be made concerning calculating with complex numbers. Basic arithmetic operations are trivial but exponentiation and especially root extraction can be somewhat confusing. Exponentiation is defined in the polar form

$$Z = |Z|\cdot\exp(\mathrm{i}\phi) = |Z|\cdot\exp\left(\mathrm{i}\arctan\frac{\mathrm{Im}(Z)}{\mathrm{Re}(Z)}\right) \tag{D.4}$$

by

$$Z^n = |Z|^n\cdot\exp(\mathrm{i}n\phi) \tag{D.5}$$

and consequently the root is

$$\sqrt[n]{Z} = Z^{\frac{1}{n}} = |Z|^{\frac{1}{n}}\cdot\exp\left(\frac{\mathrm{i}\phi}{n} + k\cdot\frac{2\pi\mathrm{i}}{n}\right) \tag{D.6}$$

with $k = 0, 1, \ldots, n-1$. Thus the nth root always has n solutions. For the important case of the square root there are two results

$$\sqrt{Z} = \begin{cases} \sqrt{|Z|} \cdot \exp\left(\frac{\mathrm{i}\phi}{2}\right) \\ \sqrt{|Z|} \cdot \exp\left(\frac{\mathrm{i}\phi}{2} + \frac{2\pi\mathrm{i}}{2}\right) = \sqrt{|Z|} \cdot \exp\left(\mathrm{i}\left(\frac{\phi}{2} + \pi\right)\right). \end{cases} \tag{D.7}$$

Utilizing Euler's formula this can be written as

$$\sqrt{Z} = \begin{cases} \sqrt{|Z|} \cdot \left(\cos\frac{\phi}{2} + \mathrm{i}\sin\frac{\phi}{2}\right) = Z_{\mathrm{Re}} + \mathrm{i}Z_{\mathrm{Im}} \\ \sqrt{|Z|} \cdot \left(\cos\left(\frac{\phi}{2} + \pi\right) + \mathrm{i}\sin\left(\frac{\phi}{2} + \pi\right)\right) = -Z_{\mathrm{Re}} - \mathrm{i}Z_{\mathrm{Im}}. \end{cases} \tag{D.8}$$

Finally, the square root of $\mathrm{i} = \sqrt{-1}$ shall be calculated. Here, the phase is

$$\phi = \arctan\frac{\mathrm{Im(i)}}{\mathrm{Re(i)}} = \frac{\pi}{2} \tag{D.9}$$

and the square root

$$\sqrt{\mathrm{i}} = \begin{cases} \exp\left(\frac{\mathrm{i}\pi}{4}\right) = \cos\frac{\pi}{4} + \mathrm{i}\sin\frac{\pi}{4} = \sqrt{2}/2 + \mathrm{i}\sqrt{2}/2 \\ \exp\left(\frac{5\mathrm{i}\pi}{4}\right) = \cos\frac{5\pi}{4} + \mathrm{i}\sin\frac{5\pi}{4} = -\sqrt{2}/2 - \mathrm{i}\sqrt{2}/2. \end{cases} \tag{D.10}$$

D.3. Energy and wavelength

In particle and accelerator physics photons are usually characterized by their energy E in electronvolts (eV), for geometrical considerations it is often more useful to know the photon wavelength λ in m or nm. Conversion is performed following Planck's law

$$E = h\nu = \frac{hc}{\lambda} \Longleftrightarrow \lambda = \frac{hc}{E} \tag{D.11}$$

with the energy unit

$$1\mathrm{eV} = 1.602177 \cdot 10^{-19}\mathrm{J} \tag{D.12}$$

and Planck's constant h

$$h = 6.626069 \cdot 10^{-34}\mathrm{Js} = 4.135666 \cdot 10^{-15}\mathrm{eV}. \tag{D.13}$$

The conversion factor between E (in eV) and λ (in m) is then

$$hc = 1.239841 \cdot 10^{-6}. \tag{D.14}$$

Further wavelength and energy bandwidths can be converted by

$$\frac{\Delta\lambda}{\lambda} = \frac{hc}{\lambda}\left(\frac{1}{E_2} - \frac{1}{E_1}\right) = \frac{hc \cdot (E_1 - E_2)}{\lambda E_1 E_2} = \frac{hc}{\lambda} \cdot \frac{\Delta E}{E^2} = \frac{\Delta E}{E}. \tag{D.15}$$

D.4. Critical angle

At total reflection condition the transmitted angle is $\alpha_\mathrm{t} = 0°$ and Snell's law for a vacuum-matter-interface

$$\cos\alpha_\mathrm{i} \quad = \quad n\cos\alpha_\mathrm{t}. \tag{D.16}$$

becomes

$$\cos\alpha_\mathrm{i} \quad = \quad n \cdot 1. \tag{D.17}$$

Using Taylor series for small angles

$$\cos x \quad \approx \quad 1 - \frac{x^2}{2} \tag{D.18}$$

leads (considering only the real part of n) to

$$1 - \frac{\alpha_\mathrm{c}^2}{2} \quad \approx \quad n = 1 - \delta \tag{D.19}$$

and finally to the critical angle of total reflection

$$\alpha_c \quad \approx \quad \sqrt{2\delta}. \tag{D.20}$$

D.5. Transmission angle of the penetrating beam

Snell's law

$$\cos\alpha_\mathrm{i} \quad = \quad n\cos\alpha_\mathrm{t}. \tag{D.21}$$

for small angles with approximation D.18 leads to

$$\begin{aligned} 1 - \frac{\alpha_\mathrm{i}^2}{2} &= n \cdot \left(1 - \frac{\alpha_\mathrm{t}^2}{2}\right) \\ 2 - \alpha_\mathrm{i}^2 &= 2n - n\alpha_\mathrm{t}^2 \\ n\alpha_\mathrm{t}^2 &= \alpha_\mathrm{i}^2 - 2 + 2n. \end{aligned} \tag{D.22}$$

With $n = 1 - \delta + i\beta$ it follows

$$n\alpha_{\mathrm{t}}^2 = \alpha_{\mathrm{i}}^2 - 2\delta + 2i\beta. \tag{D.23}$$

Considering the orders of magnitude of parameters in this equation $\alpha_{\mathrm{i}} \approx \alpha_{\mathrm{t}} \approx O(10^{-3})$ and $\delta \approx \beta \approx O(10^{-6})$ it can be estimated

$$\begin{aligned} n\alpha_{\mathrm{t}}^2 = \alpha_{\mathrm{t}}^2 - 2\delta\alpha_{\mathrm{t}}^2 + 2i\beta\alpha_{\mathrm{t}}^2 &= \alpha_{\mathrm{i}}^2 - 2\delta + 2i\beta \\ O(10^{-6}) - O(10^{-12}) + O(10^{-12}) &= O(10^{-6}) - O(10^{-6}) + O(10^{-6}). \end{aligned} \tag{D.24}$$

The second and third expression on the left side can obviously be neglected leading to[1]

$$\alpha_{\mathrm{t}} \approx \sqrt{\alpha_{\mathrm{i}}^2 - 2\delta + 2i\beta} \tag{D.25}$$

for the complex transmission angle $\alpha_{\mathrm{t}} = \alpha_{\mathrm{t,r}} + \mathrm{i}\alpha_{\mathrm{t,i}}$.

D.6. Transmission angle in different notations

As mentioned in chapter 2.1.1 the transmission angle α_{t} in equation 2.34 can be written in two different notations

$$\alpha_{\mathrm{t}} = \sqrt{\alpha_0^2 - 2\delta + 2\mathrm{i}\beta} \tag{D.26}$$

or

$$\alpha_{\mathrm{t}} = \sqrt{\alpha_0^2 - 2\delta - 2\mathrm{i}\beta} \tag{D.27}$$

depending on the definition of the electromagnetic wave. To facilitate comparison of formulae comprising this transmission angle, α_{t} is discussed in more detail now. For simplification the square root is written

$$\alpha_{\mathrm{t}} = \sqrt{a + \mathrm{i}b} = \sqrt{Z} \tag{D.28}$$

and in polar form

$$\alpha_{\mathrm{t}} = \sqrt{|Z|} \cdot \exp\left(\frac{\mathrm{i}\phi}{2}\right) \tag{D.29}$$

with phase of Z

$$\phi = \arctan\frac{b}{a}. \tag{D.30}$$

[1] Depending on the definition of the refractive index n in equations 2.9 also the equation $\alpha_{\mathrm{t}} \approx \sqrt{\alpha_{\mathrm{i}}^2 - 2\delta - 2i\beta}$ can be found in literature [72].

First, the case $a > 0$, that means

$$\alpha_0^2 > 2\delta = \alpha_c^2 \tag{D.31}$$

is regarded: Radiation penetrates the layer for angles above the critical angle α_c. Using Euler's formula, α_t can be written as

$$\alpha_t = \sqrt{|Z|} \cdot \cos\left(\frac{1}{2}\arctan\frac{b}{a}\right) + i\sqrt{|Z|} \cdot \sin\left(\frac{1}{2}\arctan\frac{b}{a}\right) \tag{D.32}$$

and considering $\cos(-x) = \cos(x)$ and $\sin(-x) = -\sin(x)$, respectively,

$$\alpha_t = \sqrt{|Z|} \cdot \cos\left(\frac{1}{2}\arctan\left|\frac{b}{a}\right|\right) + \mathrm{sgn}(b) \cdot i\sqrt{|Z|} \cdot \sin\left(\frac{1}{2}\arctan\left|\frac{b}{a}\right|\right). \tag{D.33}$$

Substituting

$$\begin{aligned} A &= \sqrt{|Z|} \cdot \cos\left(\frac{1}{2}\arctan\left|\frac{b}{a}\right|\right) \\ &\text{and} \\ B &= \sqrt{|Z|} \cdot \sin\left(\frac{1}{2}\arctan\left|\frac{b}{a}\right|\right) \end{aligned} \tag{D.34}$$

it can be written

$$\alpha_t = \begin{cases} \sqrt{\alpha_0^2 - 2\delta + 2i\beta} & = A + iB \\ \sqrt{\alpha_0^2 - 2\delta - 2i\beta} & = A - iB \end{cases} \tag{D.35}$$

with A and B being positive real numbers because

$$\arctan\left|\frac{b}{a}\right| \in [0, \pi/2] \tag{D.36}$$

and

$$\cos\left(\frac{1}{2}\arctan\left|\frac{b}{a}\right|\right) \in [\sqrt{2}/2, 1] \tag{D.37}$$

$$\sin\left(\frac{1}{2}\arctan\left|\frac{b}{a}\right|\right) \in [0, \sqrt{2}/2]. \tag{D.38}$$

Thus, if switching notation the transmission angle has to be replaced by its complex conjugate. Now a shall be < 0, i.e. total reflection of the beam at $\alpha_0 < \alpha_c$. Writing

$$\alpha_t = \sqrt{a + ib} = \sqrt{-(-a - ib)} = i\sqrt{a^* + ib^*} \tag{D.39}$$

with substitutions

$$a^* = -a > 0 \quad \text{and} \quad b^* = -b \tag{D.40}$$

permits to directly adopt results from calculations for $a > 0$

$$\alpha_\mathrm{t} = \begin{cases} \sqrt{\alpha_0^2 - 2\delta + 2\mathrm{i}\beta} & = \mathrm{i}A^* + B^* = \mathrm{i}A - B \\ \sqrt{\alpha_0^2 - 2\delta - 2\mathrm{i}\beta} & = \mathrm{i}A^* - B^* = \mathrm{i}A + B \end{cases} \tag{D.41}$$

with

$$A^* = A \quad \text{and} \quad B^* = -B \tag{D.42}$$

as can be easily seen from equation D.34 and again A, B being positive real numbers. However, the real part of the transmission angle needs to be positive by definition. Thus, it has to be taken into account that the complex square root always has two solutions (cf. equation D.8). Hence, signs can be switched in equation D.41 resulting in

$$\alpha_\mathrm{t} = \begin{cases} \sqrt{\alpha_0^2 - 2\delta + 2\mathrm{i}\beta} & = B - \mathrm{i}A \\ \sqrt{\alpha_0^2 - 2\delta - 2\mathrm{i}\beta} & = B + \mathrm{i}A. \end{cases} \tag{D.43}$$

Again, the transmission angle needs to be replaced by its complex conjugate when changing notation. Further, it is noticable, that A and B have exchanged position in the formula. Finally, the case of $a = 0$ or $\alpha_0 = \alpha_\mathrm{c}$, respectively, delivers the simple result

$$\alpha_\mathrm{t} = \sqrt{\pm 2\mathrm{i}\beta} = \sqrt{\mathrm{i}} \cdot \sqrt{\pm 2\beta} \begin{cases} (\sqrt{2}/2 + \mathrm{i}\sqrt{2}/2) \cdot \sqrt{2\beta} = \sqrt{\beta}(1 + \mathrm{i}) \\ (-\sqrt{2}/2 - \mathrm{i}\sqrt{2}/2) \cdot \mathrm{i}\sqrt{2\beta} = \sqrt{\beta}(1 - \mathrm{i}) \end{cases} \tag{D.44}$$

using equation D.10 and the condition that the real part of α_t must be positive. This is equivalent to equation 2.27. Also here, only the complex conjugate has to be applied.

D.7. Implementation of Debye-Waller factor into matrix formalism

Using the angle dependent Debye-Waller factor $DF = \exp\left[-(q\sigma)^2\right]$ with wave vector and roughness σ the Fresnel reflection and transmission coefficients (equations 2.62 - 2.63) become

$$r = \frac{E_\mathrm{r}}{E_\mathrm{i}} = \frac{\alpha_\mathrm{i} - \alpha_\mathrm{t}}{\alpha_\mathrm{i} + \alpha_\mathrm{t}} \cdot DF = \frac{DF\alpha_\mathrm{i} - DF\alpha_\mathrm{t}}{\alpha_\mathrm{i} + \alpha_\mathrm{t}} \tag{D.45}$$

$$\begin{aligned} t &= \frac{E_\mathrm{t}}{E_\mathrm{i}} = 1 + r = \frac{DF\alpha_\mathrm{i} - DF\alpha_\mathrm{t} + \alpha_\mathrm{i} + \alpha_\mathrm{t}}{\alpha_\mathrm{i} + \alpha_\mathrm{t}} \\ &= \frac{(1+DF)\alpha_\mathrm{i} + (1-DF)\alpha_\mathrm{t}}{\alpha_\mathrm{i} + \alpha_\mathrm{t}}. \end{aligned} \tag{D.46}$$

Reorganizing both equations to E_i and equating leads to

$$E_\mathrm{r} \cdot \frac{\alpha_\mathrm{i} + \alpha_\mathrm{t}}{DF\alpha_\mathrm{i} - DF\alpha_\mathrm{t}} = E_\mathrm{t} \cdot \frac{\alpha_\mathrm{i} + \alpha_\mathrm{t}}{(1+DF)\alpha_\mathrm{i} + (1-DF)\alpha_\mathrm{t}} \tag{D.47}$$

and further

$$E_\mathrm{i} = \frac{\alpha_\mathrm{i} + \alpha_\mathrm{t}}{(1+DF)\alpha_\mathrm{i} + (1-DF)\alpha_\mathrm{t}} \cdot E_\mathrm{t} = m_{1,4} \cdot E_\mathrm{t} \tag{D.48}$$

$$E_\mathrm{r} = \frac{DF\alpha_\mathrm{i} - DF\alpha_\mathrm{t}}{(1+DF)\alpha_\mathrm{i} + (1-DF)\alpha_\mathrm{t}} \cdot E_\mathrm{t} = m_{2,3} \cdot E_\mathrm{t} \tag{D.49}$$

D.8. Continuous transition

Often the interface between two layers is not perfectly sharp with the refractive index jumping from n_1 in layer 1 to n_2 in layer 2 but the interface shows a certain "roughness". For methods only sensitive in direction z perpendicular to the interface this leads to a somewhat "smooth" (continuous) transition $n(z)$ without jumps or tilts. The easiest way to calculate such a smooth transition from -1 to 1 is by a sine function

$$f(z) = \sin(z) \tag{D.50}$$

for $z \in [-\pi, \pi]$.

A very common description in science is the error function $\mathrm{erf}(z)$ which is deduced from the Gaussian distribution function [21] and defined as

$$\mathrm{erf}(z) = \frac{2}{\sqrt{\pi}} \int_0^z \exp(-t^2)\mathrm{d}t. \tag{D.51}$$

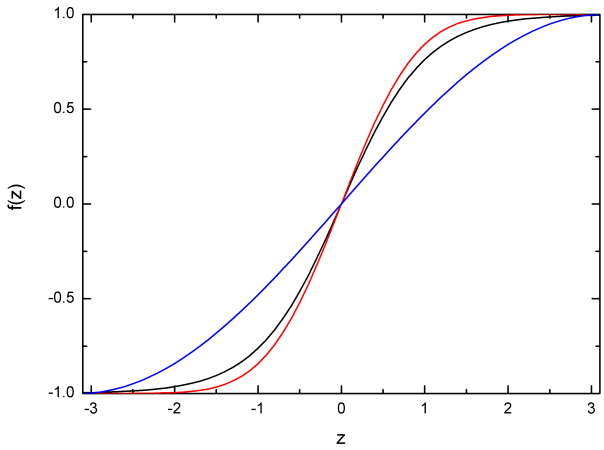

Figure D.1.: Comparison of $\sin(z)$ (blue), $\mathrm{erf}(z)$ (red) and $\tanh(z)$ (black) in the interval $z \in [-\pi, \pi]$.

$\mathrm{erf}(z)$ describes a transition between -1 and 1 with z ranging from $-\infty$ to $+\infty$ but with $|\mathrm{erf}(z)|$ very close to 1 at $\pm\pi$.

Finally, the hyperbolic tangent

$$\tanh(z) = \frac{\exp(x) - \exp(-x)}{\exp(x) + \exp(-x)} \tag{D.52}$$

shows a very similar shape and behavior. Like the error function, $\tanh(z)$ ranges from -1 to 1 with z going from $-\infty$ to $+\infty$. Again $\tanh(\pm\pi)$ is nearly ± 1.

All of these functions were utilized in this work. Figure D.1 shows $\sin(z)$, $\mathrm{erf}(z)$ and $\tanh(z)$ in the interval $z \in [-\pi, \pi]$.

D.9. Aligning an MCA energy scale

Commonly, energy spectra like the one shown in figure 2.8 in TXRF or XSW measurements are recorded using a multi channel analyzer (MCA). Usually, the number of counts are given as counts per channel rather than counts for a certain energy. Thus, the energy scale of the MCA has to be aligned. For this purpose it is necessary to have a measured spectrum with at least two significant peaks of known energy. The peak from elastic scattering (cf. 2.2.2) is present in virtually all scans, either from the selected energy at a synchrotron with monochromator or the typical fluorescence line(s) of a laboratory X-ray tube. The second peak can be from an element present in the sample or from a preceding measurement with a known reference sample. Commonly, MCAs show a linear relation between channel number and corresponding energy.

Further, the first channel should correspond to an energy of 0 but in reality it is often shifted by a small amount E_0. Thus, with given channel numbers ch_{el}, ch_2 and known energies E_{el}, E_2 of the elastic and second peak the relation

$$E(ch) = m \cdot ch + E_0 \tag{D.53}$$

holds with

$$m = \frac{E_{\mathrm{el}} - E_2}{ch_{\mathrm{el}} - ch_2} \tag{D.54}$$

$$E_0 = E_{\mathrm{el}} - m \cdot ch_{\mathrm{el}} = \frac{E_2 \cdot ch_{\mathrm{el}} - E_{\mathrm{el}} \cdot ch_2}{ch_{\mathrm{el}} - ch_2}. \tag{D.55}$$

D.10. Calculation of element fraction from the critical angle

Mixture of two elements

If two elements are mixed (homogeneously) in a sample material the resulting total dispersion factor δ_{t} can be assumed to be

$$\delta_{\mathrm{t}} = \delta_1 n_1 + \delta_2 n_2 \tag{D.56}$$

with $\delta_{1,2}$ being the dispersion values for elements 1 and 2 and $n_{1,2}$ their content in the material with

$$n_1 + n_2 = 1. \tag{D.57}$$

Using this relation, equation D.56 becomes

$$\delta_{\mathrm{t}} = \delta_1 n_1 - \delta_2 n_1 + \delta_2 = n_1(\delta_1 - \delta_2) + \delta_2 \tag{D.58}$$

and the fraction of element 1 is

$$n_1 = \frac{\delta_{\mathrm{t}} - \delta_2}{\delta_1 - \delta_2}. \tag{D.59}$$

Commonly, the critical angle α_{c} is detected rather than the dispersion δ and using formula 2.18

$$\delta = \alpha_{\mathrm{c}}^2/2 \tag{D.60}$$

turns equation D.59 into

$$n_1 = \frac{\alpha_{\mathrm{c,t}}^2 - \alpha_{\mathrm{c,2}}^2}{\alpha_{\mathrm{c,1}}^2 - \alpha_{\mathrm{c,2}}^2}. \tag{D.61}$$

Equivalently, the content of element 2 is

$$n_2 = \frac{\alpha_{\mathrm{c,t}}^2 - \alpha_{\mathrm{c},1}^2}{\alpha_{\mathrm{c},2}^2 - \alpha_{\mathrm{c},1}^2} \tag{D.62}$$

and the ratio of both elements

$$\frac{n_1}{n_2} = -\frac{\alpha_{\mathrm{c,t}}^2 - \alpha_{\mathrm{c},2}^2}{\alpha_{\mathrm{c,t}}^2 - \alpha_{\mathrm{c},1}^2}. \tag{D.63}$$

Mixture of three elements

Analysis for a mixture of three elements is more complicated. Similar to the two elements case discussed before a total dispersion factor

$$\delta_{\mathrm{t}} = \delta_1 n_1 + \delta_2 n_2 + \delta_3 n_3 \tag{D.64}$$

can be defined. If element 3 is the main component and elements 1 and 2 are of lower concentration (but also for any element concentration ratio)

$$\begin{aligned} n_2 &= x \cdot n_1 \\ &\text{and} \\ n_3 &= 1 - n_1 - n_2 = 1 - (1+x)n_1 \end{aligned} \tag{D.65}$$

can be defined. Then equation D.64 becomes

$$\delta_{\mathrm{t}} = \delta_3 - (1+x)\delta_3 n_1 + x\delta_2 n_1 + \delta_1 n_1 \tag{D.66}$$

and

$$n_1 = \frac{\delta_{\mathrm{t}} - \delta_3}{\delta_1 + x\delta_2 - (1+x)\delta_3}. \tag{D.67}$$

Again with equation 2.18 this leads to

$$n_1 = \frac{\alpha_{\mathrm{c,t}}^2 - \alpha_{\mathrm{c},3}^2}{\alpha_{\mathrm{c},1}^2 + x\alpha_{\mathrm{c},2}^2 - (1+x)\alpha_{\mathrm{c},3}^2}. \tag{D.68}$$

E. Computer programs developed during this work

E.1. MXSW - XSW simulation program

The computer program *MXSW* to simulate X-ray standing waves in a wide variety of samples is described in detail in chapter 5. Some screenshots of the program are shown in the following: Sample parameters and experimental parameters windows (figure E.1), beampath (calculated angles in each layer) and angle cut i.e. lateral intensity distribution at a given angle of incidence (figure E.2), calculated 3D XSW intensity field and calculated and measured XSW intensity angle scan (figure E.3).

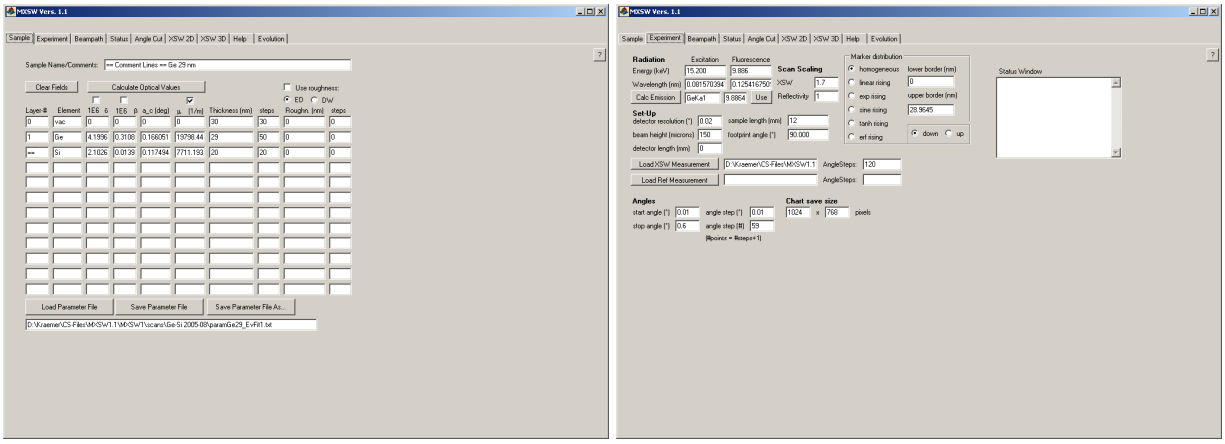

Figure E.1.: Screenshot of *MXSW* program: Enter sample (left) and experimental parameters (right).

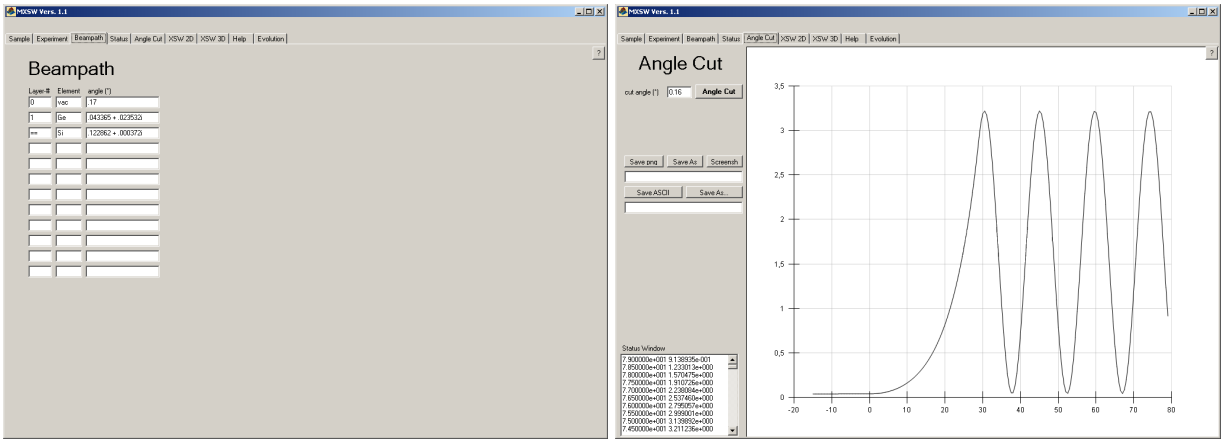

Figure E.2.: Screenshot of *MXSW* program: Beampath (calculated angles in each layer, left) and angle cut i.e. lateral intensity distribution at a given angle of incidence (right).

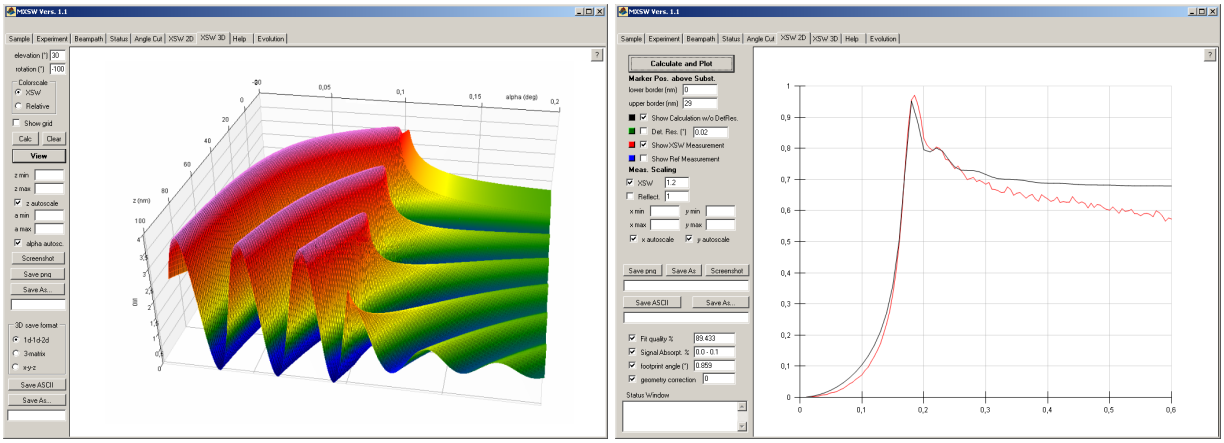

Figure E.3.: Screenshots of *MXSW* program: Calculated 3D XSW field (left) and calculated and measured XSW angle scan (right).

E.2. TxrfTool - TXRF data converter and analyzer

The TXRF spectrometer Extra II uses 2048 channels, each channel can store up to 16 million counts ($256 \cdot 256 \cdot 256$). So each channel occupies 3 bytes in the saved spectrum plus another byte as separator to the following data point resulting in 8192 bytes for 2048 channels. The length of an EXTRA II save file depends on the energy range that has been chosen during measurement. The first 192 bytes are information like sample label etc. After that, 2048 (for energy range 10 keV), 4096 (for energy range 20 keV) or 8192 (for energy range 40 keV) bytes follow that contain measurement data (in counts per channel). So if the energy range is reduced, the resolution is not increased, there are just less channels read out and saved. Finally, at the end of the file there are another 10 bytes with additional data like voltage and current of the tube, measurement time and selected energy range of the detector. With the first element of the file at position 0, a structure of the spectrum files as shown in table E.1 applies. Location is given in decimal and hexadecimal file position. To save data storage space, the number of counts per channel is not written as an

40 keV dec	40 keV hex	20 keV dec	20 keV hex	10 keV dec	10 keV hex	function
0d - 9d	00h - 09h	0d - 9d	00h - 09h	0d - 9d	00h - 09h	introduction
10d - 21d	0Ah - 15h	10d - 21d	0Ah - 15h	10d - 21d	0Ah - 15h	(empty)
22d - 35d	16h - 23h	22d - 35d	16h - 23h	22d - 35d	16h - 23h	sample label
36d - 129d	24h - 81h	36d - 129d	24h - 81h	36d - 129d	24h - 81h	(empty)
130d - 191d	83h - BFh	130d - 191d	83h - BFh	130d - 191d	83h - BFh	description
192d	C0h	192d	C0h	192d	C0h	
- 8383d	- 20BFh	- 4287d	- 10BFh	- 2239d	- 8BFh	measurement
8384d	20C0h	4288d	10C0h	2240d	8C0h	voltage (keV)
8385d	20C1h	4289d	10C1h	2241d	8C1h	(empty)
8386d	20C2h	4290d	10C2h	2242d	8C2h	current (mA)
8387d	20C3h	4291d	10C3h	2243d	8C3h	(empty)
8388d	20C4h	4292d	10C4h	2244d	8C4h	meas. time (s)
8389d	20C5h	4293d	10C5h	2245d	8C5h	(empty)
8390d	20C6h	4294d	10C6h	2246d	8C6h	energy range
8391d	20C7h	4295d	10C7h	2247d	8C7h	
- 8393d	- 20C9h	- 4297d	- 10C9h	- 2249d	- 8C9h	(empty)

Table E.1.: Structure of an EXTRA II TXRF data save file. For each selected energy range the location of data inside the file is given as decimal and hexadecimal file position.

ASCII number but as ASCII characters, the ASCII number of the characters representing the number of counts. For example, "A" means "65". To achieve 16 million counts, three characters are combined to form one number, the second character is meant to be multiplied by 256 and the third by 256*256=65536. Thus the number 2179648 is written as $64 \cdot 1 + 66 \cdot 256 + 33 \cdot 65536$ = "@B!". To convert this TXRF Format into ASCII it is necessary to read the data file, convert each ASCII character into its corresponding number and store these numbers into a matrix A.

Then intensity values can be calculated and stored into matrix I by the following formula

$$\begin{aligned} I(n) = &\quad A \quad ((n-1)\cdot 4 + 1 + 192) \\ &+ \quad A \quad ((n-1)\cdot 4 + 2 + 192)\cdot 256 \\ &+ \quad A \quad ((n-1)\cdot 4 + 3 + 192)\cdot 256\cdot 256. \end{aligned} \tag{E.1}$$

for n between 1 and the number of measured values (i.e. 2048, 4096 or 8192). The value 192 is added to n to skip the introduction data bytes. The corresponding energy values are calculated by

$$E(n) = n \cdot 0.02\,\mathrm{keV} \tag{E.2}$$

because the energy difference between two neighboring channels is 20 eV regardless of the selected energy range. Calculated intensity and energy values are then saved as an ASCII table an can be analyzed on another computer as described in the evaluation chapter 6.

The program *TxrfTool* developed in this work reads TXRF spectra from Atomika Instruments Extra IIa spectrometer and saves them in ASCII format. The data file can be loaded and saved in a program window. Here also energy range of the scan can be entered (or automatically detected) and information about the scan (like scan label) can be regarded. In a second step, the loaded spectrum can be plotted and compared to tabulated X-ray emission lines [5, 84, 146] for most elements. Figure E.4 shows a scan plotted with *TxrfTool* with selected emission element Cl. Relative heights of different emission lines are indicated to facilitate identification of peaks. Intensity (counts) can be displayed in linear and logarithmic scale for optimal visibility depending on the spectrum.

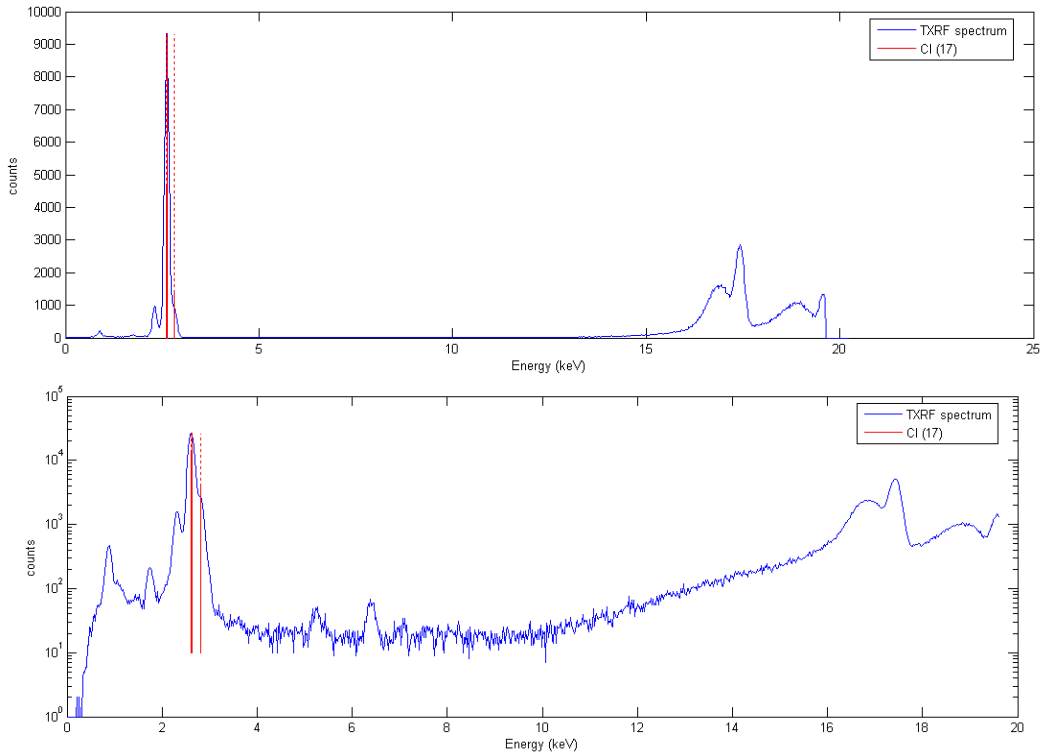

Figure E.4.: Screenshot of *TxrfTool* program: Linear and logarithmic plot of a scan and Cl emission lines.

E.3. D8opt - Analysis program for reflectivity and longitudinal diffuse scans

A software tool was developed to subtract the longitudinal diffuse intensity from the measured reflectivity. The functioning of this program is outlined here: Due to large differences in reflectivity while scanning an incident angle range of several degrees, different absorbers have to be introduced into the beam before the sample for low angles. Thus, the angle range has to be scanned in several intervals. If the absorption factor is not known precisely scans of these intervals need to be aligned manually. To facilitate alignment, angle intervals are chosen to have a certain overlap that has to be removed before evaluating the scans (cf. figure E.5). Then, both

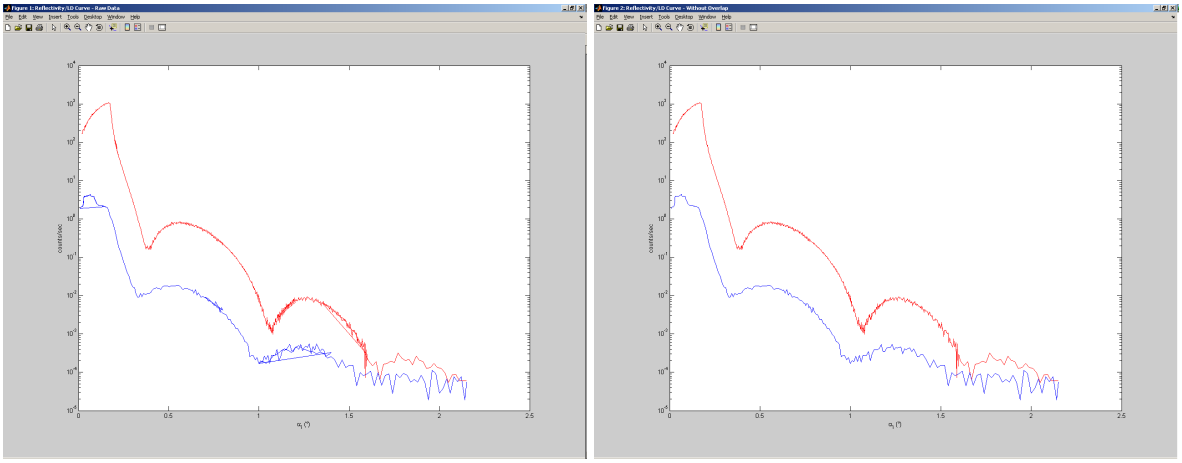

Figure E.5.: Screenshots of *D8opt* program: Measured reflectivity and LD scans before and after removal of the overlap.

scans have to be converted into q-space as already explained in evaluation chapter 4.2.1 to be subtracted from each other. Additionally, q-steps of reflectivity and LD scan have to be aligned (cf. figure E.6). Finally, intensities are subtracted and re-transformed into angle space for better visualization (cf. figure E.6).

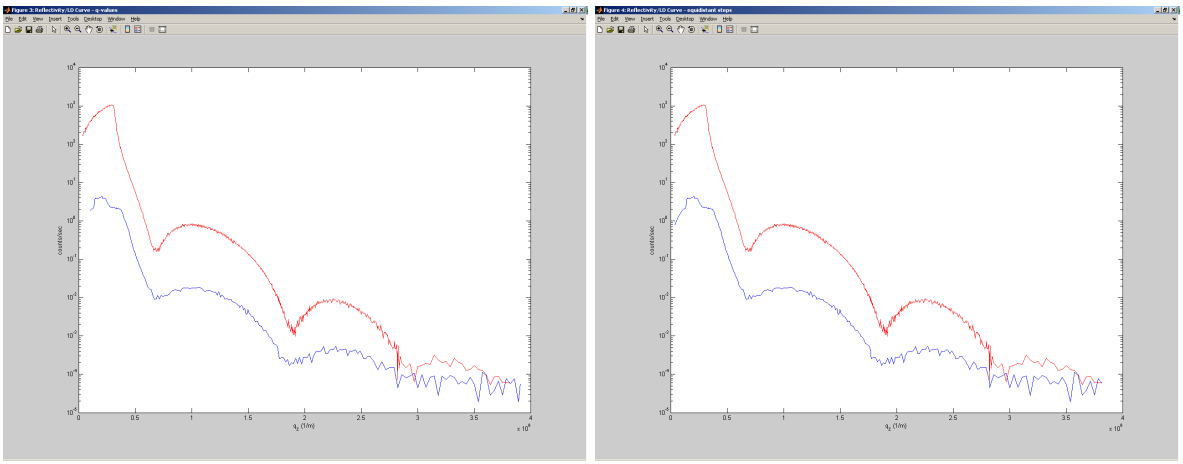

Figure E.6.: Screenshot of *D8opt* program: Conversion of the curves into q-space and calculation of equidistant q-steps.

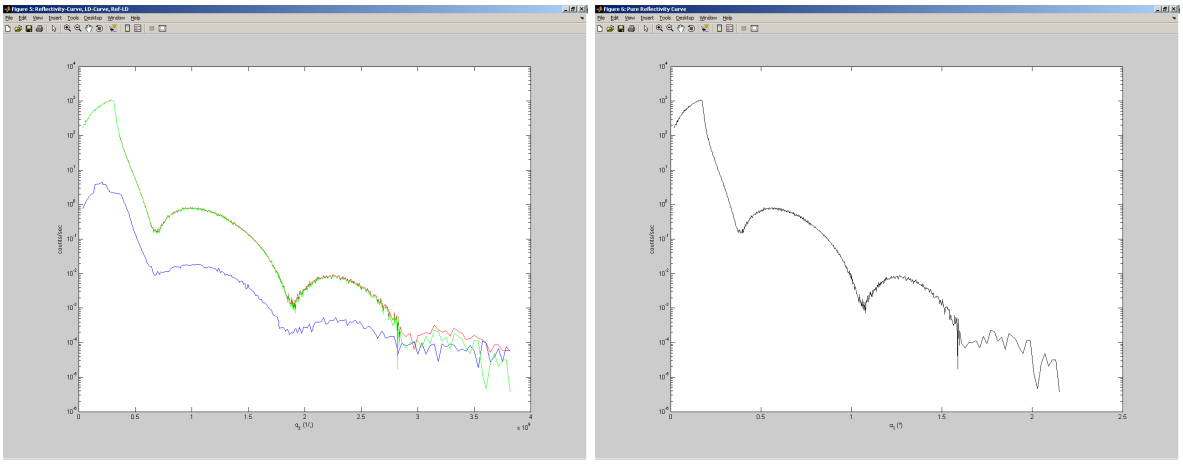

Figure E.7.: Screenshot of *D8opt* program: Difference between reflectivity and LD scan and conversion back into angle space.

F. Publications and posters related to this work

F.1. Publications in referred journals

Markus Krämer, Alex von Bohlen, Christian Sternemann, Michael Paulus and Roland Hergenröder
X-ray Standing Waves: A Method for Thin Layered Systems
Journal of Analytical Atomic Spectrometry 21, 1136-1142 (2006)

Cover picture of Journal of Analytical Atomic Spectrometry 21 (2006)
cf. figure F.1

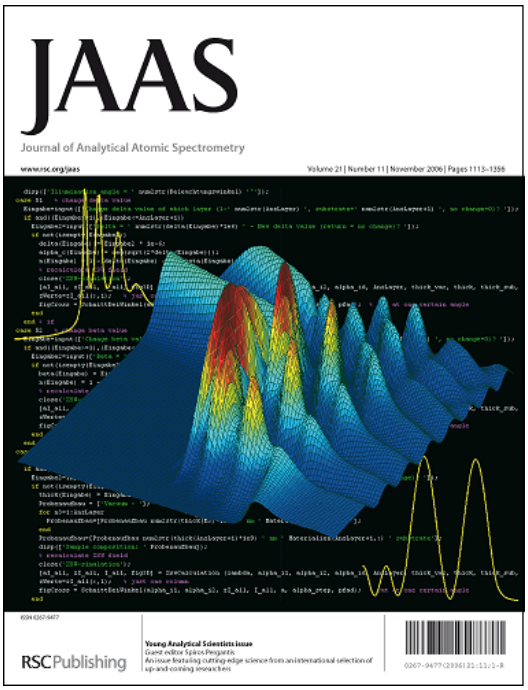

Figure F.1.: Cover picture of Journal of Analytical Atomic Spectrometry 21 (2006).

Alex von Bohlen, Markus Krämer, Roland Hergenröder and Ulf Berges
The ISAS Synchrotron Microprobe at DELTA
AIP Conference Proceedings 879, 852-855 (2006)

Markus Krämer, Alex von Bohlen, Christian Sternemann, Michael Paulus and Roland Hergenröder
Synchrotron Radiation Induced X-ray Standing Waves Analysis of Layered Structures
Applied Surface Science 253, 3533-3542 (2007)

F.2. Poster presentations

Alex von Bohlen and Markus Krämer
Dortmunder Wissenschaft und Archäologie
Tag des Offenen Denkmals, Dortmund-Asseln, Germany (12.09.2004)

Markus Krämer et al.
XSW - X-ray Standing Waves
ISAS Meeting of the Scientific Experts, ISAS, Dortmund, Germany (04.07.2005)

Markus Krämer et al.
Synchrotron Radiation Induced X-ray Standing Waves
11th Conference on Total Reflection X-ray Fluorescence Analysis and Related Methods (TXRF 2005), Budapest, Hungary (20.09.2005)
cf. figure F.2

Alex von Bohlen, Markus Krämer, Roland Hergenröder, Ulf Berges
The ISAS Synchrotron Microprobe at DELTA
SRI2006 Conference, Daegu, Korea (28.05.-02.06.2006)

Markus Krämer, Alex von Bohlen, Christian Sternemann, Roland Hergenröder
Standing Waves in Simulation and Experiment
European Conference on X-Ray Spectrometry (EXRS 2006), Paris, France (19.-23.06.2006)
Best scientific poster award, cf. figure F.2

Markus Krämer et al.
Material Analysis with Synchrotron Radiation
ISAS Meeting of the Scientific Experts, ISAS, Berlin, Germany (03.07.2006)

Roland Hergenröder, Markus Krämer, Alex von Bohlen
Analytical Applications of X-ray Micro Fluorescence
Deutsche Tagung für Forschung mit Synchrotronstrahlung, Neutronen und Ionenstrahlen an

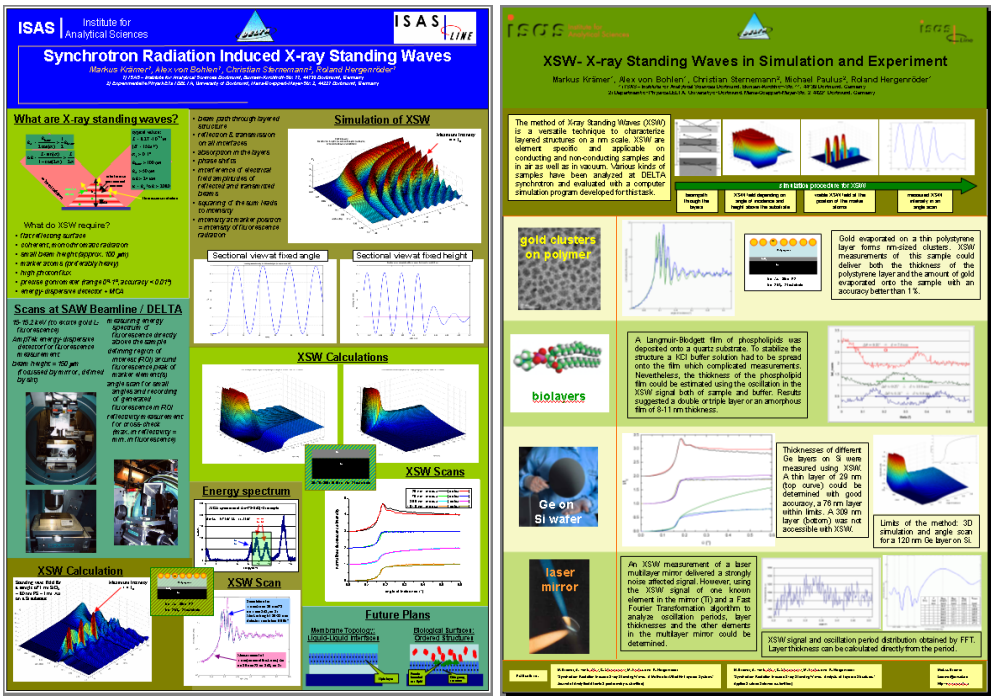

Figure F.2.: Poster presentations from TXRF2005 conference, Budapest, Hungary, and EXRS2006 conference, Paris, France.

Großgeräten 2006 (SNI2006), Hamburg, Germany (04.10.2006)

Markus Krämer et al.
Thin Film and Multilayer Analysis with Synchrotron Radiation Induced X-ray Standing Waves
Deutsche Tagung für Forschung mit Synchrotronstrahlung, Neutronen und Ionenstrahlen an Großgeräten 2006 (SNI2006), Hamburg, Germany (05.10.2006)

F.3. Invited talks

XSW - X-ray Standing Waves
DELTA Workshop, DELTA, Dortmund, Germany (25.04.2005)

Characterization of nitrobenzene films by X-ray reflectivity scans and x-ray standing waves
Institute for Analytical Sciences, Berlin, Germany (01.03.2006)

XSW - X-ray Standing Waves
Institute for Scientific Instruments (IfG), Berlin, Germany (05.05.2006)

F.4. Other talks

Application of Synchrotron Radiation in Material Analysis
Project meeting, ISAS, Dortmund, Germany (23.06.2004)

XSW Experiments at DELTA
Collaboration meeting Institute of Microstructure Technology, FZK, Karlsruhe and ISAS Dortmund, ISAS, Dortmund, Germany (27.07.2004)

X-ray Standing Waves and Test of Polymer Lenses at DELTA, Dortmund
Project meeting, ISAS, Dortmund (05.01.2005)

Justage-Genauigkeit am Goniometer
Meeting at beamline 9, DELTA, Dortmund, Germany (19.01.2005)

X-rays and organic samples
Collaboration meeting Biological-Chemical Microstructure Technology Group, Department of Chemistry, University of Dortmund, and ISAS Dortmund, ISAS, Dortmund, Germany (24.01.2005)

X-ray Standing Waves and Test of Polymer Lenses at DELTA
DELTA workshop, DELTA, Dortmund, Germany (01.04.2005)

XSW - X-ray Standing Waves
Project meeting, ISAS, Dortmund, Germany (29.06.2005)

XSW - X-ray Standing Waves at SAW2 Beamline
Delta Usermeeting, DELTA, Dortmund, Germany (30.11.2005)

XSW - X-ray Standing Waves
13. Anwendertreffen Röntgenfluoreszenz und Funkenemissionsspektrometrie, University of Applied Sciences Steinfurt/Münster, Germany (06.03.2006)

X-ray Standing Waves in the lab and on the screen
Project meeting, ISAS, Dortmund, Germany (11.10.2006)

X-ray Standing Waves created by Synchrotron Radiation and Computer Programs
Delta Usermeeting, DELTA, Dortmund, Germany (29.11.2006)

X-ray Standing Waves in Virtual and Real Space
PhD students seminar, ISAS, Dortmund, Germany (07.12.2006)

Bibliography

[1] F. Abelès
Recherches sur la propagation des ondes électromagnétiques sinosoïdales dans les milieux stratifiés. Application aux couches minces
Annales de Physique (Paris) 12, 596-640 and 706-782 (1950)

[2] Hannes Aiginger and Peter Wobrauschek
A Method for Quantitative X-ray Fluorescence Analysis in the Nanogram Region
Nuclear Instruments and Methods 114, 157-158 (1974)

[3] Avanti Polar Lipids, Inc.
Product info
Alabaster, AL 35007, USA
http://www.avantilipids.com/

[4] Lane A. Baker, Francis P. Zamborini, Li Sun and Richard M. Crooks
Dendrimer-Mediated Adhesion between Vapor-Deposited Au and Glass or Si Wafers
Analytical Chemistry 71, 4403-4406 (1999)

[5] J. A. Bearden
X-Ray Wavelengths
Reviews of Modern Physics 39, 78-124 (1967)

[6] J. A. Bearden and A. F. Burr
Reevaluation of X-Ray Atomic Energy Levels
Reviews of Modern Physics 39, 125-142 (1967)

[7] Uwe Beck
Ellipsometrie: Ein Reflexionsexperiment mit polarisiertem Licht
Journal für Oberflächentechnik 11, 14-19 (2000)

[8] B. Beckhoff, R. Fliegauf, M. Kolbe, M. Müller, B. Pollakowski, J. Weser and G. Ulm
X-ray Spectrometry for Wafer Contamination Analysis and Speciation as well as for Reference-Free Nanolayer Characterization
Proceedings of Ultra Clean Processing of Semiconductor Surfaces (UCPSS), Solid State Phenomena, in print (2007)

[9] B. Beckhoff, R. Fliegauf, G. Ulm, G. Pepponi, P. Wobrauschek, L. Fabry and S. Pahlke
Improvement of Total Reflection X-ray Fluorescence Analysis of Low Z Elements on Silicon Wafer Surfaces at the PTB Monochromator Beamline for Undulator Radiation at the Electron Storage Ring BESSY II
Spectrochimica Acta Part B 56, 2073-2083 (2001)

[10] Burkhard Beckhoff, Birgit Kanngießer, Norbert Langhoff, Reiner Wedell and Helmut Wolff (Eds.)
Handbook of Practical X-Ray Fluorescence Analysis
Springer, Berlin, Germany (2006)

[11] M. J. Bedzyk, G. M. Bommarito and J. S. Schildkraut
X-ray Standing Waves at a Reflecting Mirror Surface
Physical Review Letters 62, 1376-1379 (1989)

[12] Michael J. Bedzyk, G. Mark Bommarito, Martin Caffrey and Thomas L. Penner
Diffuse-Double Layer at a Membrane-Aqueous Interface Measured with X-ray Standing Waves
Science 248, 52-56 (1990)

[13] H. M. Berman, K. Henrick, H. Nakamura
Announcing the Worldwide Protein Data Bank
Nature Structural Biology 10, 980 (2003)

[14] Berliner Elektronenspeicherring-Gesellschaft für Synchrotronstrahlung (BESSY)
Albert-Einstein-Str. 15, 12489 Berlin, Germany
http://www.bessy.de/

[15] A. M. Bittner
Clusters on Soft Matter Surfaces
Surface Science Reports 61, 383-428 (2006)

[16] Katharine B. Blodgett and Irving Langmuir
Built-Up Films of Barium Stearate and their Optical Properties
Physical Review 51, 964-982 (1937)

[17] Angelo Bongiorno and Alfredo Pasquarello
Atomistic Structure of the Si(100)-SiO_2 Interface: A Synthesis of Experimental Data
Applied Physics Letters 83, 1417-1419 (2003)

[18] M. Born, E. Wolf
Principles of Optics
Pergamon Press, London, UK (1959)

[19] George Edward Pelham Box and Mervin Edgar Muller
A Note on the Generation of Random Normal Deviates
Annals of Mathematical Statistics 29, 610-611 (1958)

[20] J. M. Brandon
Chemtech 24, 42 (1994)

[21] Ilja N. Bronstein, Konstantin A. Semendjajew, Gerhard Musiol and Heiner Mühlig
Taschenbuch der Mathematik
4th edition, Verlag Harri Deutsch, Frankfurt am Main, Germany (1999)

[22] Michael Büchner
FT-ICR massenspektrometrische Untersuchungen: Gasphasen-Reaktivität ionisierter Halogenalkene gegenüber Nukleophilen
Dissertation at University of Bielefeld, Germany (2000)
http://bieson.ub.uni-bielefeld.de/volltexte/2003/326/pdf/0035.pdf

[23] Martin Caffrey and Jin Wang
Membrane-Structure Studies Using X-ray Standing Waves
Annual Review of Biophysics & Biomolecular Structure 28, 351-377 (1995)

[24] M. Cardona and L. Ley, Eds.
Photoemission in Solids I: General Principles
Springer-Verlag, Berlin, Germany (1978)

[25] Virginie Chamard
Université Paul Cezanne, Aix-Marseille, France
Personal notice

[26] David Leonard Chapman
Philosophical Magazine 25, 475 (1913)

[27] Likwan Cheng, Paul Fenter, Neil C. Sturchio, Zhong Zhong and Michael J. Bedzyk
X-ray Standing Wave Study of Arsenite Incorporation at the Calcite Surface
Geochimica et Cosmochimica Acta 63, 3153-3157 (1999)

[28] J. Christoffers
Organische Chemie für Verfahrensingenieure, Umweltschutztechniker und Werkstoffwissenschaftler
Lecture at Institut für Organische Chemie, Universität Stuttgart, Germany (2003)
http://www.uni-stuttgart.de/ochem/10/VLNFKap06.pdf

[29] Douglas H. Cole, Kenneth R. Shull, L. E. Rehn and P. Baldo
Metal-Polymer Interactions in a Polymery/Metal Nanocomposite
Physical Review Letters, 78, 5006-5009 (1997)

[30] J. W. Cooley and J. W. Tukey
An Algorithm for the Machine Computation of the Complex Fourier Series
Mathematics of Computation 19, 297-301 (1965)

[31] Center for X-Ray Optics, Lawrence Berkeley National Laboratory
X-Ray Interactions with Matter
http://www.cxro.lbl.gov/optical_constants/

[32] Dick K. G. de Boer
Glancing-Incidence X-ray Fluorescence of Layered Materials
Physical Review B 44, 498-511 (1991)

[33] Dortmunder Elektronen Speicherring Anlage
University of Dortmund, Dortmund, Germany
http://www.delta.uni-dortmund.de/

[34] Dendritech, Inc.
PAMAM dendrimers
3110 Schuette Drive, Midland, MI 48642, USA
http://www.dendritech.com/pamam.html

[35] V. R. Dhanak, A. G. Shard, S. D'Addato and A. Santoni
The Structure of ($\sqrt{3} \times \sqrt{3}$)R30° Iodine on Pd(111) Surface Studied by Normal Incidence X-ray Standing Wavefield Absorption
Chemical Physics Letters 306, 341-344 (1999)

[36] M. Drakopoulos, J. Zegenhagen, T.-J. Lee, A. Snigirev, I. Snigireva, V. Cimalla and O. Ambacher
GaN Polarity Domains Spatially Resolved by X-ray Standing Wave Microscopy
Journal of Physics D: Applied Physics 36, A214 (2003)

[37] Michael Drakopoulos, Jörg Zegenhagen, Anatoly Snigirev, Irina Snigireva, Maik Hauser, Karl Eberl, Vitalii Aristov, Leonid Shabelnikov and Vecheslav Yunkin
X-ray Standing Wave Microscopy: Chemical Microanalysis with Atomic Resolution
Applied Physics Letters 81, 2279 (2002)

[38] Jan Drenth
Principles of Protein X-Ray Crystallography
Springer-Verlag, Berlin, Germany (1999)

[39] P. Duhamel and M. Vetterli
Fast Fourier Transforms: A Tutorial Review and a State of the Art
Signal Processing 19, 259-299 (1990)

[40] Markus Dzyk
Beiträge zur Chemie einfacher Phosphor-Halogen-Verbindungen in den supersauren Systemen XF/MF_5 (X = H, D; M = As, Sb)
Dissertation at University of Dortmund, Germany (2000)
http://eldorado.uni-dortmund.de:8080/bitstream/2003/2425/1/dzykunt1.pdf

[41] Scott Feller
Lipid Coordinate Sets
Chemistry Department, Wabash College, Crawfordsville, IN 47933, USA
http://persweb.wabash.edu/facstaff/fellers/

[42] Robert Fendt
Strukturuntersuchungen an dünnen Flüssigkeitsfilmen
Diploma thesis at University of Dortmund, Germany (2003)

[43] J. B. Finean, R. Coleman and R. H. Michell
Membranes and their Cellular Functions
Blackwell, Oxford, UK (1974)

[44] Siegfried Finke
Versuchsanleitungen zum Anfänger-Praktikum in Physik
23th edition, Dortmund, Germany (1992)

[45] Siegfried Finke
Versuchsanleitungen zum Fortgeschrittenenpraktikum in Physik
25th edition, Dortmund, Germany (1999)

[46] Jörg Fitter
Vorlesung Kristallographie I
University of Tübingen, Tübingen, Germany
http://www.uni-tuebingen.de/uni/pki/skripten_jf/Krist_I_5.pdf

[47] J. A. Forrest and R. A. L. Jones
The Glass Transition and Relaxation Dynamics in Thin Polymer Films
in *Polymer Surfaces, Interfaces And Thin Films*
p. 251-294, World Scientific, Singapore (2000)

[48] M. Frigo and S. G. Johnson
FFTW: An Adaptive Software Architecture for the FFT
Proceedings of the International Conference on Acoustics, Speech, and Signal Processing 3, 1381-1384 (1998)
http://www.fftw.org

[49] John C. Fuggle and Nils Mårtensson
Core-Level Binding Energies in Metals
Journal of Electron Spectroscopy and Related Phenomena 21, 275-281 (1980)

[50] M. Gensch, K. Roodenko, K. Hinrichs, R. Hunger, A. G. Güell, A. Merson, U. Schade, Y. Shapira, Th. Dittrich, J. Rappich and N. Esser
Molecule-Solid Interfaces Studied with Infrared Ellipsometry: Ultrathin Nitrobenzene Films
Journal of Vacuum Science & Technology B 23, 1838-1842 (2005)

[51] S. K. Ghose and B. N. Dev
X-ray Standing Wave and Reflectometric Characterization of Multilayer Structures
Physical Review B 63, 245409 (2001)

[52] Louis Georges Gouy
Journal de Physique et le Radium 9, 457 (1910)

[53] Zenon Grabarek and John Gergely
Zero-Length Crosslinking Procedure with the Use of Active Esters
Analytical Biochemistry 185, 131-135 (1990)

[54] Frank Grunfeld
An Introduction to Langmuir-Blodgett Films
Nima Techology Ltd, Coventry, UK
http://www.nima.co.uk/downloads/lbpres.htm

[55] Hahn-Meitner Institute, Berlin, Germany
Abteilung Silizium-Photovoltaik, Kekuléstrasse 5, 12489 Berlin, Germany
http://www.hmi.de/

[56] Prosper Hartig, Thomas Dittrich and Jörg Rappich
Surface dipole formation and non-radiative recombination at p-Si(111) surfaces during electrochemical deposition of organic layers
Journal of Electroanalytical Chemistry 524-525, 120-126 (2002)

[57] Silvia Haupt
Pentahalogenide und Oxidhalogenide der Elemente der fünften Hauptgruppe - Pentahalides and oxyhalides from the elements of the 5th maingroup
Dissertation at Freie Universität Berlin, Germany (2002)
http://www.diss.fu-berlin.de/2002/30/

[58] Hermann von Helmholtz
Studien über electrische Grenzschichten
Annalen der Physik und Chemie 243, 337-382 (1879)

[59] B. L. Henke, E. M. Gullikson and J. C. Davis
X-ray Interactions: Photoabsorption, Scattering, Transmission, and Reflection at E=50-30000 eV, Z=1-92
Atomic Data and Nuclear Data Tables 54 (2), 181-342 (1993)

[60] Lars Hildebrand
Asymmetrische Evolutionsstrategien
Dissertation at University of Dortmund, Germany (2001)

[61] Karsten Hinrichs, Michael Gensch and Norbert Esser
Analysis of Organic Films and Interfacial Layers by Infrared Spectroscopic Ellipsometry
Applied Spectroscopy 59, 272A-282A (2005)

[62] Karsten Hinrichs, Michael Gensch, Arnulf Röseler and Norbert Esser
Infrared Ellipsometric Study on the Initial Stages of Oxide Growth on Si(001)
Journal of Physics: Condensed Matter 16, S4335-S4343 (2004)

[63] H. E. A. Huitema, G. H. Gelinck, J. B. P. H. van der Putten, K. E. Kuijk, C. M. Hart, E. Cantatore, P. T. Herwig, A. J. J. M. van Breemen and D. M. de Leeuw
Plastic transistors in active-matrix displays
Nature 414, 599 (2001)

[64] Jessica Irrgang, née Schöbel
Microstructure Technology Group, Department of Chemistry, University of Dortmund, Germany
Personal notice

[65] Terrence Jach, Y. Zhang, R. Colella, M. de Boissieu, M. Boudard, A. I. Goldman, T. A. Lograsso, D. W. Delaney and S. Kycia
Dynamical Diffraction and X-Ray Standing Waves from Atomic Planes Normal to a Twofold Symmetry Axis of the Quasicrystal AlPdMn
Physical Review Letters 82, 2904-2907 (1999)

[66] Shane Johnson
Technical Manual of the Imperial Forces
Modern Graphics, Rastatt, Germany (1995)

[67] Robert G. Jones, A. S. Y. Chan, M. G. Roper, M. P. Skegg, I. G. Shuttleworth, C. J. Fisher, G. J. Jackson, J. J. Lee, D. P. Woodruff, N. K. Singh and B. C. C. Cowie
X-ray Standing Waves at Surfaces
Journal of Physics: Condensed Matter 14, 4059-4074 (2002)

[68] K. Kago, H. Endo, H. Matsuoka, H. Yamaoka, N. Hamaya, M. Tanaka and T. Mori
Characterization of Thin Polymer Films by X-ray Reflectometry with Synchrotron Radiation
Journal of Synchrotron Radiation 5, 1304-1308 (1998)

[69] Robert A. Kellner, Jean-Michel Mermet, Matthias Otto and H. Michael Widmer (Eds.)
Analytical Chemistry
Wiley-VCH, Weinheim, Germany (1998)

[70] J. C. Kendrew, G. Bodo, H. M. Dintzis, R. G. Parrish, H. Wyckoff, D. C. Phillips
A Three-Dimensional Model of the Myoglobin Molecule Obtained by X-ray Analysis
Nature 181, 662-666 (1958)

[71] H. Kiessig
Interferenz von Röntgenstrahlen an dünnen Schichten
Annalen der Physik 10, 769 (1931)

[72] Reinhold Klockenkämper
Total-Reflection X-ray Fluorescence Analysis
John Wiley & Sons, New York, USA (1996)

[73] Reinhold Klockenkämper, H. W. Becker, H. Bubert, H. Jenett and Alex von Bohlen
Depth Profiles of a Shallow Implanted Layer in a Si Wafer Determined By Different Methods of Thin-Layer Analysis
Spectrochimica Acta Part B - Atomic Spectroscopy 57, 1593-1599 (2002)

[74] Reinhold Klockenkämper, Maria Becker, Alex von Bohlen, H. W. Becker, H. Krzyzanowska and L. Palmetshofer
Near-Surface Density of Ion-Implanted Si Studied by Rutherford Backscattering and Total-Reflection X-ray Fluorescence
Journal Of Applied Physics 98, 33517-1 - 33517-5 (2005)

[75] Reinhold Klockenkämper, H. Krzyzanowska and Alex von Bohlen
Density-Depth Profiles of an As-Implanted Si Wafer Studied by Repeated Planar Sputter Etching and Total Reflection X-ray Fluorescence Analysis
Surface And Interface Analysis 35, 829-834 (2003)

[76] Reinhold Klockenkämper and Alex von Bohlen
Determination of the Critical Thickness and the Sensitivity for Thin-Film Analysis by Total Reflection X-ray Fluorescence Spectrometry
Spectrochimica Acta Part B - Atomic Spectroscopy 44, 461-469 (1989)

[77] Reinhold Klockenkämper, Alex von Bohlen, H. W. Becker and L. Palmetshofer
Comparison of Shallow Depth Profiles of Cobalt-Implanted Si Wafers Determined by Total Reflection X-ray Fluorescence Analysis after Repeated Stratified Etching and by Rutherford Backscattering Spectrometry
Surface And Interface Analysis 27, 1003-1008 (1999)

[78] Donald Ervin Knuth
The Art of Computer Programming
Sec. 3.4.1, p. 117, Addison-Wesley Professional, Boston, USA (1997)

[79] Michael Kolbe, Burkhard Beckhoff, Michael Krumrey and Gerhard Ulm
Thickness Determination for Cu and Ni Nanolayers: Comparison of Completely Reference-Free Fundamental Parameter-Based X-ray Fluorescence Analysis and X-ray Reflectometry
Spectrochimica Acta Part B 60, 505-510 (2005)

[80] Martin Köckerling
Vorlesung Anorganische Chemie 1b
University of Rostock, Germany (2005)
http://www.chemie.uni-rostock.de/koeckerling/downloads/Anorg1b_7_Bindungen1.pdf

[81] Markus Krämer
Struktur und Dynamik von Gold-Clustern auf dünnen Polymer-Filmen: Untersuchungen mit kohärenter Röntgenstrahlung
Diploma thesis at University of Dortmund, Germany (2003)
http://e1.physik.uni-dortmund.de/e1anew/arbeiten/dipl_mkraemer.pdf

[82] Markus Krämer, Alex von Bohlen, Christian Sternemann, Michael Paulus and Roland Hergenröder
X-ray Standing Waves: A Method for Thin Layered Systems
Journal of Analytical Atomic Spectrometry 21, 1136-1142 (2006)

[83] Markus Krämer, Alex von Bohlen, Christian Sternemann, Michael Paulus and Roland Hergenröder
Synchrotron Radiation Induced X-ray Standing Waves Analysis of Layered Structures
Applied Surface Science 253, 3533-3542 (2007)

[84] M. O. Krause and J. H. Oliver
Natural Widths of Atomic K and L Levels, Kα X-Ray Lines and Several KLL Auger Lines
Journal of Physical and Chemical Reference Data 8, 329-338 (1979)

[85] C. Krywka, M. Paulus, C. Sternemann, M. Volmer, A. Remhoff, G. Nowak, A. Nefedov, B. Pöter, M. Spiegel and M. Tolan
The new diffractometer for surface X-ray diffraction at beamline BL9 of DELTA
Journal of Synchrotron Radiation 13, 8-13 (2006)

[86] Horst Kuchling
Taschenbuch der Physik
16th edition, Fachbuchverlag Leipzig, Germany (1996)

[87] G. Sasi Kumar, M. Raja and S. Parthasarathy
High performance electrodes with very low platinum loading for polymer electrolyte fuel cells
Electrochimica Acta 40, 285-290 (1995)

[88] T.-L. Lee and M. J. Bedzyk
High-resolution structural analysis of the Sb-terminated GaAs(001)-(2$\times$4) surface
Physical Review B 57, R15056-R15059 (1998)

[89] A.J.G. Leenaers and D.K.G. de Boer
WinGixa Software for Philips Diffractometers
Philips Analytical, MA, USA (1998)

[90] A. Lessmann, M. Schuster, H. Riechert, S. Brennan, A. Munkholm and G. Materlik
Fluorescence x-ray standing wave study on (AlAs)(GaAs) superlattices
Journal of Physics D: Applied Physics 32, A65-A70 (1999)

[91] LOT-Oriel Group Europe
Eigenschaften optischer Materialien
Darmstadt, Germany
http://www.lot-oriel.com/site/pages_de_de/useful_tips/useful_tips/optical_materials.php
(2006)

[92] Michael Mantler
LAMA III - a Computer Program for Quantitative XRFA of Bulk Specimens and Thin Film Layers
Advances in X-ray Analysis 27, 433-440 (1983)

[93] Michael Mantler
Recent Methods and Applications of X-ray Fluorescence Analysis
Progress in crystal growth and characterization of materials 14, 213-261 (1987)

[94] Michael Mantler
Quantitative XRFA of Light Elements by the Fundamental Parameter Method Advances in X-ray Analysis 36, 27-33 (1993)

[95] D. L. Marasco, A. Kazimirov, M. J. Bedzyk, T.-L. Lee, S. K. Streiffer, O. Auciello, and G.-R. Bai
Atomic-scale observation of polarization switching in epitaxial ferroelectric thin films
Applied Physics Letters 79, 515-517 (2001)

[96] Jianwei Miao, Pambos Charalambous, Janos Kirz and David Sayre
Extending the Methodology of X-ray Crystallography to allow Imaging of Micrometre-sized Non-crystalline Specimens
Nature 400, 342 (1999)

[97] Jianwei Miao, Keith O. Hodgson and David Sayre
An Approach to Three-Dimensional Structures of Biomolecules by Using Single-Molecule Diffraction Images
Proceedings of the National Academy of Sciences 98, 6641-6645 (2001)

[98] Otto Moeschlin, Eugen Grycko, Claudia Pohl and Frank Steinert
Experimental Stochastics
Springer, Berlin, Germany (1997)

[99] Peter J. Mohr and Barry N. Taylor
CODATA recommended values of the fundamental physical constants: 2002
Reviews Of Modern Physics 77, 1-107 (2005)

[100] Gerardus Johannes Mulder
On the Composition of some Animal Substances
Journal für praktische Chemie 16, 129 (1839)

[101] Matthias Müller, Burkhard Beckhoff, Gerhard Ulm and Birgit Kanngießer
Absolute Determination of Cross Sections for Resonant Raman Scattering on Silicon
Physical Review A 74, 012702 (2006)

[102] Shinichiro Nakatani, Kazushi Sumitani, Akinobu Nojima, Toshio Takahashi, Keiichi Irano, Shinji Koh, Toshifumi Irisawa and Yasuhiro Shiraki
Characterization of Amorphous-Si/1ML-Ge/Si(001) Interface Structureby X-ray Standing Waves
Japanese Journal of Applied Physics 42, 7050-7052 (2003)

[103] V. Nazmov, E. Reznikova, M. Boerner, J. Mohr, V. Saile, A. Snigirev, I. Snigireva, M. DiMichiel, M. Drakopoulos, R. Simon and M. Grigoriev
Refractive Lenses Fabricated by Deep SR Lithography and LIGA Technology for X-ray Energies from 1 keV to 1 MeV
Conference on Synchrotron Radiation Instrumentation (SRI 03), San Francisco, CA, USA (2003)

[104] V. Nazmov, E. Reznikova, J. Mohr, A. Snigirev, I. Snigireva, S. Achenbach, V. Saile
Fabrication and Preliminary Testing of X-ray Lenses in Thick SU-8 Resist Layers
Workshop on High Aspect Ratio Micro Structure Technology (HARMST), Monterey, CA, USA (2003)

[105] Vladimir Nazmov, Elena Reznikova, Andrea Somogyi, Jürgen Mohr and Volker Saile
Planar Sets of Cross X-ray Refractive Lenses from SU-8 Polymer
SPIE 49th Annual Meeting, Denver, CO, USA (2004)

[106] José R. Brandao Neto
X-ray Absorption in 2D Protein Crystals
CCP4 Newsletter on Protein Crystallography (2002)
http://www.ccp4.ac.uk/newsletters/newsletter40/00_contents.html

[107] Richard Neutze, Remco Wouts, David van der Spoel, Edgar Weckert and Janos Hajdu
Potential for Biomolecular Imaging with Femtosecond X-ray Pulses
Nature 406, 752 (2000)

[108] Christof M. Niemeyer & Group
Microarray technologies
Department of Chemistry, University of Dortmund, Germany
http://www.chemie.uni-dortmund.de/groups/niemeyer/

[109] National Institute of Standards and Technology
The NIST Reference on Constants, Units, and Uncertainty
http://physics.nist.gov/cuu/Constants/ (2002)

[110] V. Nitz, M. Tolan, J.-P. Schlomka, O. H. Seeck, J. Stettner, W. Press, M. Stelzle and E. Sackmann

Correlations in the Interface Structure of Langmuir-Blodgett Films Observed by X-ray Scattering
Physical Review B 54, 5038-5050 (1996)

[111] Haruhiko Ono, Taeko Ikarashi, Koichi Ando and Tomohisa Kitano
Infrared studies of transition layers at SiO_2/Si interface
Journal Of Applied Physics 84, 6064-6069 (1998)

[112] A. V. Oppenheim and R. W. Schafer
Discrete-Time Signal Processing
p. 611-619, Prentice-Hall, Upper Saddle River, New Jersey, USA (1989)

[113] L. G. Parrat
Surface Studies of Solids by Total Refection of X-Rays
Physical Review 95, 359-369 (1954)

[114] Michael Paulus
DELTA, University of Dortmund, Germany
Personal notice

[115] Pierce Biotechnology, Rockford, IL, USA
NHS and Sulfo-NHS - Instructions
http://www.piercenet.com

[116] PolymerProcessing.com
Information, Education, Resources and Expertise in the Field of Polymer Processing
http://www.polymerprocessing.com/polymers/

[117] Philip J. Potts, Andrew T. Ellis, Peter Kregsamer, Christina Streli, Christine Vanhoof, Margaret West and Peter Wobrauschek
Atomic Spectrometry Update - X-ray Fluorescence Spectrometry
Journal of Analytical Atomic Spectrometry 21, 1076-1107 (2006)

[118] Physikalisch-Technische Bundesanstalt (PTB)
Zahlenwerte wichtiger Naturkonstanten
http://www.ptb.de/de/naturkonstanten/_zahlenwerte.html (2002)

[119] Physikalisch-Technische Bundesanstalt (PTB)
X-ray Spectrometry Group
Abbestr. 2-12, 10587 Berlin, Germany
http://www.ptb.de

[120] C. M. Rader
Discrete Fourier Transforms when the Number of Data Samples Is Prime
Proceedings of the IEEE 56, 1107-1108 (1998)

[121] Jörg Rappich, Alexandra Merson, Katy Roodenko, Thomas Dittrich, Michael Gensch, Karsten Hinrichs and Yoram Shapira
Electronic Properties of Si Surfaces and Side Reactions during Electrochemical Grafting of Phenyl Layers
Journal of Physical Chemistry B 110, 1332-1337 (2006)

[122] Dirk O. Riese, Willem L. Vos, Gerard H. Wegdam and Frank J. Poelwijk; Douglas L. Abernathy and Gerhard Grübel
Photon Correlation Spectroscopy: X Rays versus Visible Light
Physical Review E 61, 1676-1680 (2000)

[123] J. A. Robinson
CHE 151.1: Organische Chemie für die Biologie
Lecture at Department Chemistry-Biochemistry, University of Zurich, Switzerland (2005)
http://www.oci.unizh.ch/edu/lectures/material/AC_BII/kap1.pdf

[124] Katy Roodenko
Interface Spectroscopy Group, ISAS - Institute for Analytical Sciences, Department Berlin Berlin, Germany
Personal notice

[125] Dilano K. Saldin
Protein X-ray Crystallography
University of Wisconsin, Milwaukee, USA
http://hermes.phys.uwm.edu/index.html

[126] Oliver Salomon
Charakterisierung des Ladungstransfers von immobilisiertem Cytochrom c
Dissertation at Fakultät für Mathematik, Informatik und Naturwissenschaften an der Rheinisch-Westfälischen Technischen Hochschule Aachen, Germany (2006)
http://darwin.bth.rwth-aachen.de/opus/volltexte/2006/1525/pdf/Salomon_Oliver.pdf

[127] G. Scherb, A. Kazimirov, J. Zegenhagen, T. L. Lee, M. J. Bedzyk, H. Noguchi and K. Uosaki
In Situ X-ray Standing-Wave Analysis of Electrodeposited Cu Monolayers on GaAs(001)
Physical Review B 58, 10800 (1998)

[128] D. Schirmer, U. Berges, J. Friedl, A. Gasper, M. Grewe, P. Hartmann, R. Heine, H. Huck, G. Schmidt, C. Sternemann, M. Tolan, T. Weis, C. Westphal, K. Wille and N. Zebralla
Status of the Synchrotron Light Source Delta
Procedings of The EPAC 2004, Lucerne, Switzerland 2296-2298 (2004)

[129] Jens-Peter Schlomka
Untersuchung von Schichtsystemen und lateral strukturierten Oberflächen mit Röntgenstreuung im Bereich der Totalreflexion

Diploma Thesis at Christian-Albrechts-Universität, Kiel, Germany (1994)
http://www.ieap.uni-kiel.de/solid/ag-press/r/zip/jpsdiplo.zip

[130] F. Scholze, B. Beckhoff, G. Brandt, R. Fliegauf, A. Gottwald, R. Klein, B. Meyer, U. Schwarz, R. Thornagel, J. Tümmler, K. Vogel, J. Weser and G. Ulm
High-Accuracy EUV Metrology of PTB Using Synchrotron Radiation
Proceedings of SPIE - The International Society for Optical Engineering 4344, 50 (2001)

[131] F. Schreiber, K. A. Ritley, I. A. Vartanyants, H. Dosch, J. Zegenhagen and B. C. C. Cowie
Non-dipolar Effects in X-ray Photoemission Investigated with X-ray Standing Waves
European Synchrotron Radiation Facility (ESRF), Grenoble, France (2001)
http://www.esrf.fr/info/science/highlights/2001/surfaces/SURF1.html

[132] F. Schreiber, K. A. Ritley, I. A. Vartanyants, H. Dosch, J. Zegenhagen and B. C. C. Cowie
Non-dipolar contributions in XPS detection of X-ray standing waves
Surface Science Letters 486, L519 (2001)

[133] Oliver Seeck
Untersuchung des Wetting-Systems CCl_4 auf Si-SiO_2 mittels diffuser Röntgenstreuung
Diploma Thesis at Christian-Albrechts-Universität, Kiel, Germany (1993)
http://www.ieap.uni-kiel.de/solid/ag-press/r/zip/ohsdipps.zip

[134] O. H. Seeck, I. D. Kaendler, M. Tolan, K. Shin, M. H. Rafailovich, J. Sokolov and R. Kolb
Analysis of X-ray Reflectivity Data from Low-Contrast Polymer Bilayer Systems Using a Fourier Method
Applied Physics Letters 76, 2713-2715 (2000)

[135] O. H. Seeck, C. Nöldeke, S. Grieger and V.Nitz
LsFit
Least-Square Fit-Program for Reflectivity Curves of Layered Systems

[136] F. Senf, U. Flechsig, F. Eggenstein, W. Gudat, R. Klein, H. Rabus and G. Ulm
A Plane-Grating Monochromator Beamline for the PTB Undulators at BESSY II
Journal of Synchrotron Radiation 5, 780-782 (1998)

[137] Tilo Seydel, Anders Madsen, Metin Tolan, Gerhard Grübel and Werner Press
Capillary Waves in Slow Motion
Physical Review B 63, 73409-1 - 73409-4 (2001)

[138] Leonid Shabel'nikov, Vladimir Nazmov, Franz J. Pantenburg, Juergen Mohr, Volker Saile, Vecheslav Yunkin, Sergey Kouznetsov, Valery F. Pindyurin, Irina Snigireva and Anatoly A. Snigirev
X-ray Lens with Kinoform Refractive Profile Created by X-ray Lithography
Proceedings of SPIE - The International Society for Optical Engineering 4783, 176-184 (2002)

[139] S. K. Sinha, E. B. Sirota, S. Garoff and H. B. Stanley
X-Ray and Neutron Scattering from Rough Surfaces
Physical Review B 38, 2297-2311 (1988)

[140] Anatoly A. Snigirev, Irina Snigireva, Michael Drakopoulos, Vladimir Nazmov, Elena Reznikova, Sergey Kuznetsov, Maxim Grigoriev, Jürgen Mohr and Volker Saile
Focusing Properties of X-ray Polymer Refractive Lenses from SU-8 Resist Layer
Proceedings of SPIE - The International Society for Optical Engineering 5195, 21 (2003)

[141] Otto Stern
Zeitschrift für Elektrochemie 30, 508 (1924)

[142] Christian Sternemann
DELTA synchrotron facility, University of Dortmund, Germany
Personal notice

[143] Jochim Stettner
Charakterisierung von rauhen MBE-$CoSi_2$/Si-Schichtsystemen mittels Röntgenbeugung
Dissertation at Christian-Albrechts-Universität, Kiel, Germany (1995)

[144] Horst Stöcker
Taschenbuch der Physik
3rd edition, Verlag Harri Deutsch, Frankfurt am Main, Germany (1998)

[145] Simone Streit
Lehrstuhl E1a, Department of Physics, University of Dortmund, Germany
Personal notice

[146] Albert C. Thompson, David T. Attwood, Eric M. Gullikson, Malcolm R. Howells, Kwang-Je Kim, Janos Kirz, Jeffrey B. Kortright, Ingolf Lindau, Piero Pianetta, Arthur L. Robinson, James H. Scofield, James H. Underwood, Douglas Vaughan, Gwyn P. Williams and Herman Winick
X-ray Data Booklet
Lawrence Berkeley National Laboratory, University of California, USA (2001)

[147] T. Thurn-Albrecht, W. Steffen, A. Patkowski, G. Meier and E. W. Fischer; G. Grübel and D. L. Abernathy
Photon Correlation Spectroscopy of Colloidal Palladium using a Coherent X-Ray Beam
Physical Review Letters 77, 5437 (1996)

[148] B. P. Tinkham, D. M. Goodner, D. A. Walko, and M. J. Bedzyk
X-ray studies of Si/Ge/Si(001) epitaxial growth with Te as a surfactant
Physical Review B 67, 035404 (2003)

[149] Metin Tolan
X-Ray Scattering from Soft Matter Thin Films -Materials Science and Basic Research-
Springer-Verlag, Berlin, Germany (1999)

[150] M. Tolan, T. Weis, K. Wille and C. Westphal
DELTA: Synchrotron Light in Nordrhein-Westfalen
Synchrotron Radiation News 16, 9-11 (2003)

[151] Thomas P. Trainor, Alexis S. Templeton, Gordon E. Brown Jr. and George A. Parks
Application of the Long-Period X-ray Standing Wave Technique to the Analysis of Surface reactivity: Pb(II) Sorption at α-Al_2O_3/Aqueous Solution Interfaces in the Presence and Absence of Se(VI)
Langmuir 18, 5782-5791 (2002)

[152] T. P. Trainor, A. S. Templeton and P. J. Eng
Structure and Reactivity of Environmental Interfaces: Application of Grazing Angle X-ray Spectroscopy and Long-Period X-ray Standing Waves
Journal Of Electron Spectroscopy And Related Phenomena 150, 66-85 (2006)

[153] G. K. Ujhelyi and S. T. Ribeiro
An Electro-Optical Light Intensity Modulator
Proceedings of the IEEE 52, 845 (1964)

[154] University of Waterloo, Faculty of Science
200 University Avenue West, Waterloo, Ontario, Canada
Cyberspace Chemistry (CaCt)
http://www.science.uwaterloo.ca/ cchieh/cact/c120/bondel.html

[155] U.S. Environmental Protection Agency
Nitrobenzene Fact Sheet: Support Document
OPPT Chemical Fact Sheets, CAS No. 98-95-3 (1995)
http://www.epa.gov/chemfact/

[156] Donald Voet, Judith G. Voet and Charlotte W. Pratt; Annette G. Beck-Sickinger and Ulrich Hahn (Editors)
Lehrbuch der Biochemie / Fundamentals of Biochemistry
Wiley-VCH, Weinheim, Germany (2002)

[157] Helmut Vogel
Gerthsen Physik
20th edition, Springer-Verlag, Berlin, Germany (1999)

[158] Alex von Bohlen
Material Analysis Division, ISAS - Institute for Analytical Sciences
Dortmund, Germany
Personal notice

[159] Alex von Bohlen, Markus Krämer, Roland Hergenröder and Ulf Berges
The ISAS Synchrotron Microprobe at DELTA
AIP Conference Proceedings 879, 852-855 (2006)

[160] Jin Wang
X-ray Standing Waves and their Use in Characterizing Biologically Relevant Thin Film Systems
Doctoral dissertation at Ohio State University, Columbus, OH, USA (1994)

[161] Jin Wang, Michael J. Bedzyk and Martin Caffrey
Resonance Enhanced X-rays in Thin Films: A Structure Probe for Membranes and Surface Layers
Science 258, 775-778 (1992)

[162] Jin Wang, Martin Caffrey, Michael J. Bedzyk and Thomas L. Penner
Structure Changes in Model Membranes Monitored by Variable Period X-ray Standing Waves: Effect of Langmuir-Blodgett Film Thickness on Thermal Behavior
Journal of Physical Chemistry 98, 10957-10968 (1994)

[163] Jin Wang, Martin Caffrey, Michael J. Bedzyk and Thomas L. Penner
Direct Profiling and Reversibility of Ion Distribution at a Charged Membrane/Aqueous Interface: An X-ray Standing Wave Study
Langmuir 17, 3671-3681 (2001)

[164] Rüdiger Weber
Oberflächenempfindliche Röntgenstreuung an Polymer-Metall-Grenzflächen: Strukturelle Eigenschaften und thermisches Verhalten
Dissertation at Christian-Albrechts-Universität, Kiel, Germany (2002)
http://www.ieap.uni-kiel.de/solid/ag-press/r/pd/diss/diss_rw.pdf

[165] Wikipedia - The free encyclopedia
http://en.wikipedia.org/

[166] Wikipedia - Die freie Enzyklopädie
http://de.wikipedia.org/

[167] David L. Windt
IMD-Software for Modeling the Optical Properties of Multilayer Films
Computers in Physics, 12 360-370 (1998) http://www.rxollc.com/idl/index.html
http://ftp.esrf.eu/pub/scisoft/xop2.1/Windows/Extensions/

[168] C. P. Wong, Ed.
Polymers for Electronic and Photonic Applications
Academic Press, Boston, USA (1993)

[169] Worldwide Protein Data Bank
http://www.wwpdb.org/

[170] Y. Yoneda and T. Horiuchi
Optical Flats for Use in X-ray Spectrochemical Microanalysis
Review of Scientific Instruments 42, 1069-1070 (1971)

[171] Jörg Zegenhagen
Surface structure determination with X-ray standing waves
Surface Science Reports 18, 199-271 (1993)

[172] Jörg Zegenhagen, Gerhard Materlik and W. Uelhoff
X-ray Standing Wave Analysis of Highly Perfect Cu Crystals and Electrodeposited Submonolayers of Cd and Tl on Cu Surfaces
Journal of X-Ray Science and Technology 2, 214-239 (1990)

[173] Zeta-Meter Inc.
Zeta Potential: A Complete Course in 5 Minutes
Staunton, VA, USA
http://www.zeta-meter.com/5min.pdf (2006)

[174] Ruitian Zhang, Rosangela Itri and Martin Caffrey
Membrane Structure Characterization Using Variable-Period X-Ray Standing Waves
Biophysical Journal 74, 1924-1936 (1998)

[175] S. I. Zheludeva, M. V. Kovalchuk, N. N. Novikova, A. N. Sosphenov, N. E. Malysheva, N. N. Salashenko, A. D. Akhsakhalyan and Yu. Yu. Platonov
X-ray waveguide structures of thin metal-carbon layers
Journal de Physique III France 4, 1581-1587 (1994)

[176] S. Zheludeva, M. Kovalchuk and N. Novikova
Total reflection X-ray fluorescence study of organic nanostructures
Spectrochimica Acta Part B - Atomic Spectroscopy 56, 2019-2026 (2001)

[177] Dunja Zimmermann
Department of Metabolomics, ISAS - Institute for Analytical Sciences
Dortmund, Germany
Personal notice

Index

Acknowledgements

With magic, you can turn a frog into a prince.
With science, you can turn a frog into a PhD
and you still have the frog you started with.

Terry Pratchett, *The Science of Discworld*

In any case, this frog will never be able to turn into a PhD without the help others. Thus, here I would like to thank all the people whose assistance gave me the opportunity to accomplish this PhD thesis.

Prof. Dr. K. Niemax offered me a this interesting PhD student position at ISAS Dortmund and *Prof. Dr. M. Tolan* gave me the possibility to perform my measurements at "his" synchrotron and beamline, not to forget the invaluable experiences and skills I obtained while working on my diploma thesis in his group. Finally, I would like to thank *Prof. Dr. W. Weber* to sacrifice his time to be a third referee in my PhD exam. *Dr. Roland Hergenröder* and *Alex von Bohlen* (ISAS Dortmund) were the best tutors a student could expect for my time as a PhD student. Being open for every question and - that was as important as answering - permanently asking me interesting questions, giving uncountable useful suggestions and always having "an interesting sample in the drawer" they shaped this work a lot. Not to forget the hours they spent with me performing measurements or proofreading my thesis. I want to address a very special thank you to *Dr. Christian Sternemann* and *Dr. Michael Paulus* (DELTA Dortmund). Without them experiments at DELTA would never have been successful. Knowing their beamline BL9 better than anybody else they always had a solution and never left us alone before everything was running even if it already was deep in the night. Of course also *Dr. Martin Volmer*, *Chris Krywka* and the entire *DELTA crew* did their best to provide the precious synchrotron beam and any information we required. *Dr. Lars Hildebrand* and *Hyung-Won Koh* (LS1, University of Dortmund) were very helpful with every problem that occurred while I was developing my *MXSW* simulation program. We experienced that cooperation between physicists and computer scientists can be very fruitful. And sharing an office for a day a week was always a nice time. The cooperation with *Jessica Irrgang* and *Prof. Dr. C. M. Niemeyer* (University of Dortmund) gave me the possibility to analyze a number of interesting biological samples. Further, I would especially like to thank Jessica Irrgang for proofreading my "physicist's biology texts" and for explaining to me the interesting

field of biochemistry. *Beatrix Pollakowski* (PTB Berlin) was another lone fighter in the field of grazing incidence XSW I met during a visit in Berlin. Thus, we decided to ally and thanks to an invitation from *Dr. Burkhard Beckhoff* (PTB Berlin) we had the possibility to do some interesting measurements in Berlin. I also want to thank *Katy Roodenko* (ISAS Berlin) and *Jörg Rappich* (HMI Berlin) for preparing the nitrobenzene samples and giving a lot of useful information. *Simone Streit* and *Dr. Thomas Irawan* (E1a, University of Dortmund), my former fellow students and roommates during my diploma time were still helpful after I went to ISAS. Further, Simone provided the polymer samples and gave a lot of helpful information. *Dr. Dunja Zimmermann* and *Dr. Peter Jacob* (ISAS Dortmund) helped me to prepare the cytochrome samples and could give a lot of biological and chemical assistance. *Mr. Krebs*, *Mr. Lonzynski*, *Mr. Röper* and the entire crew of the *ISAS mechanical workshop* as well as *Mr. Ackermann*, *Mr. Wilberg* and *Mr. Heming* from the *ISAS electronic workshop* were the "magicians" that turned a scientist's idea into reality, namely constructing the sample cell and any other small and big device we needed. *Mr. Weil* and *Mrs. Kleene* (ISAS construction office) being the connecting link between idea and product and also "masters" of the plotter and poster printer were often responsible for making science visible while *Dr. Hillig*, *Mr. Schubert* and *Mrs. Jepkens* (ISAS network and computer assistance) cared for my computer and Internet connection. *Walter van den Hoogenhof* and *Peter Brouwer* (PANalytical Almelo), experts in X-ray fluorescence and XSW, gave me useful hints for my *MXSW* program. *Gabriela But*, *Maria Becker* and *Dr. Natalie Palina* (ISAS Dortmund) spent many days and also some nights at DELTA during my beamtimes. My roommates *Dr. Jörg Lambert* and *Dr. André Kurowski* (ISAS Dortmund) were among the people I spent most of my time with and I can say that there was not a single boring day. *Dr. Evgeny Gurevich*, *Silke Kittel*, *Dr. Ota Samek*, *Helmut Lindner*, *Daniel Boecker*, *Yilmaz Gerikalan*, *Dr. Carmen Garcia* and all other present and former members of the great *ISAS Material Analysis group* were responsible for a wonderful working atmosphere at the institute. And *Kaoru Tachikawa*, *Sabine Bader*, *Hendrik Kortmann*, *Sandor Bessenyei*, *Michelle Hartmann* and the other *fellow PhD students* were more than just colleagues or "fellow sufferers". We had a funtastic time together and I hope that we won't lose contact after leaving into life after university. Although the work I was doing might be a mystery or magic to them, my family, namely my parents *Margret* and *Werner Krämer* and grandparents *Matthäus Ockenfels* and *Annelies Krämer*, supported me in all fields but science during my PhD time. Thus, I would like to state that I am glad to be the first PhD in *this* family. Last but not least, I want to say thank you to my wonderful and precious *Solveig*, the best girlfriend I can imagine, for the great time we had and have together, for always supporting and motivating me, and for being insightful concerning the working hours of a physicist, now and in the future.